Semiconductor Nanocrystals as Antennae for Luminescent Lanthanide Cations

by

Adrienne Michelle Yingling

B.S. in Biochemistry, Chatham College, 2003

Submitted to the Graduate Faculty of

Arts and Sciences in partial fulfillment

of the requirements for the degree of

Doctor of Philosophy

University of Pittsburgh

2009

UNIVERSITY OF PITTSBURGH

Faculty of Arts and Sciences

This dissertation was presented

by

Adrienne Michelle Yingling

It was defended on

July 28, 2008

and approved by

Dr. Marcel Bruchez, Associate Research Professor, Department of Chemistry, Carnegie Mellon University

Dr. Tara Y. Meyer, Associate Professor, Department of Chemistry

Dr. Nathanial Rosi, Assistant Professor, Department of Chemistry

Dissertation Advisor: Dr. Stéphane Petoud, Assistant Professor, Department of Chemistry

Copyright © by Adrienne Michelle Yingling

2009

Semiconductor Nanocrystals as Antennae for Luminescent Lanthanide Cations

Adrienne Michelle Yingling, PhD

University of Pittsburgh, 2009

As biological assays involving fluorophores become more prevalent, due to their high sensitivity, moderate cost and versatility for applications, there is an increasing demand for luminescent reporters with advanced properties for use in bioanalytical applications and biological imaging. The most important properties include the strong resistance to photobleaching and the ability to be discriminated from background fluorescence (biological autofluorescence). We have initiated an innovative strategy to create luminescent reporters possessing the photophysical properties that fulfill these requirements by combining the advantages of semiconductor nanocrystals (tunable emission bands, large epsilon values, and high photostabililty) with those of lanthanide cations (sharp emission bands, long luminescence lifetimes, and resistance to photobleaching). This work is aimed at creating novel antenna for the sensitization of luminescent lanthanide cations emitting in the visible and in the near-infrared. The crystals structure of semiconductor nanocrystals is also used to protect the lanthanides from nonradiative deactivations inducing the increase of the quantum yields. In additions, this synthetic strategy will allow the formation of polymetallic luminescence species, where the high density of lanthanide cations per units of volume will induce an increased number of emitted photons, a desirable condition to increase luminescence detection sensitivity.

Photophysical and structural characterization of various lanthanide containing nanocrystal materials have been studied, including CdSe:Ln, ZnS;Ln, ZnSe:Ln and LnS. The

coating of the surface of the nanocrystals in order to control their properties is also discussed in this work.

ACKNOWLEDGEMENTS

There are many individuals that have tremendously contributed to the completion of my Ph.D. First I would like to thank Professor Stephane Petoud, my advisor and mentor throughout my graduate career. I thank him for his patience and understanding over the years and am I grateful for all the opportunities I had while in his research group.

I would like to thank the members of my committee, who have also shown a great deal of patience and understanding throughout this entire process: Prof. Tara Meyer, who has not only served as a member of my committee and my proposal mentor, but she has also served as an inspiration for me over the years; Prof. Nathaniel Rosi, who has served on both my proposal and thesis committees; and Prof. Marcel Bruchez at Carnegie Mellon University, who has served as a member of my committee and as a source of inspiration for the described research – Marcel is a pioneer in the field and I am grateful for having the chance to meet and discuss research with him over the years.

Without my fellow group members, both past and present, I probably would not have made it through this process. I thank you for your encouragement and support over the years. These members include, but are not limited to Dr. Paul Badger, Dr. Jason Cross, Dr. Jian Zhang, Demetra Chengelis Czegan, Matthew Lockett, Hyounsoo Uh, David Oxley, Chad Shade, Kristy Gogick, and the many undergraduate researchers with whom I had the pleasure of working.

I would like to thank all of the individuals and shops that provided support throughout the research: Albert Stewart (EDAX/SEM), Joseph Suhan (TEM), Electronics shop (Chuck Fleishaker, Bob Muha, Dave Emala, and Jim McNerney), Machine shop (Tom Gasmire and Jeff Sicher), and anyone else whose name I may have mistakenly omitted. I would also like to thank Fran Nagy for all of her patience, guidance and support over the years. I truly believe that without Fran many of us would be in trouble.

Lastly I would like to thank my family. I am grateful to have all of you in my life and I am very grateful for all of the support you have shown me over the years. I thank my mother and father, who have put up with all of the years of school and insanity and have provided a great deal of love and support, my brother Sean, for just being an inspiration and putting a smile on my face when I truly need it, my sisters (Hollie and Stacey) and their families for their support and for only slightly making fun of me for being in school so long, and finally my husband, David (Sam) who I met in graduate school and who has been a source of love and support over the years – I cannot imagine what the Petoud group would have been like without you. I love you all very much!

TABLE OF CONTENTS

LIST OF TABLES

LIST OF FIGURES

1.0 INTRODUCTION

Due to their unique electron configuration, lanthanide cations have special luminescence properties that are highly desirable for *in vivo* and *in vitro* bioanalytical and imaging applications and can complement or replace widely used fluorophores such as organic dyes and semiconductor nanocrystals[1-3]. Among these properties, several lanthanides have electronic structures which are suitable for emission in the visible and NIR domains. Since the emission bands arise from f → f transitions, and the f-orbitals are only marginally involved in chemical bonding, lanthanide metal ions emit as sharp atom-like bands, even when bound to ligands in solution or doped in a solid matrix (e.g. Nd:YAG laser). The band maxima positions do not shift upon change of the experimental conditions (temperature, pressure, solvent, etc.). The sharp bands allow simple discrimination between signals arising from different cations, making lanthanide cations excellent candidates for multiplex analysis.

In addition to their spectral discrimination, lanthanide cations have luminescent decay profiles in the micro- to millisecond range and offer excellent temporal discrimination from fluorescence. The presence of short-lived background fluorescence arising from biological molecules (autofluorescence) is a major limiting factor for the sensitivity and accuracy of measurements in biological samples. By using time-gated detection one can discriminate the lanthanide emission from the autofluorescence, greatly improving the signal-to-noise ratio and detection sensitivity.

The use of luminescent lanthanide complexes is one alternative to currently used organic fluorophores, however typical coordination complexes often experience deactivation of the Ln^{3+} excited states through high frequency vibrations of the ligand structure.[4,5] The ligands typically used also often do not fully protect the lanthanide cations from solvent vibrations leading to additional non-radiative deactivation of the excited states, therefore reducing luminescence intensity.

The use of semiconductor nanocrystals, or quantum dots, as luminescent reporters for bioanalytical applications also offers several advantages over the current organic fluorophores.[6-27] These materials possess tunable emission and excitation wavelengths that are controlled through nanocrystals size. The broad absorption in these particles is associated with large absorption coefficients. This allows for optimization of nanocrystal properties for use *in vivo* in addition to allowing for multiplex imaging through use of multiple emission colors using single wavelength excitation sources. Relatively high quantum yields are observed for quantum dots with appropriate surface passivation in aqueous solution, up to 60% compared to organic fluorophores which reach 15% in aqueous solutions.[28,29] In addition, quantum dots illustrate strong resistance to photobleaching, whereas organic fluorophores are generally highly susceptible to rapid photobleaching.[30]

While quantum dots do offer many advantages over traditionally used organic fluorophores, they also possess their own intrinsic limitations. These materials are synthesized using inorganic materials, usually a CdX (X = Te, Se, or S) followed by addition of a wider band gap shell, usually ZnS or ZnSe. The shell of these materials serves two purposes: the enhancement of the luminescence properties by reducing trap states, and the prevention of the release of potentially toxic core materials. The addition of a shell may significantly increase the

particle size. Further surface modification of these materials are necessary to render the particles soluble in aqueous media, thus further increasing particle size.

As an alternative to organic fluorophores and traditional quantum dots, luminescent lanthanide cations can be incorporated into semiconductor nanocrystal structures to create an improved luminescent species. These materials possess only low energy lattice vibrations, decreasing the extent of non-radiative deactivation felt by the lanthanide cations. Lanthanide cations doped within the core of these materials are further protected from deactivation by solvent vibrations. The energy levels (band gaps) of the nanocrystals can be tuned to match the accepting levels of different lanthanide cations through nanocrystals size and material.

1.1 LUMINESCENT LANTHANIDE CATIONS

1.1.1 General Lanthanide Information

The lanthanides are the elements located in the first row of the f-block of the periodic table, ranging from cerium (Z = 58) to lutetium (Z = 71). These elements, although referred to as "rare-earth" elements, are rather abundant on Earth. Most of the lanthanide cations are present in the 3+ oxidation state although there are 5 lanthanides that can adopt the tetravalent state (neodymium, dysprosium, praseodymium, terbium, and cerium) and some can adopt the 2+ oxidation state (Sm^{2+}, $Eu^{2+}$and Yb^{2+}). These elements are hard Lewis acids and tend therefore to form the strongest bonds with hard Lewis bases, such as oxygen donor ligands.[31]

The emission of the lanthanides ranges from ultra violet through the visible and into the near infrared regions depending on the location of the f-orbital energy levels of a specific cation

(Figure 1.1). Four lanthanide cations are known to emit in the visible range: Eu^{3+}, Tb^{3+}, Sm^{3+}, and Dy^{3+}. There are five lanthanides that can emit in the NIR range: Nd^{3+}, Ho^{3+}, Er^{3+}, Tm^{3+}, and Yb^{3+}. Some lanthanides, such as Pr^{3+}, emit in both the visible and NIR ranges.

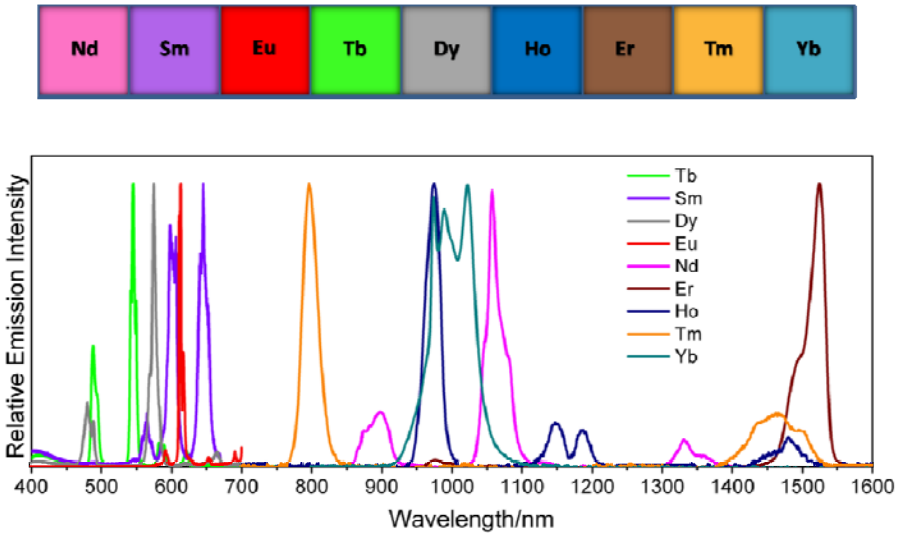

Figure 1.1. Luminescent lanthanide cations and their characteristic emission bands[32,33]

The f-orbitals of these elements, although higher in energy than the 5s and 5p orbitals, are shielded by these 5s and 5p resulting in unique electronic properties (photophysical and magnetic) and are therefore internal.[2] The f-f transitions are parity, or Laporte, forbidden which results in long luminescence lifetimes (μs to ms) and low molar absorption coefficients (10 $cm^{-1}mol^{-1}$ or less). The forbiddeness of these transitions can be explained by the Laporte selection rule which states that transitions cannot occur within a single quantum shell. This means that p→p, d→d, and f→f transitions should not occur. Unlike the d-block elements, the 4f-orbitals of the lanthanides are shielded from the surrounding environment and therefore emission bands resulting from lanthanide cations appear as sharp atom-like bands located at fixed wavelengths. These forbidden transitions become partially allowed due to interactions including vibrational

coupling, spin-orbit coupling, crystal field splitting, and the mixing between d and f orbitals. The forbidden nature of these transitions results in the low probability of population of the excited states, resulting in extremely low extinction coefficients and the free cations having low luminescence intensity.

1.1.2 Limitations of Organic Fluorophores

Organic fluorophores are commonly used as biological imaging agents despite their limitations. These molecules often experience rapid photobleaching upon exposure to light making it difficult to perform long term and repeated measurements.[34] This limitation also affects the storage of the fluorophore (shelf life of the compound). In addition, the emission and excitation wavelengths are significantly influenced by the experimental conditions.

1.1.3 Antenna Effect – Sensitization of Luminescent Lanthanide Cations

In order to obtain efficient lanthanide excitation and subsequent intense emission, a sensitizer needs to be placed at relatively close proximity to the lanthanide cation. This concept was first explored by Weissman in 1942, using organic ligands as sensitizers.[35] The sensitizers absorb the excitation light and transfer the resulting energy to the accepting levels of the lanthanide cation. This process, termed the "antenna effect" is schematized in Figure 1.2.[35]

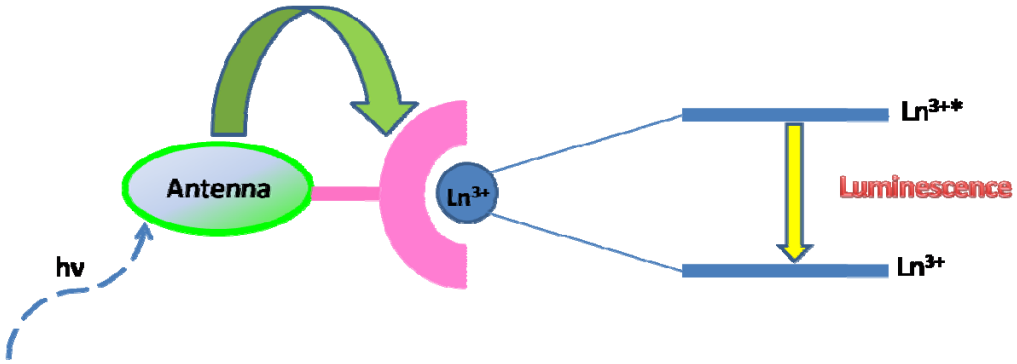

Figure 1.2. Photosensitization: Antenna effect

In order to function as an antenna, an organic ligand must contain both a chromophoric group to harvest the energy and a binding atom or group for coordination of the lanthanide cation.[36] An important parameter that controls the efficiency of an antenna is the matching of the energy between its donating levels and the accepting levels of the lanthanide cation. The distance between the antenna and the lanthanide cation is another parameter that controls the energy transfer.

The lanthanide cation needs to be well protected from surrounding solvent molecules in order to maximize luminescence intensity. Non-radiative relaxation pathways are created by interaction of lanthanide cations with oscillating solvent molecules such as O-H, C-H, and N-H.[37] For such protection, high coordination numbers in lanthanide complexes are required (between 8 and 12 in solution).

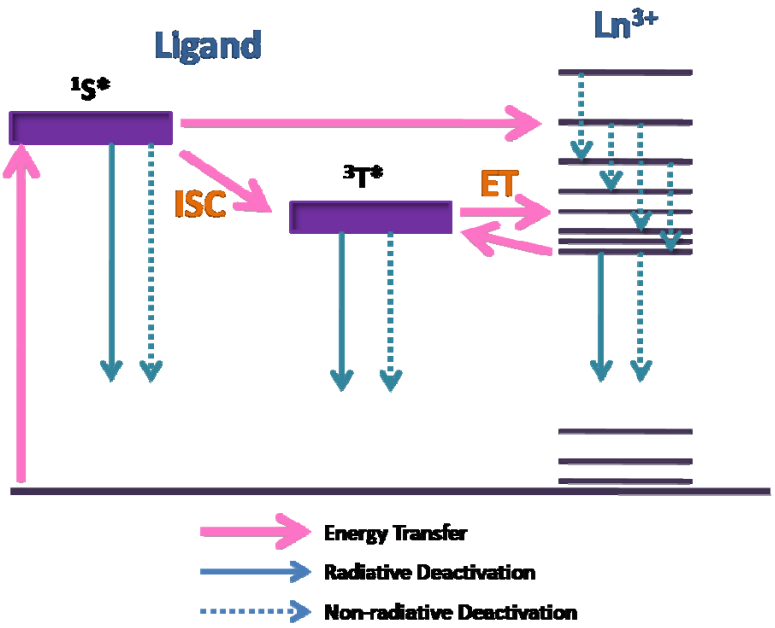

Figure 1.3. Jablonski diagram illustrating energy transfer mechanisms from antenna to lanthanide cations as well as competitive processes

A Jablonski diagram is used to describe the energy transfer mechanism occurring between an organic antenna and the lanthanide (Figure 1.3). A transition from the ground singlet state, S_0, to the excited singlet state, S_1 first occurs upon excitation of the organic antenna. From this state, there are a number of different pathways for the energy to migrate including fluorescence (emission of a photon), non-radiative deactivation, or intersystem crossing (ISC) between the excited singlet and an excited triplet state of the antenna molecule. The triplet state can be de-populated through similar mechanisms as the singlet state (phosphorescence – emission of a photon, non-radiative relaxation, or energy transfer to the lanthanide cation).[38,39] When energy transfer occurs, the lanthanide cation electrons are promoted to its excited state and relax back to the ground state through either non-radiative processes or through luminescence.

In some cases, energy transfer has been shown to occur from the excited singlet states directly to the lanthanide accepting levels, however the alternative pathways are more likely.[40,41]

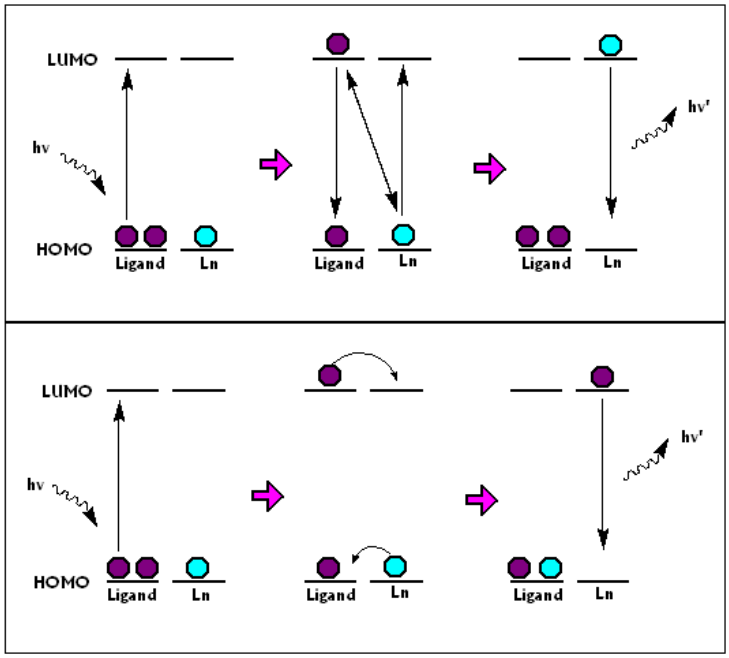

Figure 1.4. Diagram illustrating Forster energy transfer mechanism (Top) and Dexter energy transfer mechanism (Bottom)

Three possible mechanisms can explain energy transfer between an antenna and the lanthanide cation (Figure 1.4). The first is the Förster mechanism, which states that a dipole-dipole interaction (resonant energy transfer) is necessary in order for the energy transfer to occur. This theory requires sufficient overlap between the emission band of the donor (antenna) and the absorption band of the acceptor (lanthanide cation).[42,43] In this model an electron from the donor's ground state is promoted to an excited state upon light absorption. The energy that is released upon relaxation of the electron to the ground state of the donor is transferred to the lanthanide cation. This energy transfer results in promotion of an electron from the acceptor

ground state to the acceptor excited state. The acceptor electron then returns to the ground state releasing its energy in the form of light, non-radiative deactivation or photoreaction. Efficiency of energy transfer via this mechanism is dependent on the distance between the donor and acceptor, r, more specifically r^{-6}. The second mechanism, Dexter, involves electron transfer between donor and acceptor. In the Dexter model, the transfer mechanism is based on concerted electron transfers, which implies orbital overlap between the donor and the acceptor.[44] In this mechanism, an electron from the donor ground state is promoted to the excited state followed by simultaneous exchanging of electrons from the excited state of the donor to the excited state of the acceptor and from the ground state of the acceptor to the ground state of the donor, none of the species changing of oxidation. The electron now present in the acceptor excited state can relax to the ground state via emission of a photon or via non-radiative relaxation. Efficiency of energy transfer via a Dexter mechanism is proportional to e^{-r}. The third mechanism is an electron transfer mechanism. This process will be dependent upon the oxidation and reduction potentials of the donor and metal ion respectively and is limited to the few lanthanide cations that can be reduced (Eu^{3+}, Sm^{3+}, Yb^{3+}) relatively easily.[45-47]

1.1.4 Lanthanide Cations and Complexes

Lanthanides are attractive for biological applications for a number of reasons.[4,48] They posses long luminescence lifetimes (on the order of μs – ms) which allow for the removal of autofluorescence through time resolved measurements and are resistant to photobleaching.[49] Their emission bands will appear at the same wavelengths regardless of the experimental conditions. These complexes also experience a large shift in energy between their excitation and emission bands.

Small energy gaps between the ground and lowest excited states within lanthanide complexes can result in competing non-radiative relaxation processes that reduce efficiency of energy transfer within lanthanide complexes.[50,51] Ln^{3+} can experience rapid deactivation as the result of high frequency vibrations including O-H, N-H, and C-H vibrations of either solvent or ligand molecules.[37] These quenching effects are more prevalent in NIR emitting lanthanides. Several steps can be taken to minimize quenching effects observed in lanthanide complexes.

The global goal of our research group is to develop efficient antennae for sensitizing the different lanthanide cations. If we can optimize their photophysical properties we will create compounds that are attractive for biological sensing and imaging.

1.2 SEMICONDUCTOR NANOPARTICLES

1.2.1 Properties of Semiconductor Nanoparticles

Nanoparticles can be defined as materials with finite size having properties that lie between the atomic/molecular level and bulk materials. These systems are governed by the rules of quantum mechanics because their physical size becomes comparable to the wavelength of particles interacting with them. Often, these systems are described by examining the behavior of bulk solids and monitoring how it changes as the system is confined in different dimensions.[52,53]

The semi-conductor nanocrystals ("quantum dot") are nanoparticles with specific optical properties. In such nanomaterials, the physical size, and thus the separation of charge carriers (electron-hole pairs) is confined in all three dimensions, creating a zero-dimensional structure.

When a particle is restricted to the nano size scale, the surface atoms account for a large fraction of the total atoms present. As a result these surface atoms will tend to have a tremendous influence on the overall properties of the nanocrystal.[53]

Although there are a number of different types of nanocrystals discussed in the literature, quantum confinement effects are more prominent in semiconductor nanocrystals (because of their unique electronic structure), and so it is easier to study and tune their properties. When the size of a semiconductor is restricted, the charge carriers begin to behave as a particle in a box, yielding a discrete energy level spectrum.

While we can apply rules of quantum mechanics to better rationalize these systems, the energy structure within nanocrystals is, nonetheless, very complicated due to the large number of parameters that control their properties. There are two main approaches usually taken to rationalize energy levels or continuum in such systems. The first method is a top down approach in which we start with the bulk material and study the band structure as the dimensions are reduced to the nanometer scale. The second approach is the bottom up approach. This involves starting with a single atom and studying how the energy levels evolve as atoms begin to interact with one another. One of the simplest ways to illustrate the latter is to examine the case of silicon particles (outlined below).

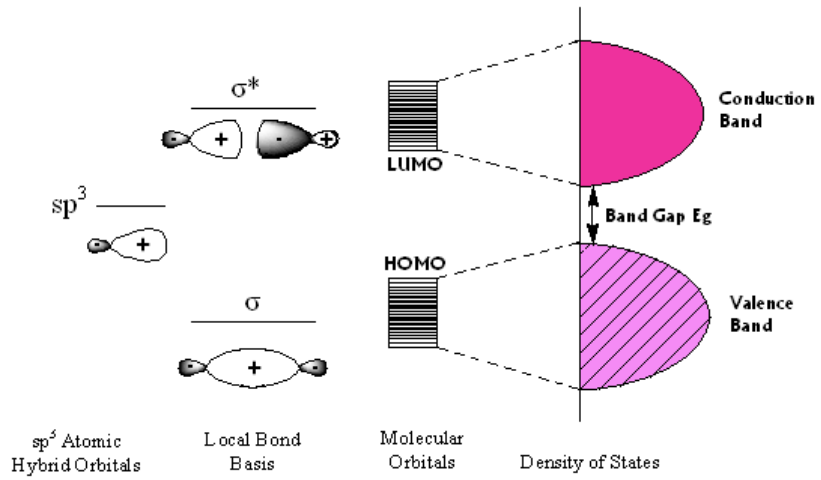

Figure 1.5. Molecular orbital model for band structure of silicon[54]

As atoms are brought together, their orbitals combine and form sets of bonding and antibonding orbitals, with each new atom the sets grow.[54] As a result of this orbital interaction, a spread of energies begins to develop and the band gap emerges from what was initially referred to as the HOMO-LUMO separation for the single atoms (Figure 1.5)

1.2.2 Colloidal Nanoparticles

Colloidal nanocrystals are materials that are synthesized using wet chemistry approaches and result in "free-standing" particles in solution.[55] There are two main approaches for the synthesis of colloidal particles: (1) aqueous and (2) organometallic, the latter of which will be discussed in greater detail in this work.

In general, three main steps are involved in the synthesis of nanocrystals. The first step is referred to as the "nucleation" step. This is followed by a period of "growth" and finally a

period involving the "focusing", or narrowing, of the nanocrystal size distribution. The key to a successful and controlled synthesis is determining the right balance between these steps.

If the nucleation and growth events occur too rapidly, the system becomes vulnerable to a process known as "Ostwald ripening".[53] This process results in a broader size distribution (greater than 15%) because larger particles are growing at the expense of smaller particles. Before further discussion of this concept, some basic terminology must first be defined and explained.

A colloidal nanocrystal synthesis involves the addition of precursors to a reaction flask followed by heating to high temperatures (250-300 °C). These temperatures allow for the decomposition of precursors, leading to formation of the "monomers" (new reactive species which will be involved in the nucleation and growth processes). Another important component that is loaded into the initial reaction flask is the "surfactant". The surfactant adsorbs to the nanocrystals' surfaces during growth and provides access for addition of monomers to the surface while preventing aggregation.

The optimal synthesis involves careful regulation of monomer concentration throughout the reaction in addition to proper choice of surfactant molecules (if the surfactant binds too weakly to the nanocrystal surface, the particles will tend to aggregate, if it binds too strongly growth may be inhibited). For these reasons the precursors chosen will be specific for a particular nanocrystals type, desired size range, and shape.

1.2.3 Photophysical Properties of Nanocrystals

Semiconductor nanocrystals differ from bulk materials in that their optical properties are heavily dependent on size and shape, and are a direct result of the band gap separation within the

nanocrystal structure. Quantum confinement effects are used to explain a system's energy when the size of that system is comparable to the exciton Bohr radius, or the separation between charge carriers (electron-hole separation). As the size of a nanocrystal is increased through growth, the band gap separation begins to decrease. This decrease in band gap results in a red shift in nanocrystal emission (a smaller band gap is at lower energy and the emission will therefore also be at lower energy). This phenomenon is most clearly exhibited in the case of CdSe nanocrystals, whose band gap energies, and thus emission colors, can be tuned to span the entire visible spectrum (as seen in Figure 1.6). In addition to size dependent emission properties, the absorption of semiconductor nanocrystals is also size dependent. Nanocrystals can only absorb light that is at least the same energy corresponding to the band gap, and not lower. As a result of this, the smaller nanocrystals will absorb shorter wavelength light while the larger nanocrystals will absorb longer wavelength light.

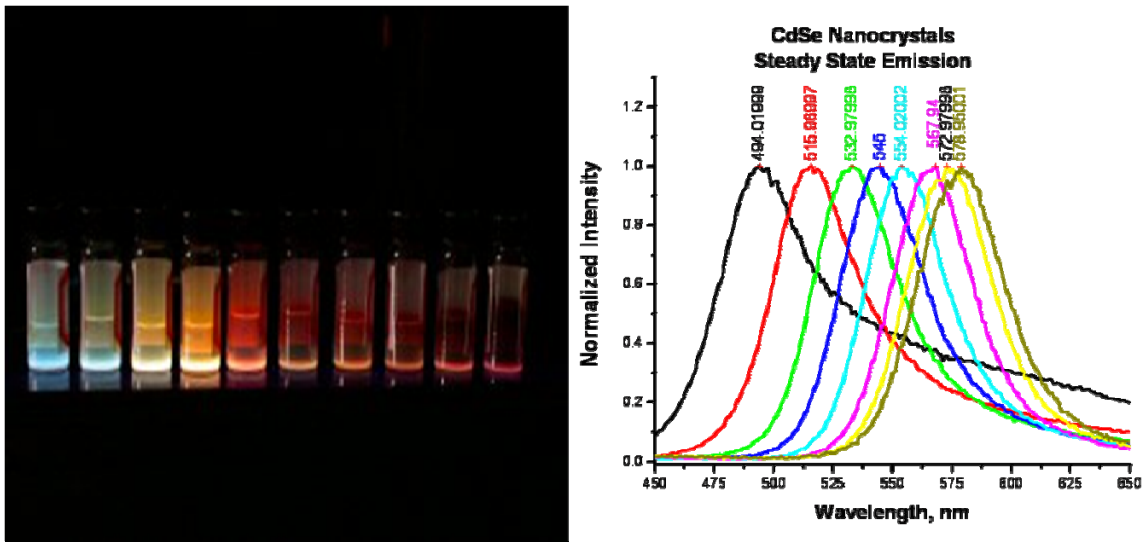

Figure 1.6. Image and corresponding spectra of CdSe nanocrystals spanning the visible region

1.2.4 Semiconductor Nanocrystals as Antennae for Lanthanides – Project Goals

In order to take advantage of the attractive properties of luminescent lanthanides, the lanthanide complexes must be efficient at sensitization, must protect the metal ions from non-radiative deactivation through quenching, and must be strongly emissive in solution (possess strong absorption).[35,37] By combining semiconductor nanocrystals with luminescent lanthanides, a new class of reporters is created (Figure 1.7). The energy levels of the nanocrystals can be tuned, through controlling sizes through growth time, to match the various accepting levels of different lanthanide cations. These systems can be further optimized by using various types of semiconductor nanocrystal systems to match the band gap energy with the specific accepting energy of different lanthanides. This will provide an appropriate level of sensitization of the lanthanide cations using the band gap energy as the antenna.

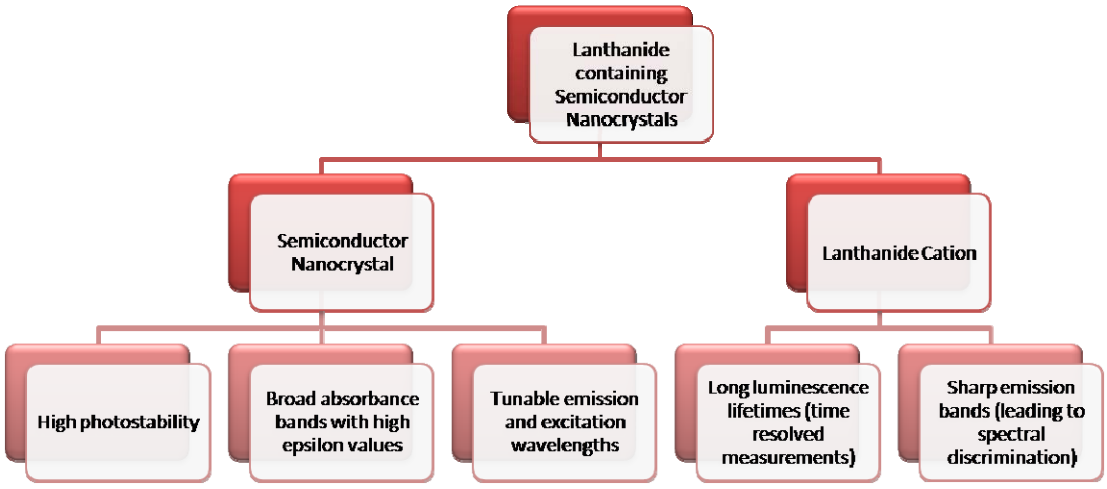

Figure 1.7. Diagram illustrating properties of lanthanide containing nanocrystals

Nanocrystals posses only low energy lattice vibrations and will therefore be less efficient at deactivating the lanthanide excited states than the high frequency vibrations of typical organic

ligands. The nanocrystal structure will also isolate the lanthanide cations from the high frequency solvent vibrations, thus minimizing quenching.

In addition to using traditional semiconductor nanocrystals as antennae, a new class of nanoparticles may be created to take advantage of the attractive properties of lanthanide cations while minimizing or eliminating the need for doping. Doping within these crystal structures places strain on the overall crystal lattice and thus has the potential for the formation of trap states. These materials are still in the nanoscale regime and exhibit a band gap emission; however this band gap arises partly from the lanthanides interaction within the material.

A promising strategy to maximize the number of absorbed an emitted photons is the development of reporters that possess more than one luminescent metal ion by synthesizing polymetallic lanthanide compounds. The use of nanocrystals for the sensitization of lanthanide cations provides this additional advantage, forming polymetallic lanthanide compounds with a high density of luminescent cations per unit of volume. It will result in the maximization of the number of photons emitted per unit of volume allowing improved detection sensitivity. The resultant materials possess large molar absorptivity resulting in strongly emissive species.[56]

1.3 REFERENCES

(1) Bünzli, J.-C. G. *Acc. Chem. Res.* **2006**, *39*, 53.

(2) Bünzli, J.-C; Choppin, G. R. *Lanthanide propes in life, chemical, and earth sciences: theory and practice*; Elsevier: Amsterdam, New York, 1989.

(3) Bünzli, J.-C; Piguet, C. *Chem. Soc. Rev.* **2005**, *34*, 1048.

(4) Beeby, A.; Botchway, S. W.; Clarkson, I. M.; Faulkner, S.; Parker, A. W.; Parker, D.; Williams, J. A. G. *J. Photochem. Photobiol., B* **2000**, *57*, 83.

(5) Mathis, G. *J. Biomol. Screen.* **1999**, *4*, 309.

(6) Fu, A.; Gu, W.; Larabell, C.; Alivisatos, A. P. *Curr. Opin. Neurobiol.* **2005**, *15*, 568-575.

(7) Giepmans, B. N. G.; Adams, S. R.; Ellisman, M. H.; Tsien, R. Y. *Science* **2006**, *312*, 217.

(8) Green, M. *Angew. Chem., Int. Ed. Engl.* **2004**, *43*, 4129.

(9) Chan, W. C. W.; Nie, S. *Science* **1998**, *281*, 2016 - 2018.

(10) Mattoussi, H.; Mauro, J. M.; Goldman, E. R.; Anderson, G. P.; Sundar, V. C.; Mikulec, F. V.; Bawendi, M. G. *J. Am. Chem. Soc.* **2000**, *122*, 12142 - 12150.

(11) Alivisatos, A. P.; Gu, W.; Larabell, C. *Annu. Rev. Biomed. Eng.* **2005**, *7*, 55-76.

(12) Jaiswal, J. K.; Mattoussi, H.; Mauro, J. M.; Simon, S. M. *Nature Biotechnology* **2003**, *21*, 47 - 51.

(13) Lim, Y. T.; Kim, S.; Nakayama, A.; Stott, N. E.; Bawendi, M. G.; Frangioni, J. V. *Mol. Imaging* **2003**, *2*, 50 - 64.

(14) Larson, D. R.; Zipfel, W. R.; Williams, R. M.; Clark, S. W.; Bruchez, M. P.; Wise, F. W.; Webb, W. W. *Science* **2003**, *300*, 1434 - 1436.

(15) Dubertret, B.; Skourides, P.; Norris, D. J.; Noireaux, V.; Brivanlou, A. H.; Libchaber, A. *Science* **2002**, *298*, 1759 - 1762.

(16) Silver, J.; Ou, W. *Nano Lett.* **2005**, *5*, 1445 - 1449.

(17) Kim, S.; Lim, Y. T.; Soltesz, E. G.; De Grand, A. M.; Lee, J. K.; Nakayama, A.; Parker, J. A.; Mihaljevic, T.; Laurence, R. G.; Dor, D. M.; Cohn, L. H.; Bawendi, M. G.; Frangioni, J. V. *Nature Biotechnology* **2004**, *22*, 93 - 97.

(18) Parak, W. J.; Gerion, D.; Pellegrino, T.; Zanchet, D.; Micheel, C.; Williams, S. C.; Boudreau, R.; Le Gros, M. A.; Larabell, C. A.; Alivisatos, A. P. *Nanotechnology* **2003**, *14*, R15-R27.

(19) Parak, W. J.; Boudreau, R.; Le Gros, M.; Gerion, D.; Zanchet, D.; Micheel, C. M.; Williams, S. C.; Alivisatos, A. P.; Larabell, C. *Adv. Mater.* **2002**, *14*, 882-885.

(20) Michalet, X.; Pinaud, F. F.; Bentolila, L. A.; Tsay, J. M.; SDoose, S.; Li, J. J.; Sundaresan, G.; Wu, A. M.; Gambhir, S. S.; Weiss, S. *Science* **2005**, *307*, 538 - 544.

(21) Lagerholm, B. C.; Wang, M.; Ernst, L. A.; Ly, D. H.; Liu, H.; Bruchez, M. P.; Waggoner, A. S. *Nano Lett.* **2004**, *4*, 2019 - 2022.

(22) Alivisatos, P. *Nature Biotechnology* **2004**, *22*, 47-52.

(23) Wu, X.; Liu, H.; Liu, J.; Haley, K. N.; Treadway, J. A.; Larson, J. P.; Ge, N.; Peale, F.; Bruchez, M. P. *Nature Biotechnology* **2003**, *21*, 41-46.

(24) Ballou, B.; Lagerholm, B. C.; Ernst, L. A.; Bruchez, M. P.; Waggoner, A. S. *Bioconjugate Chem.* **2004**, *15*, 79 - 86.

(25) Pellegrino, T.; Parak Wolfgang, J.; Boudreau, R.; Le Gros Mark, A.; Gerion, D.; Alivisatos, A. P.; Larabell Carolyn, A. *Differentiation; research in biological diversity* **2003**, *71*, 542-8.

(26) Clapp, A. R.; Medintz, I. L.; Mauro, J. M.; Fisher, B. R.; Bawendi, M. G.; Mattoussi, H. *J. Am. Chem. Soc.* **2003**, *126*, 301 - 310.

(27) Bentzen, E. L.; Tomlinson, I. D.; Mason, J.; Gresch, P.; Warnement, M. R.; Wright, D.; Sanders-Bush, E.; Blakely, R.; Rosenthal, S. J. *Bioconjugate Chem.* **2005**, *16*, 1488 - 1494.

(28) Frangioni, J. V. *Curr. Opin. Biotech.* **2003**, *7*, 626.

(29) Waggoner, A. S. *Curr. Opin. Biotech.* **2006**, *10*, 62.

(30) Yanus, W. M. M.; Sheng, C. K.; Yanus, W. M. Z. W. *J. Nonlinear Opt. Phys.* **2003**, *12*, 91.

(31) Kaltsoyannis, N.; Scott, P. *The f Elements*; Oxford University Press Inc.: New York, 1999.

(32) Petoud, S.; Cohen, S. M.; Buenzli, J.-C. G.; Raymond, K. N. *J. Am. Chem. Soc.* **2003**, *125*, 13324-13325.

(33) Zhang, J. P.; Badger, P. D.; Geib, S. J.; Petoud, S. *Angew. Chem., Int. Ed. Engl.* **2005**, *44*, 2508 - 2512.

(34) Ye, Z.; Tan, M.; Wang, G.; Yuan, J. *Anal. Chem.* **2004**, *76*, 513.

(35) Weissman, S. I. *J. Chem. Phys.* **1942**, *10*, 214-17.

(36) Sabbatini, N.; Guardigli, M.; Lehn, J. M. *Coord. Chem. Rev.* **1993**, *123*, 201-28.

(37) Beeby, A.; Clarkson, I. M.; Dickins, R. S.; Faulkner, S.; Parker, D.; Royle, L.; de Sousa, A. S.; Williams, J. A. G.; Woods, M. *J. Chem. Soc., Perkin Trans. 2* **1999**, 493-504.

(38) Hayes, A. V.; Drickamer, H. G. *J. Chem. Phys.* **1982**, *76*, 114.

(39) Sato, S.; Wada, M. *Bull. Chem. Soc. Jpn.* **1970**, *43*, 1955.

(40) Hebbink, G. A.; Klink, S. I.; Grave, L.; Oude Alink, P. G. B.; van Veggel, F. C. J. M. *Chem. Phys. Phys. Chem* **2002**, *3*, 1014.

(41) Yang, C.; Fu, L. M.; Wang, Y. A.; Zhang, J. P.; Wong, W. T.; Ai, X. C.; Qiao, Y. F.; Zou, B. S.; Gui, L. L. *Angew. Chem., Int. Ed. Engl.* **2004**, *43*, 5010.

(42) Forster, T. *Ann. Phys.* **1948**, *2*, 55.

(43) Forster, T. *Discuss. Faraday Soc.* **1959**, *No. 27*, 7.

(44) Dexter, D. L. *J. Chem. Phys.* **1953**, *21*, 836.

(45) Faulkner, S.; Beeby, A.; Carrie, M. C.; Dadabhoy, A.; Kenwright, A. M.; Sammes, P. G. *Inorg. Chem. commun.* **2001**, *4*, 187.

(46) Hebbink, G. A.; Grave, L.; Woldering, L. A.; Reinhoudt, D. N.; van Veggel, F. C. J. M. *J. Phys. Chem. A: Gen. Phys.* **2003**, *107*, 2483.

(47) Horrocks, W. D., Jr.; Bolender, J. P.; Smigh, W. D.; Supkowski, R. M. *J. Am. Chem. Soc.* **1997**, *119*, 5972.

(48) Faulkner, S.; Matthews, J. L. *Compr. Coord. Chem. II* **2004**, *9*, 913-944.

(49) Mathis, G. *J. Biomol. Screen.* **1999**, *4*, 309-313.

(50) Siebrand, W. *J. Chem. Phys.* **1967**, *46*, 440.

(51) Stein, G.; Wurzberg, E. *J. Chem. Phys.* **1975**, *62*, 208.

(52) Bukowski, T. J.; Simmons, J. H. *Crit. Rev. Solid State Mater. Sci.* **2002**, *27*, 119 -142.

(53) Schmid, G. *Nanoparticles: From Theory to Application*; WILEY-VCH: Weinheim, Germany, 2004.

(54) Steigerwald, M. L.; Brus, L. E. *Acc. Chem. Res.* **1990**, *23*, 183-8.

(55) Caruso, F. *Colloids and Colloid Assemblies*; WILEY-VCH: Weinheim, 2004.

(56) Chengelis, D. A.; Yingling, A. M.; Filipczyk, G.; Petoud, S. *Proc. SPIE-Int. Soc. Opt. Eng.* **2006**, *6370*, 6370y-1 - 6370y-13.

2.0 GENERAL EXPERIMENTAL INFORMATION

2.1 INSTRUMENTATION

The analysis of semiconductor nanocrystals that we have synthesized requires a series of measurements to obtain information about the physical and photophysical properties. The specific analytical techniques and methods that have been used are outlined below. Specific information will be described in the specific chapters relating the analysis to each type of material.

2.1.1 Transmission electron microscopy

Transmission electron microscopy (TEM) images were obtained using Ted Pella 300 mesh copper grids with 50 angstrom carbon coating as a solid support for low resolution measurements while measurements using high resolution transmission electron microscopy (HRTEM) were obtained on samples placed on Ted Pella 400 mesh Ultrathin Carbon coated copper grids. Purified nanocrystal solutions (in their appropriate solvent) were either aerated or dropped onto the copper grids and the solvent was removed. Prepared grids were then washed with water and allowed to dry prior to analysis to further remove impurities that might be present.

Low resolution imaging was performed on an FEI Morgagni 268 TEM located in the University of Pittsburgh Biology Department Microscopy Center, maintained by Tom Harper.

This instrument operated at 80 kV does not have sufficient resolution to record clear images of our nanocrystals (2 – 10 nm in diameter) and did not allowed to assess the level of crystallinity of our samples. As an alternate instrument, we have used a JEOL 1210 TEM operating at 120 kV located in the University of Pittsburgh Center for Biological Imaging. Additional low resolution TEM imaging was obtained through collaboration with Prof. Marcel Bruchez at Carnegie Mellon University in Pittsburgh. Through the help of Joe Suhan we were able to obtain low resolution images for some of our nanocrystals systems. The instrument used was a Hitachi H-7100 TEM operating at 75 kV. Digital images were obtained using an AMT Advantage 10 CCD Camera System.

Low resolution imaging was also performed through collaboration with the University of Pittsburgh Department of Materials Science Engineering. The instrument used was a JEOL 2000-FX Scanning Transmission Electron Microscope operated at a maximum of 200 kV, used to obtain initial images of particles to verify sample thickness, and was operated through collaboration with Cole Van Ormer.

High resolution imaging was performed through collaboration with Dr. James McBride from Vanderbilt University. The measurements were performed at Oak Ridge National Laboratory using a VG Microscopes model HB603U STEM. The instrument operates at 300 kV and is fitted with a C_s corrector from Nion. Data collection occurs through a digital micrograph coupled to a personal computer.

High resolution images were also obtained through the Nanoscale Fabrication and Characterization Facility (NFCF) housed within the Petersen Institute of NanoScience and Engineering (PINSE) within the department of Materials Science and Engineering at the University of Pittsburgh. These images were obtained using a JEOL-2100 CF operating between

120kv and 200kv. The JEOL-2100 CF was fitted with an X-ray energy dispersive spectroscopy (XEDS) analyzer attachment from Oxford Instruments (Inca platform) and GIF TRIDIEM post column energy filter (Gatan Inc.) to allow for compositional analysis. Imaging was performed by Chad M. Shade of the Petoud group through collaboration with Dr. Andreas Kulovits.

2.1.2 X-ray diffraction

X-Ray diffraction samples were analyzed on the instrument located in the University of Pittsburgh undergraduate physical chemistry laboratory (an in house XRD-5 Diffractometer interfaced to a personal computer). Samples were prepared as follows: a glass microscope slide was lightly coated with silicone based vacuum grease. The solid nanocrystal samples were poured onto the center of the slide (over the vacuum grease). The samples were then pressed into the grease by placing a second glass slide over top of the first and applying light pressure. Scans were performed between $2\theta = 15$ and $2\theta = 80$.

2.1.3 Inductively coupled plasma

Inductively coupled plasma-atomic emission spectroscopy (ICP-AES) data was obtained through collaboration with Amy Wolfe, a graduate student in the Geology Department at the University of Pittsburgh. Lanthanide, cadmium, selenium and sulfur concentrations were measured on a SpectroFlame EOP ICP-AES (Kleve, Germany). Accuracy of measurements is within ± 5% of true values. Instrument calibration was carried out using a suite of different concentrations of standard solutions for each element analyzed in 2% nitric acid matrix. All the aqueous samples were preserved in 2% nitric acid matrix before ICP-AES measurements.

2.1.4 Energy dispersive x-ray spectroscopy

Energy dispersive x-ray spectroscopy was performed using three different instruments housed in the engineering department at the University of Pittsburgh. The first instrument was coupled to a Philips XL-30 field emission scanning electron microscope. Compositional information was obtained through attached energy dispersive x-ray spectroscopy detectors. This particular instrument set up allowed for analysis of a larger spot size of our sample.

The second instrument was coupled to the JEOL-2100 CF HRTEM, located within PINSE. This allowed for analysis of a more focused spot size to gain better information of the composition of individual nanocrystals rather than the overall sample. Energy dispersive x-ray spectroscopy measurements were obtained through the use of an Inca platform attachment from Oxford instruments.

The third and final instrument was a Genesis 2000 from EDAX Inc. The instrument was coupled to a Philips XL30 FEG SEM. This instrument was used for all LnS analysis.

2.1.5 Infrared spectroscopy

Infrared spectra were recorded on a Perkin-Elmer Spectrum BX FT-IR instrument. FT-IR spectra were obtained from KBr pellets on a Perkin Elmer BX spectrometer.

2.1.6 Absorption

Absorption spectra were recorded on a Perkin-Elmer Lambda 9 BX Spectrometer in 1 cm quartz cells coupled with a personal computer using software supplied by Perkin-Elmer.

2.1.7 Fluorescence and phosphorescence

Time resolved and steady state emission and excitation spectra were analyzed using either a Varian Cary Eclipse coupled to a personal computer with software supplied by Varian or a modified Jobin-Yvon Horiba Fluorolog-322 spectrofluorimeter.

Samples were dissolved in an appropriate solvent (chloroform, toluene, butanol except otherwise stated) and placed in 1 cm and 1 mm quartz fluorescence cells purchased from NSG Precision Cells, Inc. (Farmingdale NY).

2.1.8 Luminescence lifetimes

The Ln^{3+} luminescence lifetime measurements were performed by excitation of solutions in 1 mm quartz cells (NSG Precision Cells, Inc.) using either a Xenon flash lamp being part of the JY Horiba instrument described previously or a Nd:YAG Continuum Powerlite 8010 laser (354nm, third harmonic) as the excitation source. Emission was collected at a right angle to the excitation beam, and wavelengths were selected by means of the Spex FL1005 double monochromator or a Spectral Products CM 110 1/8 meter monochromator (with two independent gratings). The signal was monitored by either a Hamamatsu R928 photomultiplier (visible) or a cooled Hamamatsu R316-2 photomultiplier (NIR) to a 500 MHz bandpass digital oscilloscope (Tektronix TDS 620B). Signals from > 500 flashes were collected and averaged. Luminescence lifetimes were averaged from at least three independent measurements using samples from several different batches. Experimental luminescence decay curves were imported into Origin 7.0 scientific data analysis software, and analyzed using the Advanced Fitting Tool module. The decay curves were fitted in single, double, and triple exponential fitting modes, depending on the

system. Of these modes, the one which provided the best fit of the experimental data was chosen based on reduced chi square criteria.

2.1.9 Quantum yield measurements

Absorption spectra were recorded on a Perkin-Elmer Lambda 9 Spectrometer coupled to a personal computer using software supplied by Perkin-Elmer. Steady state luminescence quantum yields were measured using quinine sulfate reference solutions (Φ=0.546). Emission spectra were collected using a modified JY Horiba Fluorolog-322 Spectrofluorimeter and spectra were corrected for the instrumental function.

The quantum yields were calculated using the following equation:

$$\Phi_x/\Phi_r = [A_r(\lambda_r)/A_x(\lambda_x)][I(\lambda_r)/I(\lambda_x)][\eta_x^2/\eta_r^2][D_x/D_r]$$

where subscript r stands for the reference and x for the sample; A is the absorbance at the excitation wavelength, I is the intensity of the excitation light at the same wavelength, η is the refractive index (η = 1.333 in H_2O, η = 1.4960 in toluene) and D is the measured integrated luminescence intensity.

2.2 SYNTHESIS

2.2.1 General high temperature procedures

Nanocrystals were synthesized in a three neck round bottom flask which had been fitted with two water condensers. The three openings were necessary to allow for temperature regulation, argon

or nitrogen gas flow, and for injection of stock solutions. All nanoparticles were synthesized using standard high temperature synthetic procedures. Briefly, cation precursors were dissolved in an organic solvent at high temperatures (above 250 °C) under a nitrogen atmosphere. Once the cation solution was completely dissociated, indicated by an optically clear solution, one of two situations occurred.

In cases where a dopant ion was included in the reaction, a dopant cation stock solution was rapidly injected upon dissolution of the initial, primary, cation precursor. The dopant was typically dissolved in a similar organic solvent as used in the initial reaction mixture. Dissolution of dopant cation precursor usually occurred within 1-2 hours and was followed by rapid injection of an anion stock solution. This procedure allowed for nucleation and subsequent growth of the nanoparticles. Aliquots were removed from the reaction mixture at various growth times depending upon desired nanoparticle size.

If dopant cations were not used in the reaction, upon dissolution of the initial reaction mixture the anion stock solution was rapidly injected and aliquots removed at desired growth times.

2.2.2 Nanocrystal purification

Synthesized nanocrystal materials were purified through standard solvent/nonsolvent precipitation procedures. Raw nanocrystals were dissolved in 5 mL of butanol followed by precipitation with methanol (methanol is added to the nanocrystal solution until flocculation was observed). Samples were centrifuged and solvent was then poured off, leaving solid nanocrystal precipitate behind. The precipitate was once again dissolved in butanol (1 mL) and precipitated with methanol followed by centrifugation. The second precipitate was dissolved in 2 mL of

octanol (the nanocrystals are soluble in octanol but the side products from the reaction are not). The samples were once again centrifuged but this time to precipitate out the side products. The solution was transferred to a new vial where the nanocrystals were precipitated from the octanol using methanol (with a small amount, 1-2 mL of ethyl acetate for miscibility). The solid precipitate was dried under a gentle stream of nitrogen and redissolved in an appropriate solvent for analysis.

2.2.3 Surface modifications

Surface exchanges were performed on the nanocrystal samples to increase their solubility in water. Initial experiments were inspired from established procedures using mercaptoacetic acid as a surface passivant. The exchange process involved the addition of the mercapto- acid to purified nanocrystals. The solution was then gently heated to approximately 60°C for several hours, followed by precipitation with a strong base such as potassium tert-butoxide. The preliminary work was completed through collaboration with Michael Bowers of the Rosenthal group at Vanderbilt University. Success of the ligand exchange process could be qualitatively determined through visually monitoring the appearance of the nanocrystal solution throughout the process (strong quenching occurs within these systems which results in immediate darkening of the solution color). Additional verification of surface exchange involves monitoring the emission spectra of the nanocrystal both with and without the surface passivant. An apparent red shift in band gap emission is observed upon addition of the mercapto acid coating.

In addition to using established mercapto-acid surface exchanges, we performed surface exchanges using diethylenetriaminepentaacetic acid, DTPA. The idea behind this method was that the multidentae ligand would bind the surface of the nanocrystals. This method involved

dissolving nanocrystals in a minimal amount of chloroform and adding excess of a DTPA solution , which had been deprotonated with 5 equivalents of KOH to remove all acidic protons and subsequently allow binding. The samples were then sonicated for 2 hours to ensure thorough mixing of the aqueous and organic phases. Centrifugation ensured complete separation of phases once again, and the aqueous phase, containing DTPA coated nanocrystals, was removed for analysis. Surface exchange with DTPA was monitored using infrared spectroscopy.

3.0 LANTHANIDE CONTAINING CADMIUM SELENIDE NANOCRYSTALS

This work has been done through collaboration with Demetra A. Chengelis and Chad M. Shade and has been published as Chengelis, Demetra A.; Yingling, Adrienne M.; Badger, Paul, D.; Shade, Chad M.; Petoud, Stephane. *J. Am. Chem. Soc.,* **2005**, 127, 16752 – 16753.

As biological assays based on luminescent reporters become more prevalent, there is an increasing demand for reporters with more advanced properties, including strong resistance to photobleaching and the ability to be discriminated from background fluorescence to increase detection sensitivity. Classical methods of sensitizing lanthanide cations involve the use of organic ligands incorporating conjugate chromophoric groups.[1-4] One of the limitations of the ligand coordination is the risk of deactivation of the Ln^{3+} excited states, due to the presence of high frequency vibrations of -OH, -NH and -CH present within the ligand structure, resulting in reduced lanthanide centered emission.[5-7] In addition, the coordinated ligand(s) are often not efficient at protecting the lanthanide cations from the coordination of quenching solvent molecules, another important source of non-radiative deactivation. To address these limitations, we propose to test a novel sensitization strategy by combining semiconductor nanocrystals with lanthanide cations. By incorporating Ln^{3+} cations into semiconductor nanocrystals, we expect to achieve three main goals. First, we will attempt to sensitize the lanthanide luminescence through

the electronic structure of the nanocrystal by taking advantage of their broad absorption bands and their large extinction coefficients, in addition to the tunability of their electronic levels through control of the sizes of the nanocrystals.[8-11] Secondly, the nanocrystal structure will provide protection for the lanthanide ions from the high frequency vibrations of surrounding solvent molecules with the nanocrystal structure. Nanocrystals are attractive candidates for lanthanide sensitization because they possess only low energy lattice vibrations whose overtones will not deactivate the lanthanide excited states as readily as the high frequency vibrations of organic molecules.[12] The third goal is to form polymetallic lanthanide compounds, a strategy to maximize the number of lanthanide cations per unit of volume, thus maximizing the number of photons emitted and increasing the corresponding detection sensitivity.

The quantum confinement effects induced in semiconductor nanocrystals[13,14] provide the materials with unique photophysical properties such as size dependent emission bands and broad absorption and excitation wavelengths with extremely large epsilon values.[8,9,11,13] It has been demonstrated that CdSe semiconductor nanocrystals have advantageous properties over traditional organic fluorophores in a broad variety of biological imagery applications.[8,11,15-17] Here we propose to combine the attractive photophysical properties of semiconductor nanocrystals with those of lanthanide cations by using the semiconductor nanocrystals as antennae for the lanthanide cations.

3.1 BACKGROUND

3.1.1 Current state of the work on cadmium selenide nanocrystals

Semiconductor nanocrystals have been widely studied because of their unique photophysical properties. They have been used successfully in applications such as thin film electroluminescent devices, optical amplifiers for telecommunication networks, and biological fluorescent labels among others.[13,16-24] Through advances in synthetic procedures, high quality nanocrystals can be formed with narrow size distribution, good crystallinity, and relatively controllable surface functionalization. All of these parameters lead to controlled luminescence properties including emission wavelengths and quantum yields. All of the photophysical properties of semiconductor nanocrystals result from the electron confinement observed within these systems. In bulk CdSe the electronic carriers are free to move along all three Cartesian coordinates. The arrangement of atoms in a crystalline structure results in large overlap of atomic orbitals due to the proximity of the atoms. This orbital overlap results in the formation of a band gap, a forbidden region where electrons can be excited across into the conduction band but cannot reside within, allowing for the separation of electron-hole pairs.[13] As these charge carriers begin to be spatially restricted in one dimension, via restriction of crystal growth along a particular plane, the properties of the material are altered and the energy of the system changes. If the concept of confinement is applied further and the system's charge carriers are confined in all three dimensions, the energy of the system is altered to the extent that it now resembles a particle in a box situation.[13] The major consequence of this special confinement is the increase in band gap width as the particle size is restricted further (Figure 3.1).

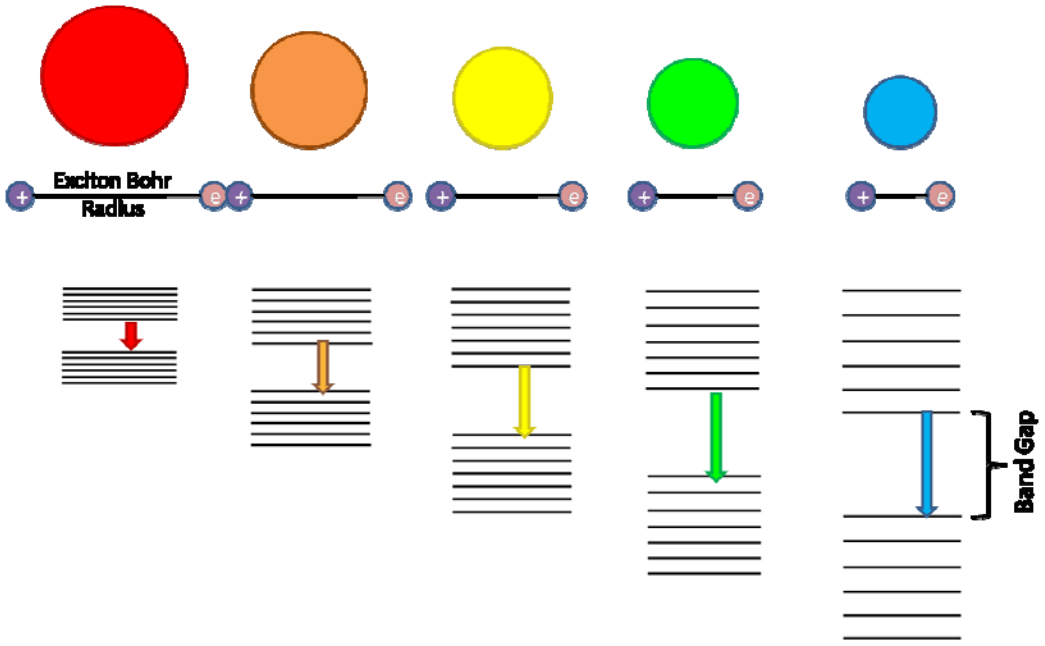

Figure 3.1. Cartoon illustrating band gap emission color in nanocrystals as a function of particle size.

3.1.2 Current state of the work on cadmium selenide nanocrystals

Despite claims that doping of CdSe and other nanomaterials of wurtzite or rock salt structure is unlikely and even impossible,[25-28] many research groups have made attempts at incorporating dopant ions within CdSe host lattices. These approaches, which are described briefly below, are often aimed at using dopant ions to tune or enhance the attractive photophysical properties possessed by CdSe nanocrystals.

3.1.2.1 Transition metal dopands

Cadmium selenide typically adopts a wurtzite crystal structure. The literature strongly suggests that it is not conducive to doping based on the surface energy ratios within these materials, and

that doping within these materials is only possible through the use of polychalcogenide precursors.[26] It has been shown however that CdSe crystal phase can be forced into the zinc blende crystal structure through modification of their synthetic conditions. This structure is known to incorporate dopant ions more readily using the typical high temperature injection syntheses.[26,29] Overall, it is suggested that doping concentration within host lattices is strongly dependent on a number of factors including surface morphology, nanocrystal shape, and most importantly, the crystal structure.[26,28]

A great deal of literature can be found regarding the doping of CdSe nanocrystals with transition metal ions. There are currently two separate approaches to achieving this goal: (1) the formation of zinc blende crystal structures to incorporate dopant ions based on surface energies[26,28] and (2) the use of single source or polychalcogenide precursors to form wurtzite structures with dopant ions.[30-32] To date, successful doping with cobalt, manganese, and manganese has been reported.[26,28,30-32] Most of the studies on these materials focus on transition metal dopants and the resulting magnetic properties observed upon incorporation into the host lattice, a topic beyond the scope of this research project.

Wurtzite structures have been reported containing either cobalt or manganese, while zinc blende structures have been observed for magnesium and manganese.[26,28,30-32] The advantage of forcing the CdSe nanocrystals to adopt a zinc blende structure is that the reactions can take place at slightly lower temperatures, and more facile synthetic methods can be employed. For instance, complicated single source precursors are not required, the preparation of which can be time consuming and difficult. The formation of the zinc blende structure is believed to result from the reduced synthetic temperatures at approximately 220 °C.

While most work does focus on magnetic properties, more recent studies have shown that the incorporation of dopants may lead to better tunability of band gap energies and, as a result, better control of emission properties. The tuning of the band gap through dopants has only been studied using zinc blende crystal structures, and studies using transition metal dopant ions to achieve this goal are just being established.

3.1.2.2 Lanthanide dopants

Transition metal dopants are attractive for the resulting magnetic properties that arise from doped CdSe nanocrystals; however, doping with rare earth metals has been increasingly attractive to obtain nanomaterials with novel and/or improved photophysical properties. A number of studies have reported fluorescence enhancement through the use of trivalent lanthanide dopant ions[33,34], while others have focused on magnetic properties arising from lanthanide dopants.[19] Additional studies have been conducted on doping of CdS with lanthanide cations.[35-38] Some studies involve doping a matrix containing nanocrystals, while others describe the doping of the nanocrystal material itself. Additional studies illustrate advantages of surface bound lanthanide cations. In all cases, characteristic lanthanide emission resulting from forbidden f → f transitions has been observed. Trivalent europium and terbium are most widely studied in these systems due to their visible emission.

In the case of silica matrices containing CdSe nanocrystals alongside Eu^{3+}, the antenna effect was not observed, however enhanced emission intensities of Eu^{3+} were found in the presence of CdSe.[34] This enhancement is the result of non-radiative energy transfer to the Eu^{3+} from the CdSe electron-hole recombination.[34] While many studies exist on doping of CdS

nanocrystals with lanthanides, the only known attempt of doping CdSe was by Strouse et al. This work focused on structural characterization of CdSe:Eu nanocrystals, where it was found Eu^{3+} are incorporated/associated with CdSe nanocrystals, however an antenna effect was not reported.[19]

We propose in this work that through the use of CdSe nanocrystals, we can synthesize a novel system in which the band gap serves as an antenna for different luminescent lanthanide cations. Our systems are aimed at optimizing nanocrystals size, and thus energy, for the most efficient energy transfer to the accepting levels of the lanthanide cations. In our systems the lanthanide is incorporated within (surface or internal sites) the nanocrystals and not incorporated into a matrix surrounding the nanocrystals. While the majority of the data presented herein has been limited to CdSe:Tb and CdSe:Eu nanocrystals, it is believed that their behaviors can be applied to other CdSe:Ln systems based on similar trends in photophysical properties. The accepting levels of terbium and europium lie at comparable energies. Using the criteria of energy levels, samarium and dysprosium should also be possible candidates for sensitization by the band gap of CdSe nanocrystals.

3.2 EXPERIMENTAL

3.2.1 Chemicals

Trioctylphosphine [TOP] (90%), trioctylphosphine oxide [TOPO] (99%), cadmium oxide (99.99% puratrem), n-tetradecylphosphonic acid [TDPA] (98%), 1-hexadecylamine [HDA] (98%), hexamethyldisilthiane, diethylzinc, europium nitrate (99.998%) and terbium nitrate (99.998%) were purchased from Sigma-Aldrich-Fluka. Selenium powder (99.99%), dysprosium nitrate (99.998%), and neodymium nitrate (99.998%) were purchased from Strem Chemicals. Methanol, ethyl acetate and ethylenediaminetetraacetic acid (EDTA) were purchased from Fischer Scientific, and chloroform was purchased from EMD. Gadolinium nitrate (99.998%) was purchased from Alfa Aesar. 1-octanol (98%) was purchased from Acros Organics and 1-butanol and potassium hydroxide were purchased from J.T. Baker. Argon and nitrogen gas was purchased from Valley National, Pittsburgh. All chemicals were used as purchased without purification.

3.3 RESULTS/DISCUSSION

3.3.1 Synthesis

We have synthesized CdSe nanocrystals with lanthanide cations incorporated within the crystal structure (occupying surface and/or core sites) using procedures adapted from the works from Peng et al.[29,39,40] and Strouse et al.[19] These syntheses involve the use of the less toxic CdO

precursor compared to the previously used $Cd(CH_3)_2$ at high temperatures (~300 °C) in TOPO/TOP solvent systems. From the original procedures, the cation concentrations were adjusted to account for lanthanide cations, however the total cation concentrations remain constant.

Preparation of Selenium Stock Solution: 1.0 mmol of selenium powder was dissolved in a mixture of 4 mL of TOP and 0.10 mL of toluene under vigorous stirring in a Schlenk tube. Excess air was removed through Schlenk de-gassing techniques under nitrogen and the solution was stored under nitrogen until used.

In the following procedure, trioctylphosphine oxide (TOPO) was used as the solvent, cadmium oxide (CdO) and lanthanide nitrates ($Ln(NO_3)_3 \bullet 5H_2O$) were used as precursors (doping levels for the different samples were comprised between 10-18%), and hexadecylamine (HDA) or N-tetradecyl phosphonic acid (TDPA) were used as a ligand for the Cd^{2+} and Ln^{3+}. Nucleation occurred upon injection of the Se stock solution into the reaction mixture (at 300°C) followed by subsequent decreasing of the temperature to 230°C for nanocrystal growth.

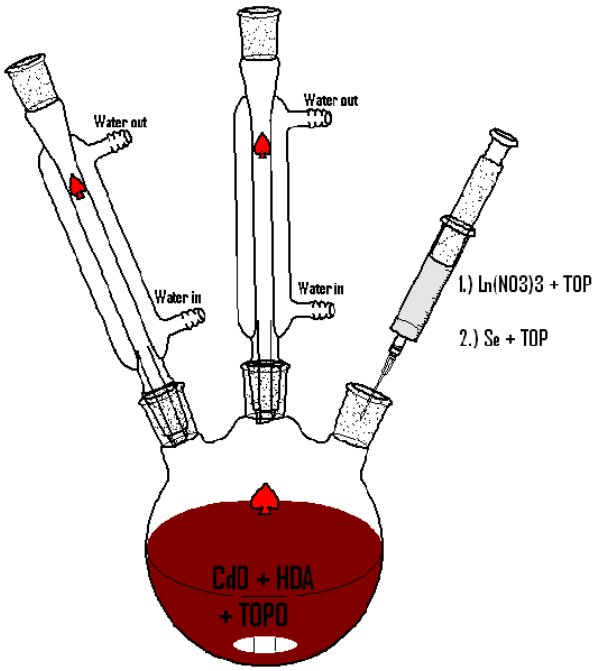

Figure 3.2. Cartoon illustrating general reaction set-up for the synthesis of CdSe nanocrystals.

In the initial synthetic procedures, the lanthanide salt, $Ln(NO_3)_3$, was placed in the reaction flask with CdO, HDA, and TOPO. In this procedure, the reaction mixture was not able to be completely dissolved because of the presence of the dopant material. In order to allow for complete dissolution of CdO procedures were modified, including subsequent injection of the lanthanide stock solution. The adapted procedures are as follows: the following reagents were placed in a three neck 50 mL round bottom flask, the necks of which had been fitted with water condensers (Figure 3.2): 10 mmol TOPO, 0.33-0.36 mmol CdO, and 0.80 mmol HDA or TDPA. Contents were placed under argon and heated to 300˚C. A terbium stock solution (0.04-0.07 mmol $Ln(NO_3)_3$) was injected once the reaction mixture reached 300˚C and the solution became clear (approximately 3 hours). The reaction was left to stir for 1 hour before a second stock solution containing selenium was added and the temperature was reduced to approximately

250˚C for the remaining duration of growth (since the stock solution was at room temperature when injected the reaction temperature immediately dropped and then stabilized over a period of minutes). Alternatively, for slower growth, the selenium stock solution was injected at 250˚C and nanocrystals were grown at 230˚C. For injection and growth at higher temperatures, growth times of 15 to 30 seconds were optimal, while at the lower temperatures, growth times of 30 seconds to 1 minute were best to maximize terbium sensitization (maximum of the lanthanide signal). Aliquots were removed at different synthetic times ranging from seconds to hours after injection using a glass syringe. Resulting products were stored as a raw solid until photophysical analysis was performed, at which point they were purified and suspended in chloroform.

Samples can be purified by precipitation with methanol and centrifugation followed by re-dissolution of the nanocrystals. We have found that this method leaves with the sample a large amount of unreacted starting material (HDA, TOPO). Since these reagents tend to interfere with some characterization techniques including TEM and EDAX analysis, a more efficient and sophisticated purification procedure was used. The nanocrystals were suspended in butanol and precipitated with methanol twice. To the precipitated nanocrystals, a small amount of octanol was added. The nanocrystals remain soluble in the octanol however the excess of HDA precipitates out. The octanol solution is then transferred into a new vial, leaving behind the precipitate, and 1-2 mL of ethyl acetate (which allows the octanol and methanol to be miscible) are added followed by the addition of an excess of methanol. The solution was centrifuged and the decant was poured off. The precipitated nanocrystals were redissolved in chloroform.

3.3.2 Surface modifications

Semiconductor nanocrystals have unique photophysical properties that make them attractive for use in a broad range of bioanalytical applications. For these applications, it is crucial to ensure sufficient water solubility and biocompatibility of these nanoparticles. We have developed a procedure for the synthesis of CdSe:Ln nanocrystals that is reproducible and yields stable product. It is necessary, however, to develop a protocol for coating these nanocrystals that will increase their stability and increase their solubility in water for use in biological systems without decreasing their favorable photophysical properties. In addition to creating a biologically compatible coating, we have decided to choose the coating material based on its ability to prevent Cd^{2+} ions to be released from the nanocrystal structure (resulting from photo-oxidation of the surface).

Preliminary coating experiments focused on the use of polydentate chelating ligand, such as EDTA. It was hypothesized that EDTA would bind the nanocrystal surface and render them at least partially water soluble. The experiments involved preparation of saturated EDTA solution in water (the EDTA was fully deprotonated to ensure removal of all acidic protons in order for chelating to occur). The aqueous EDTA solution was then added to the nanocrystals dissolved in chloroform. The mixture was shaken and layers were separated. Both chloroform and aqueous layers were analyzed for the presence of nanocrystal band gap as well as terbium emission.

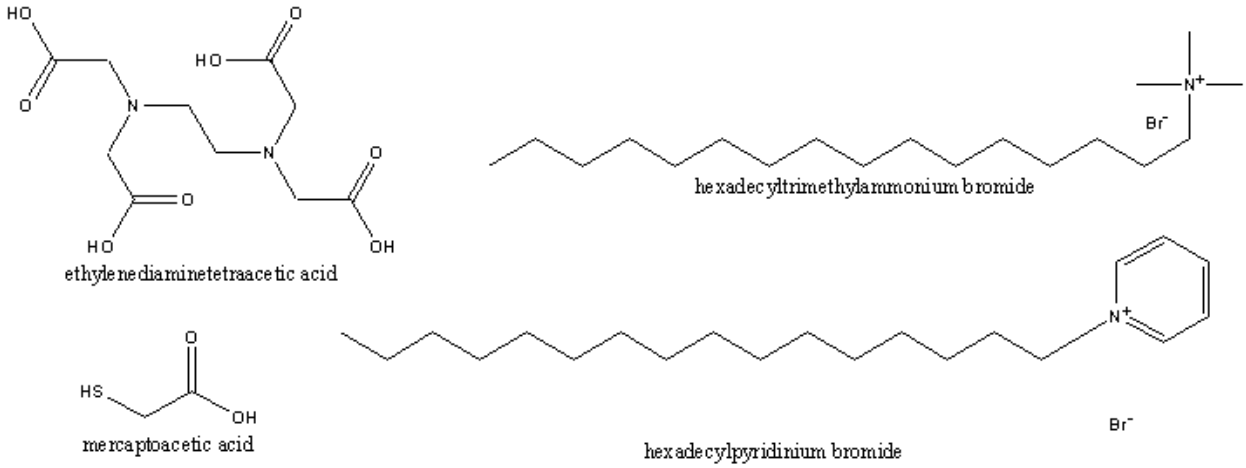

Figure 3.3. Chemical structures of different surface passivants used for surface modification of CdSe nanocrystals.

In addition to the chelating ligand approach with EDTA, we have also decided to test different micellar solutions to promote the water-solubility of the nanocrystals. The two micellar agents that we have tested were hexadecylpyridinium bromide and hexadecyltrimethyl-ammonium bromide (solutions will be referred to as micelle 1 and micelle 2 for future reference respectively). The nanocrystal samples were mixed with the micellar solutions followed by spectral analysis of water soluble samples to determine the presence of CdSe nanocrystals and Tb^{3+} emission bands. In the micelle approach, we have coated the existing organic passivants (such as TOPO) with a shell of micelle material. The additional layer allowed water solubility at the cost of increasing nanoparticle size.

An alternative strategy to increase the solubility of the nanocrystals in water is to strip away the organic ligands passivating the surface from the synthesis (TOPO) and replace them with water soluble capping ligands. A thiol ligand, mercaptoacetic acid was used to achieve this

goal with this nanocrystal system. The exchange procedure includes the addition of the desired ligand to precipitated nanocrystals. The solution was then heated to 60°C while stirring for two hours. Once the exchange process occurred, the particles were precipitated using a strong base such as potassium tert-butoxide. Nanocrystals were then analyzed to test for band gap and lanthanide emission properties.

While water solubility is required if we are to exploit the properties of these systems for biological applications, surface exchanges tend to result in strong quenching of the nanocrystal emission.[41-43] One approach to minimize, or counteract the quenching process, is to coat semiconductor nanocrystals with a shell of nanomaterial with larger band gap such as ZnS. Raw CdSe nanocrystals were added to round bottom flask containing a mixture of TOPO and HDA. The flask was placed in a glovebox and heated to temperatures between 140 and 220 °C. The temperature used is dependent upon the size of the nanocrystal. Larger particles are heated to higher temperatures in order to prevent further growth of the core materials. The amount of Zn/S precursors that were required to produce the shell was determined by using the total molar ratio of Cd/Se present in the initial reaction mixture (the overall ratio of CdSe:ZnS should be 1:4 based on existing experiments in the literature on nanocrystals of similar size).[44,45] The amount of shell grown on a CdSe core is usually less than the amount of ZnS reactants added because of incomplete reaction of precursors.[45] Equimolar amounts of Zn and S precursors were used in the form of diethylzinc and hexamethyldisilthiane. The Zn/S precursors were dissolved in 3 mL of TOP in an addition funnel. Once the core nanocrystal solution reached the desired temperature, the shell stock solution was slowly added.[45] Aliquots of the core/shell reaction mixture were removed and dissolved in chloroform for analysis of spectral properties. Successful shelling of

these materials is indicated by a red shift in the band gap emission profile relative to the core particles. The observed red shift is explained by expansion of the exciton into the ZnS shell.[45,46]

Data on surface modification of CdSe nanocrystals is found in Appendix B.

3.3.3 Physical characterization

The synthesized CdSe:Tb nanocrystals were visualized using transmission electron microscopy (TEM). Initial analysis was performed by first aerating purified and isolated samples dissolved in hexane onto carbon coated copper grids. Low resolution TEM data were obtained through the use of a TEM instrument housed within the University of Pittsburgh Department of Materials Science and Engineering and operated by Cole Van Ormer. The instrument, a JEOL 2000-FX scanning transmission electron microscope (STEM) operating at 200 kV, was fitted with a detector for energy dispersive X-ray spectroscopy (EDX) allowing simultaneous imaging and composition determination. Figure 3.4 shows the results of this experiment. Low resolution TEM images, shown left, are of poor quality however they do illustrate the presence of nanometer sized particles which are believed to be CdSe:Tb nanocrystals. We can estimate from this image that the particles are comprised between 2 and 3 nm in diameter (this is within the typical size range reported for undoped CdSe nanocrystals emitting in the visible region). It is difficult in this image to identify whether we are observing individual particles or aggregates of particles. The EDX spectrum on the right confirms the presence of Cd, Se and Tb within our samples.

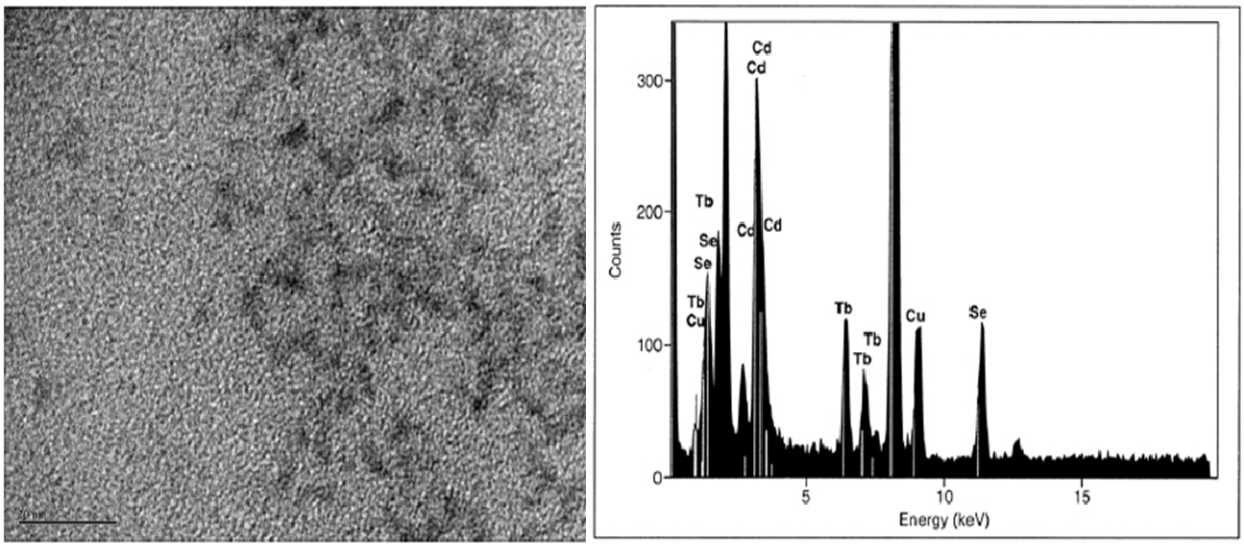

Figure 3.4. Left: TEM image of CdSe:Tb nanocrystals taken at 850 K (size bar represents 20 nm), Right: Energy dispersive X-Ray spectroscopy analysis of nanocrystals (copper peak is from grids used for sample preparation).

Additional TEM images were obtained through the use of a low resolution instrument at Carnegie Melon University, a Hitachi H-7100 TEM instrument operating at 75 kV. Only very limited improvement over the data observed above was obtained. The most significant advancement in the imaging of our CdSe nanocrystals came through collaboration with Dr. James McBride of the Rosenthal group at Vanderbilt University and Oak Ridge National Laboratory. The high resolution TEM image shown below clearly illustrates the crystallinity of our nanoparticles (Figure 3.5). This image was obtained only after extensive purification of the nanocrystals involving dissolution of particles in butanol, precipitation in methanol, redissolution in octanol, and further precipitation in methanol followed by addition of the appropriate solvent to the nanocrystal precipitate for analysis (chloroform, methanol, hexanes). This individual nanocrystal image demonstrates that the nanocrystals are not present as aggregates in solution,

but are rather individual discrete nanoparticles. The image additionally demonstrates that the material formed is crystalline rather than amorphous particles.

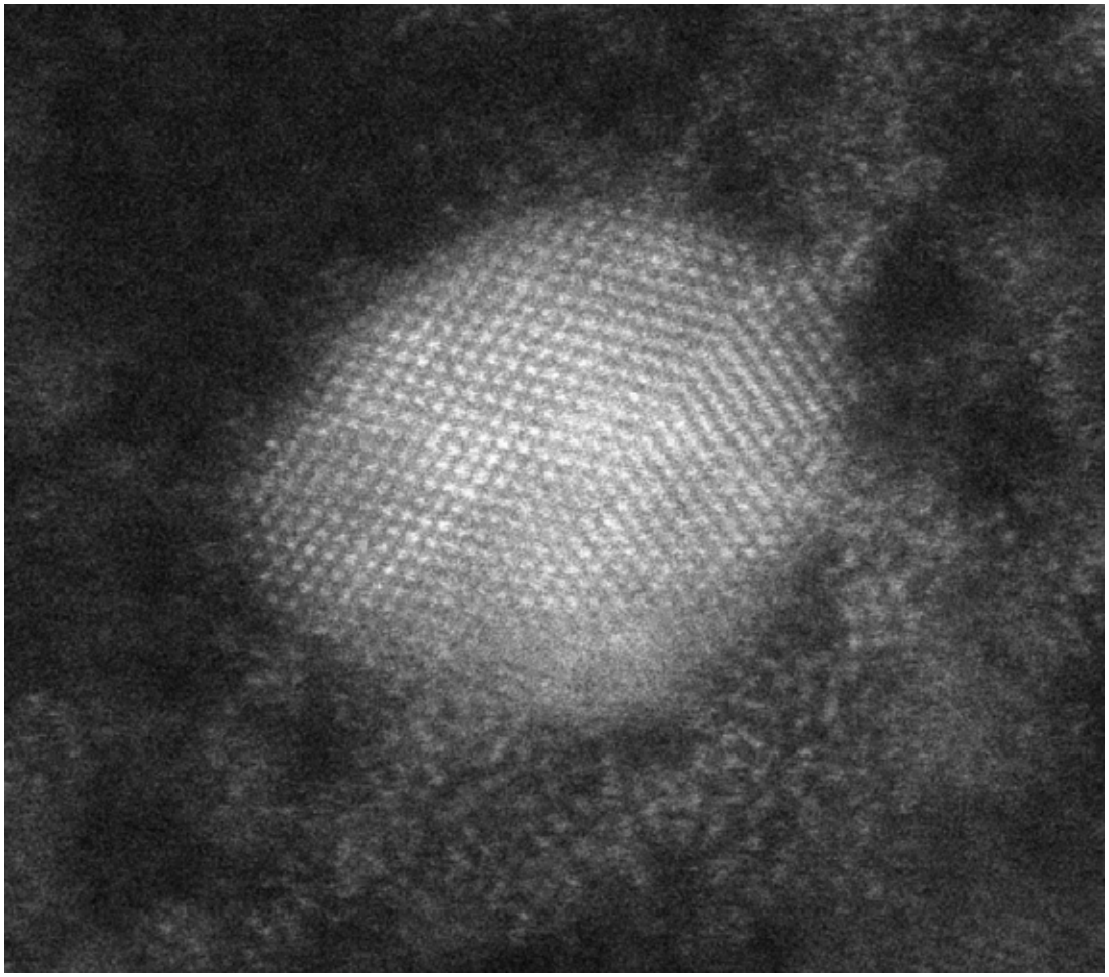

Figure 3.5. High resolution TEM image of the synthesized CdSe:Tb nanocrystals (obtained through collaboration with Dr. James McBride and Dr. Sandra Rosenthal - Vanderbilt University and Oak Ridge National Laboratory).

The CdSe nanocrystal systems were also characterized using X-ray powder diffraction. Figure 3.6 shows the preliminary data obtained on the crystal structure of CdSe:Tb nanocrystals compared to undoped CdSe nanocrystals. Some of the observed peaks are slightly shifted and broadened, which are believed to arise from slight strain in the lattice structure upon the

introduction of dopant ions. The graphs on the left represent actual data obtained from our synthesized CdSe doped and undoped nanocrystals, while the data on the left illustrates literature diffraction patterns for both wurtzite and hybrid zinc blende/wurtzite CdSe. Based on comparison of our data to the literature data, it can be hypothesized that our materials possess some variation of a hybrid crystal structure.

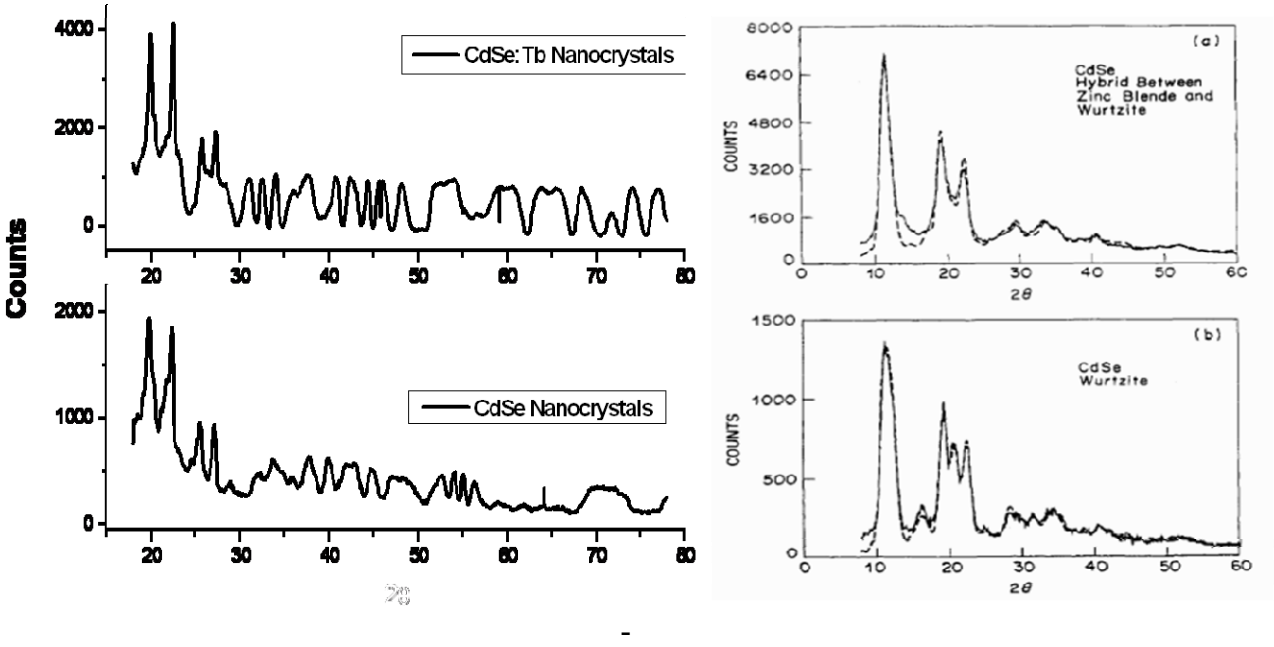

Figure 3.6. XRD patterns of synthesized CdSe and CdSe:Tb nanocrystals (left) and published CdSe nanocrystals having hybrid and wurtzite structure (right).[47]

Additional low resolution TEM images have been obtained for CdSe:Eu nanocrystals (Figure 3.7), confirming the presence of spherical nanometer sized particles similar to what was observed for CdSe:Tb. The figure below shows particles of approximately 4.8 ± 0.5 nm in diameter (determined by analysis with NIH Image J software) and some aggregated particles as

well. The aggregation may be the result of drying effects upon grid preparation not representative of nanoparticle behavior in solution.

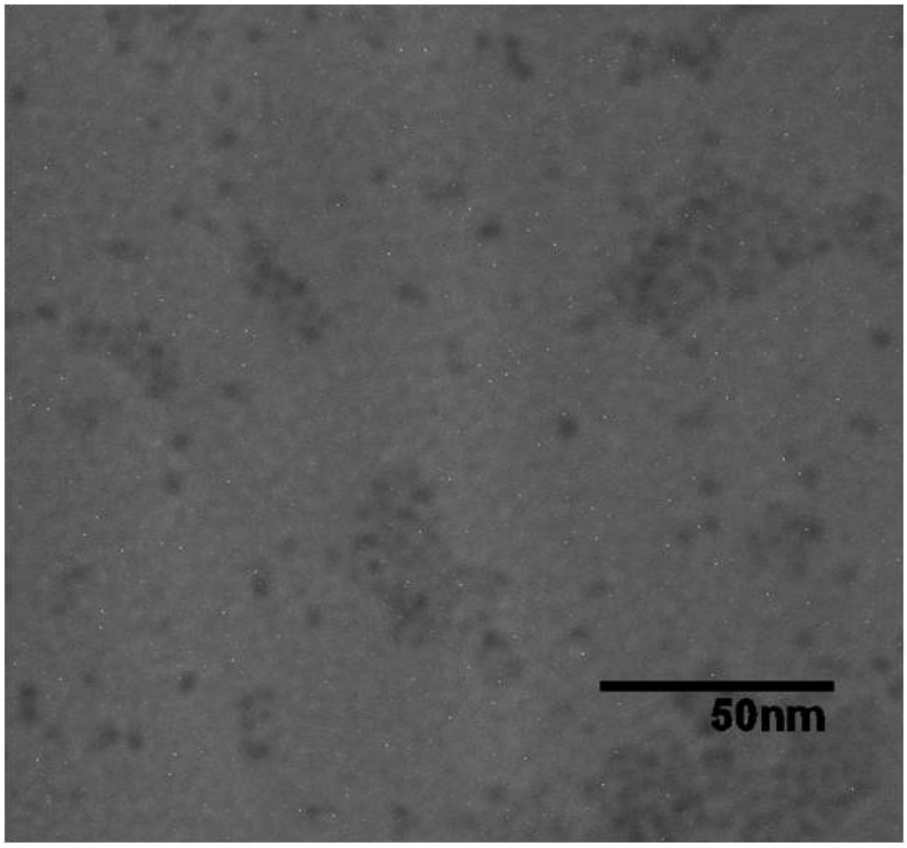

Figure 3.7. Low resolution TEM image obtained through collaboration with Carnegie Melon University.

ICP measurements have also been conducted on purified CdSe:Tb and CdSe:Eu nanocrystal systems. From these measurements we should be able to determine the amount of lanthanide within the nanocrystal system. Of the nanocrystals submitted for analysis, results have only been obtained thus far for two samples from the same nanocrystal batch. Additional samples are presently being analyzed.

Table 3.1. ICP-AES results obtained through collaboration with Amy Wolfe and Professor Brian Stewart in the Geology Department at the University of Pittsburgh. All calibration data can be found in Appendix G.

Element and Sample Analyzed	MV, mg/L	+/-, mg/L	% error	Concentration, mol/L
Cd in CdSeTb 2-1	1.601	0.0520	3.249	1.42E-05
Cd in CdSe Tb 2-2	2.635	0.0537	2.040	2.34E-05
Se in CdSeTb 2-1	0.6230	0.0102	1.637	7.89E-06
Se in CdSeTb 2-2	0.7590	0.0188	2.470	9.61E-06
Tb in CdSeTb 2-1	2.626	-2.981	3.824	1.65E-05
Tb in CdSeTb 2-2	3.650	-3.126	1.141	2.30E-05

The data shown in Table 3.1 summarizes results of ICP analysis on CdSe:Tb nanocrystals. The data are expressed in mg/L and have been converted to a molar concentration to directly compare the stoichiometrical amounts of each species present within the sample solutions. The original reaction mixture for CdSe:Tb nanocrystals contained 15% terbium (based on total cation concentration). The analysis by ICP results indicates that impurities may be present in the nanocrystal samples, perhaps as unreacted starting materials. The cadmium and terbium are present in almost a 1:1 ratio in these samples, and the selenium is present at half that amount. The ratios do not match the relative amounts of materials placed into the reaction mixture, nor do they result in reasonable composition of the nanocrystals. We are awaiting further results to more clearly determine doping within these nanocrystal samples. The discrepancy of these results could result from sample preparation.

3.3.4 Photophysical characterization

The UV-Vis absorption spectra recorded on nanocrystals that have been produced using different growth times, shown in Figure 3.8, exhibit the characteristic shift in wavelength as the nanocrystal growth time and size increase. As the particle size increases, the absorbance shifts to lower energy and corresponds to quantum confinement affects within CdSe particles.[13,29,39,48,49] The broad absorption of these particles is an attractive feature because it allows for excitation at a broad range of wavelengths.

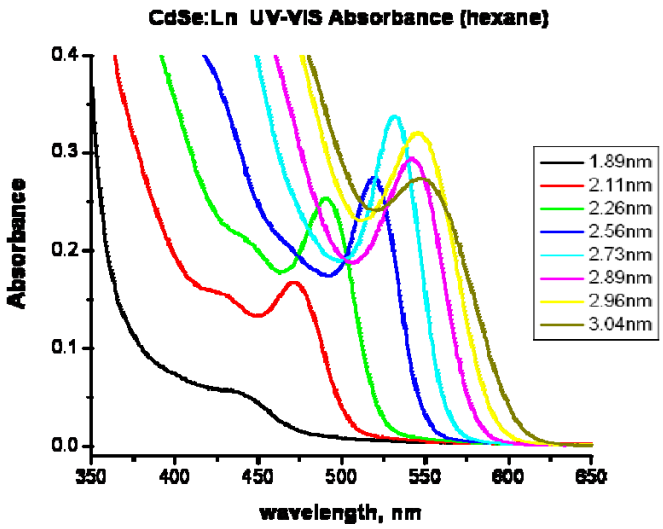

Figure 3.8. UV-vis absorption spectra of CdSe:Ln nanocrystals in hexane illustrating shift in band position with nanocrystal size (size determination performed by calculations based on the work of Peng et al. and Alivisatos et al.)[50,51]

For CdSe nanocrystals, the absorption bands and steady state emission consistently exhibit red shifts with increasing growth time, regardless of the lanthanide dopant added, corresponding to increase in nanocrystal size. This result indicates that the presence of the

lanthanide cations as a component of the synthesis does not affect the formation of the nanocrystals. Size determination was performed using UV-vis absorption and calculations based on the work of Peng et al. and Alivisatos et al.[50,51] The absorbance spectra above are representative of the overall CdSe samples studied.

CdSe:Ln systems formed with 5 different lanthanides were studied, with the goal of using the CdSe band gap as an antenna for the four visible emitting trivalent lanthanides: Eu, Tb, Sm and Dy. The materials include: CdSe:Tb, CdSe:Eu, CdSe:Dy, CdSe:Sm, and CdSe:Gd. CdSe:Gd nanocrystals serve as a control in these doped systems and the study of their photophysical properties because Gd^{3+} is a lanthanide cation silent for luminescence since its accepting levels are too high in energy to accept energy from a sensitizer. The photophysical data obtained for Gd^{3+} doped materials resemble those of undoped CdSe nanocrystals.

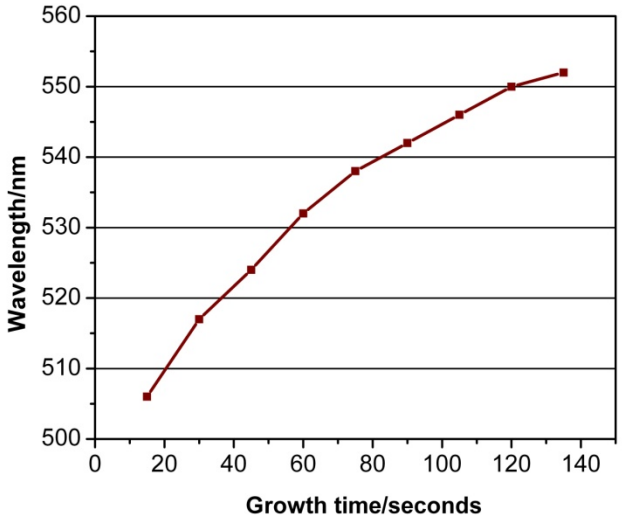

Figure 3.9. CdSe:Tb SCNC Emission: Growth time versus the wavelength of the fluorescence maximum. This graph demonstrates the ability to control the size and photophysical properties of the doped nanocrystals through the synthesis.

The CdSe:Tb SCNCs of nanocrystals obtained after different growth times display a bathochromic shift, which demonstrates that doping does not interfere with the quantum confinement properties (Figure 3.9). Steady state and time resolved emission and excitation spectra were collected for the CdSe:Tb nanocrystal aliquots obtained at different growth times. The emission arising from the lanthanide cation can be discriminated from the nanocrystal luminescence through time resolved measurements using a typical delay after flash of 200 μs. The total emission of the nanocrytals as well as the Tb^{3+} specific emission was quantified and analyzed for different samples, leading to several interesting findings. In steady state mode, the total emission of the CdSe:Tb SCNCs appears as a relatively broad band (green, Figure 3.10), much broader than those reported for undoped CdSe nanocrystals.[52,53] This can be explained by the short material growth time of samples used for this photophysical investigation, leading to a polydisperse size distribution of nanocrystals since the system does not have suffiecient time to equilibrate the the combined dynamic process of nucleation and breaking. Longer growth times and alternative synthetic methods should lead to less dispersity and thus sharper emission bands. The corresponding excitation spectrum (black, Figure 3.10) displays a sharp maximum around 300 nm and appears as an asymmetrical band. Emission arising from Tb^{3+} cannot be observed on the steady state emission spectrum due to its low intensity relative to the band gap emission. In order to monitor specifically the Tb^{3+} emission, the instrument needs to be switched to time resolved mode. Tb^{3+} emission appears as narrow, atom-like luminescence. Time resolved emission spectrum revealed the four main observable Tb^{3+} transitions ($^5D_4 \rightarrow {}^7F_J$, J = 6, 5, 4, 3 by decreasing the order of energy, green in Figure 3.10.) The time resolved excitation spectrum (red, Figure 10) monitoring the Tb^{3+} $^5D_4 \rightarrow {}^7F_5$ transition (λ_{em} = 545 nm) revealed a profile that resembles the steady state excitaiton spectrum and differs from the excitaiton profile of the

lanthanide salt $Tb(NO_3)_3$ (Figure 3.11.) These findings confirm that the nanocrystal structure is acting as an antenna for Tb^{3+} since the energy is following the same path for both cases: in other words, Tb^{3+} emission is sensitized through the electronic structure of the SCNCs.

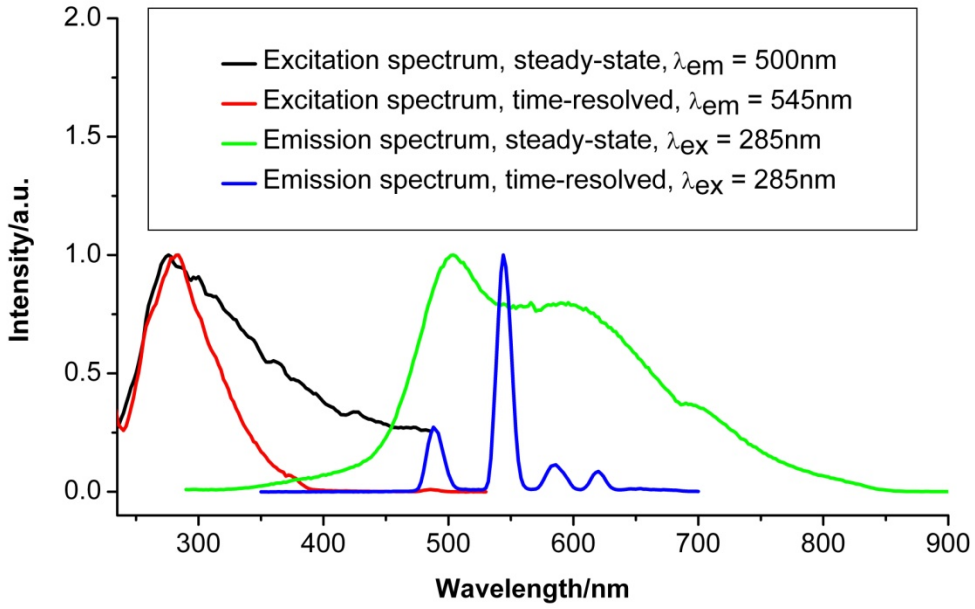

Figure 3.10. CdSe:Tb SCNCs (in chloroform): normalized steady state and time resolved excitation and emission spectra. The Tb^{3+} emission is in the same range as the nanocrystal emission; however, it is easily distinguished through time resolved measurements.

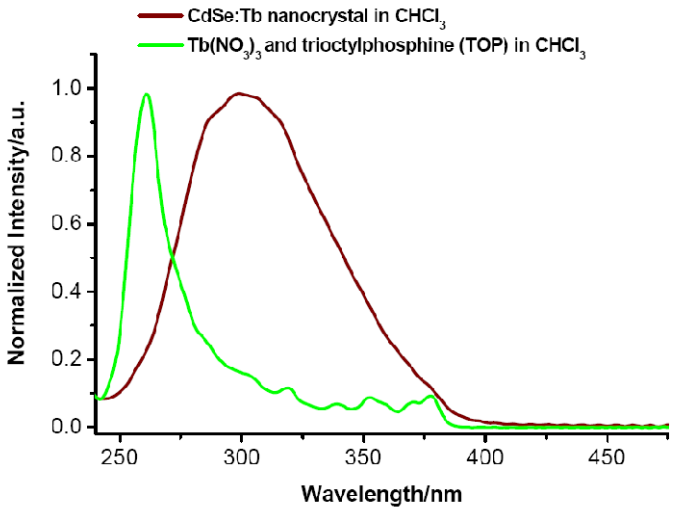

Figure 3.11. Normalized time resolved excitation spectra of CdSe:Tb nanocrystals in chloroform (brown) and of a solution of TOP, $Tb(NO_3)_3$ in chloroform (green); λ_{em} = 545 nm, room temperature. CdSe:Tb nanocrystals used for this experiment have been collected 30 s after injection of Se.

Through optimization of synthetic procedures (lanthanide stock solution was originally placed in the reaction mixture at the start of the synthesis and was later injected post dissolution of the CdO), the broad nanocrystal emission bands indicating that the nanocrystals previously synthesized were polydisperse. Samples have been replaced by samples emitting as more narrow bands (Figure 3.12). Full width at half maximum values (fwhm)obtained here range from 41 – 48 nm, showing a slight increased dispersity over undoped CdSe reported in the literature (fwhm of undoped have been reported as 27 – 40 nm).[52,53] The narrow bands indicate more monodisperse nanoparticles through the new synthetic method. This new synthetic method was employed after publication of our preliminary work.[12]

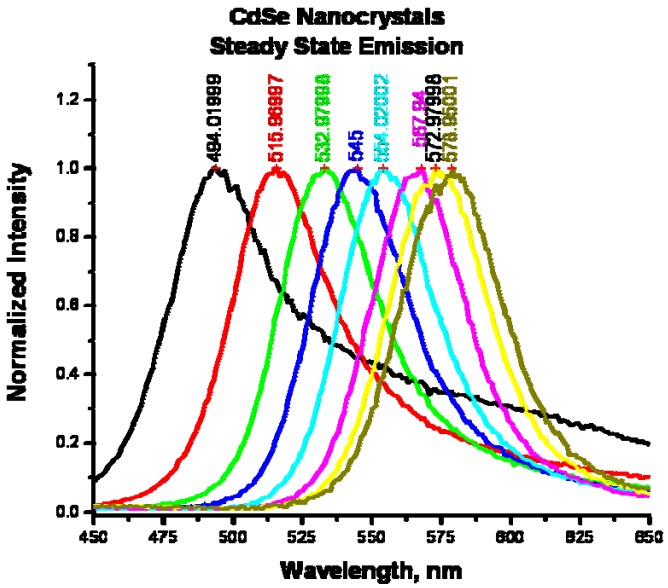

Figure 3.12. Normalized emission spectra of CdSe:Ln nanocrystals in hexane illustrating shift in emission maxima with nanoparticle size(higher energy corresponds to smaller particles). These spectra are characteristic of CdSe nanocrystal band gap emission and indicate that their spectroscopic properties are not affected by the presence of dopant ions.

As observed for CdSe:Tb nanocrystals, the steady-state emission spectrum of CdSe:Eu nanocrystals upon excitation at 400 nm indicates mainly the presence of abroad emission band with an apparent maximum located at 500 nm that can be attributed to the band gap transition of CdSe, Figure 3.13. No significant signal arising from Eu^{3+} can be observed. In order to observe such transition, we had to record this spectrum in time-resolved mode.

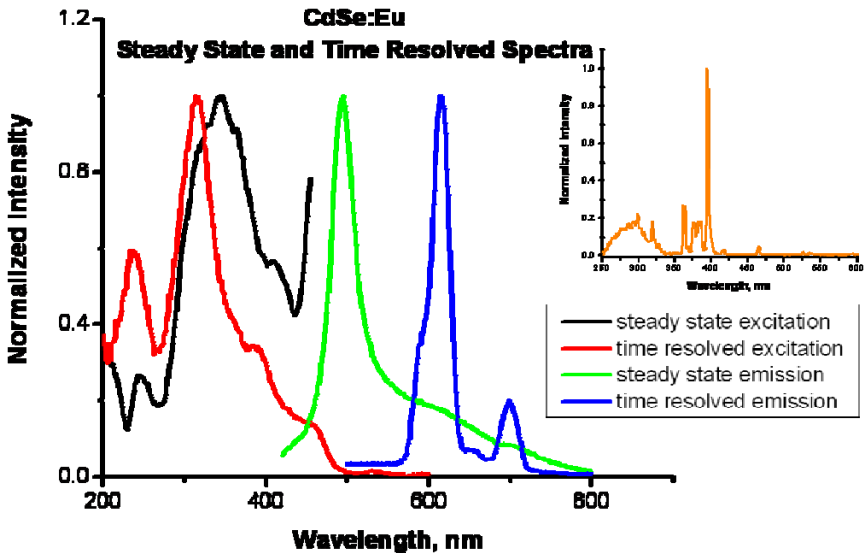

Figure 3.13. Normalized steady state and time resolved emission and excitation spectra for CdSe:Eu nanocrystals in hexane (SSEM: λ_{ex} = 400 nm, SSEX: λ_{em} = 450 nm, TREX λ_{em} = 545 nm, TREM: λ_{ex} = 400 nm). Direct excitation profile of Eu^{3+} (recorded on $Eu(NO_3)_3$ in methylene chloride) upon monitoring emission at 614 nm.

The analysis of the steady state and time resolved excitation and emission spectra of the CdSe:Eu nanocrystals allowed for conclusions that the electronic structure of CdSe can provide an antenna effect to Eu^{3+} (Figure 3.13). Lanthanide emission is obtained through energy transfer from the nanocrystal band gap, which is evident based on the overall shape and position of the steady state and time resolved excitation spectra. The excitation spectra collected in steady state and time resolved modes, corresponding to nanocrystal centered excitation and lanthanide excitations respectively, are fairly similar, indicating similar energy pathways.

When comparing CdSe:Eu to CdSe:Tb, we can observe that the degree of sensitization of the lanthanide cations varies based on the degree of overlap between the nanocrystal and

lanthanide excitation profiles. This overlap results from energy matches between the nanocrystal band gap energy and the energy position of the lanthanides' accepting levels. In the case of CdSe nanocrystals, only small sized particles should have appropriate energy to transfer to Tb^{3+}. This is supported experimentally through growth time studies monitoring the emission intensity that arises from the Ln^{3+} cations. The most efficient sensitization occurs at short growth times (30 s) which correspond to particles with calculated diameters of approximately 2 nm (Figure 3.14 right). Figure 3.14 (left) illustrates band gap energy nanocrystals relative to lanthanide energy levels. The nanocrystal shown here, labeled QD, illustrates representative band gap energy that will change as the particle size changes (smaller particles will have higher energy and thus wider band gaps and larger particles will have smaller band gaps). As the band gap energy is decreased, the conduction band of the nanoparticle is lowered relative to the lanthanide accepting levels and at one point will reach a level where it is no longer suited for or results in minimized energy transfer to Tb^{3+}. The energy positions of the lanthanide accepting levels are specific for each lanthanide. It results in different sized nanoparticles being better suited for optimized energy transfer to each specific lanthanide according to their size. The attractiveness of using semiconductor nanocrystals to sensitize lanthanide cations is the possibility to obtain such optimization of the energy transfer based on band gap energy controlled by the nanoparticle size. By varying the size of the particles the energy can be tuned for energy transfer to occur for a number of different lanthanide systems. As a demonstration, both Tb^{3+} and Eu^{3+} are sensitized by the nanocrystal band gap as illustrated by the overlap in excitation profiles. This sensitization is further supported through comparison to energy level diagrams. A basis for the representation of optimized energy transfer to lanthanide cations through the control of the size of the nanoparticle is depicted below through a series of matrix plots.

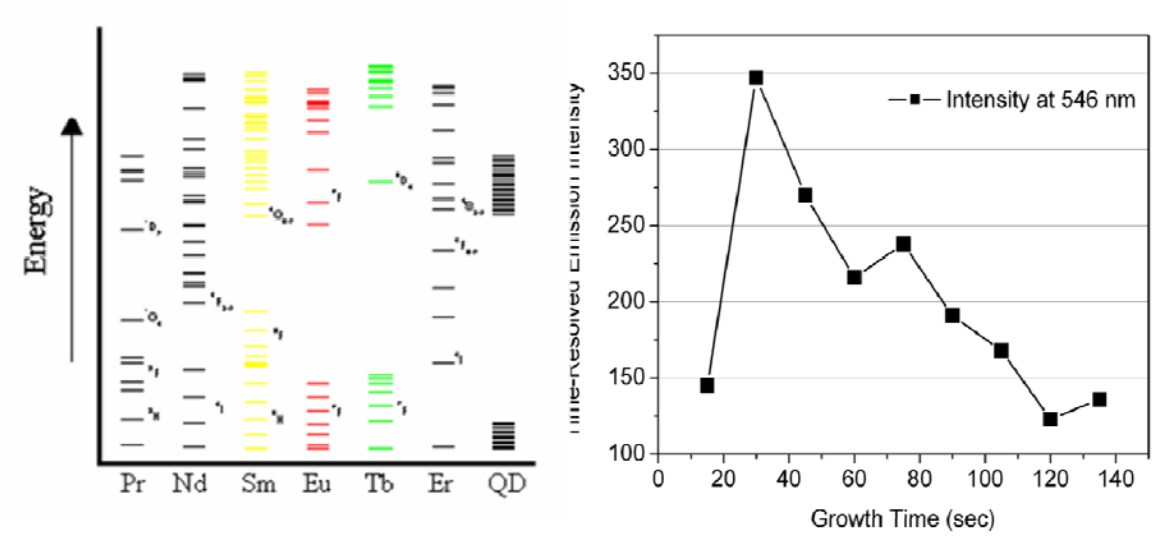

Figure 3.14. Left: diagram illustrating the energy levels of the lanthanide cations and representative nanocrystal band gap. Right: plot illustrating growth time (corresponding to nanocrystal size) versus emission intensity of the $^5D_4 \rightarrow {}^7F_5$ transition of Tb^{3+}.

We have prepared a series of energy level diagrams representing the energy levels of the trivalent lanthanide cations overlaid with a matrix correlating either emission maxima (Figures 3.15 to 3.18) or excitation maxima (Figures 3.19 to 3.21) of the band gaps of lanthanide-doped nanocrystals obtained at different growth times. This series of analyses was performed in order to probe the sensitization of luminescent lanthanide cations in the current lanthanide doped CdSe nanocrystals as a function of their size to rationalize our experimental results and to be able to synthesize lanthanide containing nanocrystals with predictable properties. As the nanocrystals grow in size, their band gap emission is shifted towards lower energies. This shift in energy indicates the possible tuning of the band gap emission to match the accepting levels of various lanthanide cations. In the case of smaller nanocrystals emitting at 494 nm (2.26 nm calculated nanocrystal diameter), Figure 3.15, the band gap emission is located at suitable energy to transfer

to Tb^{3+} and Eu^{3+}, as well as Sm^{3+} and potentially Er^{3+}, Ho^{3+}, Nd^{3+}, and Pr^{3+}. Energy transfer to Tb^{3+}, Eu^{3+} and Sm^{3+} were observed to varying degrees, and extensive studies on CdSe:Tb confirm maximum emission resulting from doping of smaller CdSe nanocrystals. Nanocrystals having smaller diameters with emission maxima corresponding to 460 nm (1.89 nm calculated nanocrystal diameter) would be suited for energy transfer to Dy^{3+} as well.

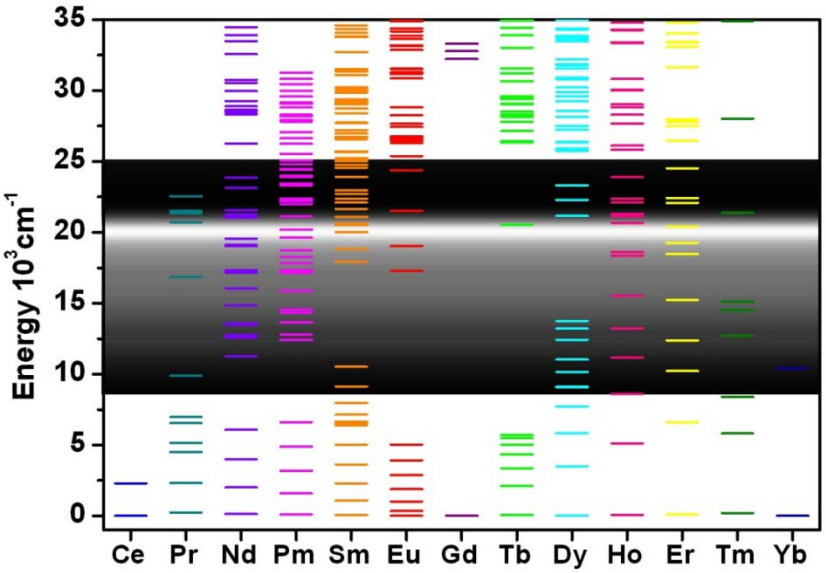

Figure 3.15. Energy level diagram for Ln^{3+} cations. The dark region is a matrix representing the energies as obtained from their fluorescence spectra upon excitation of the nanocrystal band gap (λ_{ex} = 350 nm). The white region represents the apparent emission maximum (λ_{em} = 494 nm).

As the nanocrystal band gap emission is shifted towards lower energy, we can predict that Tb^{3+} will no longer be sensitized efficiently by the band gap of the material. This is evident for the energy diagrams representing emission at 516 nm (2.56 nm calculated nanocrystal diameter) and longer, Figures 3.16 through 3.18, where the energy position of the emission maxima shifts below the accepting levels of Tb^{3+}. The emission energy is therefore no longer in

a position to allow for transfer from the band gap to the lanthanide if the mechanism involved is a Förster mechanism. The emission band is now residing below the accepting levels of the Tb^{3+} results in a situation that is detrimental to the overall nanocrystal to Tb^{3+} energy transfer. Experimental results do agree with this model in that, at longer wavelengths, time resolved excitation spectra give rise to direct excitation bands rather than overlapping excitation bands. This indicates that energy transfer is no longer occurring from nanocrystal band gap to lanthanide accepting levels and any lanthanide emission is the result of direct excitation.

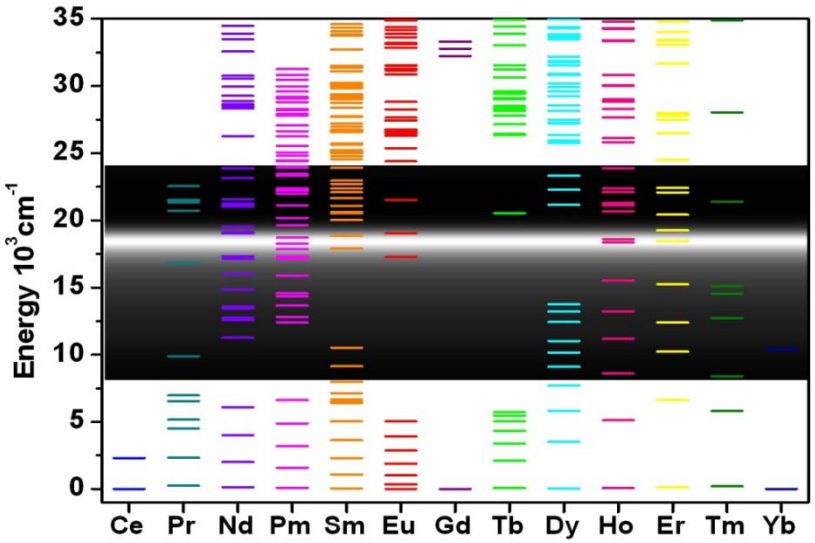

Figure 3.16. Energy level diagram for Ln^{3+} cations. The dark region is a matrix representing the fluorescence obtained upon excitation of the nanocrystal band gap (λ_{ex} = 350 nm). The white region represents the emission maximum (λ_{em} = 516 nm). Matrix plots were created using OriginPro 7 software and were overlaid at appropriate energy positions.

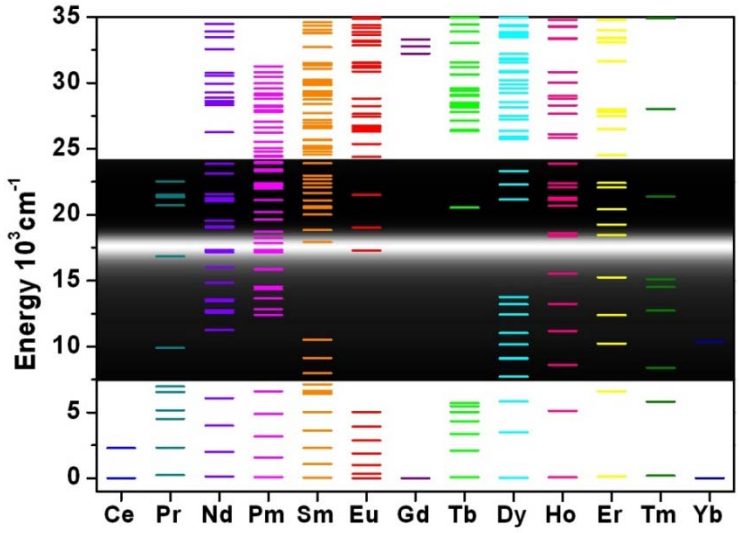

Figure 3.17. Energy level diagram for Ln^{3+} cations. The dark region is a matrix representing the fluorescence obtained upon excitation of the nanocrystal band gap (λ_{ex} = 350 nm). The white region represents the emission maximum (λ_{em} = 543 nm). Matrix plots were created using OriginPro 7 software and were overlaid at appropriate energy positions.

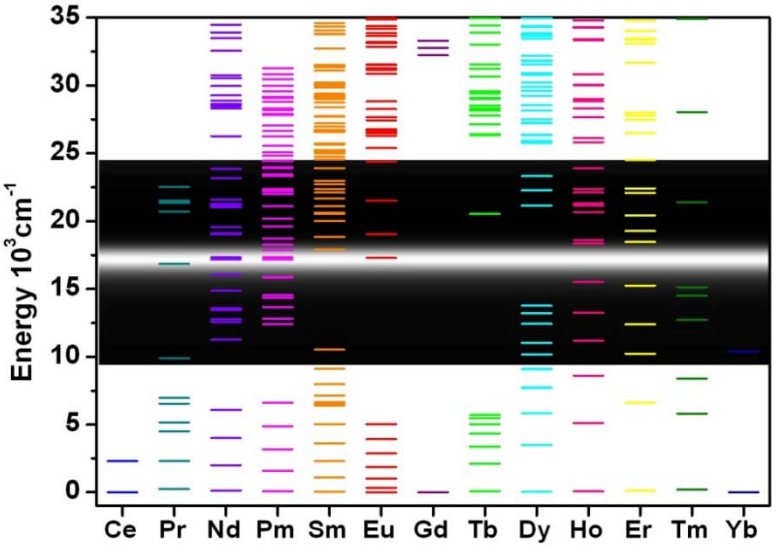

Figure 3.18. Energy level diagram for Ln^{3+} cations. The dark region is a matrix representing the fluorescence obtained upon excitation of the nanocrystal band gap (λ_{ex} = 350 nm). The white region represents the emission maximum (λ_{em} = 574 nm). Matrix plots were created using OriginPro 7 software and were overlaid at appropriate energy positions.

In addition to the comparison of the energies of the band gap emission with the energies of the accepting levels of the various trivalent lanthanide cations, the excitation spectra were also analyzed and compared for nanoparticles with different sizes. Figures 3.19 to 3.21 illustrate the result of this analysis. Because the band gap excitation spectra are located at higher energy, they are positioned more appropriately to transfer, the energy to the lanthanides than in the case of the emission overlay. This data would hold true in the case of a Dexter energy transfer mechanism, where simultaneous exchange of electrons from the excited state of the donor to the excited state of the acceptor.

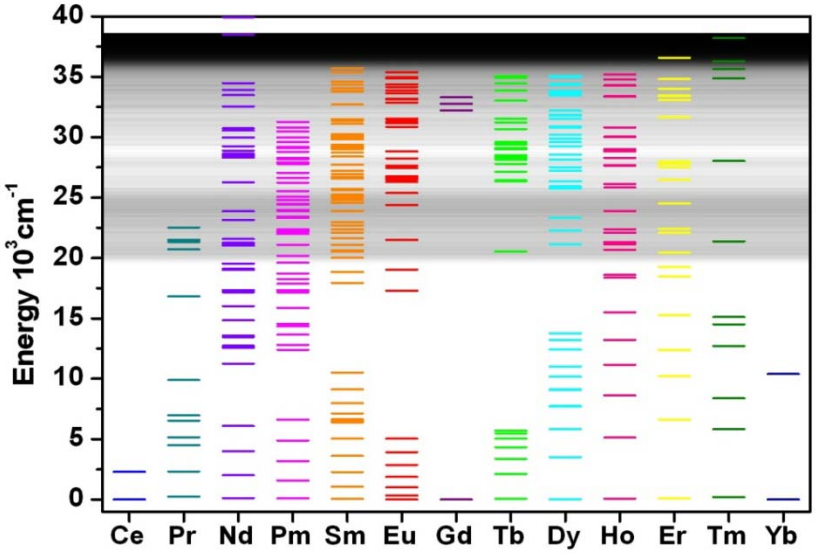

Figure 3.19. Energy level diagram for Ln^{3+} cations. The darkened region is a matrix representing the nanocrystal excitation wavelengths (λ_{em} = 494 nm). The lighter/white regions represent excitation maxima. Matrix plots were created using OriginPro 7 software and were overlaid at appropriate energy positions.

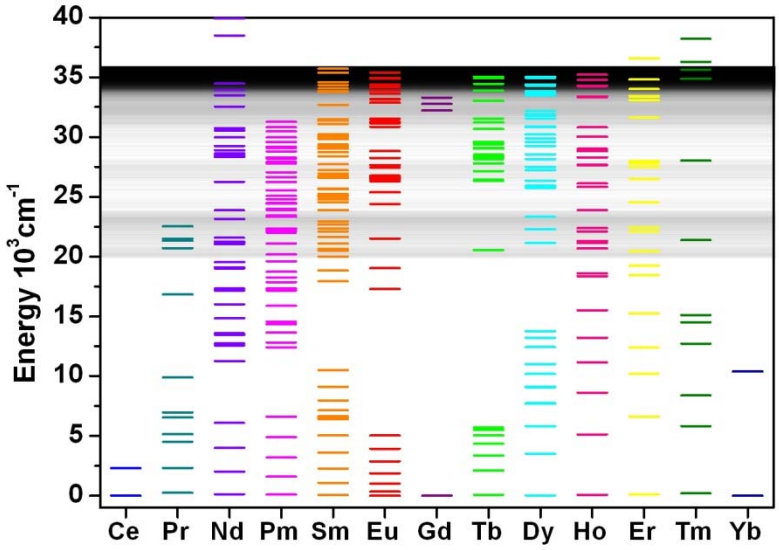

Figure 3.20. Energy level diagram for Ln^{3+} cations. The darkened region is a matrix representing the nanocrystal excitation wavelengths (λ_{em} = 516 nm). The lighter/white regions represent excitation maxima. Matrix plots were created using OriginPro 7 software and were overlaid at appropriate energy positions.

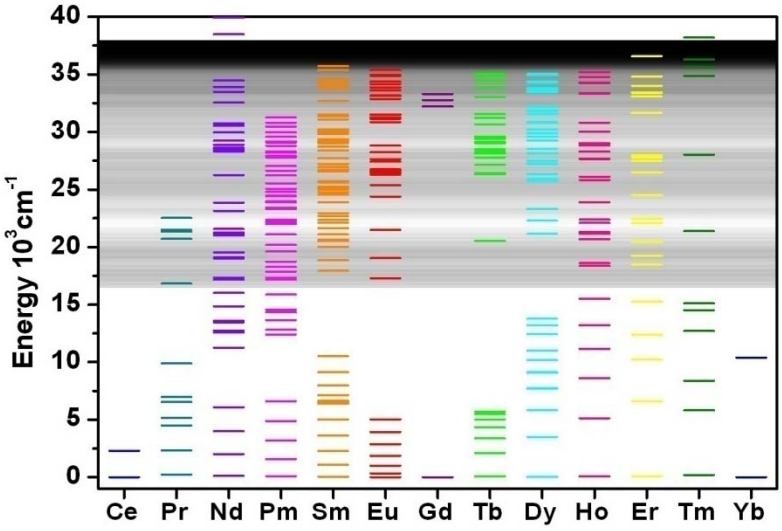

Figure 3.21. Energy level diagram for Ln^{3+} cations. The darkened region is a matrix representing the nanocrystal excitation wavelengths (λ_{em} = 574 nm). The lighter/white regions represent excitation maxima. Matrix plots were created using OriginPro 7 software and were overlaid at appropriate energy positions.

Doping procedures were carried out in the same fashion for Dy^{3+} and Sm^{3+} as for Tb^{3+} and Eu^{3+}, and nanocrystals of corresponding growth times were analyzed and found to yield similar trends in emission spectra with an observed bathochromic shift in emission with increased particle size. Spectra were collected for CdSe:Dy nanocrystals and are shown in Figures 3.22 and 3.23. Lanthanide emission in these materials are faint as previously described for the corresponding Eu^{3+} and Tb^{3+} nanocrystals and were not apparent in the steady-state emission spectra. As in the case of Eu^{3+} and Tb^{3+}, time-resolved measurements were required to observe the signal arising from the lanthanide cations. Unlike what was observed for the Eu^{3+} and Tb^{3+} nanocrystals, the corresponding emission bands did not appear as well defined narrow-bands but instead appear as shoulders in these spectra, the other component arising from the band gap emission of the nanocrystal. This observation can be explained by the presence of a long lived component of the nanocrystal band gap emission. The luminescence lifetimes of the nanocrystal emission are similar to lifetimes observed for Sm^{3+} and Dy^{3+}, which are shorter than Tb^{3+} and Eu^{3+}. Both signals can therefore not be discriminated from each other.

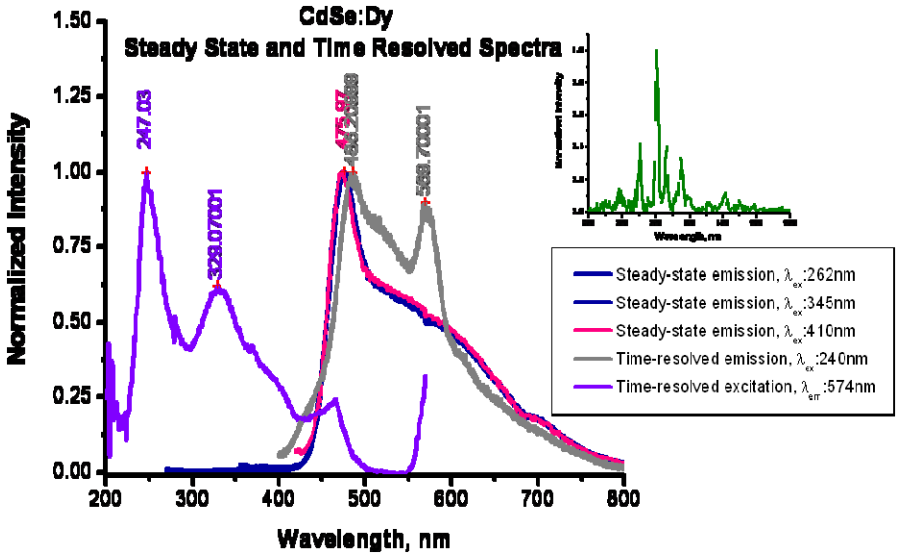

Figure 3.22. Normalized luminescence spectra of CdSe:Dy nanocrystals in hexane. Measurements were collected with a Varian Cary Eclipse using 1 mm cuvettes with an excitation wavelength of 245 nm. Maximum slit widths were used to obtain the lanthanide signal (20 nm emission and excitation slits). Delay time: 0.20 ms, decay time: 0.020 s, scan rate: slow (0.25 nm intervals with an averaging time of 0.5 s), PMT voltage: High (800 V), flashes: 1.

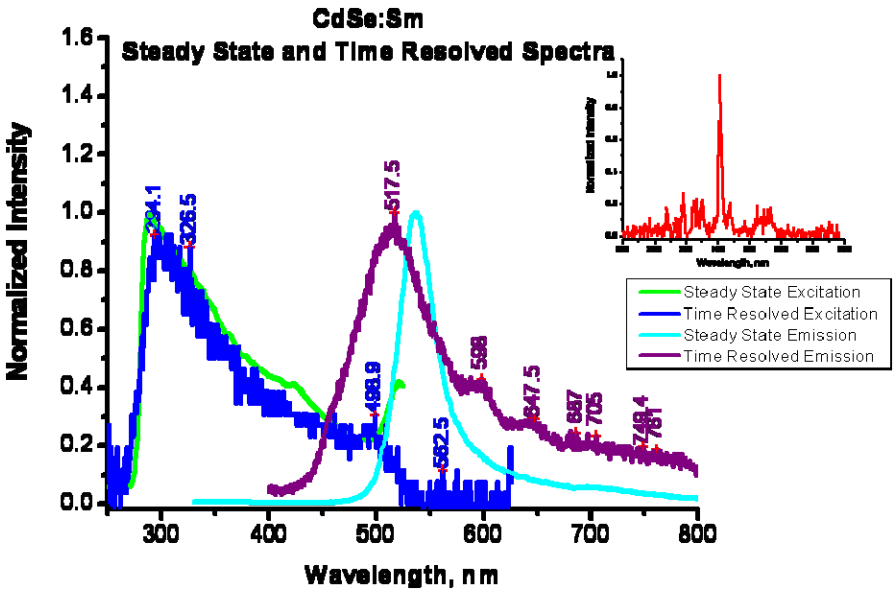

Figure 3.23. Normalized luminescence spectra of CdSe:Sm nanocrystals in hexane analyzed using time resolved mode of a Varian Cary Eclipse. Measurements were collected using 1 mm cuvettes with an excitation wavelength of 298 nm. Maximum slit widths were used to obtain the lanthanide signal (20 nm emission and excitation slits). Delay time: 0.10 ms, decay time: 0.020 s, scan rate: slow (0.5 nm intervals with an averaging time of 0.2 s), PMT voltage: High (800 V), flashes: 5.

While Sm^{3+} and Dy^{3+} are sensitized to some extent as supported by these experimental data (at least partially in the case of small CdSe nanocrystals), the signal is difficult to discriminate from nanocrystal signal for reasons mentioned previously. Predictions using hypotheses based on matrix analysis above indicates that the sensitization of several other lanthanides based on band gap emission wavelengths should also be possible: Er^{3+}, Ho^{3+}, Nd^{3+}, and Pr^{3+}. Preliminary studies on some of the NIR emitting lanthanides did not result in observation of NIR signals. This can be attributed to the reduced discrimination of the Ln^{3+} signal from nanocrystal background due to similar luminescence lifetimes; however, further work is needed in the future.

The luminescence lifetimes of CdSe:Tb, CdSe:Eu, CdSe:Gd, CdSe:Dy, and CdSe:Sm were measured and analyzed. For these decay curves, three component exponential models were used to fit best the experimental data (depending on the time window analyzed).

Overall luminescence lifetime values were determined using the criteria of the chi squared values for multiple exponential decay fittings, lower chi squared values indicate a better quality of fit (results shown in Tables 3.2 through 3.4). CdSe:Dy and CdSe:Sm lifetimes were more difficult in their analysis because their respective signals could not be clearly discriminated from that of the nanocrystal (determined by comparison to CdSe:Gd with lifetimes of 70μs, 11μ, and 4 μs).

Table 3.2. Luminescence lifetime data for CdSe:Eu nanocrystals, values are attributed to lanthanide luminescence

Sample	Size (nm)	Solvent	λ_{ex} (nm)	λ_{em} (nm)	Ln centered lifetimes	
					t1 (A1)	t2 (A2)
CdSeEu 4-1	1.9	Hexane	354	614	0.677 ms (46%)	2.45 ms (54%)
CdSeEu 4-2	2.1	Hexane	354	614	0.653 ms (39%)	2.49 ms (61%)
CdSeEu 4-3	2.3	Hexane	354	614	0.635 ms (58%)	2.16 ms (42%)
CdSeEu 4-4	2.6	Hexane	354	614	0.693 ms (38%)	2.54 ms (62%)
CdSeEu 4-6	2.9	Hexane	354	614	0.629 ms (52%)	2.10 ms (48%)
CdSeEu 4-8	3.0	Hexane	354	614	0.651 ms (42%)	2.36 ms (58%)

Table 3.3. Luminescence lifetime data for CdSe:Tb nanocrystals, values are attributed to lanthanide luminescence

Sample	Size (nm)	Solvent	λ_{ex} (nm)	λ_{em} (nm)	Ln centered lifetimes	
					t1 (A1)	t2 (A2)
CdSeTb 1-1	-	$CHCl_3$	354	545	2.07 ms (59%)	5.0 ms (41%)
CdSeTb 1-1	-	Hexane	354	545	1.00 ms (55%)	3.19 ms (45%)
CdSeTb 1-2	-	$CHCl_3$	354	545	2.20 m (65%)	5.2 ms (35%)
AY 12-1 CdSeTb	2.2	Hexane	354	545	2.513 ms (62%)	5.457 ms (38%)
AY 12-2 CdSeTb	2.6	Hexane	354	545	2.371 ms (64%)	5.317 ms (36%)
AY 12-3 CdSeTb	3.1	Hexane	354	545	2.622 ms (65%)	4.907 ms (35%)
AY 12-5 CdSeTb	3.8	Hexane	354	545	2.102 ms (43%)	4.013 ms (57%)
CdSe:Tb		60/40 mixture toluene/THF (containing 6000 ppm water)	354	545	2.02	4.7

Table 3.4. Luminescence lifetime data for CdSe:Dy and CdSe:Sm nanocrystals, values are attributed to lanthanide luminescence

Sample	Size (nm)	Solvent	λ_{ex} (nm)	λ_{em} (nm)	Ln centered lifetimes		
					t1 (A1)	t2 (A2)	t3 (A3)
CdSeDy 1-1	2.0	$CHCl_3$	337	574	7.47 µs (88%)	33.7 µs (10%)	12.8 µs (2%)
CdSeDy 1-2	2.4	$CHCl_3$	337	574	7.19 µs (94%)	27.8 µs (5%)	12.1 µs (1%)
CdSeDy 1-3	2.6	$CHCl_3$	337	574	7.34 µs (96%)	29.1 µs (4%)	12.6 µs (0.4%)
CdSeSm 1-2	2.4	Toluene	337	644	7.94 µs (96%)	57.8 µs (4%)	

Luminescence lifetime data indicates the presence of more than one lanthanide environment within these systems as demonstrated by biexponential decay fits. It is hypothesized that the longest lifetime component is the result of lanthanide cations residing at internal sites within the crystal structure protected from solvent vibrations, while the shorter component correspond to surface bound lanthanide cations. In all cases, the minor component is the longer lifetime, while shorter components contribute more to the overall signal. The surface is more readily exposed to solvent vibrations and will therefore experience shorter lifetimes as the result of quenching.

CdSe:Eu^{3+} exhibits a biexponential decay with a longer component of 2.4 ± 0.7 ms, most likely resulting from lanthanide cations embedded in the core of the nanocrystal structure and a slightly shorter component of 1.3 ± 0.2 ms resulting from surface bound lanthanide cations. These lifetimes are significantly longer (more than twice the value) than lifetimes reported in the literature for lanthanide complexes in solution, which only posses monoexponential fits corresponding to one lanthanide environment.[54] The level of protection of the lanthanides and subsequent assignment of location within the nanocrystal is based on comparison of lifetime values to values typically observed for Eu^{3+} (2 to 3 ms)[5].

Nanocrystals doped with Tb^{3+} exhibit the same trend as observed for CdSe:Eu^{3+}. The longest component arising from lanthanides residing within the crystal structure is 4.7 ± 0.8 ms, while the shorter component arising from surface bound lanthanides is 2.1 ± 0.5 ms. The same criterion was used to assess level of protection and location of the lanthanide cations within the crystal structure. Terbium naturally has a longer lifetime than europium and is therefore expected to yield longer values within the nanocrystal system. Well protected lanthanide complexes in solution found in the literature have reported lifetime values of 1.3 ms,[54] significantly shorter than reported here, further illustrating the superior protection of lanthanide cations within the nanocrystal structure.

In addition to CdSe:Ln (Ln = Tb, Eu), CdSe:Dy and CdSe:Sm lifetimes were collected. Uncertainties do arise from the analysis of CdSe:Dy and CdSe:Sm however. These lifetimes are on the same order of magnitude as the lifetimes obtained from CdSe:Gd (0.07± 0.01 ms, 0.011 ±0.001ms, and 0.0037 ± 0.0005 ms). This indicates that the lifetimes resulting from the nanocrystals themselves cannot be discriminated easily from the Dy^{3+} or the Sm^{3+} lifetimes.

Table 3.5. Measured lanthanide centered quantum yield data (samples were analyzed in toluene).

Sample	Lanthanide Centered Quantum Yield
CdSe:Tb^{3+}	1.48 (±0.03) x 10E-05
CdSe:Eu^{3+}	6.6 (±0.2) x 10E-05

Quantum yield values were measured for Tb^{3+} and Eu^{3+} doped CdSe nanocrystals in chloroform. The lanthanide centered quantum yield values are reported in Table 3.5. While the quantum yields observed in CdSe:Tb and CdSe:Eu nanocrystals are significantly lower than values obtained for lanthanide complexes in solution (63% for Tb^{3+} and 2.3 % for Eu^{3+}),[54] these values are compensated by the formation of polymetallic species. Multiple lanthanide cations incorporated within the crystal structure result in enhanced emission intensity despite low quantum yield values.

Lanthanide centered quantum yield data could not be obtained for Dy^{3+} or Sm^{3+} due to instrument limitations. While emission has been observed for both systems, the methods used to obtain emission does not allow for quantification of the efficiency of these two lanthanide systems. Spectra for both Dy^{3+} and Sm^{3+} could only be observed using the Varian Cary Eclipse. Correction functions are difficult to establish for this instrument. Quantum yield measurments are typically collected using the JY Horiba Fluorolog Spex, where correction functions have been created to adjust for the response of the detector and emission monochromator. Since the Dy^{3+} and Sm^{3+} have lifetime values very close to nanocrystal lifetimes, the time delay was not appropriate to separate out the lanthanide signal from the nanocrystals signal.

3.4 CONCLUSIONS AND FUTURE DIRECTIONS

The lanthanide doped CdSe:Ln nanocrystal systems synthesized and studied here offer several advantages over luminescent semiconductor nanocrystals or molecular lanthanide complexes for applications in solution. These include the formation of polymetallic species to overcome limitations of lower quantum yields of molecular lanthanide complexes. Despite low efficiency of energy transfer in these systems, the emission intensity is enhanced by the incorporation of a large number of lanthanide cations within the nanocrystal. The lanthanide cations are contained within the crystal structure, resulting in long luminescence lifetimes due to the complete protection of the lanthanide cations from vibrations present from surrounding solvent molecules. The nanocrystal structure possesses only low energy lattice vibrations and will therefore not significantly quench the emission.

These materials exhibit emission spanning the visible spectrum as well as broad absorbance bands allowing for excitation in suitable ranges for bioanalytical applications. In addition, by tuning the band gap energy within the nanocrystals, we can hope to better match the energy with the excited states of the Ln^{3+} for more efficient energy transfer. This results in the observed antenna effect for CdSe:Eu and CdSe:Tb nanocrystals.

While a number of different lanthanide doped CdSe nanocrystals systems have been synthesized and characterized for their photophysical properties, we have yet to determine the exact location of the lanthanides within the crystal structure (surface sites vs. internal sites, interstitial doping vs. substitution). Electron energy loss spectroscopy (EELS) and superconducting quantum interference devices (SQUID) should both provide information regarding the lanthanides' location in these systems. Also, further studies should be conducted

to monitor the effect of synthetic conditions on the dopant incorporation. Quantification of dopant concentrations can be obtained through the use of techniques such as X-ray photoelectron spectroscopy, X-ray fluorescence spectroscopy, and inductively coupled plasma atomic emission spectroscopy (ICP-AES).

Only initial studies on water solubility and surface passivation have been conducted to date. It may be worth exploring additional surface modifications in an attempt to minimize luminescence quenching in these systems. Quantum yields should be collected on these materials if they are to be perused for bioanalytical application to determine the extent of quenching upon addition of the various surface passivants. Toxicity of these materials *in vivo* should be studied in greater detail as not much information is available regarding CdSe nanocrystal toxicity, despite the known toxicity of Cd^{2+}.

3.5 REFERENCES

(1) Petoud, S.; Cohen, S. M.; Buenzli, J.-C. G.; Raymond, K. N. *J. Am. Chem. Soc.* **2003**, *125*, 13324-13325.

(2) Sabbatini, N.; Guardigli, M.; Lehn, J. M. *Coord. Chem. Rev.* **1993**, *123*, 201-28.

(3) Bünzli, J.-C. G. *Acc. Chem. Res.* **2006**, *39*, 53.

(4) Bünzli, J. C.; Piguet, C. *Chem. Soc. Rev.* **2005**, *34*, 1048.

(5) Beeby, A.; Clarkson, I. M.; Dickins, R. S.; Faulkner, S.; Parker, D.; Royle, L.; de Sousa, A. S.; Williams, J. A. G.; Woods, M. *J. Chem. Soc., Perkin Trans. 2* **1999**, 493-504.

(6) Horrocks, W. D., Jr.; Sudnick, D. R. *Acc. Chem. Res.* **1981**, *14*, 384-92.

(7) Faulkner, S.; Matthews, J. L. *Compr. Coord. Chem. II* **2004**, *9*, 913-944.

(8) Bruchez, M., Jr.; Moronne, M.; Gin, P.; Weiss, S.; Alivisatos, A. P. *Science* **1998**, *281*, 2013-2016.

(9) Chen, W.; Zhang, J. Z.; Joly, A. *J. Nanosci. Nanotech.* **2004**, *4*, 919 - 947.

(10) Kim, S.; Lim, Y. T.; Soltesz, E. G.; De Grand, A. M.; Lee, J. K.; Nakayama, A.; Parker, J. A.; Mihaljevic, T.; Laurence, R. G.; Dor, D. M.; Cohn, L. H.; Bawendi, M. G.; Frangioni, J. V. *Nature Biotechnology* **2004**, *22*, 93 - 97.

(11) Wu, X.; Liu, H.; Liu, J.; Haley, K. N.; Treadway, J. A.; Larson, J. P.; Ge, N.; Peale, F.; Bruchez, M. P. *Nature Biotechnology* **2003**, *21*, 41-46.

(12) Chengelis, D. A.; Yingling, A. M.; Badger, P. D.; Shade, C. M.; Petoud, S. *J. Am. Chem. Soc.* **2005**, *127*, 16752-16753.

(13) Bukowski, T. J.; Simmons, J. H. *Crit. Rev. Solid State Mater. Sci.* **2002**, *27*, 119-142.

(14) Rossetti, R.; Nakahara, S.; Brus, L. E. *J. Chem. Phys.* **1983**, *79*, 1986.

(15) Rosenthal, S. J. *Nature Biotechnology* **2001**, *19*, 621-622.

(16) Alivisatos, P. *Nature Biotechnology* **2004**, *22*, 47-52.

(17) Alivisatos, A. P.; Gu, W.; Larabell, C. *Annu. Rev. Biomed. Eng.* **2005**, *7*, 55-76, 3 plates.

(18) Parak, W. J.; Gerion, D.; Pellegrino, T.; Zanchet, D.; Micheel, C.; Williams, S. C.; Boudreau, R.; Le Gros, M. A.; Larabell, C. A.; Alivisatos, A. P. *Nanotechnology* **2003**, *14*, R15-R27.

(19) Raola, O. E.; Strouse, G. F. *Nano Lett.* **2002**, *2*, 1443-1447.

(20) Fu, A.; Gu, W.; Larabell, C.; Alivisatos, A. P. *Curr. Opin. Neurobiol.* **2005**, *15*, 568-575.

(21) Lim, Y. T.; Kim, S.; Nakayama, A.; Stott, N. E.; Bawendi, M. G.; Frangioni, J. V. *Mol. Imaging* **2003**, *2*, 50 - 64.

(22) Larson, D. R.; Zipfel, W. R.; Williams, R. M.; Clark, S. W.; Bruchez, M. P.; Wise, F. W.; Webb, W. W. *Science* **2003**, *300*, 1434 - 1436.

(23) Parak, W. J.; Boudreau, R.; Le Gros, M.; Gerion, D.; Zanchet, D.; Micheel, C. M.; Williams, S. C.; Alivisatos, A. P.; Larabell, C. *Adv. Mater.* **2002**, *14*, 882-885.

(24) Ballou, B.; Lagerholm, B. C.; Ernst, L. A.; Bruchez, M. P.; Waggoner, A. S. *Bioconjugate Chem.* **2004**, *15*, 79 - 86.

(25) Shim, M.; Guyot-Sionnest, P. *Nature* **2000**, *407*, 981.

(26) Erwin, S. C.; Zu, L. J.; Haftel, M. I.; Efros, A. L.; Kennedy, T. A.; Norris, D. J. *Nature* **2005**, *436*, 91-94.

(27) Zu, L. J.; Norris, D. J.; Kennedy, T. A.; Erwin, S. C.; Efros, A. L. *Nano Lett.* **2006**, *6*, 334-340.

(28) Kwak, W.-C.; Kim, T. G.; Chae, W.-W.; Sung, Y.-M. *Nanotechnology* **2007**, *18*, 1 - 4.

(29) Qu, L.; Peng, X. *J. Am. Chem. Soc.* **2002**, *124*, 2049-2055.

(30) Bhattacharyya, S.; Zitoun, D.; Gedanken, A. *J. Phys. Chem. C: solid State Phys.* **2008**, *112*, 7624 - 7630.

(31) Magana, D.; Perera Susanthri, C.; Harter Andrew, G.; Dalal Naresh, S.; Strouse Geoffrey, F. *J. Am. Chem. Soc.* **2006**, *128*, 2931-9.

(32) Archer, P. I.; Santangelo, S. A.; Gamelin, D. R. *J. Am. Chem. Soc.* **2007**, *129*, 9809 - 9818.

(33) Kompe, K.; Lehmann, O.; Haase, M. *Chem. Mater.* **2006**, *18*, 4442.

(34) Jose, G.; Jose, G.; Thomas, V.; Joseph, C.; Ittyachen, M. A.; Unnikrishnan, N. V. *Mater. Lett.* **2003**, *57*, 1051 - 1055.

(35) Julian, B.; Planelles, J.; Cordoncillo, E.; Escribano, P.; Aschehoug, P.; Sanchez, C.; Viana, B.; Pelle, F. *J. Mater. Chem.* **2006**, *16*, 4612 - 4618.

(36) Tiseanu, C.; Mehra, R. K.; Kho, R.; Kumke, M. *Chem. Phys. Lett.* **2003**, *377*, 131 - 136.

(37) Okamoto, S.; Kobayashi, M.; Kanemitsu, Y.; Kushida, T. *Phys. Status Solidi B* **2002**, *229*, 481 - 484.

(38) Chowdhury, P. S.; Patra, A. *Phys. Chem. Chem. Phys.* **2005**, *8*, 1329 - 1334.

(39) Peng, Z. A.; Peng, X. *J. Am. Chem. Soc.* **2001**, *123*, 183-184.

(40) Peng, Z. A.; Peng, X. *J. Am. Chem. Soc.* **2002**, *124*, 3343-3353.

(41) Gao, M. Y.; Mohwald, H.; Rogach, A. L.; Kornowski, A.; Eychmuller, A.; Weller, H. *J. Phys. Chem. B: At. Mol. Opt. Phys.* **1998**, *102*, 8360 - 8363.

(42) Rogach, A. L.; Kornsowski, A.; Gao, M. Y.; Eychmuller, A.; Weller, H. *J. Phys. Chem. B: At. Mol. Opt. Phys.* **1999**, *103*, 3065.

(43) Dubois, F.; Mahler, B.; Dubertret, B.; Doris, E.; Mioskowski, C. *J. Am. Chem. Soc.* **2007**, *129*, 482 - 483.

(44) Hines, M. A.; Guyot-Sionnest, P. *J. Phys. Chem.* **1996**, *100*, 468-71.

(45) Dabbousi, B. O.; Rodriguez-Viejo, J.; Mikulec, F. V.; Heine, J. R.; Mattoussi, H.; Ober, R.; Jensen, K. F.; Bawendi, M. G. *J. Phys. Chem. B: At. Mol. Opt. Phys.* **1997**, *101*, 9463-9475.

(46) Reiss, P.; Bleuse, J.; Pron, A. *Nano Lett.* **2002**, *2*, 781 - 784.

(47) Steigerwald, M. L.; Brus, L. E. *Acc. Chem. Res.* **1990**, *23*, 183-8.

(48) Yu, W. W.; Peng, X. *Angew. Chem., Int. Ed. Engl.* **2002**, *41*, 2368-2371.

(49) Murray, C. B.; Nirmal, M.; Norris, D. J.; Bawendi, M. G. *Z. Naturforsch., D* **1993**, *26*, 231-3.

(50) Yu, W. W.; Qu, L.; Guo, W.; Peng, X. *Chem. Mater.* **2003**, *15*, 2854-2860.

(51) Striolo, A.; Ward, J.; Prausnitz, J. M.; Parak, W. J.; Zanchet, D.; Gerion, D.; Milliron, D. J.; Alivisatos, A. P. *J. Phys. Chem. B: At. Mol. Opt. Phys.* **2002**.

(52) Talapin, D. V.; Rogach, A. L.; Kornowski, A.; Haase, M.; Weller, H. *Nano Lett.* **2001**, *1*, 207 - 211.

(53) Sundar, V. C.; Lee, J. K.; Heine, J. R.; Bawendi, M. G. *Adv. Mater.* **2000**, *12*, 1102.

(54) Petoud, S.; Muller, G.; Moore, E. G.; Xu, J.; Sokolnicki, J.; Riehl, J. P.; Le, U. N.; Cohen, S. M.; Raymond, K. N. *J. Am. Chem. Soc.* **2006**, *129*, 77 - 83.

4.0 LANTHANIDE CONTAINING ZINC SULFIDE NANOCRYSTALS

We have demonstrated recently that it is possible to use the electronic structure of CdSe nanocrystals in order to sensitize and protect several luminescent lanthanide cations.[1] This luminescent material has proven to have additional properties when compared to organic fluorophores and undoped CdSe semi-conductor nanocrystals (QDs) such as long luminescence lifetimes (an advantage to improve the signal to noise ratio through time-resolved measurements)[2-4] and sharp emission bands whose wavelengths are unaffected by the experimental conditions (temperature, pressure, pH, hydrophilic and hydrophobic environments etc).[2,5-7]

One major limitation of the CdSe:Tb and CdSe:Eu systems is their low efficiency of energy transfer from the electronic structure of the semiconductor nanocrystal to the accepting nanocrystal to the accepting levels of Eu^{3+} and Tb^{3+}. Another drawback of this system is the high toxicity of its constituents (Cd and Se), a negative aspect in respect to the environment when such compounds are required to be manufactured in large quantities, transported and eliminated and/or if such luminescent reporters need to be injected in patient for diagnostic purpose. Lanthanide cations are not toxic when bound to or encapsulated by appropriate substituents that prevent them from being released as free metal ions in solution where they

could form hydroxides in aqueous solution, especially in physiological conditions. This has been demonstrated with several Gadolinium complexes used as MRI contrast agents.[8]

For toxicity *in vivo*, even if several experiments have not revealed any toxicity of the luminescent CdSe nanocrystals themselves[9-11], their constituents are still an issue if nanocrystals are dissociated, creating limitations for injection in living biological systems and waste management.[12] For example, it has been demonstrated that free cadmium binds to mitochondrial proteins and induces stress, eventually leading to dysfunction and hepatic injury.[13] Only few studies relative to the total work published on nanocrystals actually describe the cytotoxicity of CdSe nanocrystals, leaving the topic open for more debate.[12,14-23]

We have developed and characterized a new class of lanthanide doped ZnS:Ln nanocrystals whose electronic structures sensitize luminescent lanthanide cations emitting in the visible, Tb^{3+} and Eu^{3+}, where the constituents of the nanocrystals are non- or less toxic in comparison to lanthanide doped CdSe we have used previously. This work results in the creation of a novel type of lanthanide containing semi-conductor nanocrystals that have high absorption and that emit in the visible region having emission both through the band gap of the semiconductor nanocrystal and through the electronic states of the lanthanide cations. The signal of the lanthanides can be distinguished by taking advantage of their sharp emission bands and long luminescence lifetimes. In comparison to lanthanide doped CdSe, this ZnS antenna is more efficient in transferring the energy to the lanthanide cations.

4.1 BACKGROUND

With rapid advancements being made in the field of semiconductor nanocrystals, especially CdSe, these materials are becoming increasingly more attractive for a broad range of bioanalytical applications.[24,25] They offer numerous advantages over organic fluorophores because of their broad excitation bands, tunable emission wavelengths and resistance to photobleaching. Low or non toxic properties of such materials are necessary for luminescent reporters to be used in living systems, which is potentially a major limitation of the CdSe and CdSe:Ln nanocrystals.

The cytotoxicity of CdSe nanocrystals is not fully established although there are proposed cytotoxic effects in the literature. There are believed to be three major pathways by which nanocrystals can result in cell impairment: (1) the corrosion of particles within the cell may lead to Cd^{2+} ions being released, (2) the adhesion of nanocrystals to cell surfaces may lead to interference with normal cell function, and (3) the shape of the nanoparticles may prove fatal for the cell. For example, nanorods have been found to impale cells.[17] *In vivo* studies have demonstrated the severe toxic effects of cadmium itself, especially to the liver where it tends to accumulate.[26]

We have previously demonstrated the successful doping of CdSe nanocrystals with luminescent lanthanide cations; however, their potential inherent toxicity may limit their use for applications *in vivo*. A second important limitation of these nanocrystals is the inefficiency of energy transfer observed between the nanocrystal electronic structure and the accepting levels of lanthanide cations (Eu^{3+} and Tb^{3+}).

ZnS nanocrystals provide multiple advantages for use as lanthanide antennae over the CdSe system. ZnS is a larger band gap material which is expected to have a more favorable energy match with the accepting levels of several lanthanide cations including Eu^{3+} and Tb^{3+} in comparison to CdSe nanocrystals. This more favorable electronic match is expected to lead to more efficient energy transfer within the doped nanocrystals. In addition to being a better energy match for lanthanides, ZnS contains non or less toxic components in comparison to other materials used for, making them less of a concern for cytotoxicity and more attractive for bioanalytical applications.

4.1.1 Current state of the work on zinc sulfide nanocrystals

Most of the work done on undoped ZnS nanocrystals has been focused on its use as a wide band gap shell for other nanocrystals such as CdSe and CdS.[27-33] The ZnS shell helps to passivate the nanocrystal surface and eliminate surface traps that may arise from defect sites.[27,30,33] ZnS nanocrystals on their own are not highly attractive for application in bioimaging because their emission is confined to the blue-UV region, where blood and water absorbance strongly interfere with imaging.[34] The current most practical application for undoped ZnS is for use as phosphors.

In addition to application studies on zinc sulfide, some focus has been placed on understanding reaction dynamics within these systems. Optimizing synthetic conditions and understanding the importance of non-coordinating vs. coordinating solvent systems, aliphatic amines vs. phosphonic acids have been studied in some detail.[35] Work has also been carried out on understanding how surface chemistry will effect crystallinity of these materials.[36]

4.1.2 Current state of the work on doped zinc sulfide nanocrystals

While it was initially believed that doping of semiconductor nanocrystals such as ZnS was impossible as the result of a supposed "self-purification" mechanism involved in particle synthesis[37], a study conducted by Erwin et al. discredits this claim.[38] They systematically carried out a series of experiments which led them to establish the ability of semiconductor materials to incorporate dopant ions as a result of a number of different factors including surface morphology, overall nanocrystal shape, and the surfactants present in the nanocrystal growth solution.[38] The literature suggests that a zinc blende crystal structure is preferred to maximize incorporation of dopant ions and has in fact led to many successful doped nanocrystal systems.[39,40]

Proof of successful doping can be found in the literature and elaborate methods are proposed for the determination of doping within nanocrystals.[38,39,41] One proposed method is based on the examination of the photoluminescence spectroscopy data. In doped nanocrystal systems, it has been hypothesized that the emission spectra should reveal two distinct emission bands.[38] One band results from exciton recombination of the semiconductor material band edge (band gap emission) and the other results from the presence of internal dopant ions. It is suggested that the average number of dopant ions present within a system can be determined by comparing the ratio of these two emission bands ($I_{dopant}/I_{bandgap}$).[38] A second important criterion to prove nanocrystal doping is based on the excitation spectrum upon monitoring dopant emission. If the nanocrystal absorption band is present within this excitation spectrum, it is possible to conclude that energy transfer is taking place from the nanocrystal electronic states to

the dopant and that the dopant is located close to the nanocrystal (either at surface or core sites of the nanocrystal).

4.1.2.1 Current state of the work on doped zinc sulfide nanocrystals

Much of the work done on transition metal dopants in ZnS nanocrystals is based on incorporation of Mn^{2+},[38,39,42-45] with only few studies on other transition metals such as Cu^{1+} and Pb^{2+}.[46,47] The use of Mn^{2+} is attractive for developing phosphors with enhanced photoluminescence emitting in the orange and the bulk of the studies performed are directed towards this. A great deal of research has focused on recognizing, understanding and solving problems associated with doping,[38,39] while less work has been done on effects of annealing and surface passivation within these systems[48].

Lee et al. have developed procedures for room temperature synthesis of Mn^{2+} doped ZnS using a chemical precipitation method followed by surface passivation with 3-methacryloxypropyl trimethoxysilane.[42]. These nanocrystals exhibit a 30-fold enhancement in photoluminescence compared to unpassivated particles,[42] however the first reports of enhanced photoluminescence (PL) by doping ZnS with Mn^{2+} were the result of work by Bhargava et al. resulting in 18% quantum efficiencies, the best reported at that time.[45] Mu et al. focus their studies on how annealing effects both the structural and optical properties of nanocrystals with and without surface passivation.[48] Their observations show that a silica coating on doped ZnS nanocrystals will aid in thermal stability and reduced decreased or changing PL as the result of phase transformations within the crystal structure.[48]

Doping of ZnS nanocrystals with Cu^{2+} and Cu^{1+} are of interest because copper ions form strong interaction with the ZnS host and are expected to result in larger emission shifts to lower energy with respect to bulk material.[46] In addition, copper ions doped into bulk ZnS have the ability to yield blue, green or red emission.[46] As the result of this tunable emission, these materials are attractive for a number of uses including photoluminescent and electroluminescent devices.

Like copper dopants in bulk ZnS materials, bulk Pb^{2+} is known to emit in the blue, green and red regions as well. A study by Borse et al. exploited these properties to produce ZnS:Pb nanocrystals possessing white emission. Their work also explored the pH and dopant concentration dependence of the resulting photoluminescence properties within this system.[47]

4.1.2.2 Lanthanide dopants

Several attempts at doping ZnS materials, both bulk and nanocrystalline, have been reported. While it has been described by Zhang et al. and Stapor et al.[49,50] that bulk ZnS can be doped with trivalent lanthanide cations, and that lanthanide emission can be observed upon excitation through the band gap of the bulk materials, extremely high temperatures are required to obtain such results (above 900 °C).[49-54] While attempts at doping nanocrystalline ZnS with lanthanide cations such as Sm^{3+}, Er^{3+}, Tb^{3+} and Eu^{3+} are abundant in the literature, the question of proof of incorporation is still unanswered as well as the proof that an antenna effect was provided by the electronic structure of the ZnS nanocrystal.[55-58]

It has been proposed by Bol et al.[59] that successful incorporation of Ln^{3+} can be proven by comparison of lanthanide excitation spectra with the absorption band of the ZnS host. If the

ZnS absorption band is present in the excitation spectrum upon monitoring Eu^{3+} emission, successful incorporation has been obtained.[59] If the absorption band is not present in the excitation spectrum upon monitoring Eu^{3+} emission then the lanthanide cations are at best located on the nanoparticle surface rather than being incorporated within the structure (the other possibility being that they are only present in close proximity to ZnS associated with the crystal structure). Doping of ZnS with the rare earth metals is potentially not a favorable process for a number of reasons. The ionic radius of any particular lanthanide cation is significantly larger than that of Zn^{2+}, and therefore the host lattice would need to deform to accommodate such differences. The inability of lanthanide cations to incorporate within a ZnS host is also supported by the preferred coordination number of Ln^{3+} ions, which typically adopt octadentate or higher coordination environments; the coordination number in the crystal lattice is four. Charge differences are also expected to play a role in the efficiency of doping within these systems.[59] The lanthanide cations which have a 3+ charge are expected to replace the divalent Zn^{2+}. To date, ZnS nanocrystals have not been observed to provide antenna effect to luminescent lanthanide cations.[59]

4.2 EXPERIMENTAL

4.2.1 Chemicals

Trioctylphosphine (TOP) (90%), zinc stearate (tech), octadecene (90% tech), and tetracosane (99%) were purchased from Sigma-Aldrich-Fluka. Sulfur, toluene, and methanol were

purchased from Fisher Scientific. Terbium nitrate (99.9%) was purchased from Strem. N-Hexane and 1-octanol were purchased from Acros and ethyl acetate was purchased from EMD. Argon gas was purchased from Valley National. All chemicals were used as purchased without purification except toluene, which was distilled over sodium under nitrogen.

4.3 RESULTS/DISCUSSION

4.3.1 Synthesis

The general synthetic procedures for the reported ZnS:Ln nanocrystals were adapted and modified from our previously reported CdSe:Ln systems[1] and the work of Peng et al.[35] Various synthetic conditions were tested for the formation of ZnS:Ln nanomaterials, all of which are described below. Doping percentages tested ranged from 5% to 20% of the total cation precursor, however 15% was used in most cases as it was found to yield the most intense steady state lanthanide luminescence emission for Eu^{3+} and Tb^{3+}. In all cases, the reaction mixture containing the solvent system and cation precursor was heated to 350°C while stirring under nitrogen for approximately 2 hours. After the dissolution of the cation precursor within the reaction mixture, a dopant lanthanide solution was injected and left to stir for a 30 minute to one hour time period. The sulfur stock solution, containing elemental sulfur dissolved in the appropriate solvent was then injected to initiate nucleation of the nanoparticles. In all syntheses aliquots were removed at various growth times and dissolved in an appropriate organic solvent (chloroform, hexanes, etc.) for spectral analysis. Purification of the raw nanocrystal samples

involved dissolving samples in butanol followed by precipitation with methanol. Precipitated nanocrystals were dissolved in octanol to remove excess solvent (octadecene/tetracosane), and then precipitated once more with methanol through the addition of ethyl acetate.

4.3.1.1 Non-coordinating solvent system

Preparation of the sulfur stock solution includes the dissolution of the sulfur powder in octadecene through vigorous magnetic stirring. The lanthanide stock solution was prepared by dissolving 0.12 mmol of lanthanide nitrate salt in octadecene and TOP through vigorous stirring and heating. Tetracosane and octadecene served as co-solvents in the reaction mixture. Zinc stearate and terbium nitrate were used as cation precursors. Nucleation of the nanocrystals occurred upon injection of the sulfur stock solution into the heated reaction mixture.

Tetracosane (4.0 g), octadecene (3.0 mL) and 0.68 mmol of zinc stearate were placed in a three neck 50 mL round bottom flask. The flask necks were fitted with water condensers. The starting materials were placed under argon and heated to 350°C. The lanthanide stock solution was injected after approximately two hours of heating and allowed to stir within the reaction mixture for at least 30 minutes. The sulfur stock solution was injected after the lanthanide nitrate had been given time to completely dissolve (approximately 1 hour). The reaction temperature was then decreased to values comprised between 270 and 300 °C for the remaining duration of nanocrystal growth. Aliquots were removed at different times ranging from 1 to 120 minutes

post injection through a glass syringe. The resulting nanocrystals were redispersed in an appropriate solvent for spectroscopic analysis.

4.3.1.2 Coordinating solvent system

While the general synthetic condition used are identical to the non-coordinating solvent systems (reaction temperature, atmosphere and stirring), the chemicals were varied. Zinc stearate (0.68 mmol) was dissolved in 10 mmol of TOPO and 1.5 mL of TOP while stirring under nitrogen at 300°C. In this reaction system the TOPO and TOP serve as the coordinating solvents. The lanthanide stock solution was prepared by dissolving 0.12 mmol of lanthanide nitrate salt in 1.0 mL TOP, and was injected into the hot reaction mixture upon dissociation of the zinc precursor. The lanthanide salt was left for dissolution for approximately 30 minutes prior to injection of the sulfur stock solution (0.4 mmol sulfur in 1.0 mL TOP). Injection of the sulfur initiated nucleation and aliquots were removed from the reaction mixture at various growth times for spectral analysis.

4.3.1.3 Coordinating solvent system

The coordinating solvent system was chosen for this particular synthetic protocol because dissolution was believed to behave similarly to CdSe nanocrystals where CdO served as the precursor with employed coordinating solvent system. The zinc precursor was changed from zinc stearate to zinc oxide because it was believed the stearate was interfering with subsequent imaging of the nanoparticles. The molar ratios of the cation and anion precursors remained the

same, 0.68 mmol of zinc oxide was placed in a reaction flask with 10 mmol of TOPO and 1.5 mL of TOP. The reaction was stirred while heating under argon to 350°C to dissolve the zinc oxide. Once the reaction mixture was completely dissolved, the lanthanide stock solution, containing 0.12 mmol $Ln(NO_3)_3$ dissolved in 1 mL of TOP, was injected and left to stir for 30 minutes to an hour. The sulfur stock solution, prepared by dissolving 0.4 mmol of elemental sulfur in 1.0 mL of TOP, was rapidly injected into the hot reaction mixture and aliquots were removed at various growth times for spectral analysis.

4.3.2 Surface modification

ZnS:Tb nanocrystals were tested with surface exchange using DTPA. Concentrated solutions of raw ZnS:Tb nanocrystals were prepared in chloroform. An excess of an aqueous DTPA solution prepared by dissolving 1.0 g DTPA in 20 mL of water through deprotonation with KOH (5 equivalents of KOH to ensure deprotonation of DTPA) was added to the nanocrystals solution in chloroform. The samples were sonicated for 2 hours to ensure complete mixing of the aqueous and organic phases. Afterwards, sonication samples were centrifuged and the layers separated. In some cases the DTPA nanocrystals were very dilute and therefore were concentrated down by removal of water using standard vacuum techniques. Emission and excitation spectra were collected in order to assess whether the nanocrystals were present in the aqueous DTPA phase.

While several synthetic methods were reported for the synthesis lanthanide containing ZnS nanocrystals, the most intense lanthanide luminescence was observed for systems employing the non-coordinating solvent system. This has led to more extensive photophysical and spectroscopic characterization of ZnS:Ln in noncoordinating solvents relative to the

alternative procedures. The initial spectroscopic data is reported briefly below for ZnS:Ln synthesized using ZnO precursors (Figure 4.1) as well as those particles synthesized using coordinating solvent systems (Figure 4.2).

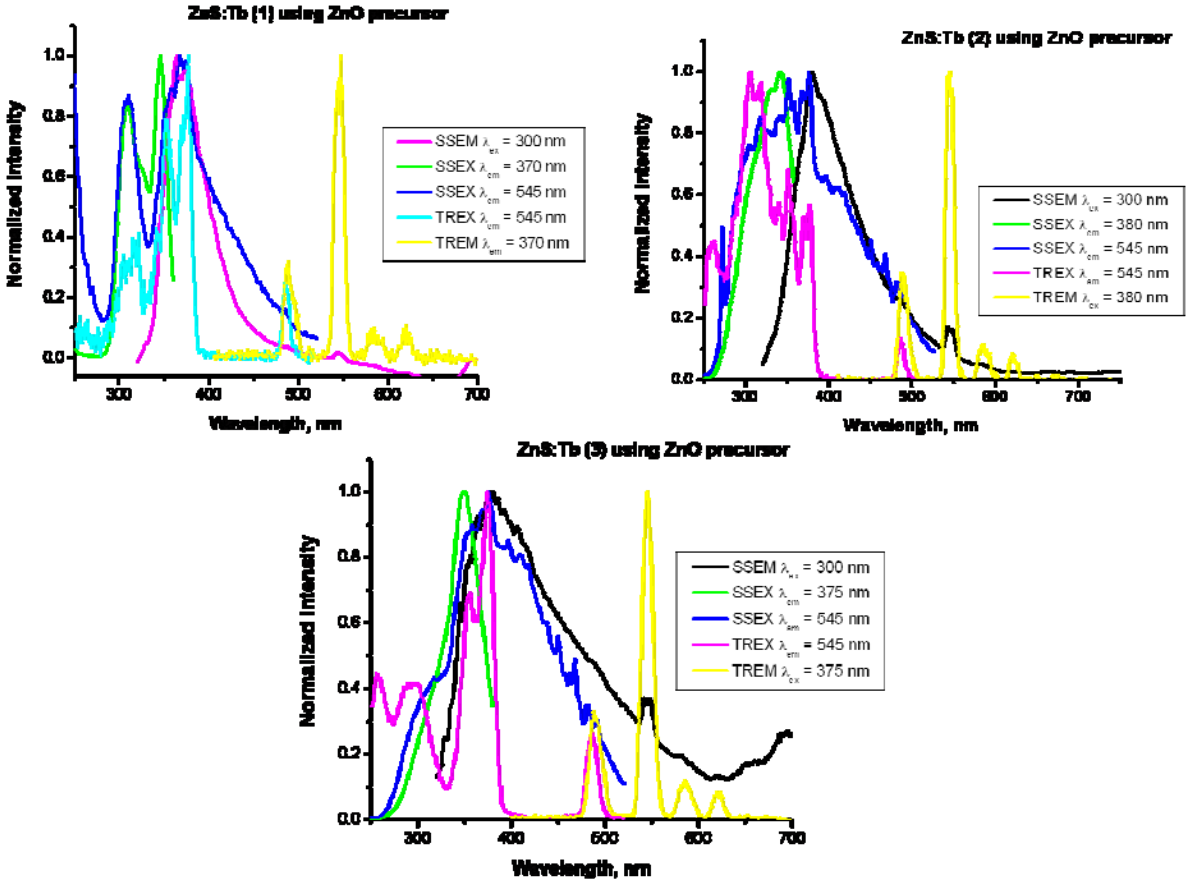

Figure 4.1. Normalized steady state and time resolved emission and excitation spectra collected for different batches of Tb^{3+} containing ZnS nanocrystals synthesized using ZnO precursors. All steady state emission spectra were collected upon excitation at 300 nm on nanocrystal solutions in chloroform. Steady state excitation was collected upon monitoring both nanocrystal band gap emission and Tb^{3+} emission. Time resolved excitation upon monitoring Tb^{3+} is overlaid to illustrate degree of sensitization within these systems ($Tb(NO_3)_3$ in chloroform was used for direct excitation profiles).

Several batches of ZnS:Tb nanocrystals were synthesized through the use of ZnO precursors, the spectroscopic data from which are shown in Figure 4.1. These batches are representative of the several batches synthesized. The most important feature to note is the absence or weakened emission arising from Tb^{3+} using the steady state mode of the fluorimeter. Tb^{3+} signal can be discriminated through time resolved measurements, however the attractiveness of this system was originally derived from the observation of Tb^{3+} emission in steady state mode as an indication of a more efficient band gap to lanthanide energy transfer. Therefore, this synthetic route has been concluded to offer no advantage over the non-coordinating solvent system.

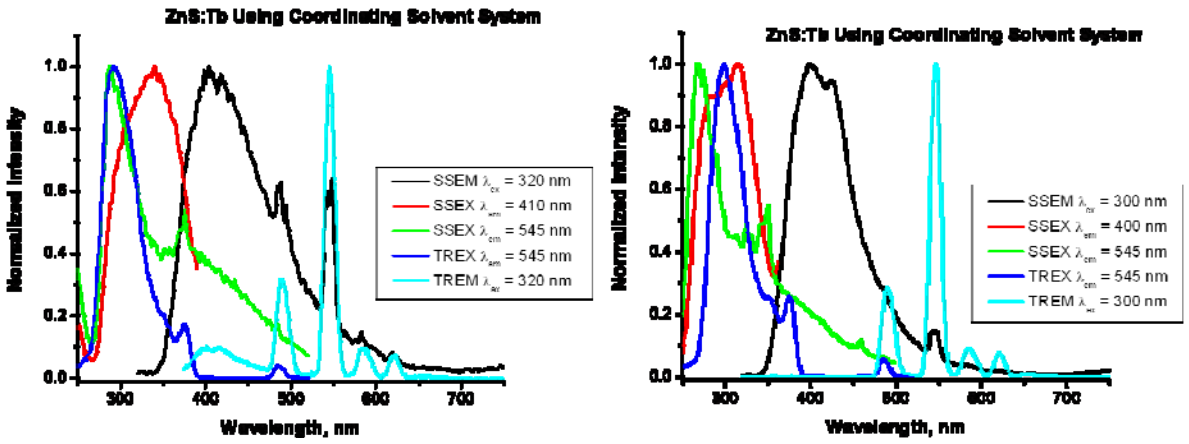

Figure 4.2. Normalized steady state and time resolved emission and excitation spectra collected for ZnS:Tb nanocrystals synthesized using a coordinating solvent system and dissolved in chloroform. Emission spectra were collected upon excitation at 300 nm while excitation spectra were collected upon monitoring emission of both the nanocrystal band gap and the 545 nm emission band of Tb^{3+} ($Tb(NO_3)_3$ in methylene chloride was used as the source of direct excitation).

Results obtained from the syntheses for the coordinating solvent system are shown in Figure 4.2. From these spectra, it was determined that reproducible data were not obtainable for steady state emission spectra in this particular system. Even though steady state Tb^{3+} emission is observed, the intensity is less than that observed in the non-coordinating solvent systems discussed below. The spectra collected for samples from the batch on the left does not match spectra collected for samples from the batch on the right in Figure 4.2. On the basis of non-reproducible data, the synthetic preparation based on this solvent system was not employed for detailed spectroscopic studies.

4.3.3 Physical characterization

Low resolution TEM imaging was performed by Joseph Suhan at Carnegie Melon University through collaboration with Prof. Marcel Bruchez. Low resolution images, like in the case of CdSe nanocrystals, only indicate what appear to be small aggregates of particles which seem to have large size dispersity (Figure 4.3, left). While the sample is not highly monodisperse, the nanocrystals do appear to be in a range of size from 5 to 30 nm in diameter; however it should be noted that the appearance of large particles may result from aggregation of smaller particles.

Like CdSe nanocrystals, ZnS nanocrystals were also subjected to extensive purification procedures in an effort to obtain higher quality images by removing the carbon material. However due to differences in the nature of the starting materials between ZnS and CdSe, further modifications were necessary. Different zinc precursors were used in the synthetic procedures (see experimental sections above) as well as different solvent systems (non-coordination vs. coordinating) in order to optimize the quality of the TEM images.

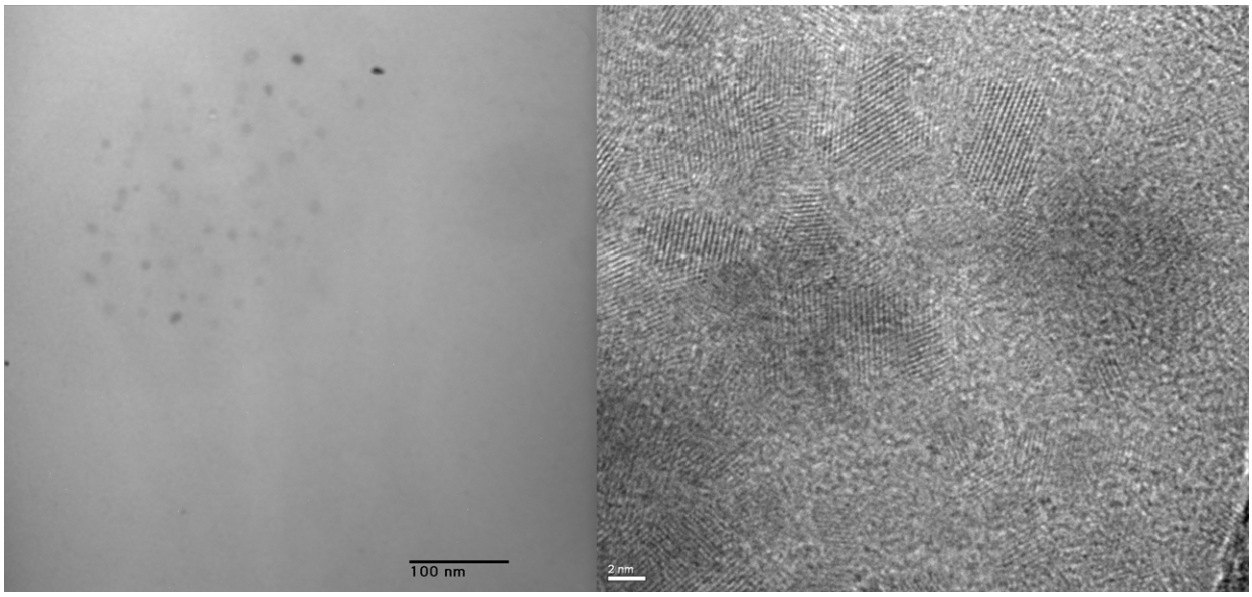

Figure 4.3. Left: low resolution TEM images obtained through collaboration with Carnegie Melon University using a Hitachi H-7100 TEM operating at 75 kV. Right: high resolution TEM obtained through collaboration with University of Pittsburgh Department of Engineering and Materials Science using a JEOL-2100 CF operating between 120kv and 200kv.

After systematic modification of reaction conditions and purification procedures, including solvent systems employed as well as thorough washing procedures of particles post synthesis using solvent/non-solvent combinations (described previously in Chapter 3), high resolution TEM images were obtained with the help of the NFCF housed within PINSE at the University of Pittsburgh and are shown in Figure 4.3 (right). Similar procedures to those used for the purification of CdSe nanocrystals were used to clean these particles, but several additional washes at each solvent step were included. While samples still appear to be somewhat aggregated, it is evident from the image that these particles are constituted of crystalline materials based on the observed lattice fringes. Sample size dispersity also does not appear to be as broad in the case of HRTEM as was observed for low resolution TEM. This result confirms

the likelihood that samples appeared larger in diameter due to the formation cluster of overlapping nanocrystals. From the HRTEM image, the size distribution of ZnS:Tb nanocrystals was calculated using Image J software to be 3.3 ± 0.4 nm in diameter.

4.3.4 Photophysical characterization

UV-vis absorption spectra collected of the ZnS:Tb nanocrystals in chloroform, Figure 4.4, illustrate absorption by the nanocrystals throughout a broad wavelength continuum among the visible spectrum. Due to the broad type of the absorption band, it is possible to use a large range of wavelengths to excite these nanocrystals. Being able to excite these materials over a broad range of wavelengths allows for the analysis of these materials to be compatible with existing instrumentation, an advantage for practical applications.

It should be noted that a small feature around 375 nm is observable on this absorption spectrum, shifting only slightly with a direct relationship to the growth time, which is a characteristic of the photophysical properties of semiconductor nanocrystals exhibiting quantum confinement. The position of this shoulder is based on nanocrystal size and is an indication of the formation of a band gap.

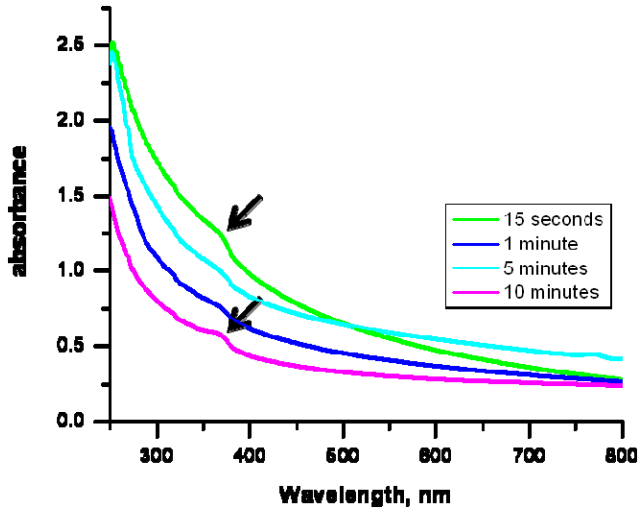

Figure 4.4. Characteristic UV-Vis absorbance spectra of ZnS nanocrystals in chloroform.

ZnS nanocrystals have been synthesized using both Tb^{3+} and Eu^{3+} as dopant ions present as 15% of the total cation precursor during the synthesis. In both cases their steady state emission spectra indicate the presence of the broad band gap emission as well as characteristic narrower emission arising from the lanthanide cations as an indication of a more efficient energy transfer from the nanocrystal electronic structure to the accepting levels of the lanthanide cations. The signal intensity was weaker in the case of europium in comparison to the ZnS:Tb nanocrystals. Both materials show enhanced lanthanide sensitization over CdSe nanocrystals since time-resolved measurements are no longer required to observe the signal arising from the lanthanide cations. By placing appropriate cut-off filters in front of quartz cells containing solutions of ZnS:Tb and ZnS:Eu nanocrystals exposed to excitation photons at a wavelength of 354nm, the respective emission colors of green for Tb^{3+} and orange/red for Eu^{3+} can be easily observed by the naked eye as depicted in the picture located in the Figure 4.5.

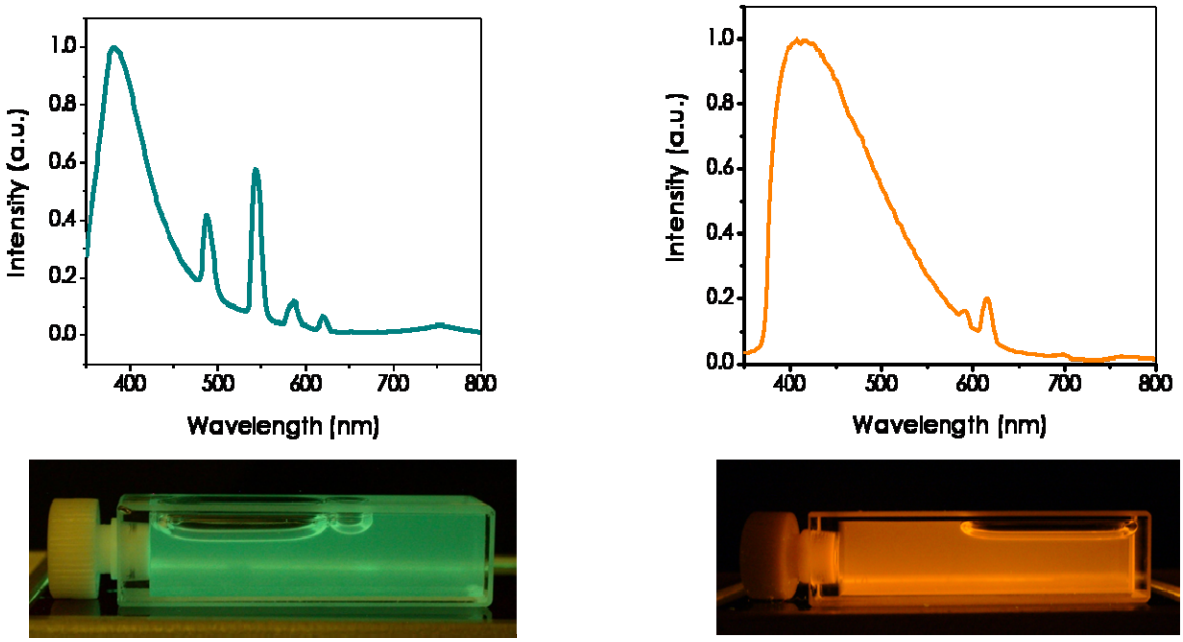

Figure 4.5. Top: normalized steady state emission spectra of ZnS:Tb (top left) and ZnS:Eu (top right) of nanocrystal samples dissolved in chloroform using an excitation wavelength of 320 nm collected using a JY Horiba Spex Fluorolog-322. Bottom Left: picture illustrating blue-green emission arising from raw ZnS:Tb nanocrystals in chloroform upon excitation with a laboratory UV lamp (λ_{ex} = 375 nm). A 475 nm cut-off filter was placed in front of the objective of the digital camera to remove contributions from the UV lamp and the ZnS band edge emission, so mainly photons arising from Tb^{3+} would be selected. Bottom Right: similar picture taken in similar conditions of raw ZnS:Eu nanocrystals exhibiting the red Eu^{3+} luminescence. A 550 nm cut-off filter was placed in front of the objective of the digital camera to remove contributions from the UV lamp and the ZnS band edge emission.

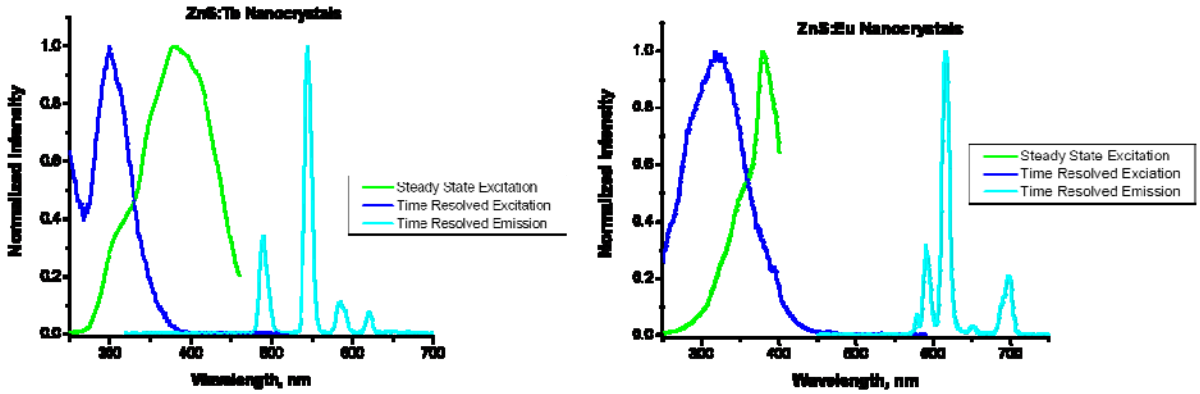

Figure 4.6. Overlay of normalized steady state and time resolved excitation spectra of ZnS:Tb (left) and ZnS:Eu (right) dissolved in chloroform.

Information regarding the efficiency of sensitization (antenna effect) of Tb^{3+} and Eu^{3+} in ZnS:Tb and ZnS:Eu systems respectively can be inferred by comparing steady state and time resolved excitation spectra of these two types of compounds. If the antenna effect is not observed, the time resolved excitation spectra will resemble that of the respective free lanthanide cation in solution. Sensitization or energy transfer from the band gap to the lanthanide cations is suggested if overlaps are observed in the steady state and time resolved excitation spectra. Figure 4.6 left represents the spectra for ZnS:Tb. There is a small portion of the excitation signals which overlaps, indicating some degree of sensitization of the accepting levels of the lanthanide cations through the electronic states of the semiconductor nanocrystals. This is also the case for ZnS:Eu, shown in Figure 4.6 right. The time resolved spectra do not contain sharp direct excitation bands of Tb^{3+} and Eu^{3+} respectively, another indication the presence of the antenna effect within these systems.

Articles describing the doping of ZnS nanocrystals with rare earth ions have emerged starting as early as the mid 1990s. Claims of doping nanocrystals in an effort to create a superior

phosphor material have been made. Many of these papers show emission spectra indicating the presence of trivalent lanthanide cations, but in all cases excitation spectra were omitted. These spectra are important to determine (1) whether or not doping has occurred, and (2) whether or not sensitization of the lanthanide cations take place through the nanocrystal band gap.[57,60] Bol et al. have surveyed the literature reports of doping ZnS with trivalent lanthanide cations, examining the multiple approaches to achieving doping, including organometallic syntheses and microemulsion techniques.[59] Chen et al. examined doping of Eu^{2+} within ZnS nanocrystals. Emission spectra support the presence of a broad band centered at 530 nm corresponding to Eu^{2+} emission.[57] This study reports no excitation spectra to support their claims of doping. Attempts by Bol et al. to reproduce this work have been unsuccessful and only nanocrystal emission bands are present upon excitation of the nanoparticles at 330 nm.[59] Microemulsion techniques attempted by Bol et al. for doping ZnS with Eu^{3+} did exhibit characteristic Eu^{3+} emission bands upon excitation of the nanocrystal, however excitation spectra collected upon monitoring this Eu^{3+} emission resulted in only a direct excitation profile.[59] Final attempts at reproducing ZnS:Ln spectra published in the literature involved the use of organometallic syntheses adapted from the work of Bhargava et al. on Mn doped ZnS.[59,61] This work focused on doping with Tb^{3+} and while steady state lanthanide emission was once again detected, these procedures also failed to yield excitation spectra other than those resembling direct excitation profiles of Tb^{3+}.

The work presented here is novel in that in addition to observation of steady state emission spectra illustrating bimodal emission resulting from the lanthanides and the nanocrystals, excitation spectra collected upon monitoring the lanthanide emission does not represent direct excitation. Broadening of the time resolved spectra is observed and the excitation bands overlap to some extent with the excitation observed upon monitoring

nanocrystal emission. To the best of our knowledge, this is the first report of sensitization of Eu^{3+} and Tb^{3+} through the band gap of the nanocrystals.

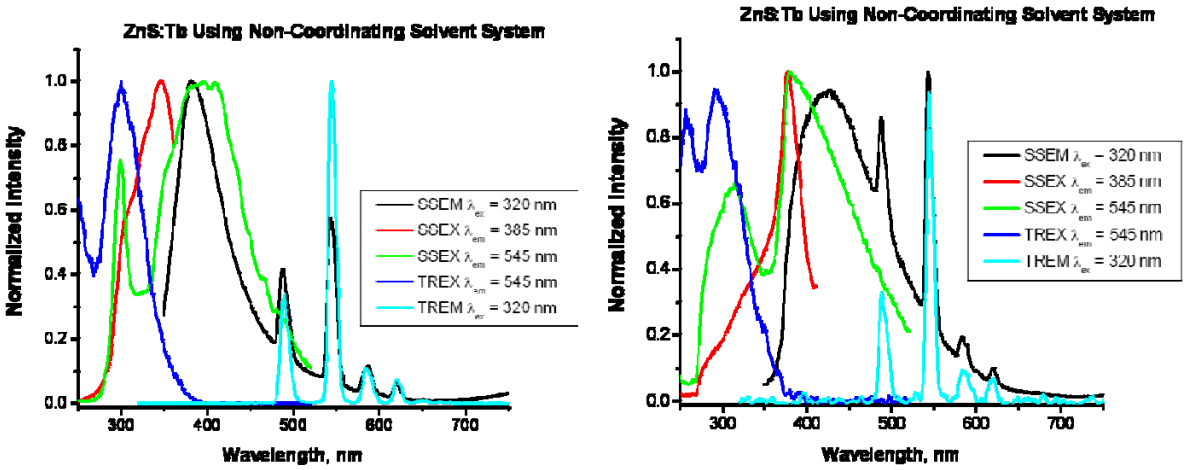

Figure 4.7. Additional batches of ZnS:Tb nanocrystals in chloroform illustrating both steady state emission of Tb^{3+} and excitation profiles deviating from characteristic direct excitation of Tb^{3+} (normalized spectra).

In order to evaluate the number of different lanthanide environments present in the nanocrystals and the extent of which each was protected from non-radiative deactivation, luminescence lifetimes were measured at room temperature using the third harmonic wavelength (354 nm) of a Nd:YAG laser as the excitation source and detecting specifically the emission signal arising from the lanthanide cations. Experimental luminescence lifetimes collected on Tb^{3+} and Eu^{3+} for ZnS:Tb and ZnS:Eu nanocrystals respectively were analyzed and compared to the previously reported lifetimes for CdSe:Tb and CdSe:Eu nanocrystals and are shown in Table 4.1. In both cases, the terbium and europium experimental luminescence lifetimes fit best as a biexponential decay curve. It can be noticed that such bi-exponential decay was also observed in the case of CdSe:Ln nanocrystals. This result can be explained by the presence of two different

lanthanide environments within the crystals. We assign these sites to lanthanide cations at the surface and in the core of the nanocrystal.

Table 4.1. Individual luminescence lifetimes for Tb^{3+} and Eu^{3+} doped ZnS and CdSe nanocrystals as obtained from the experimental decay curve. ZnS lifetimes were recorded in chloroform while CdSe lifetimes were collected in hexanes. ZnS:Tb and CdSe:Tb were monitored at 545 nm (corresponding to Tb^{3+}), while ZnS:Eu and CdSe:Eu were monitored at 614 nm (corresponding to Eu^{3+}). All samples were excited using a 354 nm excitation source.

Sample	τ1 (ms)	τ2 (ms)
ZnS:Tb	2.50 ± 0.06	0.92 ± 0.01
CdSe:Tb	4.7 ± 0.2	2.02 ± 0.06
ZnS:Eu	3.6 ± 0.15	2.0 ± 0.014
CdSe:Eu	2.8 ± 0.21	1.26 ± 0.24

Literature luminescence lifetime values for well protected lanthanide complexes with Tb^{3+} and Eu^{3+} are 1.3 ms and 0.78 ms respectively.[62] These values are reported for complexes with organic ligands and are reported in MeOH where little quenching may occur through the vibrations of the ligand itself. The values reported here for lanthanide containing semiconductor nanocrystals are significantly longer (the longest component in each system is at least double the observed lifetimes when organic ligands are used as sensitizers). These results confirm well protected lanthanide environments and gives strong indication that the lanthanides reside both within the crystal structure (core) where quenching from solvent vibrations is minimized and at the surface of the nanocrystals where more significant quenching is occurring.

Table 4.2. Calculated quantum yield values of overall (total steady state emission) and lanthanide centered emission for CdSe:Tb and ZnS:Tb nanocrystal systems. CdSe:Tb quantum yields were collected in toluene (λ_{ex} = 300nm, 305 nm, and 310 nm) – overall quantum yields were collected through steady state mode while lanthanide centered were collected through time resolved measurements. ZnS:Tb quantum yields were collected in chloroform (λ_{ex} 315 nm, 320 nm, 325 nm) – both overall and lanthanide centered quantum yields were collected through steady state measurements.

Material	Overall ϕ	Lanthanide Contribution to ϕ
ZnS:Tb	$1.2 \times 10^{-1} \pm 2.5 \times 10^{-2}$	$5.1 \times 10^{-2} \pm 5.6 \times 10^{-3}$
CdSe:Tb	$2.5 \times 10^{-2} \pm 1.0 \times 10^{-3}$	$1.5 \times 10^{-5} \pm 0.03 \times 10^{-5}$

The luminescence efficiency of these materials was determined through quantum yield measurements. The average values for both overall and lanthanide centered quantum yields were collected at room temperature and are reported in Table 4.2. The values for ZnS:Tb are compared to those obtained for CdSe:Tb nanocrystals. In the case of CdSe, the lanthanide emission was only observed in time resolved measurements so the contribution from the lanthanide was discriminated temporally from the nanocrystal signal. However, for ZnS the lanthanide signal is observed in steady state spectra and the contribution from the Tb^{3+} centered emission on the overall was discriminated spectrally by integrating the narrow emission bands arising from the Tb^{3+}.

The quantum yield values indicate significant improvement in the luminescence efficiency of both the overall system (including band gap and lanthanide emission) and the Tb^{3+} contribution alone. The observed increase for the lanthanide centered emission in ZnS:Tb is 1000-fold relative the Tb^{3+} centered quantum yield observed for CdSe:Tb.

Table 4.3. Calculated lanthanide centered quantum yields. Values were determined through the analysis of multiple samples at multiple excitation wavelengths (ZnS:Ln – λ_{ex} = 315 nm, 320 nm, and 325 nm; CdSe:Ln - λ_{ex} = 300 nm, 305 nm, and 310 nm) ZnS:Ln samples were measured in chloroform while CdSe:Ln samples were measured in toluene.

Material	Lanthanide Centered ϕ
ZnS:Tb	$5.1x10^{-2} \pm 5.6x10^{-3}$
ZnS:Eu	$1.3x10^{-4} \pm 4.2x10^{-5}$
CdSe:Tb	$1.5 \times 10^{-5} \pm 0.03 \times 10^{-5}$
CdSe:Eu	$6.6x10^{-5} \pm 0.2x10^{-5}$

Lanthanide centered quantum yields were calculated for ZnS:Eu nanocrystals as well. Values for ZnS:Tb and ZnS:Eu versus CdSe:Tb and CdSe:Eu are illustrated in Table 4.3. ZnS:Eu nanocrystals exhibit a significantly shorter (100 fold decrease) relative to ZnS:Tb nanocrystals. This can be explained by the less appropriate matching of energy levels within these systems. Despite the differences between ZnS:Tb and ZnS:Eu, these systems are collectively more efficient than their CdSe counterparts. CdSe:Eu exhibits a lanthanide centered quantum yield a factor of 10 smaller than that calculated for ZnS:Eu nanocrystals.

Luminescence intensity is significantly larger for Eu^{3+} doped ZnS nanocrystals than for CdSe nanocrystals. Two main explanations can be hypothesized regarding this result. First the nanocrystal to lanthanide energy transfer is more efficient in Tb^{3+} doped ZnS than in Tb^{3+} doped CdSe. The more efficient energy transfer could be explained by the energy of the donating ZnS

levels relative to the accepting levels of those centered on Tb^{3+} and Eu^{3+}. The visible emission arising from ZnS is blue shifted compared to that of CdSe indicating a larger energy gap between the ground and excited states in comparison to CdSe. This is illustrated pictorially in Figure 4.8, where matrices have been assembled to show band gap energy of ZnS (top) verses CdSe (bottom) relative to the accepting energy levels of the lanthanide cations. Band gap emission is better positioned to transfer energy to Tb^{3+} more easily in the case of ZnS than in the case of CdSe.

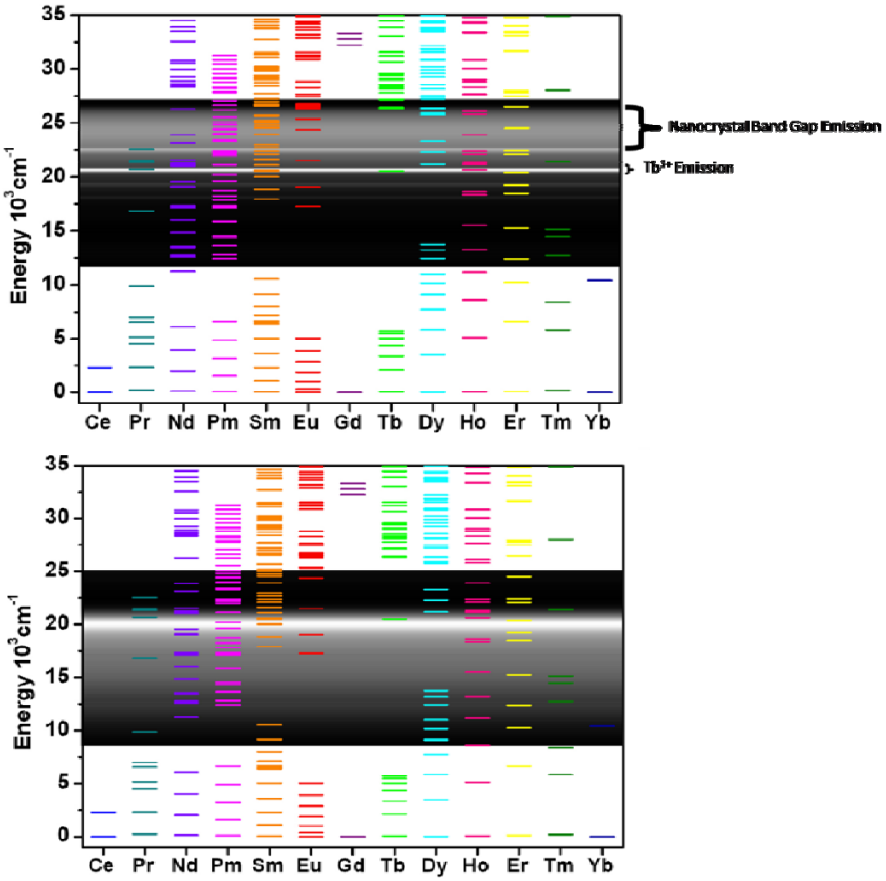

Figure 4.8. Energy level diagram for Ln^{3+} cations. Top: matrix plot illustrating ZnS emission overlaid with lanthanide energy levels. Bottom: matrix plot illustrating CdSe emission overlaid with lanthanide energy levels. The dark region is a matrix representing the fluorescence obtained upon excitation of the nanocrystal band gap. The lighter region within this matrix represents the emission maximum.

Figure 4.8 illustrates the energy of the band gap emission relative to the lanthanide accepting levels for ZnS (top) versus CdSe (bottom). Based on band gap energy of these systems relative to one another, ZnS has higher energy and is therefore better suited to transfer energy to a wider variety of lanthanide cations than CdSe.

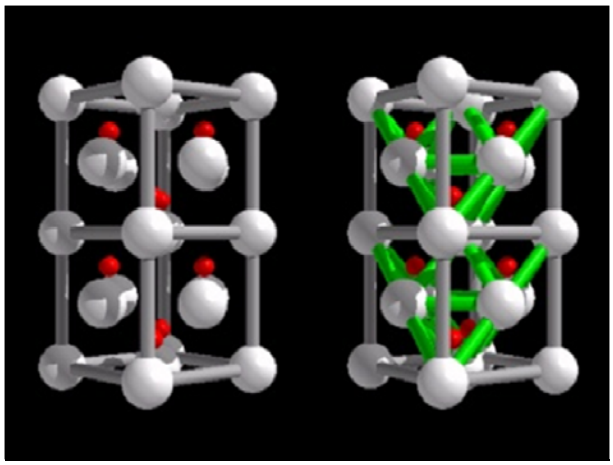

Figure 4.9. Cartoon illustrating zinc blende vs wurtzite geometries.

Another complementary possible explanation for the larger signals observed for the lanthanide cations in ZnS:Ln in comparison to the corresponding CdSe:Ln nanocrystals could be attributed to a larger doping efficiency in the ZnS:Ln nanocrystals. ZnS nanocrystals have been described to preferentially adopt zinc-blende crystal structure whereas the CdSe posses preferentially a wurtzite geometry (Figure 4.9).[38,39] It has been reported[38] that dopants will more efficiently incorporate into zinc blende material. This statement is based on a survey of a large number of published work on Mn^{2+} doped zinc-blende structures (ZnS, CdS, etc.) versus wurtzite structures (CdSe) and rock salt structures (PbS, PbSe, etc.).[38] Most efficient doping has been performed on zinc-blende structures, while little success has been achieved through other

nanocrystal structures. It is suggested this results from the ability of dopant ions to adsorb onto the zinc-blende (001) facets.

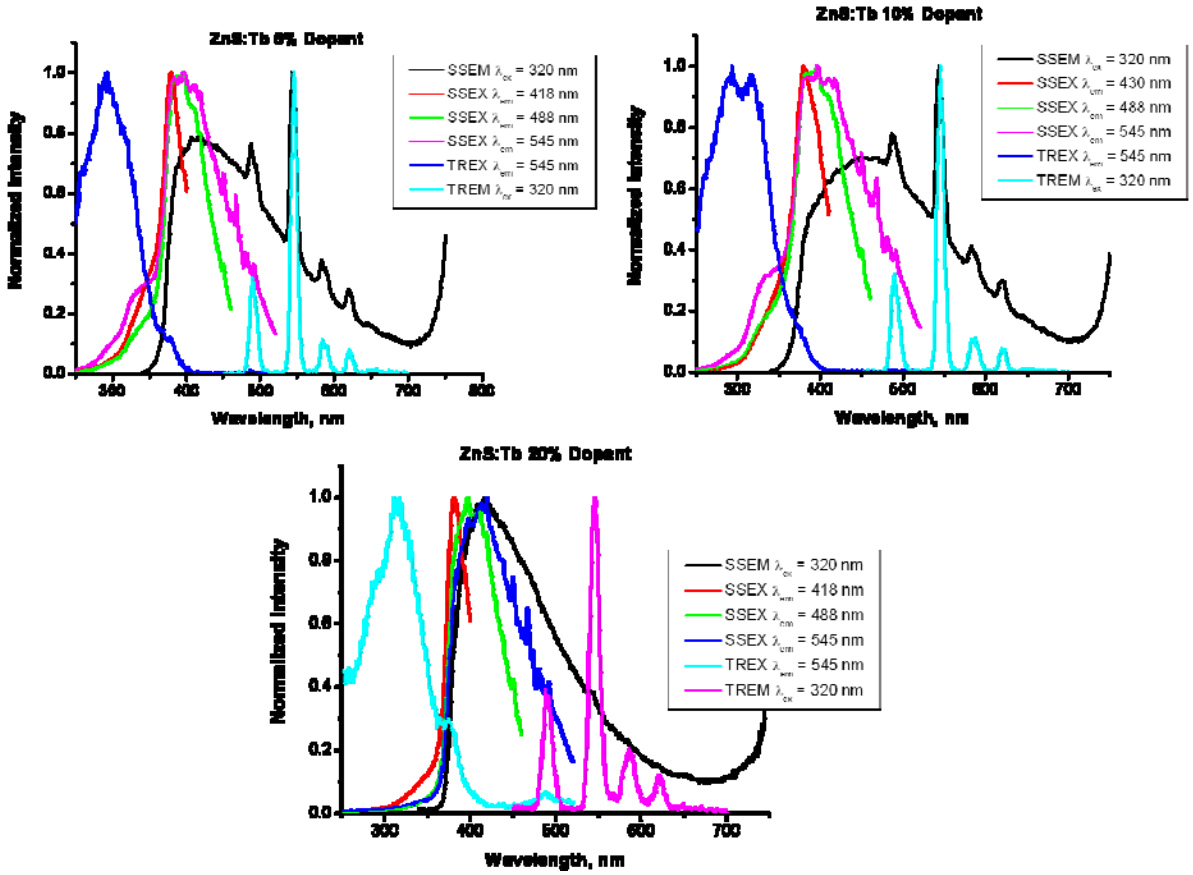

Figure 4.10. Overlay of normalized steady state and time resolved emission and excitation spectra collected for ZnS:Tb nanocrystals solutions containing varying dopant concentration. Dopant concentration represents the percentage of the total cation precursor in the initial reaction mixture.

Figure 4.10 illustrates spectra collected for ZnS:Tb nanocrystals synthesized using varying dopant ratios. Ratios between 5% and 20% doping relative to the total cation concentration were used for the synthesis of these materials. Little difference is observed in the overall spectra when changing the dopant concentration from 5% to 10%, with the exception of a

slight shift in the position of the band gap emission. Significant contribution from Tb^{3+} can be observed in the steady state emission spectra, however when increasing the doping to 20%, this lanthanide emission is drastically reduced.

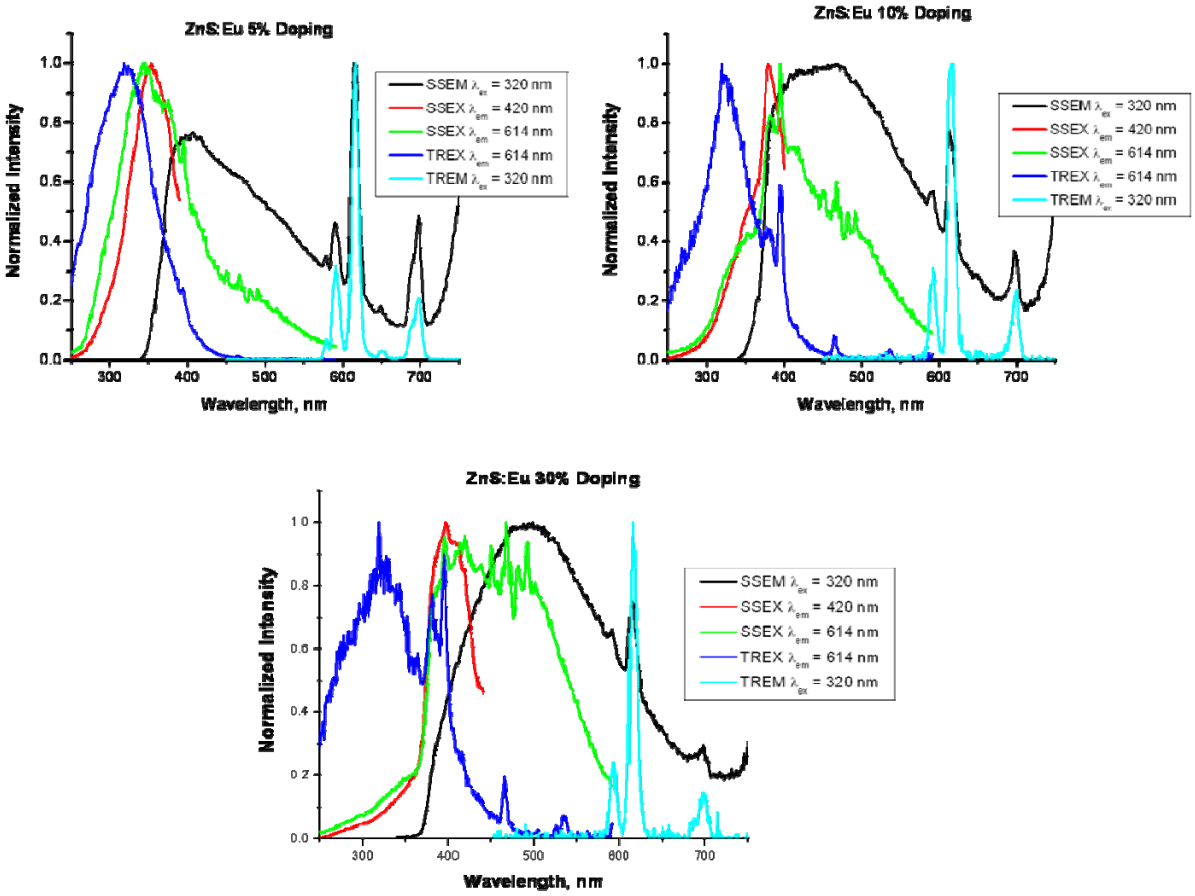

Figure 4.11. Normalized steady state and time resolved emission and excitation spectra of ZnS:Eu nanocrystals in solution containing varying dopant concentration. Doping percentage represents the percentage of the total cation precursors in the initial reaction mixture.

Studies regarding dopant concentration were also conducted for ZnS:Eu nanocrystals, where the doping concentration was adjusted from 5% to 30% (Figure 4.11). Again, the band gap emission profile is shifted to lower energy with increasing dopant concentration. However

in the case of ZnS:Eu the decrease in steady state lanthanide emission is not as drastic as what was observed for ZnS:Tb. An increase is found for samples corresponding to doping comprised between 5% and 10%.

DTPA surface exchanges were performed on ZnS:Tb nanocrystals in an attempt to obtain water soluble particles. The reasoning was that the DTPA would bind to lanthanide cations at the nanocrystal surface. A DTPA stock solution was prepared by dissolving DTPA in 20 mL of deionized water through de-protonation with KOH (5:1 equivalents of KOH:DTPA for full de-protonation, resulting in a ligand with several available binding sites for attachment to the nanocrystal surface).

The following procedure was performed on raw nanocrystals as well as nanocrystal that had undergone one round of purification via methanol precipitation (raw nanocrystals dissolved in chloroform were precipitated with excess methanol to remove unwanted biproducts of the initial reaction and then redissolved in chloroform for analysis). Nanocrystals were dissolved in a minimal amount of chloroform resulting in concentrated solutions. An excess of the aqueous DTPA stock solution was then added to the nanocrystals in chloroform. The samples were sonicated for 2 hours to ensure interaction of the aqueous and organic phases. After sonication, samples were centrifuged to separate the layers and the aqueous phase was removed for analysis. In some instances these procedures resulted in very dilute aqueous DTPA coated nanocrystal samples in which case samples were concentrated by removal of water via standard vacuum techniques.

The water soluble DTPA coated nanocrystals were spectrally analyzed and their luminescence spectra compared to TOPO/TOP passivated nanocrystals dissolved in chloroform.

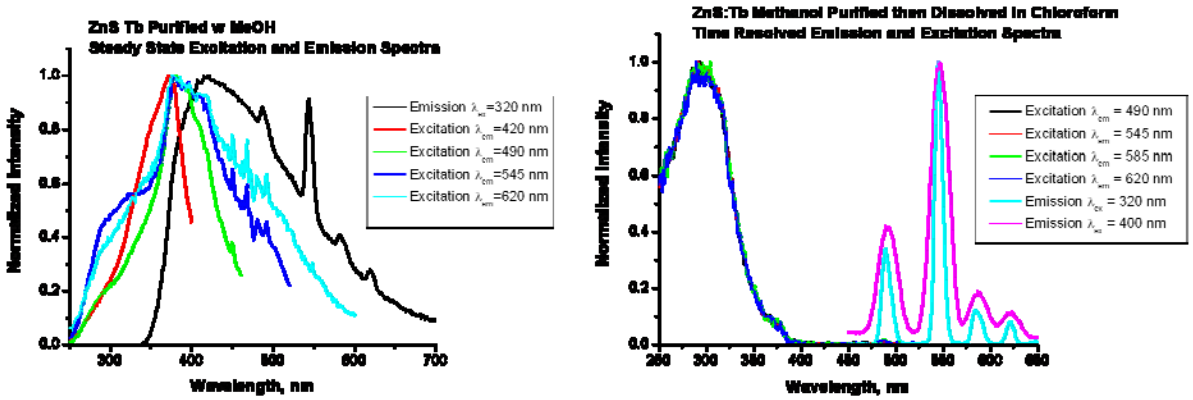

Figure 4.12. Normalized steady state and time resolved emission and excitation spectra of ZnS:Tb nanocrystals purified through precipitation with methanol and redisolved in chloroform.

Figure 4.12 shows steady state and time resolved emission and excitation spectra of ZnS:Tb nanocrystals dissolved in chloroform. The steady state fluorescence spectra indicate the presence of broad band gap emission centered at 450 nm in addition to emission resulting from the 4 characteristic Tb^{3+} transitions ($^5D_4 \rightarrow {}^7F_J$, J = 6, 5, 4, 3). Excitation spectra collected upon monitoring all 5 emission results in broad spectra. This gives some indication of energy transfer; however time resolved spectra were collected for verification. Time resolved excitation spectra were collected upon monitoring emission wavelengths of all terbium bands (490 nm, 545 nm, 585 nm, and 620 nm), all resulting in the same excitation profile as seen in Figure 4.10 (right). Time resolved emission spectra were collected upon excitation at 400 nm (where no direct excitation of Tb^{3+} is observed but nanocrystal excitation is present). The time resolved excitation spectra show a broad excitation band centered at 300 nm. This band slightly overlaps with the steady state nanocrystal excitation band (left spectra, red) and does not exhibit the characteristic sharp transitions representative of direct excitation of Tb^{3+}. Based on hypotheses

applied to CdSe:Ln comparing excitation profiles (upon monitoring lanthanide and band gap emission respectively) we observe some indication of antenna effect within the lanthanide containing ZnS materials.

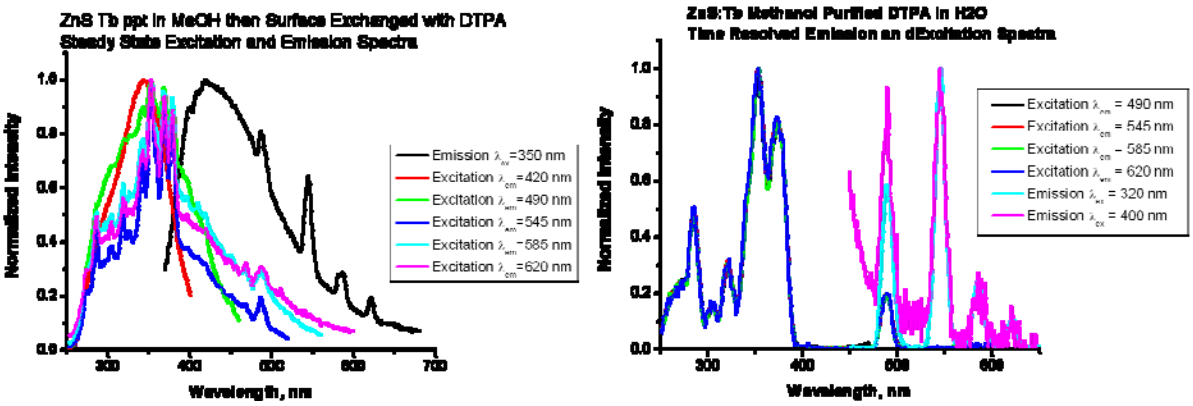

Figure 4.13. Normalized steady state and time resolved emission and excitation spectra of methanol purified ZnS:Tb nanocrystals after surface exchange with DTPA.

Spectra were also collected on the aqueous DTPA coated ZnS:Tb nanocrystals (Figure 4.13). The steady state emission spectra also show the presence of band gap emission as well as Tb^{3+} emission bands. The excitation spectra upon monitoring the Tb^{3+} emission in the aqueous samples indicates more fine structure than in the case of the chloroform ZnS:Tb samples, giving the indication of a direct excitation of Tb^{3+}. Direct excitation is confirmed through collection of time resolved excitation spectra. The excitation spectra on the right also possess more fine structure and overlap well with direct excitation of terbium in solution; this indicates that little, if any, antennae effect is observed in the aqueous samples. It is hypothesized that this is partially due to free Tb^{3+} in solution being bound by DTPA in the exchange process. The nanocrystal concentration in water is low and the spectra will therefore be dominated by the Tb:DTPA

complexes. DTPA is not a chromophore and cannot serve as an antenna, so only direct excitation can be observed for these complexes.

Table 4.4. Luminescence lifetime data representing ZnS:Tb nanocrystals dissolved in chloroform verses water soluble DTPA passivated nanocrystals (λ_{ex} = 354 nm, λ_{em} = 545 nm).

Sample	τ1 (s)	τ2 (s)
ZnS:Tb in $CHCl_3$	2.5E-03 ± 6.4E-05	9.2E-04 ± 1.5E-04
ZnS:Tb DTPA in H_2O	2.0E-03 ± 1.0E-05	7.8E-04 ± 2.9E-04

Luminescence lifetimes of Tb^{3+} within the aqueous and chloroform solution samples were also collected and analyzed. In both cases, a biexponential decay was observed and the data is reported in Table 4.4. Both lifetime components are slightly quenched in water, the longer decreasing from 2.5 ms to 2.0 ms while the shorter is quenched from 0.9 to 0.8 ms. Quenching is expected, especially for the compound that corresponds to the shorter component which is attributed to the surface bound terbium, as the result of the OH vibrations in water which will result in non-radiative deactivation of the terbium. The small degree of quenching in this system gives a good quantitative indication of the good level of protection of Tb^{3+} within the ZnS nanocrystals. If terbium cations were only located on the surface of ZnS nanocrystals, the quenching effects would be more pronounced.

4.4 CONCLUSIONS AND FUTURE DIRECTIONS

Undoped ZnS materials are less attractive for bioanalytical applications than their CdSe counterparts because their emission lies in the UV-Blue region where biological materials emit a significant amount of fluorescence, creating a detrimental fluorescence background. Despite their less attractive emission properties, these materials are constituted from components with relatively low toxicity, and upon incorporation of luminescent lanthanide cations as dopant ions, their emission properties can be tuned to obtain emission in the visible domain with signals that can be easily discriminated from background fluorescence, increasing their potential for bioanalytical applications and biological imaging. The data presented here indicates improved efficiency of ZnS over CdSe systems at sensitizing Tb^{3+} and Eu^{3+}. The emergence of steady state lanthanide emission is the first indication of improved efficiency, while calculated quantum yields further support this conclusion.

Some efforts were spent trying to optimize the synthetic conditions to enhance the photoluminescence properties of the nanocrystals and their ability to serve as lanthanide antennae. Synthetic conditions were systematically varied from non-coordinating solvent conditions using tetracosane and octadecene to coordinating solvent systems employing TOPO/TOP. Additional procedures involved the use of alternative Zn^{2+} precursors, replacing zinc stearate with zinc oxide. The luminescence intensity of the lanthanide signal was monitored in steady state mode for these materials to determine optimal synthetic conditions. Additional studies regarding maximum dopant concentration were conducted to further optimize synthetic conditions resulting in the most intense lanthanide luminescence when using 15% doping.

We have shown that the synthesis of ZnS:Ln nanocrystals results in reproducible lanthanide luminescence properties. The presence of a significant luminescence signal of the lanthanide observed in steady state measurements eliminates the need for time resolved analysis. These particles show enhanced luminescence properties compared to the previously reported CdSe:Ln nanocrystals.

It is believed that white emission can be achieved through careful and systematic adjustment of the lanthanide ratios relative to one another (green emission resulting from Tb^{3+} and red emission resulting from Eu^{3+}) and relative to the band gap emission (blue emission). By identifying the proper ratios of blue, green and red emission through the control of the amounts of each constituent, we hope to be able to create novel energy efficient white light emitting devices.

The next step in these systems is to study in greater detail the effect of lanthanide concentration on the incorporation of dopant ions in the host lattice. This can be done by varying the initial dopant concentration in the reaction mixture and monitoring the resulting spectral properties. In addition, HRTEM imaging can provide information on crystallinity and dispersity, while measurments such as ICP-AES, EELS, ZSTEM and SQUID can lead to information regarding concentration and location of the lanthanides within the nanocrystal structure.

This particular nanomaterials synthesis can also be expanded to test its ability to sensitize other luminescent lanthanide cations. Near infrared emitting lanthanide cations are attractive for use *in vivo* and should be examined as dopant materials within ZnS hosts, thus further expanding the potential for these materials as bioanalytical agents. The combination of non- or low toxic materials in conjunction with NIR emission arising from lanthanides is attractive for use in bioimaging applications.

4.5 REFERENCES

(1) Chengelis, D. A.; Yingling, A. M.; Badger, P. D.; Shade, C. M.; Petoud, S. *J. Am. Chem. Soc.* **2005**, *127*, 16752-16753.

(2) Bünzli, J.-C.; Choppin, G. R. *Lanthanide propes in life, chemical, and earth sciences: theory and practice*; Elsevier: Amsterdam, New York, 1989.

(3) Desiraju, G. R. *Acc. Chem. Res.* **1996**, *29*, 441.

(4) Mathis, G. *J. Biomol. Screen.* **1999**, *4*, 309-313.

(5) Cha, A.; Snyder, G. E.; Selvin, P. R.; Bezanilla, F. *Nature* **1999**, *402*, 809 - 813.

(6) Bünzli, J.-C.; *Acc. Chem. Res.* **2006**, *39*, 53.

(7) Bünzli, J.-C.; Piguet, C. *Chem. Soc. Rev.* **2005**, *34*, 1048.

(8) Caravan, P.; Ellison, J. J.; McMurry, T. J.; Lauffer, R. B. *Chem. Rev.* **1999**, *99*, 2293 - 2352.

(9) Jaiswal, J. K.; Mattoussi, H.; Mauro, J. M.; Simon, S. M. *Nature Biotechnology* **2003**, *21*, 47 - 51.

(10) Hanaki, K.; Momo, A.; Oku, T.; Komoto, A.; Maenosono, S.; Yamaguchi, Y.; Yamamoto, K. *Biochem. Biophys. Res. Commun.* **2003**, *302*, 496 - 501.

(11) Mattheakis, L. C.; Dias, J. M.; Choi, Y. J.; Gong, J.; Bruchez, M. P.; Liu, J.; Wang, E. *Anal. Biochem.* **2004**, *327*, 200 - 208.

(12) Derfus, A. M.; Chan, W. C. W.; Bhatia, S. N. *Nano Lett.* **2004**, *4*, 11 - 18.

(13) Santone, K. S.; Acosta, D.; Bruckner, J. V. *J. Toxicol. Environ. Health* **1982**, *10*, 169-77.

(14) Zhang, T. T.; Stilwell, J. L.; Gerion, D.; Ding, L. H.; Elboudwarej, O.; Cooke, P. A.; Gray, J. W.; Alivisatos, A. P.; Chen, F. F. *Nano Lett.* **2006**, *6*, 800 - 808.

(15) Tsuji, J. S.; Maynard, A. D.; Howard, P. C.; James, J. T.; Lam, C. W.; Warheit, D. B.; Santamaria, A. B. *Toxicol. Sci.* **2006**, *89*, 42 - 50.

(16) Lovric, J.; Cho, S. J.; Winnik, F. M.; Maysinger, D. *Chem. Biol.* **2005**, *12*, 1227 - 1234.

(17) Kirchner, C.; Liedl, T.; Kudera, S.; Pellegrino, T.; Javier, A. M.; Gaub, H. E.; Stoelzle, S.; Fertig, N.; Parak, W. J. *Nano Lett.* **2005**, *5*, 331-338.

(18) Hardman, R. *Environ. Health Perspect.* **2006**, *114*, 165 - 172.

(19) Hoshino, A.; Fujioka, K.; Oku, T.; Suga, M.; Sasaki, Y. F.; Ohta, T.; Yasuhara, M.; Suzuki, K.; Yamamoto, K. *Nano Lett.* **2004**, *4*, 2163 - 2169.

(20) Ballou, B.; Lagerholm, B. C.; Ernst, L. A.; Bruchez, M. P.; Waggoner, A. S. *Bioconjugate Chem.* **2004**, *15*, 79 - 86.

(21) Aryal, B. P.; Neupane, K. P.; Sandros, M. G.; Benson, D. E. *Small* **2006**, *2*, 1159 - 1163.

(22) Choi, H. S.; Liu, W.; Misra, P.; Tanaka, E.; Zimmer, J. P.; Ipe, B. I.; Bawendi, M. G.; Frangioni, J. V. *Nature Biotechnology* **2007**, *25*, 1165 - 1170.

(23) Karabanovas, V.; Zakarevicius, E.; Sukackaite, A.; Streckyte, G.; Rotomskis, R. *Photochem. Photobiol.* **2008**, *7*, 725 - 729.

(24) Bruchez, M., Jr.; Moronne, M.; Gin, P.; Weiss, S.; Alivisatos, A. P. *Science* **1998**, *281*, 2013-2016.

(25) Fu, A.; Gu, W.; Larabell, C.; Alivisatos, A. P. *Curr. Opin. Neurobiol.* **2005**, *15*, 568-575.

(26) Limaye, D. A.; Shaikh, Z. A. *Toxicol. Appl. Pharmacol.* **1999**, *154*, 59-66.

(27) Hines, M. A.; Guyot-Sionnest, P. *J. Phys. Chem.* **1996**, *100*, 468-71.

(28) Cao, Y.; Banin, U. *J. Am. Chem. Soc.* **2000**, *122*, 9692.

(29) Reiss, P.; Bleuse, J.; Pron, A. *Nano Lett.* **2002**, *2*, 781 - 784.

(30) Rodriguez-Viejo, J.; Jensen, K. F.; Mattoussi, H.; Michel, J.; Dabbousi, B. O.; Bawendi, M. G. *Appl. Phys. Lett.* **1997**, *70*, 2132-2134.

(31) Talapin, D. V.; Rogach, A. L.; Kornowski, A.; Haase, M.; Weller, H. *Nano Lett.* **2001**, *1*, 207 - 211.

(32) Dabbousi, B. O.; Rodriguez-Viejo, J.; Mikulec, F. V.; Heine, J. R.; Mattoussi, H.; Ober, R.; Jensen, K. F.; Bawendi, M. G. *J. Phys. Chem. B: At. Mol. Opt. Phys.* **1997**, *101*, 9463-9475.

(33) Peng, X.; Schlamp, M. C.; Kadavanich, A. V.; Alivisatos, A. P. *J. Am. Chem. Soc.* **1997**, *119*, 7019-7029.

(34) Frangioni, J. V. *Curr. Opin. Biotech.* **2003**, *7*, 626.

(35) Li, L. S.; Pradhan, N.; Wang, Y.; Peng, X. *Nano Lett.* **2004**, *4*, 2261-2264.

(36) Gilbert, B.; Huang, F.; Lin, Z.; Goodell, C.; Zhang, H.; Banfield, J. F. *Nano Lett.* **2006**, *6*, 605 - 610.

(37) Zu, L.; Norris, D. J.; Kennedy, T. A.; Erwin, S. C.; Efros, A. L. *Nano Lett.* **2006**, *6*, 334-340.

(38) Erwin, S. C.; Zu, L.; Haftel, M. I.; Efros, A. L.; Kennedy, T. A.; Norris, D. J. *Nature* **2005**, *436*, 91-94.

(39) Norris, D. J.; Yao, N.; Charnock, F. T.; Kennedy, T. A. *Nano Lett.* **2001**, *1*, 3-7.

(40) Suyver, J. F.; Wuister, S. F.; Kelly, J. J.; Meijerink, A. *Phys. Chem. Chem. Phys.* **2000**, *2*, 5445-5448.

(41) Norman, T. J.; Magana, D.; Wilson, T.; Burns, C.; Zhang, J. Z.; Cao, D.; Bridges, F. *J. Phys. Chem. B: At. Mol. Opt. Phys.* **2003**, *107*, 6309 - 6317.

(42) Lu, S. W.; Lee, B. I.; Wang, Z. L.; Tong, W.; Wagner, B. K.; Park, W.; Summers, C. J. *J. Lumin.* **2001**, *92*, 73 - 78.

(43) Chen, W.; Aguekian, V. F.; Vassiliev, N.; Serov, A. Y.; Filosofov, N. G. *J. Chem. Phys.* **2005**, *123*, 124707-1.

(44) Quan, Z.; Wang, Z.; Yang, P.; Lin, J.; Fang, J. *Inorg. Chem.* **2007**, *46*, 1354.

(45) Bhargava, R. N.; Gallagher, D.; Hong, X.; Nurmikko, A. *Phys. Rev. Lett.* **1994**, *72*, 416-19.

(46) Sun, L.; Liu, C.; Liao, C.; Yan, C. *J. Mater. Chem.* **1999**, *9*, 1655 - 1657.

(47) Borse, P. H.; Vogel, W.; Kulkarni, S. K. *J. Colloid Interface Sci.* **2006**, *293*, 437 - 442.

(48) Mu, J.; Gu, D.; Xu, Z. *Mater. Res. Bull.* **2005**, *40*, 2198.

(49) Zhang, H.; Shen, Y. *J. Lumin.* **1988**, *40* 401.

(50) Stapor, A.; Godlewski, M.; Przybylinska, H.; Hommel, D. *J. Lumin.* **1988**, *40*, 625.

(51) Yen, W. M.; Shionoya, S. *Phosphor Handbook* Boca Raton, 1999.

(52) Hommel, D.; Hartmann, H.; Godlewski, M.; Langer, J. M.; Stapor, A. *J. Cryst. Growth* **1985**, *72*, 346 - 350.

(53) Bryant, F. J.; Hagston, W. E.; Krier, A. *Phys. Status Solidi A* **1986**, *94*, 701.

(54) Swiatek, K.; Godlewski, M.; Hommel, D.; Hartmann, H. *Phys. Status Solidi A* **1989**, *114*, 127.

(55) Bol, A. A.; Ferwerda, J.; Bergwerff, J. A.; Meijerink, A. *J. Lumin.* **2002**, *99*, 325-334.

(56) Kushida, T.; Kurita, A.; Watanabe, M.; Kanematsu, Y.; Hirata, K.; Okubo, N.; Kanemitsu, Y. *J. Lumin.* **2000**, *87 - 89*, 466 - 468.

(57) Chen, W.; Malm, J.-O.; Zwiller, V.; Huang, Y.; Liu, S.; Wallengerg, R.; Bovin, J.-O.; Samuelson, L. *Phys. Rev. B: Condens. Matter* **2000**, *61*, 11021 - 11024.

(58) Su, F. H.; Fang, Z. L.; Ma, B. S.; Ding, K.; Li, G. H.; Xu, S. J. *J. Appl. Phys.* **2004**, *95*, 3344 - 3349.

(59) Bol, A. A.; van Beek, R.; Meijerink, A. *Chem. Mater.* **2002**, *14*, 1121-1126.

(60) Bhargava, R. N. *J. Lumin.* **1996**, *70*, 85 - 94.

(61) Gallagher, D.; Heady, W. E.; Racz, J. M.; Bhargava, R. N. *J. Mater. Res.* **1995**, *10*, 870.

(62) Petoud, S.; Muller, G.; Moore, E. G.; Xu, J.; Sokolnicki, J.; Riehl, J. P.; Le, U. N.; Cohen, S. M.; Raymond, K. N. *J. Am. Chem. Soc.* **2006**, *129*, 77 - 83.

5.0 LANTHANIDE CONTAINING ZINC SELENIDE NANOCRYSTALS

ZnSe, like ZnS is a wide band gap semiconductor and has been shown throughout the literature to be an attractive choice for host materials in the formation of doped nanocrystal systems.[1-3] Also, it has been noted by Norris et al. that the shape of the nanocrystals can significantly affect the number of incorporated dopants and that the zinc blende nanocrystals may be the best internal structure to favor dopant incorporation.[1,4,5] This is due to the nature of this crystal structure, i.e. the surface energy of the facets.[4] ZnSe nanocrystals have been successfully and reproducibly doped with both manganese and copper ions by numerous research groups. Successful doping of ZnSe nanocrystals in the literature has led us to hypothesize that we can dope these nanocrystals with luminescent lanthanide cations.

Table 5.1. Band gap values for semiconductors nanocrystals measured at 300K.[6]

Material	Band gap energy (eV), 300K
CdSe	1.7
ZnS	3.2
ZnSe	2.7

ZnSe, like ZnS semiconductor materials and its nanometer sized counterpart has a wider energy band gap with emission centered in the blue-UV region (Table 5.1). Because of this wider band gap of both ZnS and ZnSe in comparison to CdSe, we hypothesized that a more efficient energy transfer from the semiconductor nanocrystal to the luminescent lanthanide cations can be obtained due to a better match between donating and accepting levels. ZnS (3.2 eV) and ZnSe (2.7 eV) can be tuned more readily to match the accepting levels of various lanthanides in comparison to CdSe with its band gap of 1.7 eV. Based on previously reported data regarding sensitization of Tb^{3+} by CdSe nanocrystals, smaller nanocrystal sizes were found to be more effective at the sensitization of luminescent lanthanide cations.[7] Smaller sizes correspond to wider band gaps and therefore as the material is grown and approaches bulk, the band gap energies are no longer favorable for sensitization to occur because the band gap energy shifts to values below the accepting level of the Tb^{3+}. Because wider band gap materials have been found to be more efficient sensitizers in previous studies, ZnSe is a reasonable choice for sensitization of visible emitting lanthanide cations.

5.1 BACKGROUND

5.1.1 Current work on undoped zinc selenide

ZnSe nanocrystals have found a use as capping agents for smaller band gap semiconductor nanocrystals such as CdSe. They offer advantages over ZnS for capping CdSe because they would introduce less of a lattice mismatch between materials upon addition of the larger band gap shell.[8] Mismatches should be avoided since they introduce additional trap states which might quench luminescence. Initial observations have shown that ZnSe as shells for CdSe result in only marginal improvements in luminescence properties and are therefore not used as often as the ZnS counterparts.[9] These results are attributed to defects within the shell structure as well as defect sites located at the interface of the materials.[9] Through modification of synthetic procedures, Reiss et al. have been able to improve upon these previous results and have produced core/shell CdSe/ZnSe nanocrystals with significantly improved quantum yields, showing ZnSe can be successfully used as a passivant to enhance photoluminescence in CdSe nanocrystals.[8]

In addition to being used as capping agents, ZnSe nanocrystals are attractive for use in blue diode lasers. While procedures are well established for the synthesis of CdSe nanocrystals over the entire spectrum, including UV-blue, these nanocrystals have limitations based on the nature of the materials. Small blue emitting CdSe nanocrystals are often difficult to passivate and result in low quantum yields. Low quantum yields in these particles are the result of non-radiative relaxation occurring at the nanoparticle surface, since the surface to volume ratio is enhanced in smaller particles this phenomenon would have a more drastic impact on smaller nanocrystals than larger particles.[10] These small materials also often result in broader emission

bands than typically observed for CdSe. The reaction growth time is shorter for smaller particles and therefore there is not time for particles to undergo focusing, resulting in slightly polydispere sample. In this respect, CdSe is limited and there is a demand for alternative blue emitting nanocrystal materials. ZnSe nanocrystals are blue-UV emitting materials. They are also less toxic than the CdSe counterparts and are therefore attractive alternatives.

Initial reports of successful synthesis of ZnSe nanocrystals using organometallic precursors in high temperature reactions were from Hines et al.[11] Their work showed the possibility of synthesizing and characterizing materials with desired emission properties and slightly larger sizes than their CdSe counterparts.

In addition to work done by Hines et al., and as greener approaches to nanocrystal synthesis arose, Peng et al.[3] conducted work to better understand reaction conditions of ZnSe syntheses. Zinc carboxylate precursors replaced previously used diethyl zinc and exploration regarding the reactivity of these novel starting materials was crucial for the understanding of ZnSe nanoparticle formation.[3] Through systematic studies, Peng et al. reported the necessity of using aliphatic amines in conjunction with zinc carboxylate precursors to obtain high quality ZnSe nanocrystals with desired luminescent properties.[3]

5.1.2 Current work on doped zinc selenide

5.1.2.1 Transition metal dopants

As it was the case for ZnS, doping of ZnSe with transition metals has been widely studied. This is mainly based on the hypothesis that this nanocrystal structure is more conducive to

incorporation of dopant ions than CdSe or CdS nanocrystals. A great deal of work has been carried out on doping of ZnSe with Mn^{2+}, including several studies by Norris et al.[1,2,4,5,12,13]

Mn^{2+} is an attractive dopant because of its ability to serve as a paramagnetic center. This can lead to spin-spin exchange interactions that are further enhanced by the quantum confinement effects of the nanocrystals.[1,13] Norris et al. have done work on examining Mn^{2+} doping using electron paramagnetic resonance (EPR) as proof of incorporation of the dopant ions internally within the nanocrystal structure.[5] The work done by Norris et al. has discredited, to some extent, previous reports that doping is impossible due to "self-purification" of nanocrystals and has shown that it is possible for dopant ions to reside within the crystals structure rather than reside at surface sites through his use of EPR and photoluminescence measurements.

Additional work on ZnSe doping has been conducted by Suyver et al.[13,14] and has included work on Mn^{2+} and Cu^{2+}. This work has focused attention on understanding the luminescence properties that result from the addition of dopant ions. Photophysical analysis of ZnSe:Mn nanocrystals revealed emission properties characteristic of the dopant ion luminescence in addition to the typical bandgap emission arising from ZnSe.[2,5,13] However, in the case of Cu^{2+}, the emission properties result from the recombination of electrons rather than from the dopant ion luminescence itself, and often results in the observation of red and green emission bands.[14]

Advancements in the field of doping ZnSe occurred when Peng et al. targeted studies at optimizing doping through controlled reaction conditions.[3] The focus of their work was to produce tunable emitting alternatives to more toxic CdSe nanocrystals. Peng et al. employ the use of nucleation doping to achieve tunable emission and particles with enhanced luminescence properties through the uses of Mn^{2+} or Cu^{2+} as a dopant.[15] In these procedures, dopant and host

materials are present at the time of nucleation and the reaction conditions are subsequently tuned to render dopant precursors inactive and allow further growth of host material around dopants.

5.1.2.2 Lanthanide dopants

While a number of studies report the synthesis and photophysical properties resulting from transition metal doped ZnSe nanocrystals, little work has been done on doping these materials with rare earth metals. One particular study by Mathew et al. focuses on examining the effects of Eu^{3+} ions in close proximity with ZnSe nanocrystals. Nanocrystals and Eu^{3+} are placed in a silica matrix and the resulting photophysical properties studied. It was found that in the presence of ZnSe nanocrystals, the lanthanide emission is significantly enhanced.[16] This is the only known work using ZnSe nanocrystals in conjunction with rare earth metals leaving interesting opportunities for advancement of rare earth doped ZnSe materials.

5.2 EXPERIMENTAL

5.2.1 Chemicals

Trioctylphosphine (TOP) (90%), zinc stearate (tech), octadecene (90% tech), tetracosane (99%), europium nitrate (99.99%) and hexadecylamine were purchased from Sigma-Aldrich-Fluka. Sulfur, toluene, and methanol were purchased from Fisher Scientific. Terbium nitrate (99.9%) and dysprosium nitrate (99.9%) were purchased from Strem. N-Hexane and 1-octanol were purchased from Acros and ethyl acetate was purchased from EMD. Argon gas was purchased

from Valley National. All chemicals were used as purchased without purification except toluene, which was distilled over sodium under nitrogen.

5.3 RESULTS/DISCUSSION

5.3.1 Synthesis

The reaction mixture was prepared by dissolving 0.64 mmol zinc stearate, 5.0 g tetracosane, 6.3 mL octadecene, and 0.6 mmol hexadecylamine in a 3 neck round bottom flask heated to 320°C while stirring under argon for approximately 2 hours. After 2 hours, a lanthanide stock solution containing 0.16 mmol $Ln(NO_3)_3$ (Ln = Eu or Tb) dissolved in 2.5 mL of TOP was rapidly injected into the reaction mixture. This was left to stir for an additional hour before a second stock solution containing the anion precursor was injected. The anion precursor, selenium (0.4 mmol), was dissolved in 0.5 mL octadecene diluted with 2 mL TOP and was rapidly injected into the reaction mixture for nucleation to occur. Subsequent growth of the nanocrystals occurred at 300°C. Aliquots were removed from the reaction mixture at varying growth times ranging from 30 seconds to 2 hours. The synthesized nanocrystals were then dissolved in chloroform and their photophysical properties were studied.

Reaction conditions were chosen based on previously studied lanthanide doped nanocrystal systems, in addition to work by Peng et al. on the formation of high quality ZnSe through the activation of zinc precursors.[3] It is suggested that the amine, hexadecylamine was chosen here, attacks the carbonyl group of the stearate to release the carboxylate bound zinc.[3]

5.3.2 Physical characterization

Preliminary XRD studies were performed on ZnSe:Ln nanocrystals to analyze their structure. In Figure 5.1 are depicted XRD patterns for synthesized ZnSe:Tb nanocrystals with corresponding solvent studies for comparison. TOPO does have a crystal structure and will result in an XRD pattern. The broadening of our XRD patterns collected for ZnSe:Tb nanocrystals let us to believe impurities were present. TOPO samples as well as TOPO/TOP mixtures were analyzed using XRD to determine the source of band broadening. Figure 5.1 right depicts a published XRD pattern for ZnSe nanocrystals for comparison.[3] From the data it is observed that the organic passivant layers contribute to the broadening of the diffraction patterns, especially if samples were not extensively dried before measurements were collected and in the case of small nanoparticles. Upon comparison to diffraction patterns of undoped ZnSe published by Peng et al., three characteristic peaks can be observed in the ZnSe:Tb sample that are most likely due to contributions of the ZnSe crystal structure and not the result of crystallization of the TOPO used as the solvent system in the nanocrystal synthesis.[3] The peaks corresponding to ZnSe crystal structure are evidenced using black arrows in Figure 5.1. While additional sharp features somewhat resembling bands are observed in the TOPO and TOPO/TOP samples, they do not lie in the same positions as those found in the ZnSe:Tb sample. In the case of TOPO and TOPO/TOP, the additional features are not easily discriminated from background signal, whereas ZnSe nanocrystals exhibit peaks characteristic of the zinc blende ZnSe crystal structure.

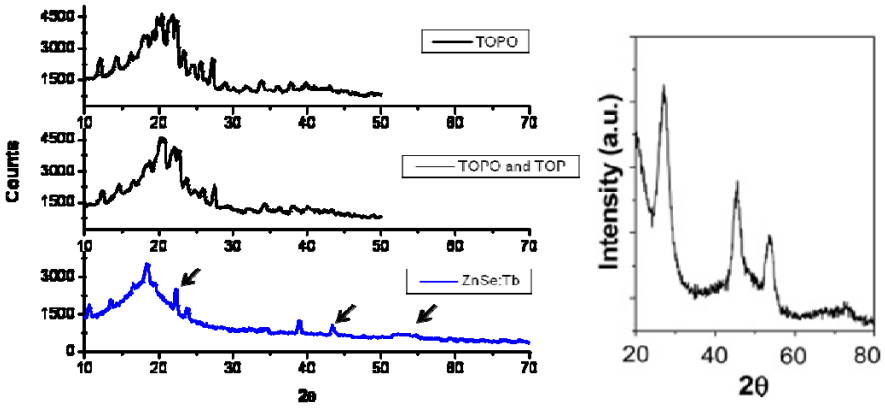

Figure 5.1. XRD patterns of synthesized ZnSe:Tb nanocrystals relative to solvent systems for background (left) and ZnSe nanocrystal XRD pattern observed by Peng et al.[3] illustrating zinc blende crystal structure. Note the black arrows indicating specific peaks in the blue spectra corresponding to synthesized ZnSe:Tb, these correspond to peaks that are also present in Peng et al.'s samples.

TEM images were obtained for ZnSe nanocrystals using a Hitachi H-7100 TEM operating at 75 kV. These measurements were performed through collaboration with Prof. Marcel Bruchez at Carnegie Mellon University and imaging was done by Joseph Suhan. The TEM image is shown in Figure 5.2. Particles with sizes comprised between 5 and 10 nm were obtained. The TEM is low resolution and therefore no conclusions can be made regarding particle crystallinity. Particles are difficult to discriminate from the background signal due to the relatively low electron density of the Zn based particles, the lower the electron density the more difficult imaging becomes.

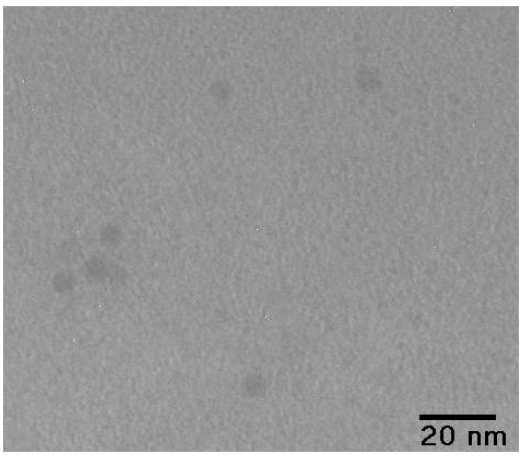

Figure 5.2. Low resolution TEM image obtained through collaboration with Carnegie Mellon University. This image was obtained using a Hitachi H-7100 TEM operated at 75 kV.

5.3.3 Photophysical characterization

UV-vis absorption spectra were collected on ZnSe to determine the presence of the characteristic band resulting from the quantum confinement observed for semiconductor nanocrystals. Figure 5.3 depicts absorbance spectra representative of doped ZnSe nanocrystals. The broad shoulder between 300 and 350 nm represents the first excitation absorption band and is indicative of quantum confinement. The spectra reported here are shifted to slightly higher energy compared to what is observed in the current literature,[3,11,15,17] possibly due to smaller sized particles (higher resolution imaging work is necessary for particle size analysis in these systems) or the effects of addition of dopant ions. The shift in wavelength of this absorbance band with nanocrystal growth time corresponding to increasing nanocrystal size is not as prominent as was observed in CdSe nanocrystals. Peng et al. do report that the ability to produce a variety of different nanocrystal sized through the use of amines is somewhat limited, especially in the case where

reaction temperature and growth temperature are not identical (as is the case for the nanoparticles synthesized here).[3]

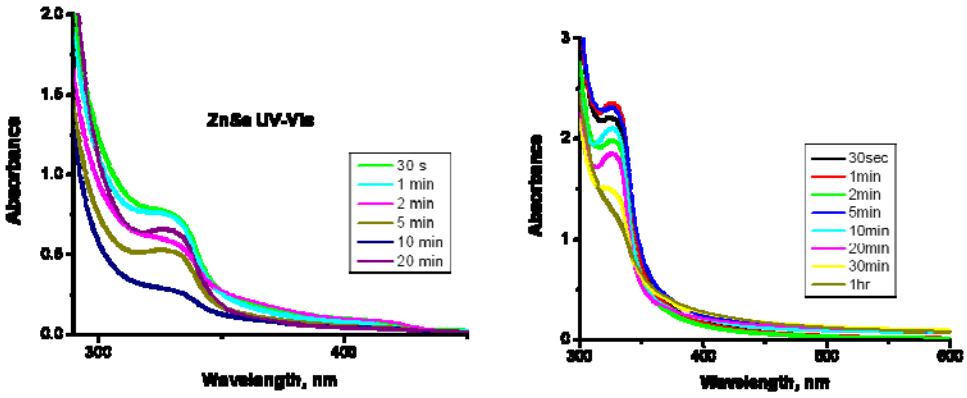

Figure 5.3. UV-vis absorbance spectra for ZnSe nanocrystals in chloroform representing 2 different batches of doped nanocrystals synthesized under the same reaction conditions.

As for all nanocrystal systems discussed thus far, photoluminescence properties of the ZnSe:Ln nanocrystal systems were studied in order to evaluate lanthanide sensitization from the band gap emission. The measurements included comparison of steady state and time-resolved emission and excitation spectra for each of the ZnSe:Ln systems.

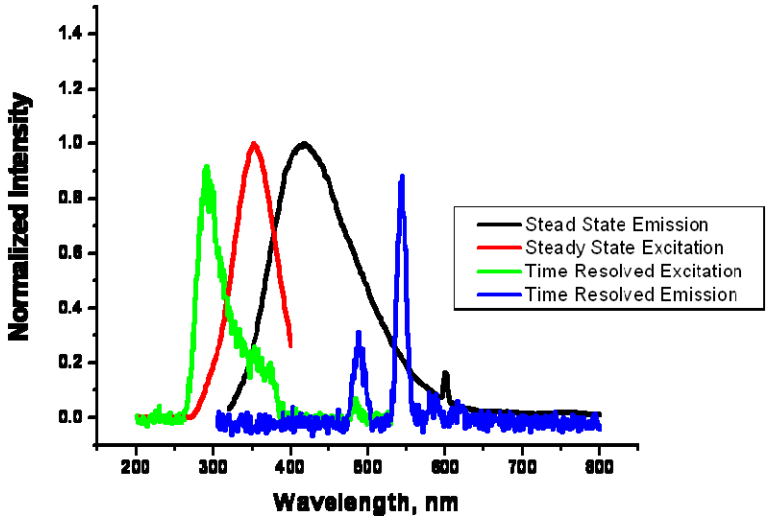

Figure 5.4. Overlay of normalized steady state and time resolved excitation and emission spectra in chloroform. Time resolved spectra were collected using the Varian Cary Eclipse while steady state spectra were collected using the JY Horiba Fluorolog-322.

An overlay of the steady state and time resolved emission and excitation spectra for ZnSe:Tb nanocrystals is shown in Figure 5.4. ZnSe behaves somewhat like CdSe in that the lanthanide emission was not initially observed through steady state measurements, and time resolved analyses were required to discriminate the Tb^{3+} signal. Upon excitation with 300 nm radiation, a characteristic band gap emission is observed in steady-state spectra (black), centered here at approximately 430 nm. Terbium emission (shown in blue) can be discriminated from the band gap emission through time-resolved measurements using a delay time of 0.2 ms. Excitation spectra upon monitoring both the nanocrystal band gap and the Tb^{3+} emission were used for determination of lanthanide sensitization. In order to demonstrate that energy transfer to occur from the band gap emission to the lanthanide, overlap must exist between the excitation spectra. The time-resolved spectra must also not resemble direct excitation profiles (Figure 5.5). In the

case of ZnSe:Tb, the time resolved excitation profile collected upon monitoring the Tb^{3+} emission (green) shows features not present in the direct excitation spectra and does exhibit some spectral overlap with the nanocrystal excitation profile collected in steady state mode (red). This data indicates some degree of lanthanide sensitization.

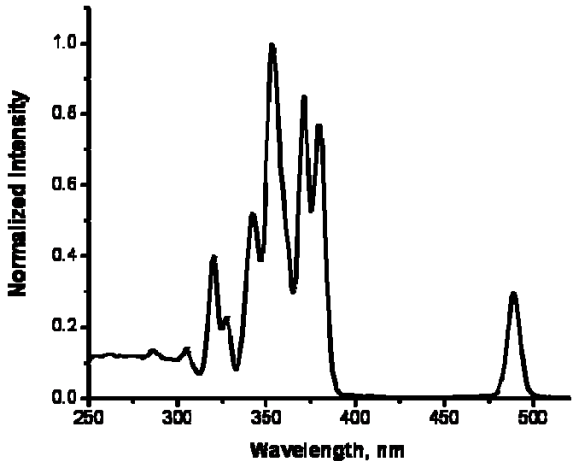

Figure 5.5. Normalized direct excitation profile of Tb^{3+} in solution collected using time resolved mode of the Cary Eclipse ($Tb(NO_3)_3$ in methylene chloride, λ_{em} = 545 nm).

Sensitization of a lanthanide cation is more clear in the case of ZnSe:Eu nanoparticles. As in ZnSe:Tb, a characteristic band gap emission profile is observed in the steady-state emission spectrum (Figure 5.6 left, black). Europium emission can be discriminated through the use of time resolved measurments and is shown in blue. Excitation profiles collected upon monitoring Eu^{3+} and nanocrystal band gap emission were examined for proof of energy transfer. The overlap of these spectra (green and red respectively) is more complete than in the case of ZnSe:Tb. In addition, as seen in the Figure 5.6 right, the direct excitation profile of Eu^{3+}, shown

in gray, does not dominate the excitation profile of Eu^{3+} within ZnSe. This is further proof that an alternative energy pathway other than direct excitation of the Eu^{3+} does take place.

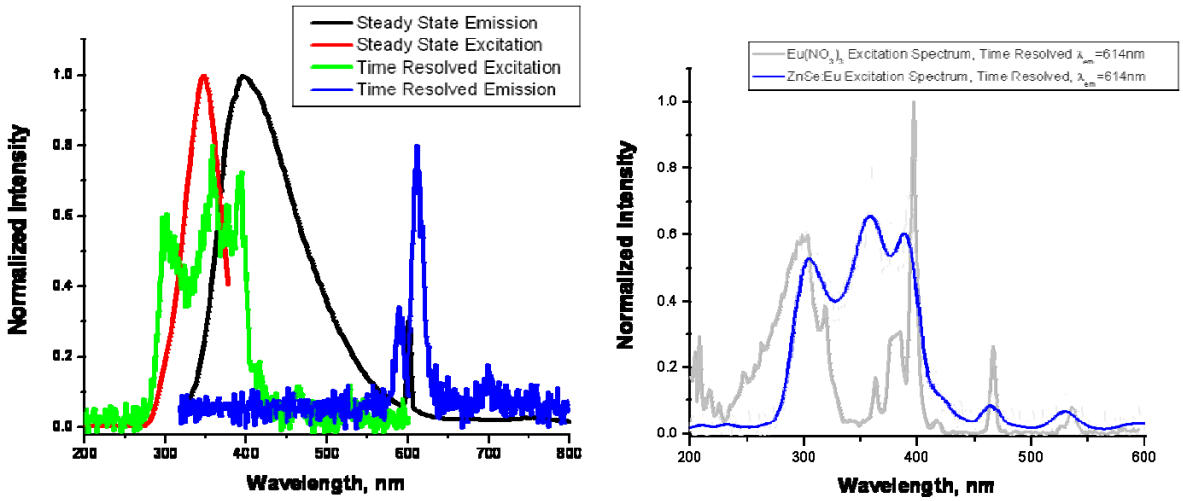

Figure 5.6. (Left) Overlay of normalized steady state emission and excitation spectra collected using the JY Horiba Fluorolog-322 and time resolved excitation and emission using the Cary Eclipse. ZnS:Tb nanocrystals were dissolved in chloroform (λ_{ex} = 300 nm, λ_{em} = 614 nm (green) and λ_{em} = 410 nm (red). (Right) An overlay of Eu^{3+} excitation profile within of the ZnSe:Eu nanocrsytal and the direct excitation profile of Eu^{3+} in solution.

The spectroscopic data shown above were improved upon through slight modifications of the synthetic conditions (initial reaction conditions involved only addition of TOP to the Selenium precursor, the ODE was added in subsequent reactions). Upon addition of more TOP, steady state lanthanide emission, albeit weak, was observed in the case of ZnSe:Tb and ZnSe:Eu, shown in Figures 5.7, 5.8, and 5.9 below. Figure 5.7 (left) demonstrates a slight shift in emission maximum with reaction time. This shift correlates to some degree with the intensity of the steady state lanthanide signal. More intense Tb^{3+} signal was observed for reaction times of 1 and

2 minutes post nucleation. The 2 minute growth time shown in green exhibits the greatest red shift in emission maximum as well as the most intense Tb^{3+} emission band centered at 545 nm. An overlay of steady state and time resolved emission and excitation profiles indicate additional benefits to the modified reaction system. The excitation profiles upon monitoring the Tb^{3+} emission (green) and the nanocrystal band gap emission (red) exhibit greater overlap than in the previous system. This observation coupled with the emergence of steady state emission of Tb^{3+} indicates improved energy transfer.

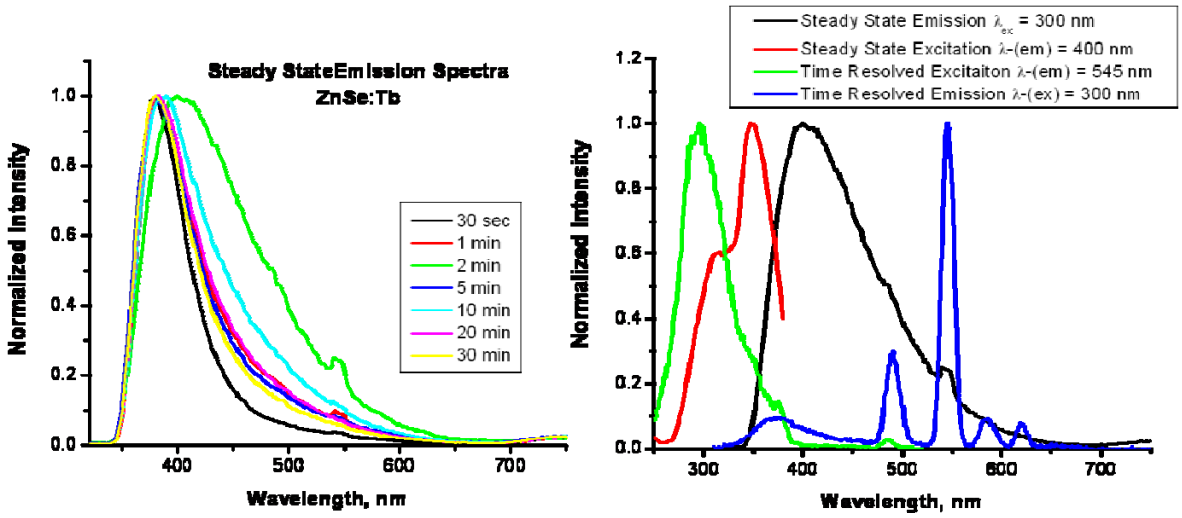

Figure 5.7. (Left) Normalized steady state emission spectra of ZnSe:Tb nanocrystals over growth times ranging from 30 seconds to 30 minutes. ZnSe:Tb nanocrystals were dissolved in chloroform (λ_{ex} = 300 nm). (Right) Overlay of steady state and time resolved emission and excitation profiles of ZnSe:Tb nanocrystals.

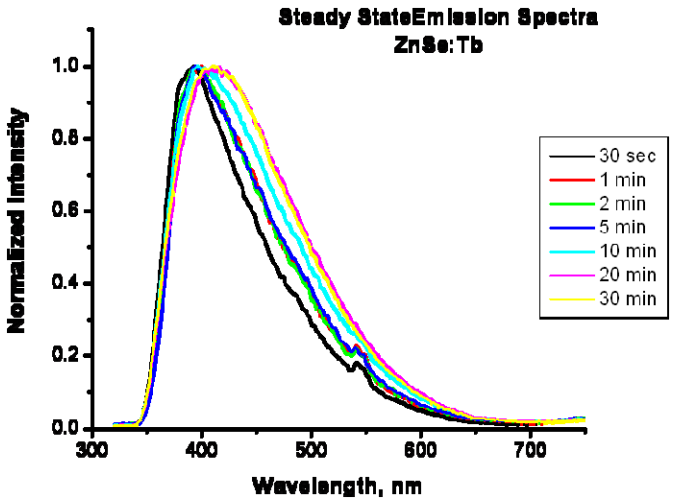

Figure 5.8. Normalized emission spectra of additional batch of ZnSe:Tb nanocrystals exhibiting improved lanthanide luminescence. ZnSe:Tb nanocrystals were dissolved in chloroform (λ_{ex} = 300 nm). Shorter growth times appear to be optimal for lanthanide emission through steady state measurements as observed from the presence of the Tb3+ narrow emission band at 545nm in addition to the bandgap emission.

Similar findings were observed for ZnSe:Eu nanocrystals as well. The overlay of their steady state and time resolved emission and excitation spectra also reveal improved luminescence properties, Figure 5.9. A faint Eu^{3+} emission band is observed at 614 nm upon recording steady state emission (green). Overlap of the excitation profiles upon monitoring Eu^{3+} and nanocrystal band gap emission also exhibit better overlap (blue and black), again indicating improved energy transfer.

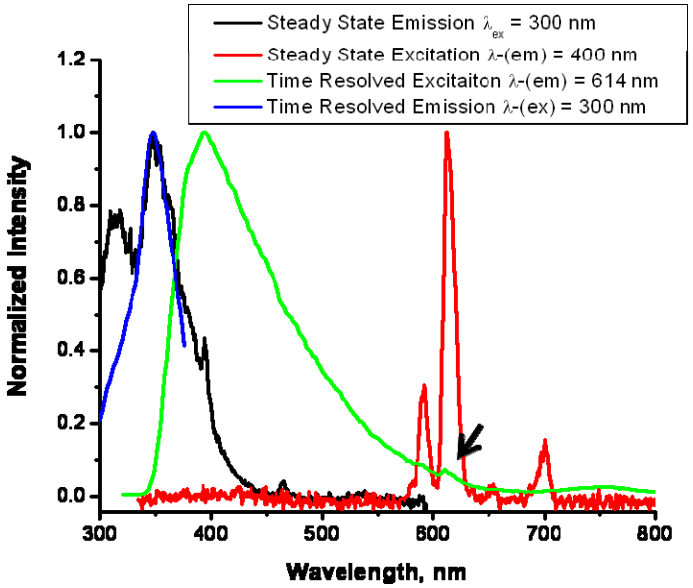

Figure 5.9. Overlay of normalized steady state and time resolved emission and excitation spectra for ZnSe:Eu nanocrystals in chloroform.

Luminescence lifetimes were collected for both ZnSe:Tb and ZnSe:Eu nanocrystal systems. The excitation was performed on the band gap absorption of the ZnSe nanocrystals and the emission of the specific lanthanide cations was selected with the help of a monochromoator. For both types of nanocrystals, the experimental exponential decay was best fitted as a combination of two single exponential decays. The final results are reported in the Table 5.2. Luminescence lifetimes of Tb^{3+} and Eu^{3+} within the nanocrystals were compared to lifetime values of well protected lanthanide complexes in solution reported in the literature by Petoud et al. (reported in Table 5.2).[18] Terbium and europium lifetimes are significantly improved at sites within the nanocrystal structure (represented by the longest component of the biexponential fit). These values are more than double the values reported in the literature. This increase can be explained by the use of the nanocrystal structure to completely encapsulate and protect the

lanthanide cations against non-radiative deactivations. Nanocrystals possess only low energy lattice vibrations, unlike the strongly quenching high frequency vibrations of organic molecules present in the H22IAM lanthanide complexes.

Table 5.2. Measured luminescence lifetimes for ZnSe:Tb and ZnSe:Eu nanocrystal systems in chloroform versus lanthanide complexes synthesized by Petoud et al in methanol.[18] Excitation wavelengths used are as follows: ZnSe nanocrystals λ_{ex} = 354, TbR(+)BnMeH22IAM λ_{ex} = 354 nm, EuR(+)BnMeH22IAM λ_{ex} = 347 nm.

Sample	τ1 (ms)	τ2 (ms)
ZnSe:Tb	3.15 ± 0.18	0.790 ± 0.003
ZnSe:Eu	2.71 ± 0.67	1.22 ± 0.27
TbR(+)BnMeH22IAM	1.27 ± 0.12	-
EuR(+)BnMeH22IAM	0.78 ± 0.09	-

The two different lifetimes observed in the nanocrystal systems most likely correspond to two different lanthanide environments within the nanocrystal structure. The longer lived values of 3.15 ms and 2.71 ms for Tb^{3+} and Eu^{3+} respectively can be attributed to lanthanide cations well protected by the nanocrystal structure at internal sites. The shorter lived components are due to lanthanide cations residing at the surface of the nanocrystals which are exposed to the solvent vibrations. These values are comparable to values obtained for the CdSe:Ln and ZnS:Ln nanocrystal systems (Table 5.3). All 3 nanocrystal systems (CdSe:Ln, ZnS:Ln, and ZnSe:Ln) systems possess a biexponential luminescence decay, illustrating well protected lanthanide cations with lifetimes in the ms range.

Table 5.3. Summary of all luminescence lifetime values measured for all lanthanide containing nanocrystal systems studied. ZnSe and ZnS nanocrystals were dissolved in chloroform while CdSe nanocrystals were dissolved in toluene (λ_{ex} = 354 nm)

Sample	τ1 (ms)	τ2 (ms)
ZnS:Tb	2.50 ± 0.06	0.92 ± 0.01
CdSe:Tb	4.7 ± 0.2	2.02 ± 0.06
ZnSe:Tb	3.15 ± 0.18	0.79 ± 0.0031
ZnS:Eu	3.6 ± 0.15	2.0 ± 0.014
CdSe:Eu	2.8 ± 0.21	1.26 ± 0.24
ZnSe:Eu	2.71 ± 0.67	1.22 ± 0.27

The lanthanide centered quantum yields were measured to quantify the efficiency of energy transfer within these systems as well as the non-radiative deactivation. Since only band gap emission was observed through steady-state measurements, quantum yield values had to be calculated from time-resolved spectra. The excitation was performed on the electronic band gap levels of the nanocrystals and was analyzed on the signals arising from the lanthanide cations. Values for CdSe:Tb, ZnS:Tb and ZnSe:Tb lanthanide centered quantum yields measured at room temperature are reported in Table 5.4. The quantum yield for ZnSe:Tb was calculated to be 1.8 (± 0.7)E-04. This value indicates an improvement in comparison to the value of 1.5 (± 0.03)E-05 observed for CdSe:Tb, but is still significantly lower than the quantum yield obtained for ZnS:Tb. The ZnSe:Tb nanocrystals do illustrate improved luminescence properties over their CdSe:Tb counterparts, however they still pale in comparison the properties obtained for ZnS:Tb.

As discussed in previous lanthanide containing semiconductor nanocrystals chapter, the low quantum yield values relative to literature values (0.63 and 0.025 for Tb^{3+} and Eu^{3+} respectively) are compensated for by the formation of a polymetallic species. Since the level of protection of the lanthanide cations by the nanocrystal structure is comparable for the different types of nanocrystals, these quantum yields values mainly represent the efficiency of energy transfer occurring within the nanocrystals.

Based on the fact that ZnSe's band gap (2.7 eV) lies between the band gap energies for CdSe (1.75 eV) and ZnS (3.54 eV), the efficiency can be hypothesized to be intermediate between the previously reported data for ZnS:Ln and CdSe:Ln systems.

Table 5.4. Lanthanide centered quantum yield values for all lanthanide containing nanocrystal systems studied. CdSe:Tb quantum yields were collected in toluene (λ_{ex} = 300nm, 305 nm, and 310 nm) through time resolved measurements. ZnS:Tb quantum yields were collected in chloroform (λ_{ex} 315 nm, 320 nm, 325 nm) through steady state measurements. ZnSe:Tb quantum yields were collected in chloroform (λ_{ex} 315 nm, 320 nm, 325 nm) through time resolved measurements.

Sample	Lanthanide Centered ϕ
CdSe:Tb	1.50E-05 ± 0.03E-05
ZnS:Tb	5.1E-02 ± 5.6E-03
ZnSe:Tb	1.8E-04 ± 7.3E-05

5.4 CONCLUSION AND FUTURE DIRECTIONS

ZnSe nanocrystals offer many comparable advantages over organic sensitizers as other doped nanocrystal systems described herein. These materials are small, blue-UV emitting materials with band gap energies suited for energy transfer to the accepting levels of lanthanide cations. The use of Zn^{2+} containing nanocrystals has become more attractive as increasing concerns regarding CdSe nanocrystal toxicity arise. Lanthanide cations are well protected by the crystal structure as evident by the long luminescence lifetimes. Quantum yields are somewhat lower than what is observed for systems employing organic ligands as lanthanide sensitizer; however this limitation is overcome by the formation of a polymetallic species with several emitters rather than a single lanthanide cation.

ZnSe has been demonstrated to sensitize to some degree both visible emitting Eu^{3+} and Tb^{3+}. In order to more completely understand the level of sensitization within these systems further lifetime and quantum yield studies need be conducted and comparisons need made to undoped and Gd^{3+} doped nanocrystal systems. Also, only preliminary work was done on the use of Dy and Sm as dopants within the ZnSe host material. Successful doping with these cations should be possible and sensitization should be achievable based on the energy of their accepting levels.

From the data provided, nanocrystalline ZnSe appears to be an attractive sensitizer for luminescent lanthanide cations and does show improvements over previously reported CdSe systems, at least in the case of Tb^{3+}. These systems have been tuned to exhibit steady state lanthanide emission properties unlike CdSe nanocrystal systems. The efficiency of energy transfer is hypothesized to be somewhat more efficient based on this new spectral feature (the

appearance of steady state Tb^{3+} emission) in comparison to CdSe nanocrystals. In addition, improved overlap of the excitation profiles upon monitoring lanthanide and band gap emission through modification of synthetic procedures has shown that the degree of sensitization within these materials can be tuned through reaction conditions.

Information regarding lanthanide location within the nanocrystal structure must also be gathered in order to establish a good rationale between the structure and luminescence properties of these nanocrystals. This can be inferred from measurements such as EELS, Atomic Number Contrast Scanning Electron Microscopy (Z-STEM) and SQUID. ICP and EDAX measurements can be performed to determine the ratios of Zn, Se, and Ln within these systems and gain an understanding of actually dopant (either surface or interior sites) percentage of the nanocrystals and their influence on the luminescence properties of these nanocrystals.

As with previous reported nanocrystal systems, surface modification of ZnSe nanocrystals should also be explored. These materials have efficiencies lying between CdSe and ZnS nanocrystals and it should be explored whether or not surface modifications affect all systems in the same manner. Capping these materials with either wider band gap material shells, such as ZnS, or additional layers of ZnSe can be explored to determine extent of protection within these systems and to further optimize luminescence properties and eliminate surface lanthanide sites. Water solubility will make these materials attractive for use in bioanalytical and bioimaging applications.

5.5 REFERENCES

(1) Norris, D. J.; Yao, N.; Charnock, F. T.; Kennedy, T. A. *Nano Lett.* **2001**, *1*, 3-7.

(2) Norman, T. J.; Magana, D.; Wilson, T.; Burns, C.; Zhang, J. Z.; Cao, D.; Bridges, F. *J. Phys. Chem. B: At. Mol. Opt. Phys.* **2003**, *107*, 6309 - 6317.

(3) Li, L. S.; Pradhan, N.; Wang, Y.; Peng, X. *Nano Lett.* **2004**, *4*, 2261-2264.

(4) Erwin, S. C.; Zu, L.; Haftel, M. I.; Efros, A. L.; Kennedy, T. A.; Norris, D. J. *Nature* **2005**, *436*, 91-94.

(5) Zu, L.; Norris, D. J.; Kennedy, T. A.; Erwin, S. C.; Efros, A. L. *Nano Lett.* **2006**, *6*, 334-340.

(6) Yang, C. C.; Li, S. *J. Phys. Chem. C: solid State Phys.* **2008**, *112*, 2851 - 2856.

(7) Chengelis, D. A.; Yingling, A. M.; Badger, P. D.; Shade, C. M.; Petoud, S. *J. Am. Chem. Soc.* **2005**, *127*, 16752-16753.

(8) Reiss, P.; Bleuse, J.; Pron, A. *Nano Lett.* **2002**, *2*, 781 - 784.

(9) Danek, M.; Jensen, K. F.; Murray, C. B.; Bawendi, M. G. *Chem. Mater.* **1996**, *8*, 173 - 180.

(10) Costa-Fernandez, J. M.; Periero, R.; Sanz-Medel, A. *Trends Anal. Chem.* **2006**, *25*, 207 - 218.

(11) Hines, M. A.; Guyot-Sionnest, P. *J. Phys. Chem. B: At. Mol. Opt. Phys.* **1998**, *102*, 3655 - 3657.

(12) Lu, S. W.; Lee, B. I.; Wang, Z. L.; Tong, W.; Wagner, B. K.; Park, W.; Summers, C. J. *J. Lumin.* **2001**, *92*, 73 - 78.

(13) Suyver, J. F.; Wuister, S. F.; Kelly, J. J.; Meijerink, A. *Phys. Chem. Chem. Phys.* **2000**, *2*, 5445-5448.

(14) Suyver, J. F.; van der Beek, T.; Wuister, S. F.; Kelly, J. J.; Meijerink, A. *Appl. Phys. Lett.* **2001**, *79*, 4222 - 4224.

(15) Pradhan, N.; Goorskey, D.; Thessing, J.; Peng, X. *J. Am. Chem. Soc.* **2005**, *127*, 17586-17587.

(16) Mathew, S.; Rejikumar, P. R.; Joseph, X.; Unnikrishnan, N. V. *Opt. Mater.* **2007**, *29*, 1689 - 1692.

(17) Pradhan, N.; Battaglia, D. M.; Liu, Y.; Peng, X. *Nano Lett.* **2007**, *7*, 312 - 317.

(18) Petoud, S.; Muller, G.; Moore, E. G.; Xu, J.; Sokolnicki, J.; Riehl, J. P.; Le, U. N.; Cohen, S. M.; Raymond, K. N. *J. Am. Chem. Soc.* **2006**, *129*, 77 - 83.

6.0 LNS NANOCRYSTALS

We have previously shown that the structure of semiconductor nanocrystals can be used to sensitize and protect luminescent lanthanide cations. Due to the forbidden nature of the f-f transitions that are responsible for the visible and near infrared emission of lanthanides, the free cations have low absorption that limits the number of emitted photons. In order to overcome this limitation, we need to design antennae that must harvest as much light as possible and convert the resulting energy to the lanthanide cations. We have previously discussed the use of semiconductor CdSe, ZnS, and ZnSe nanocrystals for the sensitization of lanthanide cations.

LnS materials possess larger band gap energies than the semiconductor nanoparticles previously used to sensitize luminescent lanthanide cations. We hypothesized that this wider band gap will allow for the more efficient sensitization over previously reported systems as the energy levels between donating levels of the semiconductor nanocrystals and the accepting levels of lanthanide cations have a better match, a favorable condition for the design of efficient antennae for a broader range of lanthanide cations. From the design and synthetic point of view, the advantage of this type of nanocrystal in comparison to those we have described in the previous chapters (CdSe, ZnS, and ZnSe) is that only two components are involved in their synthesis instead of the three used in all others. This will allow for easier control of the properties of the luminescent nanoparticles based on their composition. Simplified synthetic schemes allows for better control of resulting materials leading to enhanced photophysical properties.

In addition, such nanocrystal can accommodate a larger number of lanthanide cations per unit of volume since it is part of the nanocrystal itself and is not a dopant. The larger number of lanthanide cations will induce the emission of a larger number of photons per unit of volume, an important advantage for sensitive detection. To date the only LnS system that has been described in the literature is bulk materials or nanomaterials studied mainly for their magnetic properties.[1-7] This report constitutes the first demonstration of the use of LnS band gaps as antennae for lanthanide cations and the first report for the sensitization of a NIR emitting lanthanide cation.

6.1 CURRENT WORK ON LNS

Studies of lanthanide chalcogenides have been conducted since the 1960s,[8-11] however it is only recently that the possibility of Ln_xS_y materials in general exhibiting quantum confinement effects in crystals on the nanometer size regime has been investigated.[6,12,13] These materials show potential for application as solar energy absorbers and for use in photovoltaic cells.[10,14] Gruber et al. have extensively studied bulk Ln_2S_3 materials and have demonstrated their ability to serve as semiconductors.[9,11] The rare earth sulfides are expected to serve as semiconductors with heavy concentration of the lanthanide energy levels spanning the band gap of the material.

Within the Ln_2S_3 materials, it has been found that 1/9 of the lanthanide positions within the crystal structure are randomly unoccupied. These vacancies can be filled with Ln^{3+} ions up to ratios of 3:4 Ln:S. The addition of Ln^{3+} provides additional free electrons, further enhancing their properties.[11]

Studies on the periodicity of Ln_2S_3 materials have been performed by Prokofiev et al. in the mid 1990s.[8] Their findings illustrate that Ln_2S_3 materials serve as insulators or wide band

gap semiconductors. The band gaps of these materials are formed by the p states of the sulfur (valence band) and the 5d(6s) states of the lanthanide ions (conduction band). The f bands are suggested to lie within or below the valence band of the material. Literature from the 1960s by Kurnick et al.[15] suggests band gaps of Ln_2S_3 to vary from 2.5 to 2.8 eV from right to left across the period.

In addition to Ln_2S_3 materials, LnS materials formed with a 1:1 stoichiometry, particularly EuS has been thoroughly examined in the literature. EuS is attractive for its photophysical and magnetic properties.[3-6,12,13]Unlike the Ln_2S_3 systems where europium is in the trivalent oxidation state, these systems adopt the 2+ state for the material formation and quickly oxidize to the 3^+ state when exposed to air. Hasegawa et al. have synthesized EuS nanoparticles of high crystallinity and thoroughly studied their size dependent properties.[1,3,4,16] They were the first to report quantum size effects on the band gap, reporting absorbance shift with particle size.[2] These studies followed reports by Hines et al. where EuS nanoparticles were synthesized successfully with no quantum confinement effects observed.[12] While initial studies of EuS report no emission or excitation properties for the nanoparticles, more recent work has shown a broad emission band centered between 350 and 425 nm, with no observed Eu^{3+} emission. This broad emission band is the result of the nanocrystal band gap formation corresponding to wide band gap energy.[3,4] This is confirmed through the work by Hasegawa et al. whom have illustrated that the band gap energy of EuS nanoparticles is 3.1 eV, much wider than the observed 1.7 eV found in bulk material.

6.2 EXPERIMENTAL

6.2.1 Chemicals

Europium acetate (99.9%), terbium acetate (99.9%), ytterbium acetate (99.9%), neodymium acetate (99.9%), erbium acetate (99.9%), trioctyophosphine (90%)[TOP], and trioctyophosphine oxide (90%) [TOPO] were purchased from Sigma-Aldrich-Fluka. Sulfur powder was purchased from Fisher Scientific. Nitric acid (ACS grade) was purchased from Mallinckrodt. Deionized water (reagent grade, type I) was purchased from Ricca Chemical Company. Diethylenetriminepentaacetic acid (DTPA) was purchased from Acros Organics and potassium hydroxide and hydrogen peroxide (30%) were purchased from J.T. Baker. All chemicals were used without further purification.

6.3 RESULTS/DISCUSSION

6.3.1 Synthesis

The lanthanide acetate (0.8 mmol) was placed in a round bottom reaction vessel with 10 mmol TOPO and 1.5 mL TOP. The reaction vessel was sealed and placed under nitrogen while heating to 300°C during gentle stirring for approximately 2 hours to allow complete dissolution of the lanthanide precursor. A sulfur stock solution was simultaneously prepared by dissolving 0.4 mmol of sulfur in 1.0 mL of TOP. Once the reaction mixture was transparent the sulfur stock solution was rapidly injected and aliquots were removed at specific growth times. The raw

nanocrystals were dissolved in chloroform and their physical and photophysical properties studied.

It is important to notice that while some syntheses of EuS nanoparticles have been reported in the literature,[1-6,12,13] the synthetic conditions described herein are more closely related to the high temperature organometallic methods which have become commonly employed for the synthesis of CdSe and ZnS nanocrystals. Previously published methods include the use of relatively complicated single source of dithiocarbamate precursors which require elaborate synthetic methods for their preparation[3-6,12] and reaction of europium metal with thiourea.[2] The materials obtained from these procedures previously found in the literature have different photophysical properties than those obtained with our synthetic protocol.

6.3.2 Surface modification

In order to render these nanoparticles water soluble, surface exchanges were performed using DTPA as a ligand. The assumption was that the DTPA would bind to lanthanide cations at the nanocrystal surface. A DTPA stock solution was prepared by dissolving 1.0 g of DTPA in 20 mL of deionized water through deprotonation with 5 molar equivalents of KOH (5:1 equivalents of KOH:DTPA allowed for deprotonation of all acidic protons, resulting in a complex with available binding sites for attachment to the nanocrystal surface).

The following procedure was performed on raw nanocrystals as well as nanocrystal that had undergone one round of purification via methanol precipitation (raw nanocrystals dissolved in chloroform were precipitated with excess methanol to remove unwanted biproducts of the initial reaction and then redissolved in chloroform for analysis). Nanocrystals were dissolved in a minimal amount of chloroform resulting in concentrated solutions. An excess of the aqueous

DTPA stock solution (determined by calculating molar concentration of DTPA solution relative to initial concentration of terbium and sulfur in the reaction mixture during synthesis – DTPA was present at a 2.5 mmol concentration indicating a large excess relative to the 0.8 mmol of terbium and 0.4 mmol of sulfur prior to the formation of nanocrystals) was then added to the nanocrystals in chloroform. The samples were sonicated for 2 hours to ensure interaction of the aqueous and organic phases. After sonication, samples were centrifuged to separate the layers. The aqueous phase was removed for analysis. In some instances these procedures resulted in very dilute aqueous DTPA coated nanocrystal samples in which case samples were concentrated by removal of water via standard vacuum techniques.

Success of the DTPA surface exchange was monitored using infrared spectroscopy. The IR data, shown in Figure 6.1, confirm that the TOPO passivation has been replaced by DTPA. The absorption bands assigned to the original nanocrystal surface passivant located at 2932 cm^{-1} and 2856 cm^{-1} (present in both the TOPO and the TOPO TbS spectra) are no longer present in the DTPA coated samples indicating modification of the surface structure. Differences between the DTPA and DTPA TbS spectra are attributed to the deprotonated version being used in the surface modification. Luminescence spectra of the aqueous phase were analyzed to confirm the presence of the band gap and lanthanide emission bands thus confirming confirm the presence of these nanocrystals in the aqueous solution and the success of the coating process. Another confirmation of the presence of LnS nanocrystals in solution was done through the HRTEM measurements where the sample grids were prepared from aqueous solution.

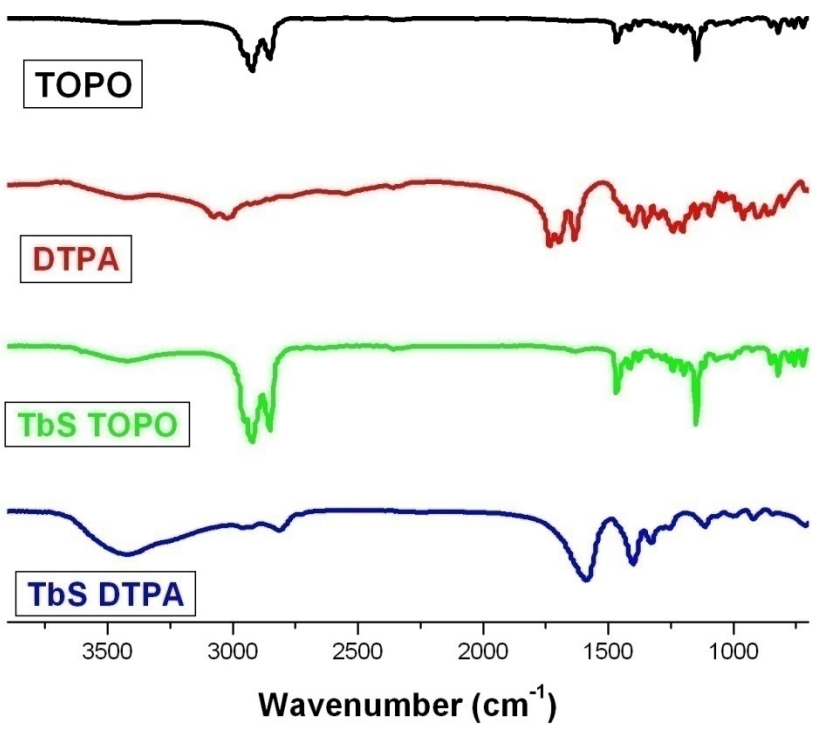

Figure 6.1. FTIR spectra of TbS passivated with TOPO compared to TbS passivated with DTPA. TOPO and DTPA alone were also analyzed for comparison. Samples were prepared by mixing TbS that had been purified and dried with KBr to form pellets.

In addition to surface exchange of TOPO by DTPA, we tested other procedures to coat the LnS nanocrystals such as the encapsulation of the nanocrystals within a ZnS shell to obtain LnS/ZnS core/shell nanocrystals. These procedures were adapted from the core/shell methods used to synthesize CdSe/ZnS nanocrystals.[17,18] Raw LnS nanocrystals were added to round bottom flask containing a mixture of TOPO (5.0 g) and HDA (2.5 g). The flask was placed in a glovebox and heated to between 140 and 220 °C, the maximum temperature depending upon the initial size of the core nanocrystals. Based on the measured size of our nanoparticles (~5 nm), temperatures of 220°C were used.[17] The amount of Zn/S precursors that were required to

produce the shell was determined using the total molar ratio of Ln/S present in the initial reaction mixture (the overall ratio of LnS:ZnS should be 1:4). Equimolar amounts of Zn and S precursors were used in the form of diethylzinc and hexamethyldisilthiane. The Zn/S precursors were measured out and dissolved in 3 mL of TOP in an addition funnel. Once the core nanocrystal solution reached the desired temperature, the shell stock solution was slowly added. Aliquots of the core/shell reaction mixture were removed and dissolved in chloroform for the analysis of spectral properties.

6.3.3 Physical characterization

Transmission electron microscopy was used to confirm the presence on nanoparticle, the particle crystallinity, and the overall size distribution. Lower resolution TEM images allowed for size distribution (calculated using Image J software)[19] and particle shape determination, while high resolution TEM images were obtained to prove crystallinity within these nanoparticle systems. In addition to using TEM for imaging purposes, the HRTEM was equipped to perform EDAX on the nanocrystal samples and attempts were made to obtain information regarding nanocrystal composition.

We were able to successfully obtain TEM images and EDAX data for four LnS nanocrystal systems obtained with four different lanthanides: TbS, EuS, NdS, and YbS. The images are depicted below (Figures 6.2 - 6.5) and illustrate size distribution, shape, and crystallinity of these nanocrystal systems. The TEM images below were successfully obtained after several modifications of grid preparation protocols. Initial imaging was performed using Ted Pella 300 mesh copper grids with 50 angstrom carbon coating as a support. The samples were prepared using two different methods: (1) aerating samples through use of a nebulizer and

(2) dropping and wicking of sample onto the grid. Early attempts at TEM yielded no images for several reasons. First, the overall TEM sample was too thick given the amount of sample and thickness of the copper grid. A second explanation is that the contrast between the background and the particles was not sufficient enough to observe any nanocrystalline material. To address the first issue, the grids used were switched to Ted Pella 400 mesh Ultrathin Carbon coated copper grids. Grids were prepared in the same way, both aerated and drop and wick procedures. It is standard to remove Formvar coating which protects the copper grids before use and so this was applied to our sample preparation. It was found through systematic study that the Formvar coating was essential to obtain proper contrast between particles and background. Nanocrystal samples prepared using drop and wick procedures were found to result in higher quality TEM and they were therefore adopted as the standard method for further sample preparation of the LnS nanocrystals.

In addition to problems resulting from grid preparation, other problems arose due to thickness and composition of the nanocrystal samples. Initial grid preparation was performed using TOPO passivated nanocrystals. The excess TOPO in these materials resulted in the blurring of the TEM images due to the presence of the large amount of carbon material and procedures were required to further purify nanoparticles (see Appendix E). Initial precipitation purification methods yielded little success and it was therefore necessary to develop surface exchange procedures to purify the particles. DTPA was chosen as an alternative passivant because of its size and multidentate binding abilities. The procedures for coating are described above. This method of purification, which has the additional advantage of rendering particles water soluble, has been found to be essential in order to obtain high quality TEM images. All samples shown below were obtained using DTPA coated samples prepared on Formvar coated

Ted Pella 400 mesh Ultrathin Carbon coated copper grids using drop and wick preparation methods.

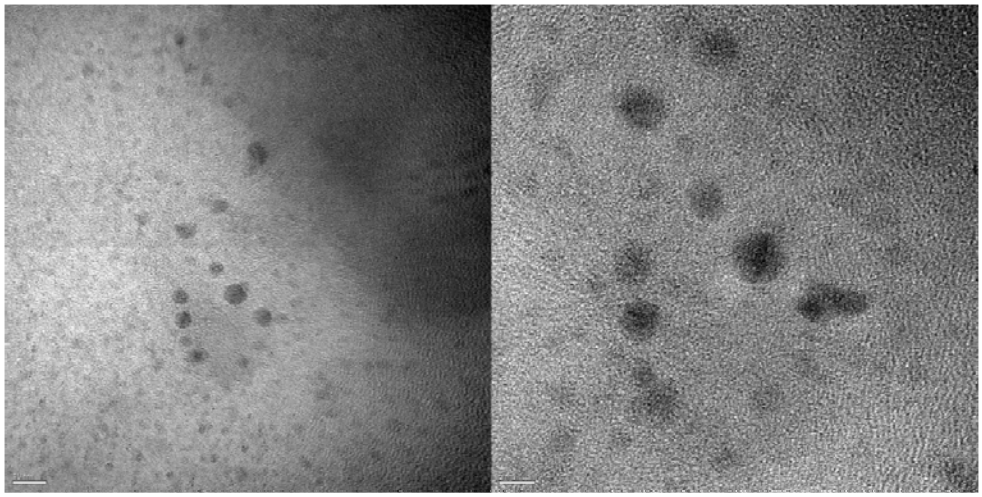

Figure 6.2. High resolution TEM images of TbS nanocrystals collected at differing magnification to determine size distribution and particle crystallinity. Bar scale represent 5 nm.

The TbS nanocrystals are slightly larger than the other lanthanide containing nanocrystal systems that we have developed previously (2-3 nm diameters for CdSe and 3.3nm ± 0.4 nm for ZnS), with nanoparticle diameters averaging approximately 5 nm (see Table 6.1 below). Nanoparticles appear to be somewhat monodisperse and adopt a slightly elliptical shape (Figures 6.2 and 6.3). While some of the nanoparticles in the image above do seem to deviate from the reported size distribution (4.7 ± 0.51 nm in Figure 2) shown in Table 6.1, it should be noted that depth of field and spot size were not defined for this image. The appearance of a broad size distribution in the picture on the left is most likely the result of particles located at different depths or in different orientation on the copper grid.

Higher resolution images of TbS nanocrystals with greater contrast from background have been obtained for larger particles, corresponding to longer growth times. These particles are illustrated in Figure 6.3 and exhibit size distributions of 10.5 ± 0.6 nm.

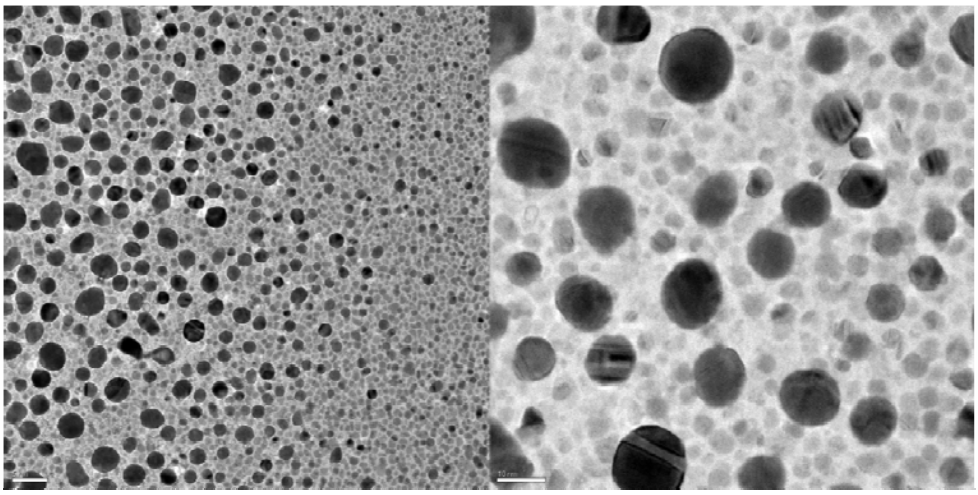

Figure 6.3. High resolution TEM images of TbS nanocrystals collected at differing magnification to determine size distribution and particle crystallinity. Bar scale represent 10 nm.

EuS nanocrystals were also characterized via HRTEM and the images are shown in Figure 6.4. Again, these materials produce nanometer sized crystalline structures. These particles are fairly monodisperse having a calculated size of 5.72 ± 1.56 nm diameters (see Table 6.1). The image on the left is taken at lower magnification to analyze size dispersity, while the image on the right depicts higher magnification imaging for information on crystallinity. It is difficult to determine from these images whether aggregates of particles are formed or whether they just give the illusion of aggregates based on sample thickness.

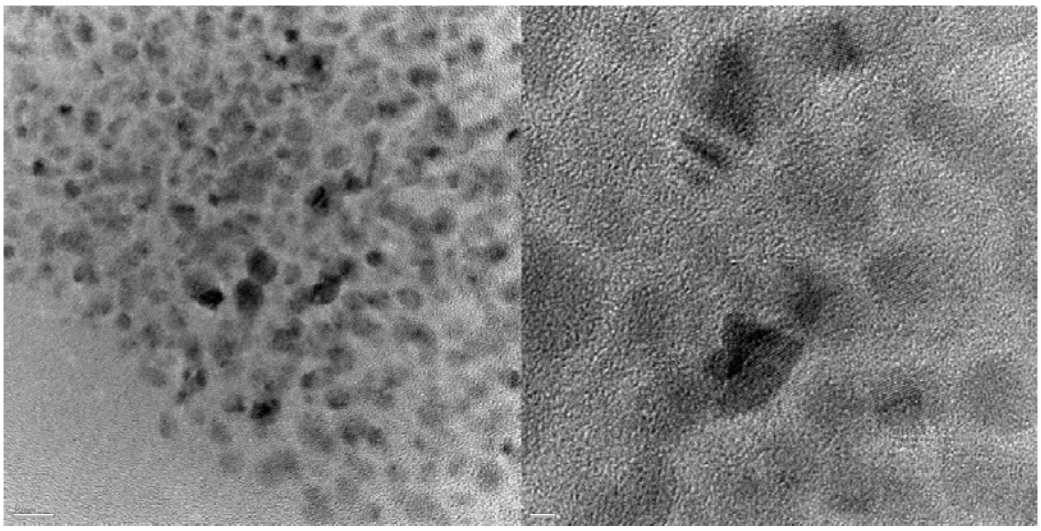

Figure 6.4. High resolution TEM images of EuS nanocrystals taken at differing magnification to determine particle size distribution and crystallinity. Size bar in left image represents 10 nm while bar in right image represents 2 nm.

The YbS nanocrystal images also illustrate fairly monodisperse samples (Figure 6.5) which have calculated diameters of 4.86 ± 0.66 nm (Table 6.1). It is unclear from the image above whether nanocrystals are beginning to aggregate or simply lie at different depths within the sample and artificially appear on top of one another. Both the image on the left and right were obtained through HRTEM, however the right image was taken at higher magnification to obtain better resolution image to analyze the nanoparticle crystallinity.

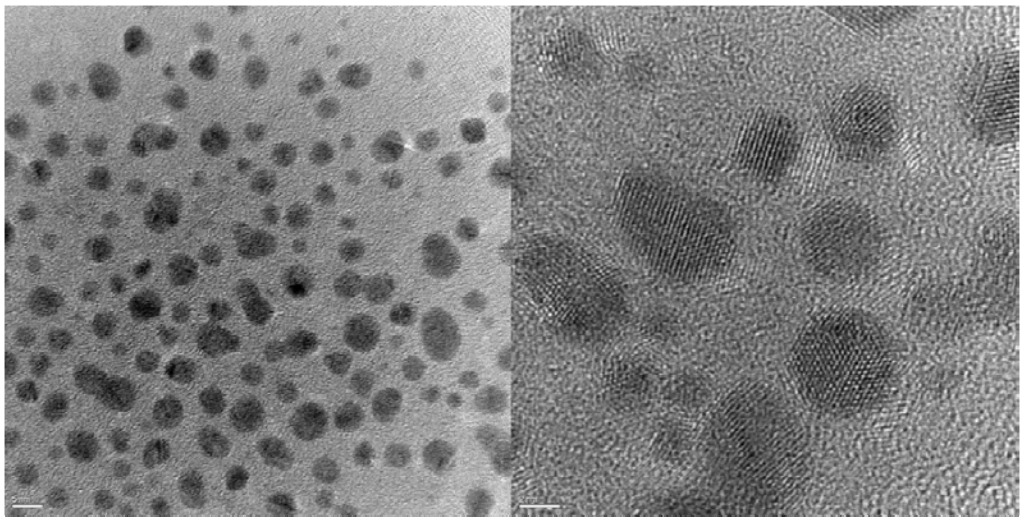

Figure 6.5. High resolution TEM images of YbS nanocrystals taken at differing magnification to determine particle size distribution and crystallinity. Size bar in left image represents 5 nm while bar in right image represents 2 nm

Another type of material analyzed through HRTEM is NdS. The high resolution images demonstrate the crystallinity of the nanoparticles on the same size regime as the previously reported systems. High and low magnification images are shown in Figure 6.6. The calculated size distribution of these particles is 5.3 ± 0.7 nm (particle diameter).

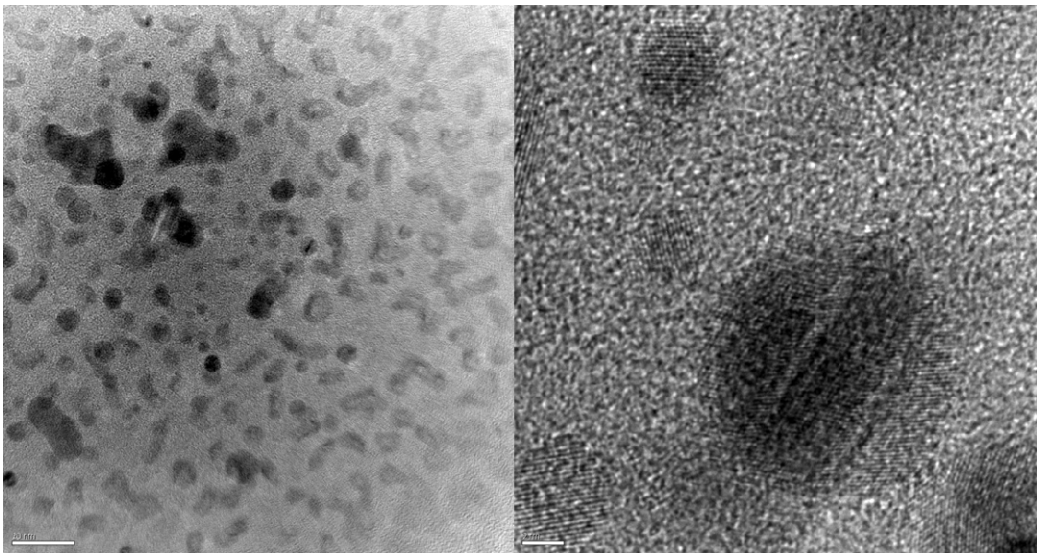

Figure 6.6. High resolution TEM images of NdS nanocrystals taken at differing magnification to determine particle size distribution and crystallinity. Size bar on the left represents 20 nm while bar on the right represents 2 nm.

Table 6.1 illustrates average size and size distributions of all LnS materials imaged using HRTEM. The particle size distributions were taken by measuring diameters of particles from various representative images and averaged to determine overall particle diameter with associated errors.

Table 6.1. Size distribution data comparing the 4 LnS nanocrystal systems. All particle size distributions were determined using Image J software (NIH software).

Sample	Size Distribution (nm)
TbS	4.7 ± 0.5
EuS	5.7 ± 0.6
NdS	5.3 ± 0.7
YbS	4.9 ± 0.7

Initial EDAX data were collected using HRTEM and is reported in Appendix E. This data was not reproduced due to extremely limited availability of the instrumentation in the PINSE center at the University of Pittsburgh. To compensate for this limitation further composition studies were performed using EDAX in conjunction with SEM (housed in the Department of Engineering and Materials Science at the University of Pittsburgh). Summary of the EDAX results are reported in Tables 6.2 through 6.5 below.

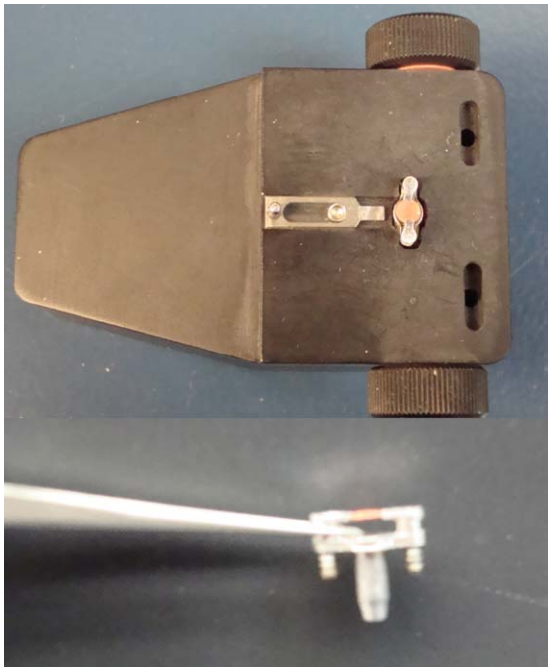

Figure 6.7. Grid holder for use with SEM. Samples were loaded onto TEM grids and placed in this holder for suspension during SEM/EDAX analysis.

The samples were loaded onto carbon coated copper TEM grids and placed in a TEM sample holder adaptor for SEM analysis (allowing the grid to be suspended – Figure 6.7). Grid

preparation required purification of nanocrystals using DTPA methods with final samples dissolved in methanol instead of water. Since the methanol is more volatile, it allowed for faster grid preparation. The methanol soluble DTPA coated LnS samples were dropped onto the grids, 10 µL at a time. Solvent was wicked away and grids were dried for 15 minutes before repetition of the operation. This procedure was repeated a total of 5 times per sample to ensure deposition of a sufficient amount of material to ensure sensitive and accurate analysis using SEM. Analysis was repeated for all four lanthanide sulfide systems.

Table 6.2. Summary of the EDAX data indicating composition of TbS nanocrystals in percentages. Samples were collected using 20 kV beam. Analysis required samples to be overloaded on a copper TEM grid.

Sample	S	Tb
TbS 4-14-2	44.63	55.37
TbS 4-14-3	43.28	56.72
TbS 4-14-4	53.65	46.35
TbS 4-14-5	58.16	41.84
TbS 4-14-6	49.83	50.17
TbS 4-11-1	58.33	41.67
TbS 4-11-2	46.02	53.98
TbS 4-11-3	62.71	37.29
TbS 4-11-4	49.34	50.66
TbS 4-11-5	58.34	41.66
Average	**52.43**	**47.57**
Standard Deviation	**6.76**	**6.76**
Standard Deviation (%)	**12.90**	**14.22**

Table 6.2 summarizes EDAX results for two different samples of TbS nanocrystals (TbS 4-14 and TbS 4-11). Grids were positioned using SEM and composition analyzed using the EDAX detector. For accurate composition determination and to analyze the reproducibility of the analysis and homogeneity of the sample, two separate nanocrystal samples were analyzed and the same samples were analyzed at different locations by varying the position of the TEM grids. The data illustrates consistent composition regardless of sample and grid position. These results are consistent with nanoparticles containing a similar amount of sulfur and lanthanide, indicating a 1:1 composition (LnS).

Table 6.3. EDAX data indicating composition of EuS nanocrystals in percentage of each component. Samples were collected using 20 kV beam. Analysis required samples to be overloaded on a copper TEM grid.

Sample	S	Eu
EuS 4-10-1	54.6	45.4
EuS 4-10-2	38.28	61.72
EuS 4-10-3	59.62	40.38
EuS 4-10-4	41.23	58.77
EuS 4-10-5	42.81	57.19
EuS 3-14-1	58.52	41.48
EuS 3-14-4	37.53	62.47
EuS 3-14-3	35.19	64.81
EuS 3-14-5	43.55	56.45
EuS 3-14-6	44.22	55.78
EuS 3-14-7	56.94	43.06
EuS 3-14-8	44.22	55.78
Average	46.39	53.61
Standard Deviation	8.67	8.67
Standard Deviation (%)	18.70	16.8

Measurements performed similarly on EuS particles reveal an identical composition as the one found for TbS. Again, two separate samples arising from different syntheses were analyzed at various locations on the TEM grids. EDAX was used to determine composition in conjunction with SEM. The data consistently yield 1:1 Eu:S ratios.

EDAX data for NdS and YbS are reported in Tables 6.4 and 6.5 respectively. Both NIR emitting lanthanides form nanoparticles with sulfur in a 1:1 ratio. These findings are consistent with what has been observed for Tb^{3+} and Eu^{3+}. These results indicate that our synthetic protocol lead to the formation of LnS types of nanocrystals with all the lanthanide cations that have been tested. Due to their internal f valence orbitals, all lanthanide cations have the same reactivity. The major difference between them is their sizes. It is interesting to notice that we have obtained LnS nanocrystals with same composition with larger ($Nd^{3+,}$ 1.12Å) and with smaller lanthanide cations (Yb^{3+}, 1.01 Å).

Table 6.4. EDAX data indicating composition of NdS nanocrystals in percentage of components. Samples were collected using 20 kV beam. Analysis required samples to be overloaded on a copper TEM grid.

Sample	S	Nd
NdS 3-25-1	45.45	54.55
NdS 3-25-2	49.2	50.8
NdS 3-25-3	58.47	41.53
NdS 3-25-4	53.72	46.28
NdS 3-25-5	53.89	46.11
NdS 3-25-6	51.62	48.38
NdS 3-25-7	45	55
NdS 3-25-8	41.85	58.05
NdS 3-25-9	54.3	45.7
NdS 3-25-10	57.45	42.55
Average	**51.10**	**48.90**
Standard Deviation	**5.56**	**5.54**
Standard Deviation (%)	**10.88**	**11.33**

Table 6.5. EDAX data indicating composition of YbS nanocrystals in percentage of components. Samples were collected using 20 kV beam. Analysis required samples to be overloaded on a copper TEM grid.

Sample	S	Yb
YbS 5-1-1	51.37	48.63
YbS 5-1-2	51.99	48.01
YbS 5-1-3	45.95	54.05
YbS 5-1-4	56.23	43.77
YbS 5-1-5	48.47	51.53
YbS 5-1-6	53.19	46.81
YbS 5-1-7	52.36	47.64
YbS 5-1-8	46.5	53.5
YbS 5-1-9	42.07	57.93
YbS 5-1-10	59.12	40.88
YbS 5-1-11	51.85	48.15
Average	**50.83**	**49.17**
Standard Deviation	**4.83**	**4.83**
Standard Deviation (%)	**9.50**	**9.82**

ICP-AES analysis was performed on all DTPA coated LnS particles (similar to those that have been analyze with EDAX) with little success. ICP sample preparation involved digestion of dried nanocrystal samples with 5 mL of a pure 1:1 HNO_3 solution. Samples were heated for 15 minutes at 95 °C followed by addition of 2.5 mL of concentrated HNO_3. Samples were then heated for an additional 30 minutes prior to addition of a 30% H_2O_2 solution (up to 5 mL until effervescence subsides). A final heating period of 1 hour at 95°C followed the addition of hydrogen peroxide. The final digested samples were sent for analysis by ICP in the Geology Department at the University of Pittsburgh.

The results from the ICP data analysis are organized in the Appendix G. Initial composition yielded lanthanide rich systems that were thought to arise from either DTPA:Ln

complex impurities in solution or loss of sulfur via H_2S formation upon digestion. Subsequent purification of samples was performed through dialysis membrane separation to remove DTPA:Ln complexes (2000 MWCO membranes were used). These samples were analyzed with conflicting results, yielding data that was typically sulfur rich. No apparent trends in data were observed and therefore the technique is considered inaccurate for analysis of LnS particles at this time with our current sample preparation protocol. It has been reported in the literature that ICP analysis of small nanocrystalline materials is sometimes difficult and the results presented herein as well as those presented in the case of CdSe:Ln nanocrystals confirm this report with our types of nanocrystals.[20]

6.3.4 Photophysical characterization

Absorbance spectra were collected for LnS nanocrystals (Ln = Eu, Tb, Yb, and Nd) and representative spectra are shown below in Figure 6.8. These materials, like all other nanocrystal materials presented herein, possess the characteristic shoulder indicating the presence of quantum confinement. Only small shifts in band position are observed for LnS nanocrystals, as was the case for our ZnS and ZnSe nanocrystals.

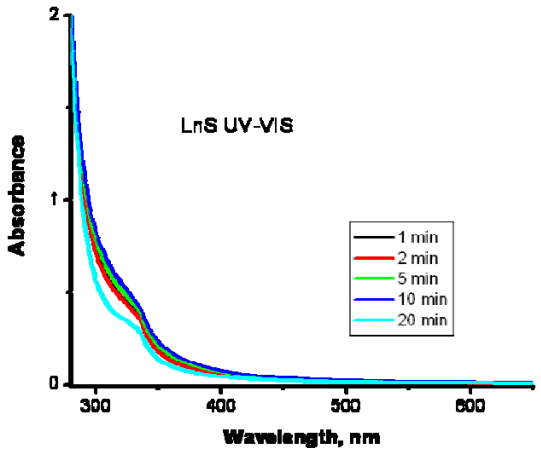

Figure 6.8. UV-vis absorbance data for LnS nanocrystals in chloroform. Concentration of nanoparticles in solution based on calculations modified from Peng et al. and Alivisatos et al.[21,22] is approximately 6.78E-05.

In order to analyze more deeply the presence of quantum confinement within these LnS systems, studies were conducted to determine the relationship between the growth times of the LnS nanocrystals with their band gap emission wavelength. The results are reported in the Figure 6.9. As the reaction time increases, the band gap emission maximum shifts to lower energy which can be attributed to formation of nanocrystals with larger sizes. This result confirms the formation of semiconductor nanocrystals with the presence of tunable band gap. Further work is required to determine the impact of this shift has on lanthanide sensitization within each of the four LnS systems studied.

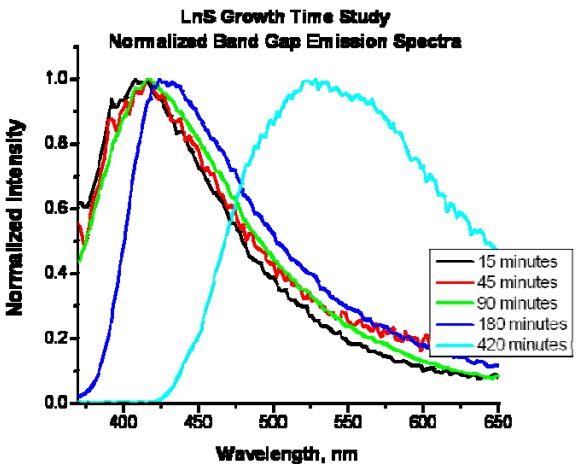

Figure 6.9. Normalized steady state emission spectra indicating the growth time dependent shift in band gap emission wavelength. This spectrum illustrates YbS nanoparticles dissolved in chloroform. All samples were excited at 320 nm

Excitation and Emission spectra were systematically collected for several types of LnS materials (Ln = Eu, Tb, Yb, and Nd) in an effort to evaluate presence of antenna effect for luminescent lanthanide cations within these materials. Since LnS nanocrystals are a wide band gap material (>3.0 eV), it is expected that the lanthanide accepting levels should fall within the band gap of the material and that it should thus be possible to sensitize a broad variety of luminescent lanthanide cations having different energies of their accepting levels. Visible (Eu^{3+} and Tb^{3+}) and NIR (Nd^{3+} and Yb^{3+}) emitting lanthanides were incorporated in the synthesis of these nanocrystalline materials. Their emission and excitation spectra were analyzed and are reported below.

YbS nanocrystals were synthesized and their emission and excitation profiles are shown in Figures 6.10 and 6.11 below. Of the LnS nanocrystal systems, YbS illustrates most clearly the presence of lanthanide sensitization through the antenna effect. The excitation profile collected upon monitoring the specific lanthanide emission of Yb^{3+} acetate in solution is shown in red.

This result represents the "direct excitation" of the lanthanide. Yb^{3+} does not have electronic levels corresponding to energies within our region of interest, therefore any excitation profile observed when studying the YbS samples (upon monitoring Yb^{3+} emission at 980 nm) results from energy transfer from the electronic levels of the semiconductor nanocrystal to the accepting levels of Yb^{3+}. This is indicated by overlap of the excitation profile upon monitoring nanocrystal emission with the excitation profile collected upon monitoring Yb^{3+} emission (cyan and pink). To the best of our knowledge, the present work represents the first example of the sensitization of a NIR emitting lanthanide cation by using the band gap of a nanocrystal.

Two separate batches of YbS nanocrystals from 2 different syntheses are reported in Figures 6.10 and 6.11. Both batches yield similar spectroscopic properties indicating the level of reproducibility of these systems. It is worth noting that protocols have been established for these materials which have been used by undergraduate researchers. One data set below was synthesized from these protocols by undergraduate researcher Markelle Gibbs. This demonstrates that the protocols established herein are reliable and reproducible.

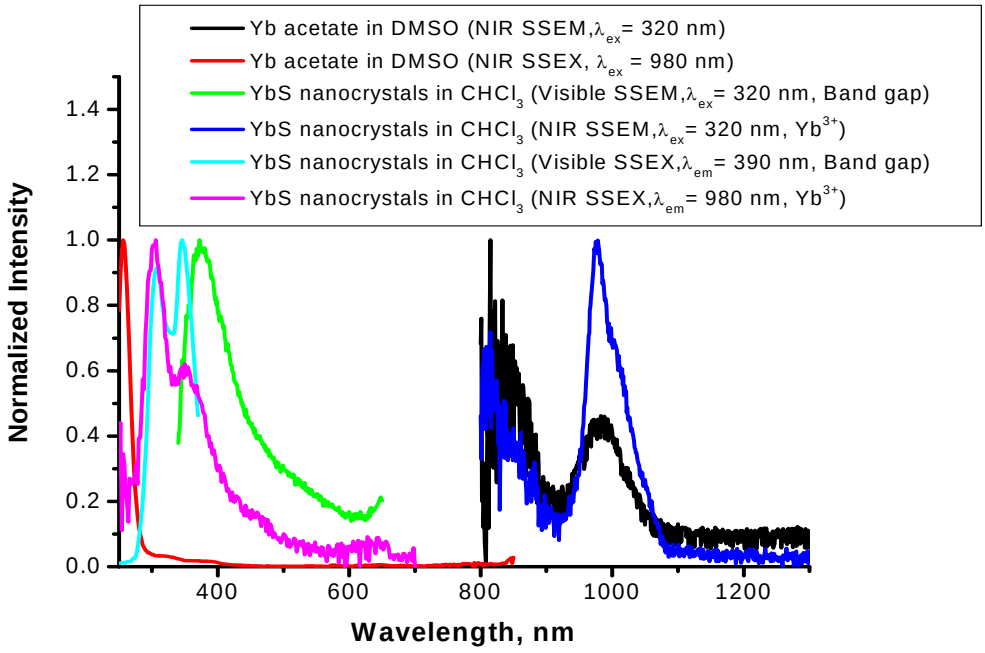

Figure 6.10. Overlay of normalized steady state and time resolved spectra for YbS nanocrystals in chloroform. Steady state spectra were collected using the visible (2 nm emission slits) and NIR (slits of 14 nm and 40 nm) detectors of the Fluorolog-322.

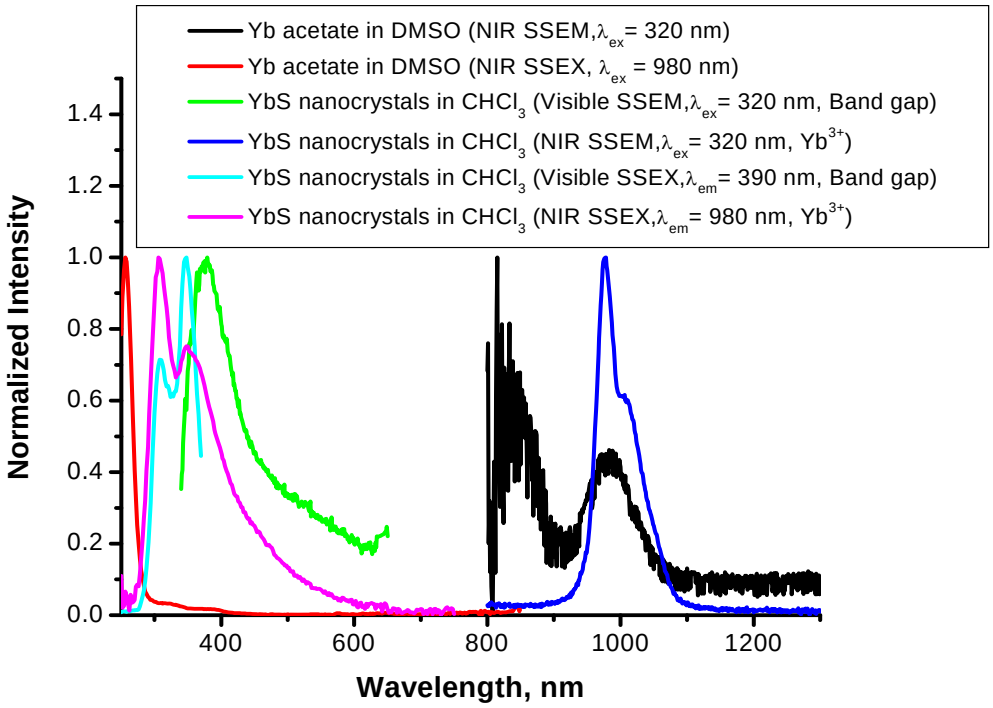

Figure 6.11. Overlay of normalized steady state and time resolved spectra for YbS nanocrystals in chloroform. Steady state spectra were collected using the visible (2 nm emission slits) and NIR (slits of 14 nm and 40 nm) detectors of the Fluorolog-322.

EuS nanocrystals result in somewhat different results than the Yb^{3+} counterparts. Both types of bands corresponding to Eu^{3+} and band gap emission are observed in the steady state emission spectra (Figure 6.12). Figures 6.12 and 6.13 illustrate emission and excitation profiles collected through steady state and time resolved measurments for two separate EuS nanocrystal batches synthesized using the same experimental methods, illustrating the reproducibility of these nanocrystal syntheses. Nanocrystal band gap emission in these EuS nanocrystals are centered between 370 nm (Figure 6.12) and 385 nm (Figure 6.13) similar to the emission profile reported for EuS by Hasegawa et al.[3,4] Unlike previously reported EuS nanocrystals, the systems

reported here exhibit both nanocrystal and lanthanide emission through steady state measurements.

The excitation spectra of the EuS nanocrystals were analyzed and compared to those obtained from the $Eu(NO_3)_3$ lanthanide salt (which identifies the spectral profile corresponding to the direct excitation of Eu^{3+}) in order to determine whether lanthanide sensitization through the electronic states of EuS band gap occurs. The excitation profiles obtained upon the monitoring of the Eu^{3+} transitions can be understood as arising from two energy transfer pathways originating from a double contribution of both nanocrystal electronic levels and direct excitation of Eu^{3+}. In the spectra shown in Figure 6.13, the excitation profile upon monitoring specifically Eu^{3+} (614 nm) emission more closely matches the spectrum collected upon monitoring the nanocrystal emission (cyan and green respectively). In this case, the nanocrystal emission band (red) is significantly lower in intensity than the lanthanide signal. This decrease in band gap emission intensity and subsequent increase in lanthanide emission intensity compared to the Figure 6.12 (with no observed significant change to the overall spectral profile except for a slight shift in band gap emission to higher energy in Figure 6.13) indicates that better energy transfer through the electronic structure of the nanocrystal is achieved. Fewer photons are emitting back through the band gap to result in emission while more are emitting from the Eu^{3+} emitting levels, enhancing its luminescence intensity. This phenomenon is coupled with slightly better overlap of the excitation profiles upon monitoring band gap and Eu^{3+} emission maxima. This illustrates that by slightly modifying the nanocrystal electronic structure through control of band gap energy, tuning of the energy transfer process is achievable.

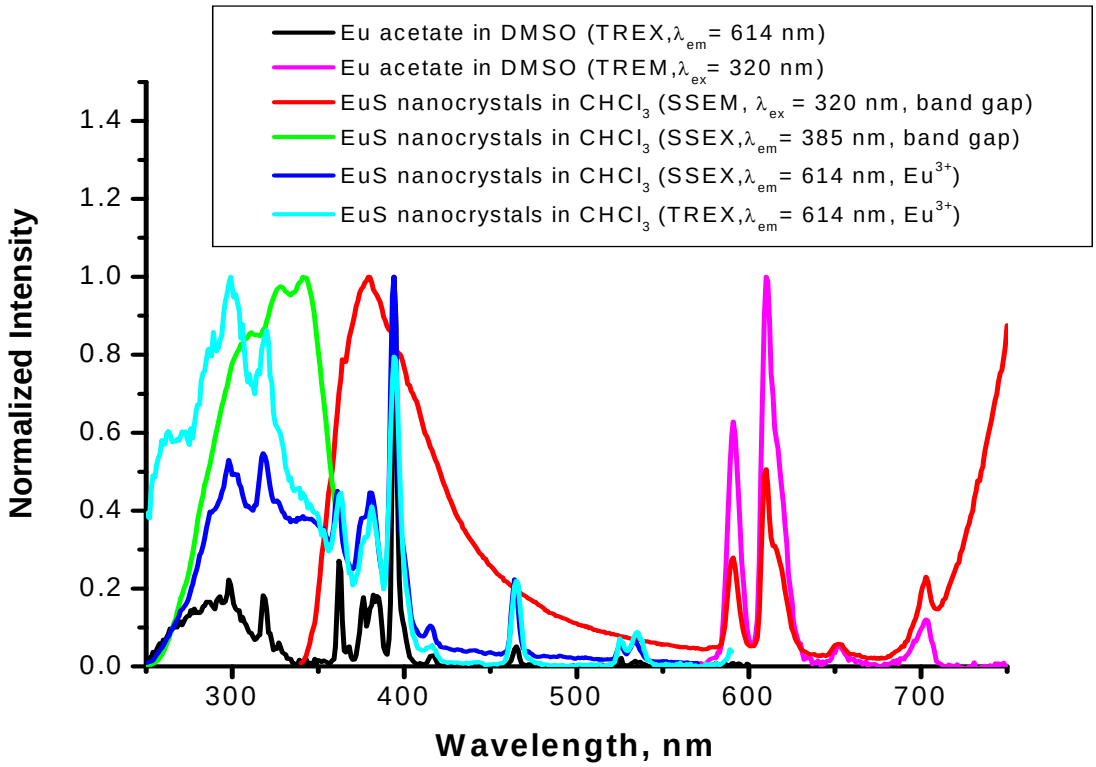

Figure 6.12. Overlay of normalized steady state and time resolved luminescence spectra for EuS nanocrystals in chloroform. Steady state spectra were collected using the Fluorolog-322 (2 nm excitation and emission slits). Time resolved spectra were recorded using the Cary Eclipse Fluorimeter (5 nm excitation and emission slits, delay time of 0.2 ms)

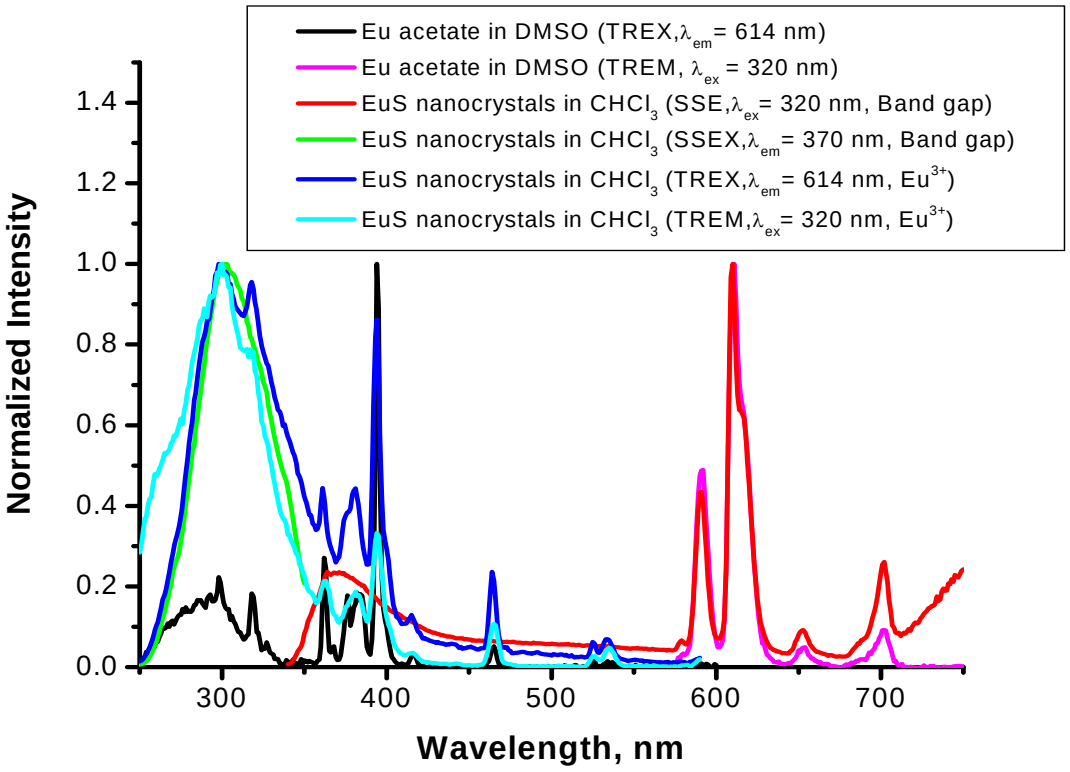

Figure 6.13. Overlay of normalized steady state and time resolved luminescence spectra for TbS nanocrystals in chloroform. Steady state spectra were collected using the Fluorolog-322 (2 nm excitation and emission slits). Time resolved spectra were recorded using the Cary Eclipse Fluorimeter (5 nm excitation and emission slits, delay time of 0.2 ms)

The conclusion based on the results obtained with TbS nanocrystals are fairly similar to those obtained with the EuS nanocrystals. Upon excitation using 320 nm wavelength, the fingerprint narrow Tb^{3+} emission bands (488 nm, 545 nm, 585 nm, and 620 nm) are observed in addition to the broader band gap emission with an apparent emission maximum at 380 nm as shown in Figure 6.14 (green). Upon recording the time resolved emission spectrum of the same solution, the Tb^{3+} signal can be discriminated from the nanocrystal band gap emission on the basis of their emission lifetimes (Figure 6.14 red). This result indicates that it is possible to

remove the blue emitting band gap contribution through temporal measurements based on the relative lifetimes of the band gap emission and the lanthanide emission energies. Excitation spectra were collected upon monitoring the band gap emission and Tb^{3+} emission in steady state mode (blue and cyan respectively) in addition to excitation upon monitoring Tb^{3+} emission in time resolved mode (black). These spectra are overlaid with a direct excitation profile for free Tb^{3+} in solution as a comparison, which represent the direct excitation of the lanthanide cations (Figure 9, pink). The overlay of the excitation profiles provides information on the path of the energy that is occurring for the lanthanide sensitization in these nanocrystals. The excitation profile upon monitoring Tb^{3+} emission in time resolved mode is contained within the excitation profile collected upon monitoring the band gap emission in steady state mode. Neither spectra exhibit the same features as the direct excitation profile, indicating that excitation of the Tb^{3+} must come from a source other than purely direct excitation, i.e. that the structure if the nanocrystals is providing an antenna effect to Tb^{3+}. These spectral results are reproducible and this reproducibility is shown in Figure 6.15.

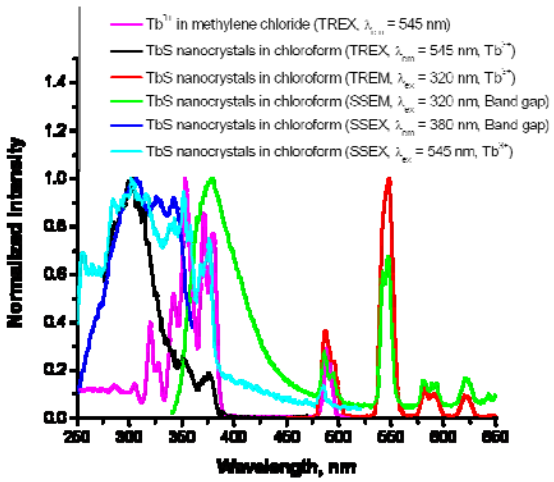

Figure 6.14. Overlay of normalized steady state and time resolved excitation and emission spectra recorded in chloroform solutions of TbS nanocrystals. Steady state spectra were collected using the Fluorolog-322 (2 nm excitation and emission slits). Time resolved spectra were recorded using the Cary Eclipse Fluorimeter (5 nm excitation and emission slits, delay time of 0.2 ms). $Tb(NO_3)_3$ was used to collect a direct excitation spectrum for comparison.

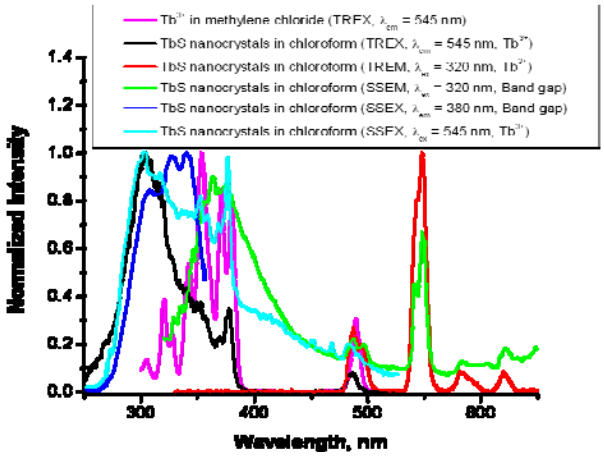

Figure 6.15. Overlay of normalized steady state and time resolved excitation and emission spectra recorded in chloroform solutions of TbS nanocrystals. Steady state spectra were collected using the Fluorolog-322 (2 nm excitation and emission slits). Time-resolved spectra were recorded using the Cary Eclipse Fluorimeter (5 nm excitation and emission slits, delay time of 0.2 ms). $Tb(NO_3)_3$ was used to collect a direct excitation spectrum for comparison.

One interesting feature that arises again in LnS systems is the presence of a region in the nanocrystal excitation profile which contains direct excitation bands. This indicates more complicated energy transfer processes than observed for previous doped nanocrystal systems. It is suggested that based on the wide band gap (indicated by blue-UV emission of the synthesized nanoparticles), the accepting levels of various lanthanides will actually reside within the energy corresponding to the band gap.[8] While band gap energy reported for bulk LnS materials is approximately 1.6 eV,[23] EuS nanocrystals possess band gap energies ranging from 1.9 eV (20 nm particles) to 3.1 eV (10 nm particles, and comparable to the diameter of particles reported here).[1,3] Figure 6.16 depicts a cartoon that schematizes this hypothesis. If the accepting levels of the lanthanides are contained within the band gap, then while some electrons are promoted to the conduction band upon excitation (pink arrow), others are promoted to the lower lying lanthanide levels (purple arrow). Those electrons that reach the conduction band could then transfer their energy to the lanthanide accepting levels resulting in the antenna effect (blue arrows), and subsequent lanthanide emission could occur. An alternative pathway for the electrons reaching the conduction band is relaxation back to the valence band resulting in band gap emission (light pink arrow). Electrons that are directly promoted to the accepting levels of the lanthanide from the conduction band will result in direct excitation profiles because energy transfer from the band gap is not taking place. In the latter case the electrons are relaxing back to the lanthanide ground state resulting in lanthanide emission.

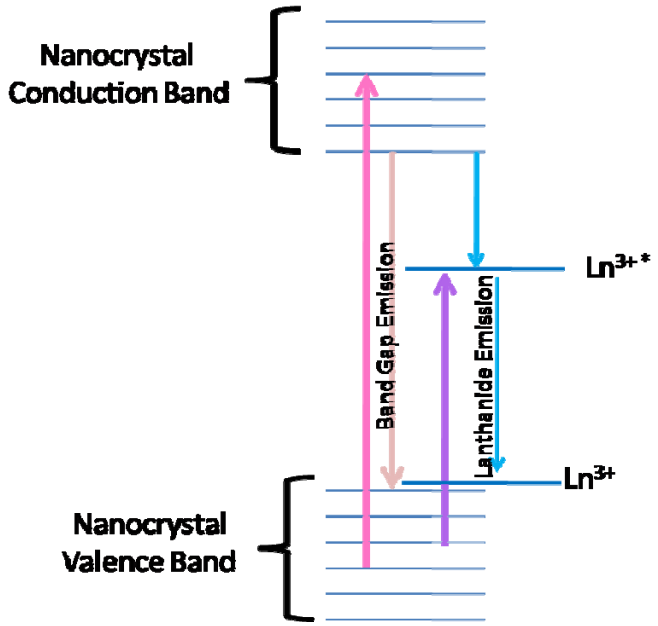

Figure 6.16. Cartoon illustrating hypothesized energy transfer within the LnS nanocrystal systems.

In addition to visibly emitting Tb^{3+} and Eu^{3+} and NIR emitting Yb^{3+}, LnS nanocrystals were also synthesized with NIR emitting Nd^{3+}. NdS nanocrystals behave similarly to TbS and EuS and spectroscopic properties are reported in Figures 6.17 and 6.18 below. They exhibit band gap emission centered at approximately 400 nm and illustrate similarly complicated excitation profiles. Steady state measurements were collected using both the visible detector (Hamamatsu R928) and the NIR detector (Electro-Optical Systems, Inc. DSS-IGA020L) of the Fluorolog-322. Characteristic nanocrystal band gap emission is detected in the visible (green), while the sharp Nd^{3+} emission bands are observed in the NIR (cyan). The direct excitation profile of Nd^{3+} salt in solution is shown in red for comparison. Upon monitoring the nanocrystal emission (380 nm), the excitation profile shows a broad band with an apparent maximum centered at 360 nm (blue). Excitation spectra collected upon monitoring the transition of Nd^{3+} that appears at 1050 nm results in more complex excitation profiles that, like in the TbS and EuS

systems, seems to contain both signals that can be attributed to the direct excitation of Nd^{3+} as well as excitation using the electronic levels of the nanocrystal (shown in pink).

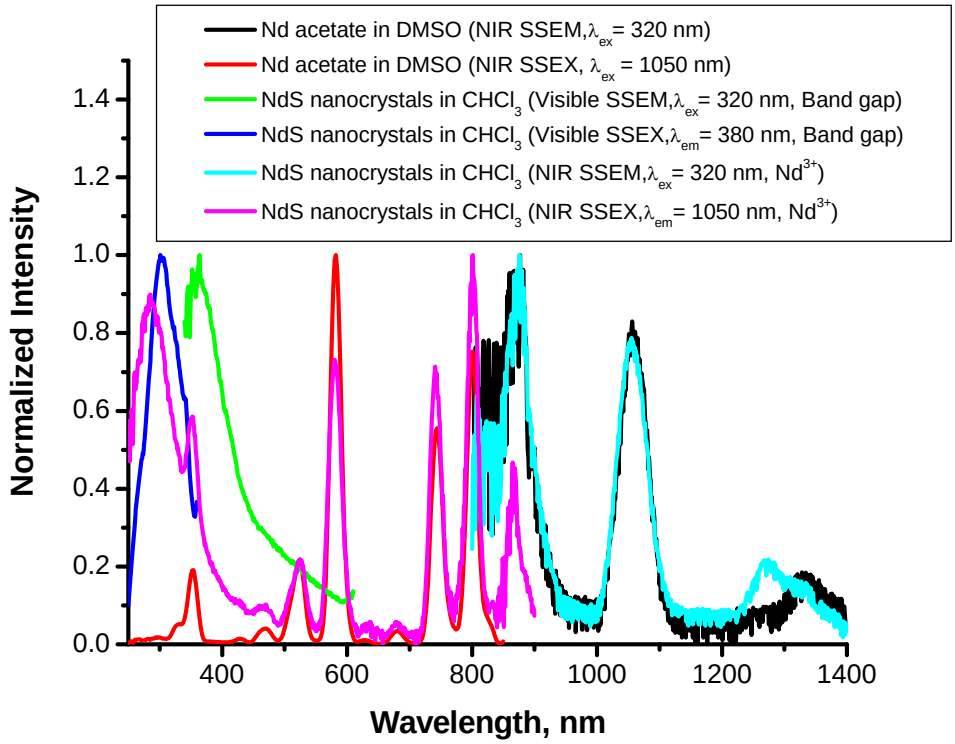

Figure 6.17. Overlay of normalized steady state and time resolved spectra for NdS nanocrystals in chloroform. Steady state spectra were collected using the visible (2 nm emission slits) and NIR (slits of 14 nm and 40 nm) detectors of the Fluorolog-322.

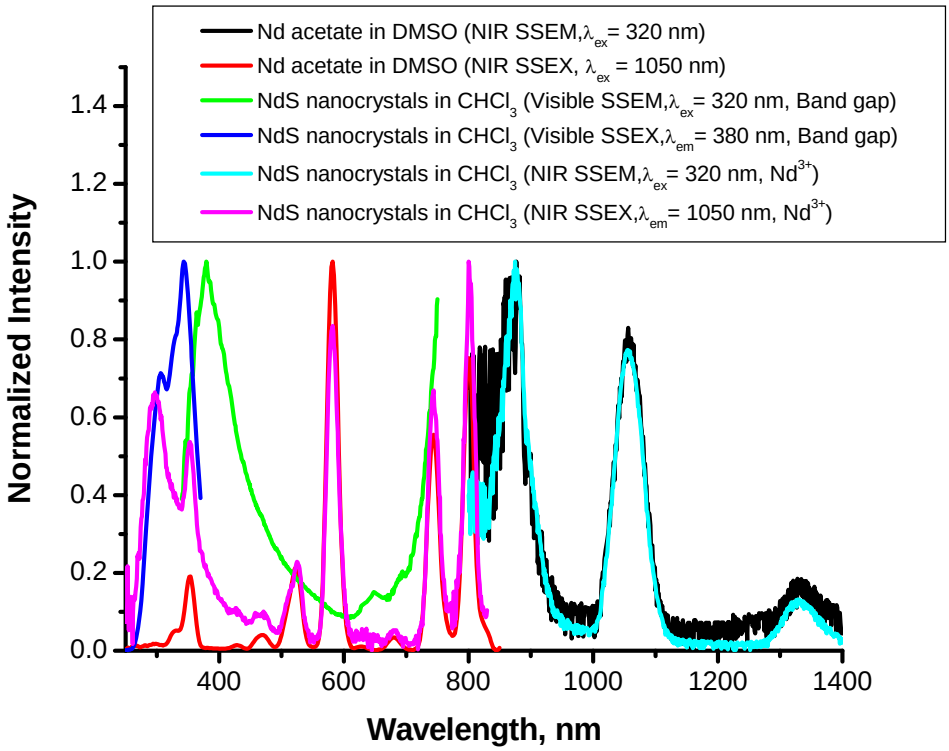

Figure 6.18. Overlay of normalized steady state and time resolved spectra for NdS nanocrystals in chloroform. Steady state spectra were collected using the visible (2 nm emission slits) and NIR (slits of 14 nm and 40 nm) detectors of the Fluorolog-322.

While all of the LnS nanocrystal materials described above do exhibit some degree of lanthanide sensitization, the level of which seems so show some variation from one lanthanide system to another. This is clearly demonstrated in the case of YbS nanocrystals, where only sensitization is observed, relative to TbS, EuS, and NdS nanocrystal systems, where there appears to be some combination of energy processes involved.

While LnS nanocrystals passivated with TOPO and dissolved in chloroform where used for determination of sensitization, further spectroscopic studies were performed on nanocrystals in aqueous solutions and are shown below.

Difficulties with imaging of the particles that were coated with TOPO (the presence of the carbon material preventing to obtain TEM images possessing sufficient resolution) led to the use of DTPA coating as a method of purification of the nanocrystals through the removal of the TOPO. Such purification was successful and has led to the acquisition of the HRTEM images that have been presented above. The steady state and time resolved emission and excitation profiles below shows both TOPO/TOP passivated nanocrystals dissolved in chloroform and their DTPA passivated counterparts dissolved in water.

Steady state emission spectra of TbS nanocrystals passivated with DTPA and dissolved in water indicate the presence of the characteristic band gap and Tb^{3+} emission, however the band gap emission is slightly broadened, most likely the result of the surface modification. Upon monitoring the excitation profiles within these systems, it is evident that additional impurities are present within the aqueous DTPA coated samples. The excitation profiles upon monitoring the Tb^{3+} emission bands in both steady state and time resolved modes gives strong indication of direct excitation, as seen in Figure 6.19.

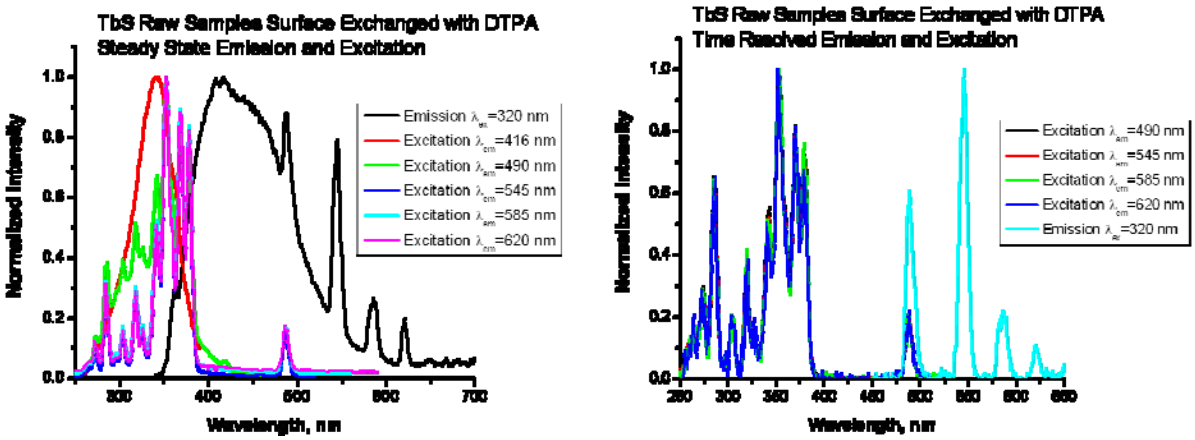

Figure 6.19. Normalized steady state emission and excitation spectra in water of TbS:DTPA nanocrystals (left) and normalized time resolved excitation and emission of TbS:DTPA nanocrystals (right).

One proposed explanation for the higher emergence of direct excitation bands in water compared to chloroform is that the DTPA is forming complexes with Tb^{3+} cations in solution. DTPA:Ln complexes have been extensively reported in the literature[24-28] and are known to be highly stable based on the multidentate binding ability of the DTPA complexes. There are 2 proposed sources of free Tb^{3+} in solution: (1) excess Tb^{3+} in from the original reaction mixture not incorporated into nanocrystals, and (2) sonication procedures required for DTPA surface exchange may result in breaking apart a portion of nanocrystals present in solution, causing Tb^{3+} to be released and subsequently bound by DTPA to form a molecular complex in solution. Since DTPA does not possess any chromophoric groups, it cannot play the role of antenna for the lanthanide cations.

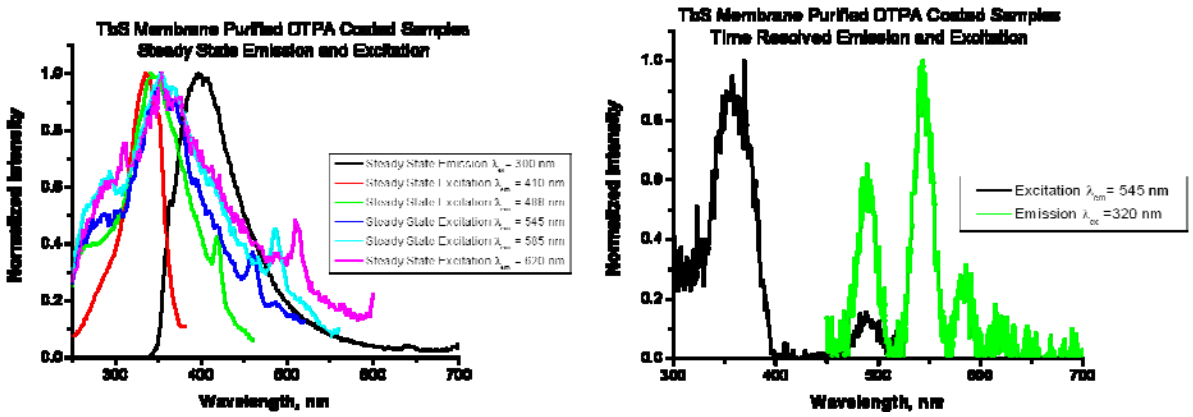

Figure 6.20. Normalized steady state (left) and time resolved (right) excitation and emission spectra of membrane purified TbS:DTPA in water. Samples were dialyzed using 10,000 MWCO membranes.

In an attempt to further purify the solutions containing the DTPA coated nanocrystals and separate out the DTPA:Tb complexes from the DTPA coated nanocrystals, a purification strategy based on dialysis membrane purification was employed. Aqueous solutions of nanocrystals were loaded into 10,000 MWCO membrane cartridges and left to separate via dialysis in water. The

samples were then removed from the membranes, concentrated down and analyzed with spectroscopic tools. The spectra, shown in Figure 6.20, indicate that particle concentration is very low since weak nanocrystal emission is observed. Steady state and time resolved emission and excitation spectra could only be recorded via careful tuning of the instrument parameters. From this data it is not entirely clear whether or not membrane purification was successful. After careful consideration of the direct excitation profiles obtained in aqueous solutions and membrane purification carried out, the membrane purification procedures were repeated using lower MWCO membranes (2,500 MWCO). The larger molecular weight membranes were believed to be incapable of removing the DTPA:Ln impurities and were in fact contributing to the loss of LnS nanocrystals (estimation of nanocrystal molecular weights using calculations based on the work of Peng et al. and Alivisatos et al. indicate particles of between 2500 and 7000 g/mol). By using smaller membranes we are increasing the chances that the impurities will be removed and the particles will stay inside the membrane. Figure 6.21 represents data obtained through the dialysis procedures carried out with the lower cut-off sized membranes. This new membrane purification procedure shows little, if any, improvement over photophysical properties within the TbS nanocrystal system. Nanocrystal band gap emission and excitation profiles are observed in membrane purified samples (Figure 6.21, green and blue respectively). The Tb^{3+} signal, however, is very weak and could only be observed using maximum slit widths on the Cary Eclipse (Figure 6.21, black). The excitation profile upon monitoring the Tb^{3+} emission is dominated by direct excitation (the bands slightly broadened as the result of wide slits). These results are nearly identical to results obtained when using 10,000 MWCO membranes.

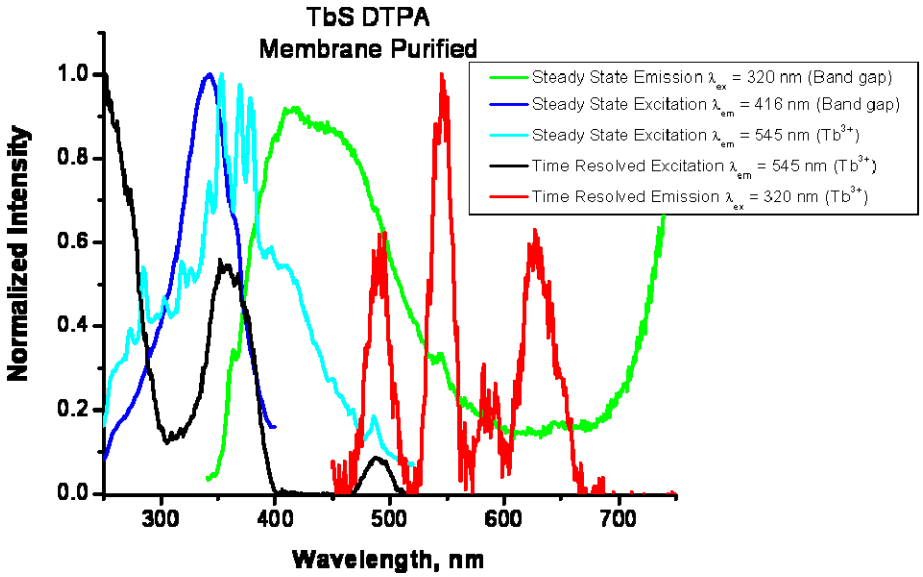

Figure 6.21. Normalized steady state and time resolved emission and excitation spectra of TbS:DTPA nanocrystals that have been dialyzed using 2,500 MWCO membranes (recorded in water).

DTPA coating experiments were performed for EuS nanocrystals as well. As in the case of TbS, the EuS exhibit a characteristic band gap emission in addition to the observed steady state Eu^{3+} emission when dissolved in chloroform. Excitation spectra indicate some level of direct excitation within the EuS nanocrystal systems. The spectra do not appear to be dominated by direct excitation and therefore some degree of sensitization occurs (described in detail and illustrated in Figures 6.12 and 6.13 above). Steady state and time resolved excitation spectra exhibit some degree of overlap for nanocrystals dissolved in chloroform.

Upon surface exchange with DTPA however, the excitation profiles appear to be completely dominated by signals corresponding to direct excitation bands (Figure 6.22). The steady state emission spectra contains signals corresponding to the dual emission feature in aqueous solution (features at 450 nm corresponding to band gap emission and 590 nm, 614 nm,

and 694 nm corresponding to Eu^{3+} emission), but the Eu^{3+} emission in this case is the result of direct excitation of the Eu^{3+} rather than energy transfer through the nanocrystal based on comparison of time resolved excitation profiles of Eu^{3+} within the nanocrystal compared to direct excitation profiles collected for Eu^{3+} in solution. This again can be explained by the presence of DTPA:Ln complexes in solution caused either by complexation with unreacted starting materials or through breaking up of nanocrystals upon sonication.

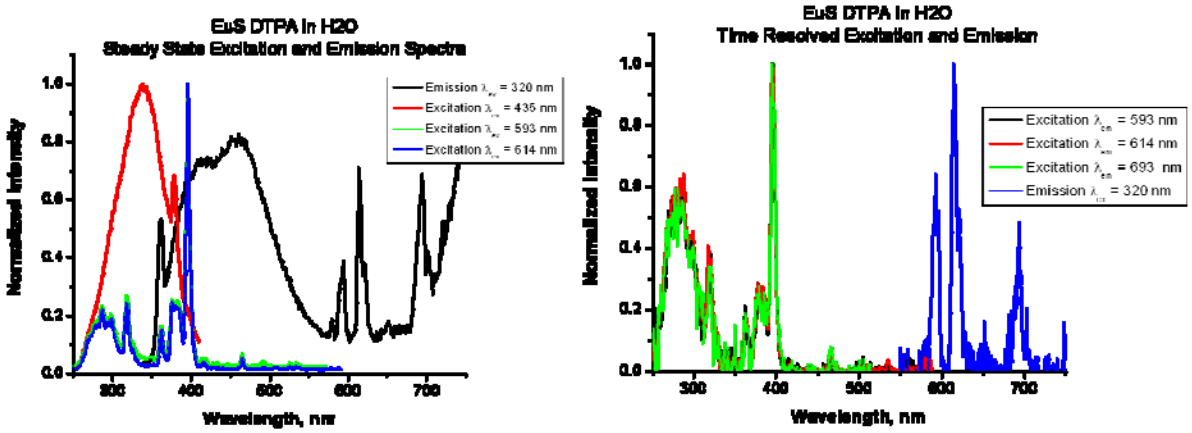

Figure 6.22. Normalized steady state emission and excitation spectra in water of EuS:DTPA nanocrystals (left) and time resolved excitation and emission of EuS:DTPA nanocrystals (right).

DTPA surface exchange procedures were also tested on YbS nanocrystals. The analysis of the YbS samples dissolved in chloroform indicate the overlap of the visible excitation profile collected upon monitoring band gap emission and the NIR excitation profile upon monitoring Yb^{3+} emission and therefore illustrate lanthanide sensitization. Both characteristic Yb^{3+} and band gap emission bands are observed upon excitation of the electronic levels of the nanocrystals (λex = 320 nm). Following the surface exchange with DTPA, the emission signal was observed to be much weaker and the NIR excitation profile is indistinguishable from instrument noise,

Figure 6.23. This result can be from a combination of the strong quenching of the luminescence from Yb^{3+} through overtones of the –OH vibrations from the water solvent and/or from thee dilution of the sample induced by the coating and purification process.

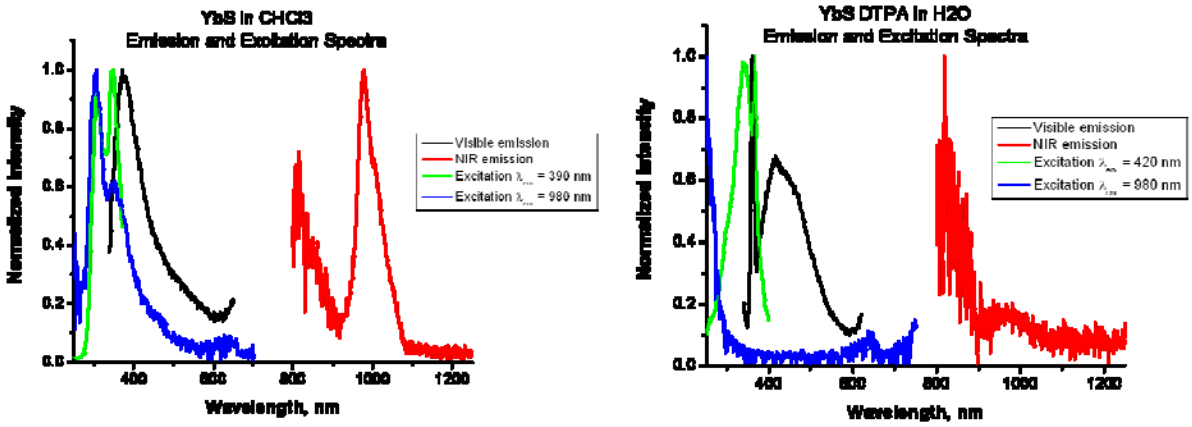

Figure 6.23. Normalized steady state emission and excitation spectra of YbS in chloroform (left) and YbS:DTPA in water (right)

A second NIR emitting lanthanide was tested, Nd^{3+}. Nanocrystals were synthesized and dissolved in chloroform for initial analysis. The visible emission and excitation spectra resemble those observed in the previous NIR system. Nanocrystal band gap emission is observed in the visible (λ_{ex} = 320 nm) and Nd^{3+} emission is observed in the NIR (λ_{ex} = 320 nm). Excitation profiles upon monitoring nanocrystal band gap emission have been compared to excitation profiles upon monitoring Nd^{3+}, the results of which are discussed in detail above and show some indication of lanthanide sensitization combined with direct excitation. The antenna effect is demonstrated to some extent within these particles.

DTPA surface exchanges were performed on NdS nanocrystals as well. Again, characteristic band gap emission and excitation profiles were observed for visible measurments and the characteristic direct excitation and subsequent emission bands were observed in NIR

spectra, Figure 6.24 below. As was the case for YbS nanocrystals, band gap emission centered at 430 nm was observed in the visible (λ_{ex} = 320 nm) with weak Nd^{3+} emission (centered at 1060 nm) observed in the NIR upon using the same excitation wavelength. Excitation profiles upon monitoring nanocrystal band gap emission (Figure 24 left, red) do not share characteristics with excitation profiles upon monitoring Nd^{3+} (Figure 24 right, green), and the Nd^{3+} excitation profile exhibits only direct excitation bands. This indicates the absence of antenna effect within these aqueous samples. Again, this is most likely due to formation of DTPA:Ln complexes whose spectral properties dominate the spectra.

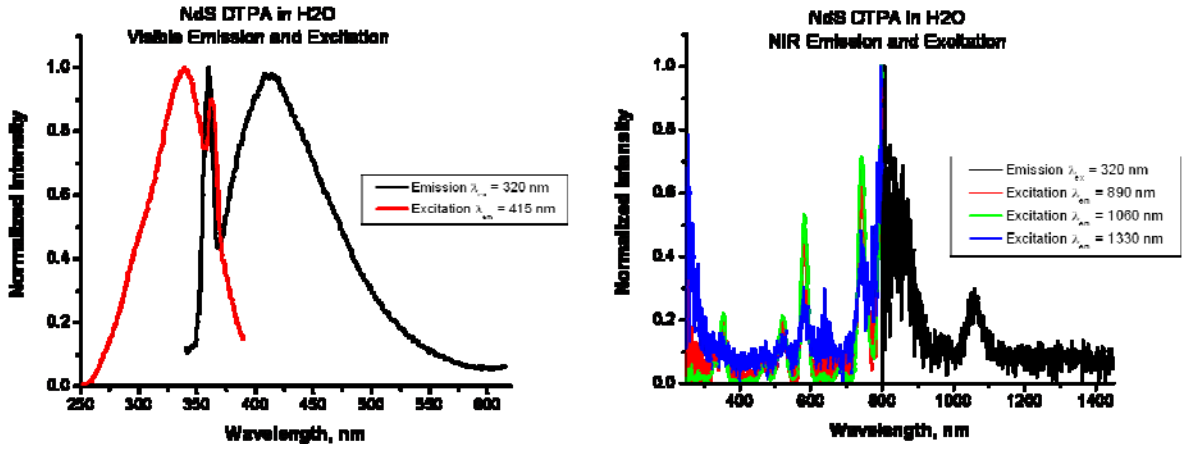

Figure 6.24. Normalized steady state emission and excitation spectra of NdS in water collected using the visible detector (left) and the NIR detector (right) of the Fluorolog-322.

In order to analyze the environments around the lanthanide cations, we have recorded the luminescence lifetimes of the emission arising from the different lanthanide cations. Different types of samples were tested in order to evaluate the effect of the environment of the nanocrystals on the protection of the lanthanide cations: LnS in chloroform (TOPO passivated),

DTPA coated LnS in water, DTPA coated LnS membrane purified in water, DTPA coated LnS in D_2O.

The exponential decay curves have been treated to extract the individual lifetime components. The results are summarized in Table 6.6.

Table 6.6. Luminescence lifetime results obtained from treatment of the experimental decay curves for different types of LnS nanocrystal systems in chloroform, water and deuterated water.(λ_{ex} = 354 nm using the third harmonic of a Nd:YAG laser)

Sample	τ1 (s)	τ2 (s)	τ3 (s)
TbS in $CHCl_3$	4.8E-03 ± 0.6E-03	1.9E-03 ± 0.5E-03	—
TbS in H_2O	2.0E-03 ± 1.1E-05	—	—
TbS in D_2O	3.6E-03 ± 4.2E-04	3.0E-04 ± 1.2E-04	
EuS in $CHCl_3$	2.7E-03 ± 1.4E-04	5.6E-04 ± 2.4E-04	—
EuS in H_2O	5.6E-04 ± 3.5E-05	4.5E-05 ± 7.1E-06	—
EuS in D_2O	2.5E-03 ± 2.2E-04	4.4E-04 ± 2.1E-05	—
YbS in $CHCl_3$	2.4E-04 ± 9.4E-05	1.4E-05 ± 5.7E-07	—
YbS in H_2O	5.5E-06 ± 7.1E-07	1.4E-06 ± 1.6E-07	—
YbS in D_2O	8.0E-06 ± 9.0E-07	1.8E-06 ± 1.7E-07	3.8E-07 ±6.3E-09
NdS in $CHCl_3$	8.8E-06 ± 9.2E-07	—	—
NdS in H_2O	2.1E-06 ± 7.7E-07	3.0E-05 ± 1.7E-05	—
NdS in D_2O	3.3E-06 ± 1.4E-07	3.7E-07 ± 6.4E-09	—

Most of the experimental luminescence lifetime values have been successfully fitted with biexponential decay with a few exceptions. In the case of TbS samples, lifetimes in chloroform were biexponential, corresponding to 2 different Tb^{3+} environments within the nanocrystals. This result can be rationalized by the distribution of the lanthanide in the core and at the surface of the nanocrystals (internal and surface sites). These values are in the range of expected values

for well protected Tb^{3+}. Lifetime values reported here are biexponential yielding values of 4.8 and 1.9 ms, lifetimes for Tb^{3+} cations in previously reported nanocrystal systems were found to be biexponential as well, with values of 4.7 and 2.02 ms (CdSe:Tb) and 2.50 and 0.92 ms (ZnS:Tb). The luminescence lifetimes obtained for the TbS nanocrystals in water were significantly shorter, the longest component attributed to the lanthanide cations present in the core of these nanocrystals was shortened by a little more than half, and the shorter component, attributed to the to surface Tb^{3+} cations was not observed. This result can be explained by the quenching resulting from solvent vibrations. The second component may not be observed due to the strength of the quenching that prevent the observation of this signal, the number of photons being below the limit of detection of our instrument. Nevertheless it can be noticed that the luminescence lifetimes recorded in water is significantly longer than those reported for molecular complex in aqueous solution (2.00 ± 0.01 ms reported here compared to literature value of 1.20 ± 0.04 ms)[29] as indication of a superior protection of the Tb^{3+} in nanocrystals in comparison to molecular complexes. To further analyze this protection, the samples were dissolved in D_2O and the measurments were repeated to assess the effect of the –OH vibration to the quenching of the excited states of the lanthanide cations. In the presence of deuterated water, the exponential decay was biexponential. The luminescence lifetimes are still slightly shorter than those recorded for the same type of nanocrystals in chloroform.

The exponential decays recorded on the EuS nanocrystals fit best with a biexponential decay in all 3 solvent systems indicating the presence of the two different environments for Eu^{3+} in the core and at the surface of the nanocrystals. Similar quenching effects were observed as for TbS. Samples in chloroform yielded the longest lifetimes and were on the order of what was expected for well protected Eu^{3+}. Previously reported CdSe:Eu nanocrystal systems in

chloroform have resulted in biexponential decay fits of 3.6 ms and 2.0 ms for Eu^{3+}, while ZnS:Eu nanocrystals yielded values of 2.8 and 1.3 ms. These values match well with the 2.7 ms component observed for EuS. Upon surface exchange with DTPAand solubilization in water, the lifetimes were shortened by a factor of ten for both values. Lifetimes have been reported in the literature with values of 0.78 ms for complexes of Eu^{3+} in methanol[30] are on the same order of magnitude as the lifetimes observed for EuS in water (0.56 ms).The quenching can be explained by the high energy solvent vibrations and solvent exchange to D_2O is expected to, and in fact did significantly lengthen the lifetimes of the DTPA coated nanocrystals.

The experimental decays signal recorded on YbS nanocrystals were fitted with biexponential values in chloroform and water; however, unlike other LnS systems, the D_2O samples fit to a triexponential decay. Yb^{3+} lifetimes of 240 and 14 μs were obtained; these values indicate very good protection of the Yb^{3+} by the nanocrystal structure. Ytterbium complexes in solution have reported lifetime values of 33.71μs ± 0.03μs in deuterated methanol,[31] significantly lower than those observed here. In addition, Yb^{3+} lifetimes have been reported for doped $NaYF_4$ nanoparticles utilizing tropolonate ligands, resulting in biexponential values of 63μs and 4.1 μs, still shorter than values obtained within YbS nanocrystals.[32] Comparison of values obtained for YbS with literature values provides indication of good protection of Yb^{3+} by the nanocrystal structure from deactivation from the vibrations of solvent molecules. The lifetime values are reduced by almost a factor of 100 upon DTPA surface exchange and solubility in water. NIR lifetimes are readily quenched by water because of the overlap of vibrational overtones of O-H. Upon addition of D_2O the lifetime values are increased, however not to the extent observed for the visibly emitting lanthanides. The appearance of a third lifetime value may result from either the presence of DTPA:Ln complexes in solution,

which were overshadowed by the longer lifetimes observed in the case of EuS and TbS, or they may result from the lifetime of emission signals arising from the nanocrystal band gap.

The last system that was studied in detail was NdS. These nanocrystals dissolved in chloroform exhibit only monoexponential luminescence decays in the microsecond range, typical for Nd^{3+}. Solvent studies performed using azulene based ligands for sensitization of Nd^{3+} have resulted in lifetime values of 2.68 μs in deuterated acetonitrile,[31] while the Nd^{3+} values reported for NdS in chloroform were found to be 8.8 μs. The improvement in lanthanide protection is not as significant as in the case of Yb^{3+}, however the values reported for YbS are more than double previously reported values indicating some improvement in protection through the nanocrystal structure. Upon DTPA surface modification and subsequent dissolution in water, the lifetime values are decreased by about 25%. This quenching can also be explained by the presence of vibrational overtones of solvent molecules, the effect being more pronounced for NIR emitting lanthanide cations than the visible ones. The recovery of lifetime values from NdS systems upon dissolution in D_2O is even less significant than in the case of YbS.

Lanthanide centered quantum yields were obtained for TbS and YbS nanocrystals (Table 6.7). TbS nanocrystals exhibit a Tb^{3+} centered quantum yield of 1.9E-04, which is an improvement over Tb^{3+} centered quantum yields reported for CdSe:Tb nanocrystals (1.5E-05), but is a factor of almost 100 smaller than observed for ZnS:Tb nanocrystals (5.1E-02). Previously reported nanocrystal systems were not used to sensitize Yb^{3+} and therefore the quantum yield values observed here cannot be directly compared to other nanocrystal systems. Azulene complexes of Yb^{3+} in acetonitrile have resulted in quantum yields of 2.7E-02, almost a factor of 100 larger than observed here.[31]

Table 6.7. Lanthanide centered quantum yields of LnS nanocrstals in chloroform (λ_{ex} = 315 nm, 320 nm and 325 nm).

Sample	Lanthanide Centered φ
TbS	1.9E-04 ± 2E-05
YbS	6.3E-04 ± 3E-05

While the quantum yield values are somewhat lower than reported for lanthanide complexes formed with organic ligands in solution (Yb^{3+}: 2.7E-02 and Tb^{3+}:0.63)[30,31], these values are compensated by the high density of luminescent cations per unit of volume in these polymetallic materials.

6.4 CONCLUSION AND FUTURE DIRECTIONS

We have demonstrated that we can synthesize LnS nanocrystals with 1:1 Ln:S ratios possessing emission in the visible and in the NIR region (YbS and NdS). These materials offer the advantage over previously described lanthanide containing nanocrystals, such as CdSe:Ln, ZnS:Ln and ZnSe:Ln, in that LnS syntheses involve only 2 components, thus allowing for better control of synthetic parameters. Also, unlike the previously described systems, lanthanides serve as a major component in this material rather than a dopant, creating a polymetallic material with an even larger number of emitting species per volume.

While the antenna effect is observed only to some extent in the LnS nanocrystals, where Ln = Eu^{3+}, Tb^{3+}, and Nd^{3+}, this is the first known report of Yb^{3+} sensitization through the band

gap of a semiconductor nanocrystal. EuS, TbS, and NdS nanocrystals appear to exhibit more complex energy transfer processes than what was observed for doped nanocrystal systems (indicated by the presence of both band gap and lanthanide excitation profiles upon either excitation monitoring band gap emission or excitation upon monitoring lanthanide emission). Although there is a larger volume of surface lanthanides which can be quenched by solvent vibrations, lanthanides within the core of these particles, as well as surface atoms to some extent, are well protected within these nanocrystal systems (as indicated by long luminescence lifetimes).

An additional advantage arises from the use of surface bound DTPA complexes for particle purification and solubility in water. DTPA complexes with lanthanides have to potential for further modification for use in a variety of different potential bioapplications. Lanthanide DTPA complexes have been reported for potential use for conjugation to biomolecules.[33-35] Existing literature on modification of the DTPA moiety may allow future work on modification of these systems for use in bioassays.

Initial work has been started on formation of ternary nanocrystal systems of these materials. It is believed that by combining lanthanide cations within these systems, white emission can be obtained. White emitting particles have the potential to serve as energy efficient lighting sources. By varying the ratios of visibly emitting lanthanides such as terbium and europium, and using the blue emission from the nanocrystal band gap, it is believed that the white emission can be obtained.

Experiments in which the nanocrystals are coated with ZnS shells are in their infancy and may serve to better protect the lanthanide cations and enhance lanthanide sensitization within these systems.

6.5 REFERENCES

(1) Thongchant, S.; Hasegawa, Y.; Wada, Y.; Yanagida, S. *J. Phys. Chem. B: At. Mol. Opt. Phys.* **2003**, *107*, 2193 - 2196.

(2) Kataoka, T.; Tsukahara, Y.; Hasegawa, Y.; Wada, Y. *Chem. Commun.* **2005**, 6038-6040.

(3) Hasegawa, Y.; Afzaal, M.; O'Brien, P.; Wada, Y.; Yanagida, S. *Chem. Commun.* **2005**, 242 - 243.

(4) Hasegawa, Y.; Okada, Y.; Kataoka, T.; Sakata, T.; Mori, H.; Wada, Y. *J. Phys. Chem. B: At. Mol. Opt. Phys.* **2006**, *110*, 9008-9011.

(5) Regulacio, M. D.; Tomson, N.; Stoll, S. L. *Chem. Mater.* **2005**, *17*, 3114-3121.

(6) Regulacio, M. D.; Bussmann, K.; Lewis, B.; Stoll, S. L. *J. Am. Chem. Soc.* **2006**, *128*, 11173-11179.

(7) Zhao, F.; Sun, H.-L.; Gao, S.; Su, G. *J. Mater. Chem.* **2005**, *15*, 4209-4214.

(8) Prokofiev, A. V.; Shelykh, A. I.; Melekh, B. T. *J. Alloys Compd.* **1996**, *242*, 41 - 44.

(9) Gruber, J. B.; Burriel, R.; Westrum, E. F., Jr.; Plautz, W.; Metz, G.; Ma, X.-X. *J. Chem. Phys.* **1991**, *95*, 1964 - 1972.

(10) Henderson, J. R.; Muramoto, M.; Loh, E.; Gruber, J. B. *J. Chem. Phys.* **1967**, *47*, 3347 - 3356.

(11) Gruber, J. B.; Westrum, E. F., Jr.; Burriel, R.; Palmer, P. E.; Beaudry, B. J.; Plautz, W. A. *J. Chem. Phys.* **1989**, *91*, 4838 - 4848.

(12) Mirkovic, T.; Hines, M. A.; Nair, P. S.; Scholes, G. D. *Chem. Mater.* **2005**, *17*, 3451-3456.

(13) Regulacio, M. D.; Kar, r.; Zuniga, E.; Wang, G.; Dollahon, N. R.; Yee, G. T.; Stoll, S. L. *Chem. Mater.* **2008**, *20*, 3368 - 3376.

(14) Takeda, T. *J. Magn. Magn. Mater.* **1977**, *5*, 315 - 324.

(15) Kurnick, S. W.; Meyer, C. *J. Phys. Chem. Solids* **1964**, *25*, 115 - 121.

(16) Kataoka, T.; Tsukahara, Y.; Hasegawa, Y.; Wada, Y. *Chem. Commun.* **2005**, 6038-6040.

(17) Dabbousi, B. O.; Rodriguez-Viejo, J.; Mikulec, F. V.; Heine, J. R.; Mattoussi, H.; Ober, R.; Jensen, K. F.; Bawendi, M. G. *J. Phys. Chem. B: At. Mol. Opt. Phys.* **1997**, *101*, 9463-9475.

(18) Hines, M. A.; Guyot-Sionnest, P. *J. Phys. Chem.* **1996**, *100*, 468-71.

(19) Rasband, W.; 1.40g ed.; National Institute of Health.

(20) Erwin, S. C.; Zu, L.; Haftel, M. I.; Efros, A. L.; Kennedy, T. A.; Norris, D. J. *Nature* **2005**, *436*, 91-94.

(21) Yu, W. W.; Qu, L.; Guo, W.; Peng, X. *Chem. Mater.* **2003**, *15*, 2854-2860.

(22) Striolo, A.; Ward, J.; Prausnitz, J. M.; Parak, W. J.; Zanchet, D.; Gerion, D.; Milliron, D. J.; Alivisatos, A. P. *J. Phys. Chem. B: At. Mol. Opt. Phys.* **2002**.

(23) Eastman, D. E.; Holtzberg, F.; Methfessel, S. *Phys. Rev. Lett.* **1969**, *23*, 226.

(24) Sarka, L.; Banyai, I.; Brucher, E.; Kiraly, R.; Platzek, J.; Raduchel, B.; Schmitt -Willich, H. *Dalton Trans.* **2000**, 3699 - 3703.

(25) Rizkalla, E.; Choppin, G. R.; Cacheris, W. *Inorg. Chem.* **1992**, *32*, 582 - 586.

(26) Gritmon, T. F.; Goedken, M. P.; Choppin, G. R. *J. Inorg. Nucl. Chem.* **1977**, *39*, 2021 - 2023.

(27) Carson, A. S.; Laye, P. G.; Smith, P. N. *J. Chem. Soc. A* **1968**, 1384 - 1386.

(28) Harder, R.; Chaberek, S. *J. Inorg. Nucl. Chem.* **1959**, *11*, 197 - 209.

(29) Ferrand, A.-C.; Imbert, D.; Cauvin, A.-S.; Vandevyver, C. D. B.; Bunzli, J.-C. G. *Chem.-Eur. J.* **2007**, *13*, 8678 - 8687.

(30) Petoud, S.; Muller, G.; Moore, E. G.; Xu, J.; Sokolnicki, J.; Riehl, J. P.; Le, U. N.; Cohen, S. M.; Raymond, K. N. *J. Am. Chem. Soc.* **2006**, *129*, 77 - 83.

(31) Zhang, J.; Petoud, S. *Chem.-Eur. J.* **2008**, *14*, 1264 - 1272.

(32) Zhang, J.; Shade, C. M.; Chengelis, D. A.; Petoud, S. *J. Am. Chem. Soc.* **2007**, *129*, 14834 - 14835.

(33) Chen, J.; Selvin, P. R. *Bioconjugate Chem.* **1999**, *10*, 311 - 315.

(34) Hsieh, W.-Y.; Liu, S. *Inorg. Chem.* **2004**, *43*, 6006 - 6014.

(35) Ge, P.; Selvin, P. R. *Bioconjugate Chem.* **2004**, *15*, 1088 - 1094.

APPENDIX A

TRANSMISSION ELECTRON MICROSCOPY IMAGES OF CDSE NANOCRYSTALS

The images shown in this appendix are the combined attempts at obtaining TEM images to determine particle size and crystallinity. While the experimental section outlines several different instruments, the specific instrument models and operating voltages, as well as the collaborator information is provided alongside the images herein. Instruments used are housed in the University of Pittsburgh Biology Department, the Center for Biological Imaging (UPMC), and the Department of Engineering and Materials Science. An additional instrument was used at Oak Ridge National Laboratory.

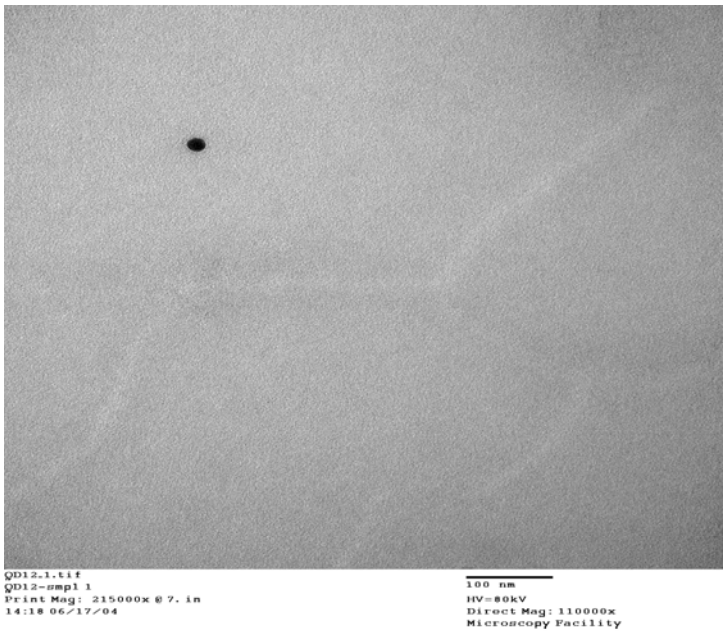

Figure A.1 Image was obtained through collaboration with Tom Harper in the University of Pittsburgh Biology Department. Images were collected using an FEI Morgagni 268operating at 80 kV.

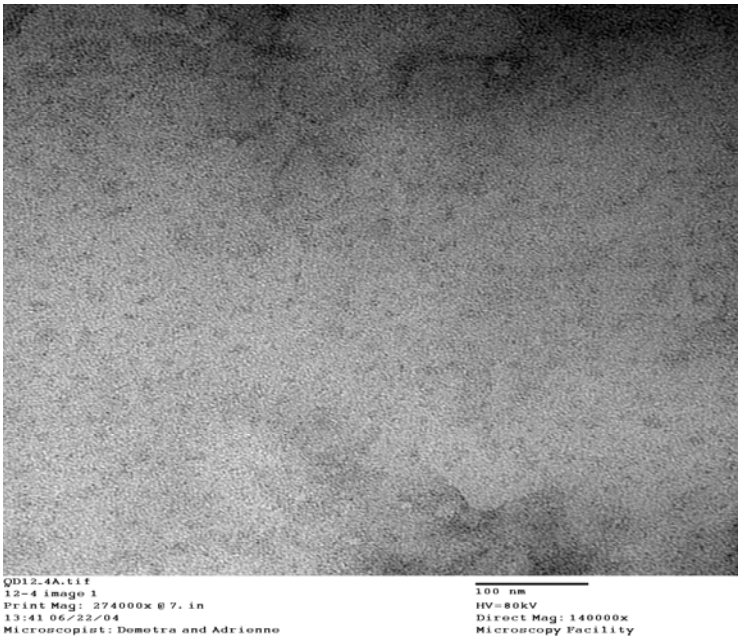

Figure A.2. Image was obtained through collaboration with Tom Harper in the University of Pittsburgh Biology Department. Images were collected using an FEI Morgagni 268operating at 80 kV.

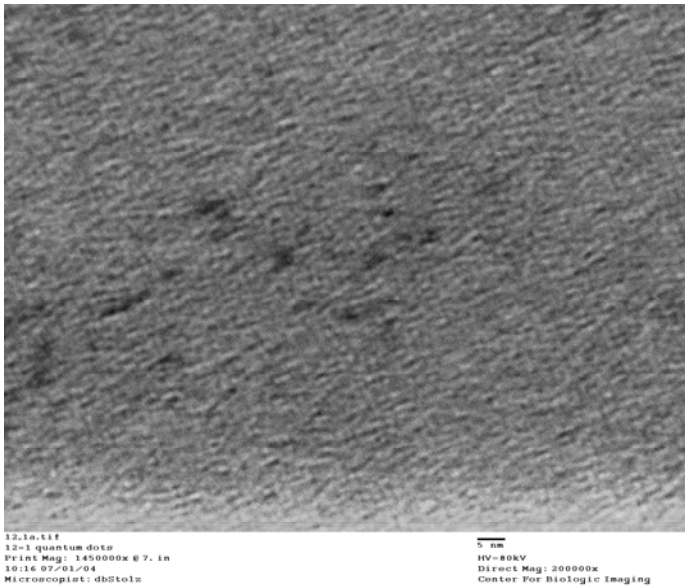

Figure A.3. Image was obtained through collaboration with the University of Pittsburgh Center for Biological Imaging and Dr. Simon Watkins. These images were collected using a JEOL 1210 TEM operating at 120 kV.

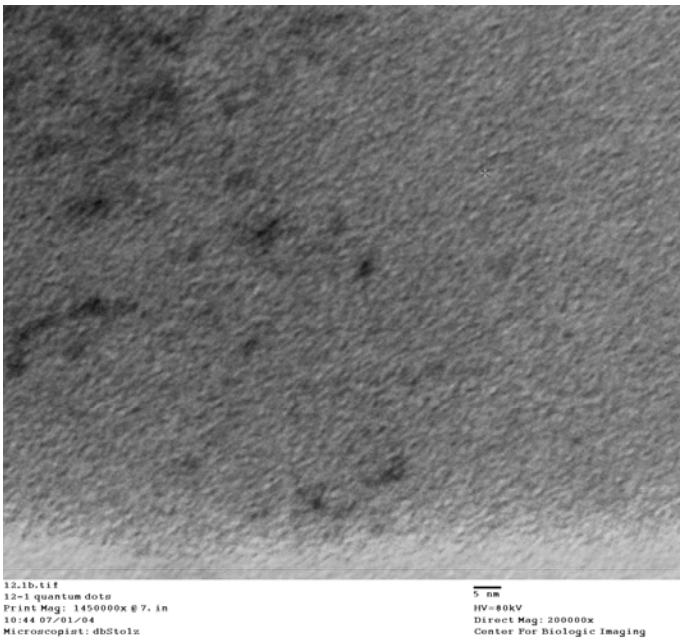

Figure A.4. Image was obtained through collaboration with the University of Pittsburgh Center for Biological Imaging and Dr. Simon Watkins. These images were collected using a JEOL 1210 TEM operating at 120 kV.

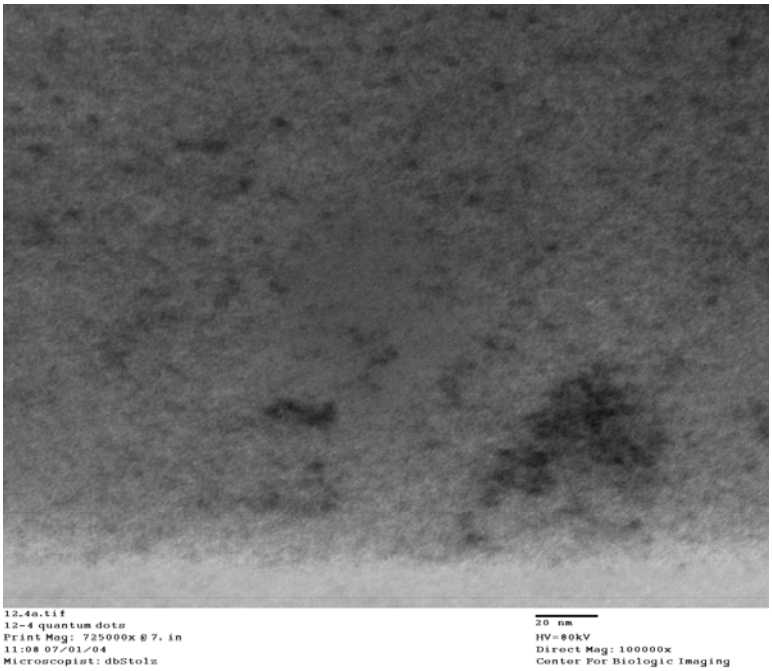

Figure A.5. Image was obtained through collaboration with the University of Pittsburgh Center for Biological Imaging and Dr. Simon Watkins. These images were collected using a JEOL 1210 TEM operating at 120 kV.

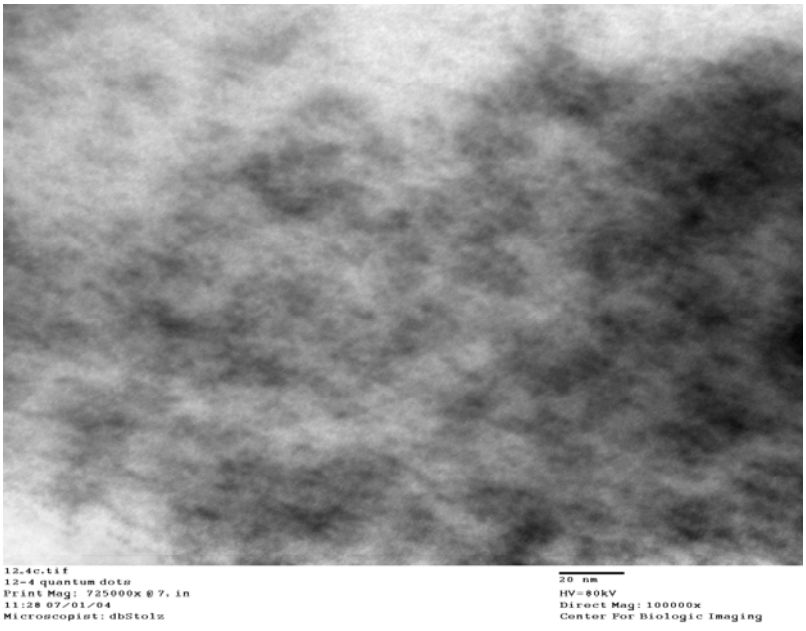

Figure A.6. Image was obtained through collaboration with the University of Pittsburgh Center for Biological Imaging and Dr. Simon Watkins. These images were collected using a JEOL 1210 TEM operating at 120 kV.

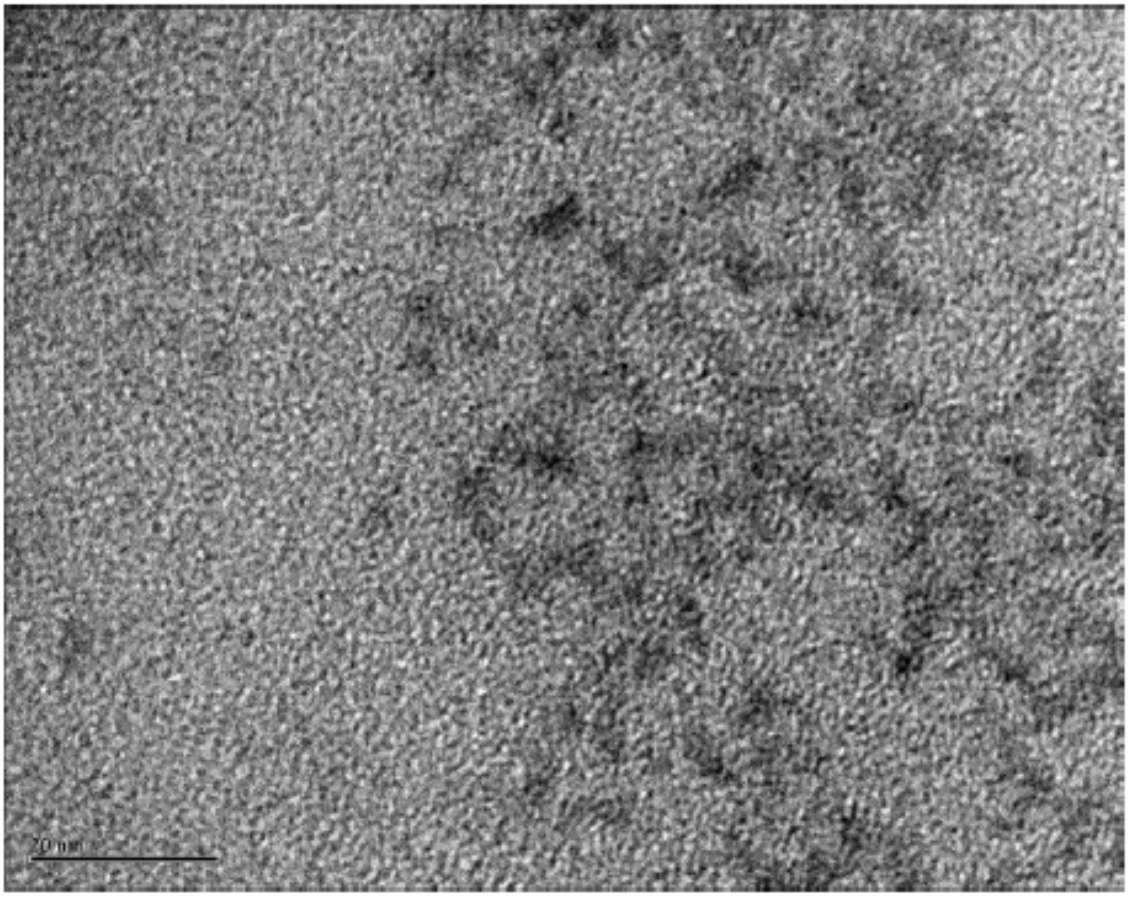

Figure A.7. Image obtained through collaboration with Cole Van Ormer in the University of Pittsburgh Department of Materials Science and Engineering. This image was obtained using a JEOL 2000-FX scanning transmission electron microscope operating at a maximum of 200 kV.

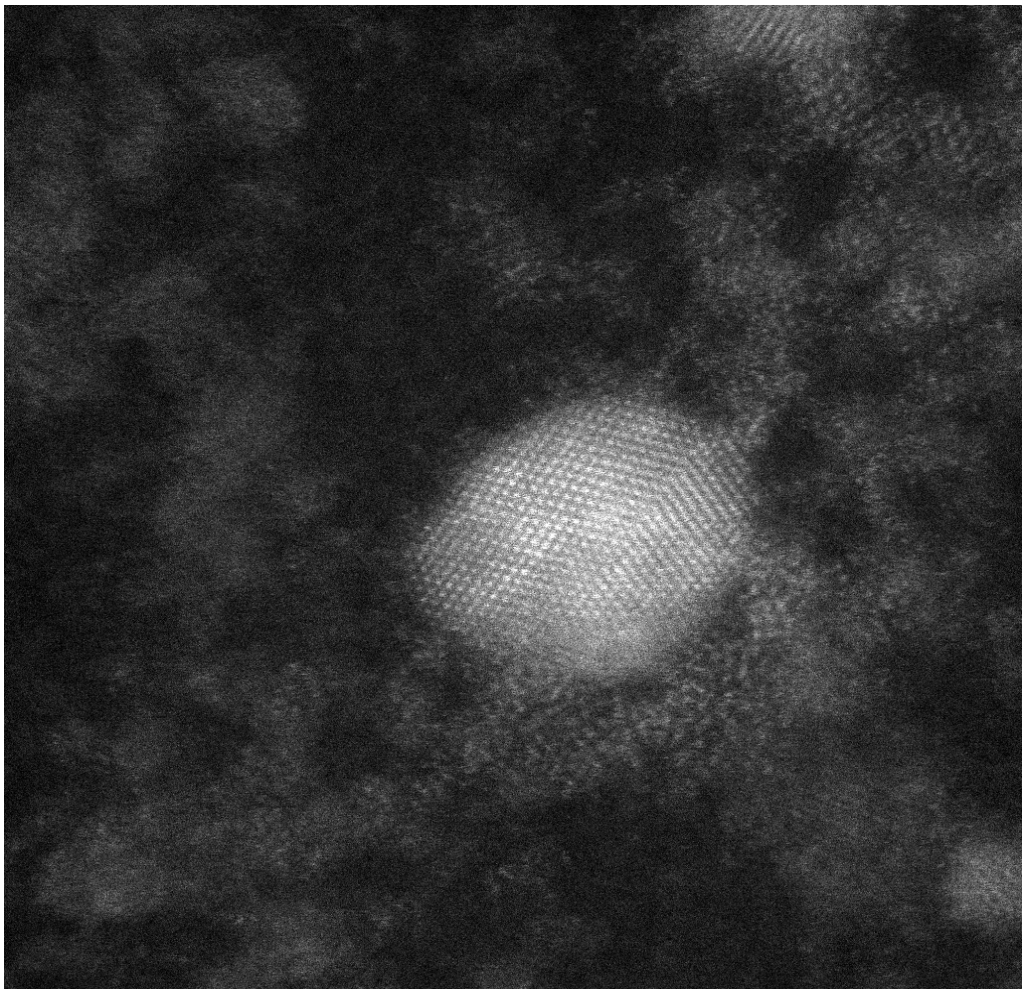

Figure A.8. The final imaging attempts made for CdSe nanocrystals were done through collaboration with Dr. James McBride and Dr. Sandra Rosenthal at Vanderbilt University in conjunction with Oak Ridge National Laboratory. This was the first access to high resolution TEM imaging. The instrument used was a VG Microscopes model HB603U STEM.

APPENDIX B

CDSE NANOCRYSTAL COATING INFORMTION

A series of preliminary surface exchange procedures were performed on CdSe:Ln nanocrystals. Surface modification using EDTA, micelles, and mercatpoacetic acid were carried out. The preliminary studies of the photophysical properties of water soluble nanocrystals are reported here. Core/shell nanocrystal syntheses were also performed, the preliminary results of which are reported below.

The initial coating experiments involved attempts at surface exchange and surface binding of EDTA, ethylenediaminetetraacetic acid. CdSe nanocrystals dissolved in a small amount of chloroform (1 mL) were added to a solution of deprotonated EDTA (in excess) in water. If an exchange would take place, it would be through binding of the multidentate ligand to the metals at the nanocrystal surface. Emission and excitation spectra were collected on CdSe:Tb nanocrystals dissolved in water, as a control, and CdSe:Tb nanocrystals dissolved in an aqueous EDTA solution (Figure B.1).

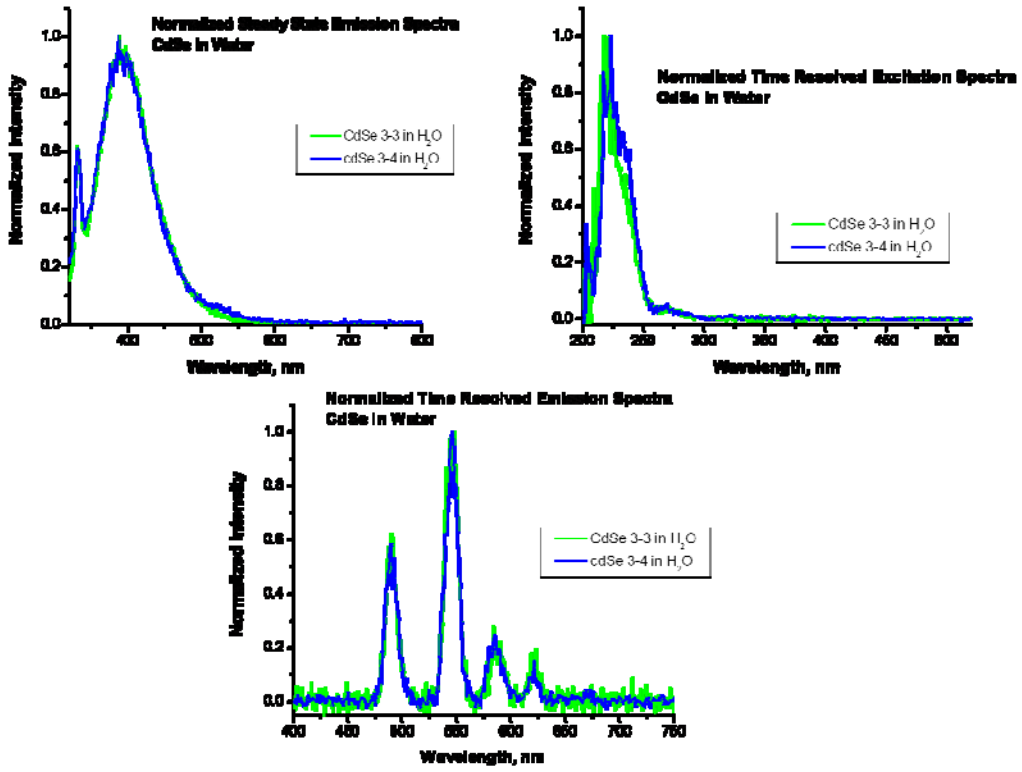

Figure B.1. Steady state and time resolved excitation and emission spectra of CdSe:Tb nanocrystals in water.

The steady state emission spectra show only a broadened band centered at 400 nm, most likely resulting from background fluorescence and not the nanocrystals, which exhibit a

broadened band centered at lower energy. The time resolved excitation spectra of CdSe in water exhibit only a band centered at approximately 225 nm and corresponding emission spectra exhibiting all 4 Tb^{3+} transitions. The lanthanide emission, based on the excitation spectra, is most likely the result of direct excitation and not the result of energy transfer through the nanocrystal band gap. If energy transfer were occurring, the excitation spectra would appear broader and at lower energy.

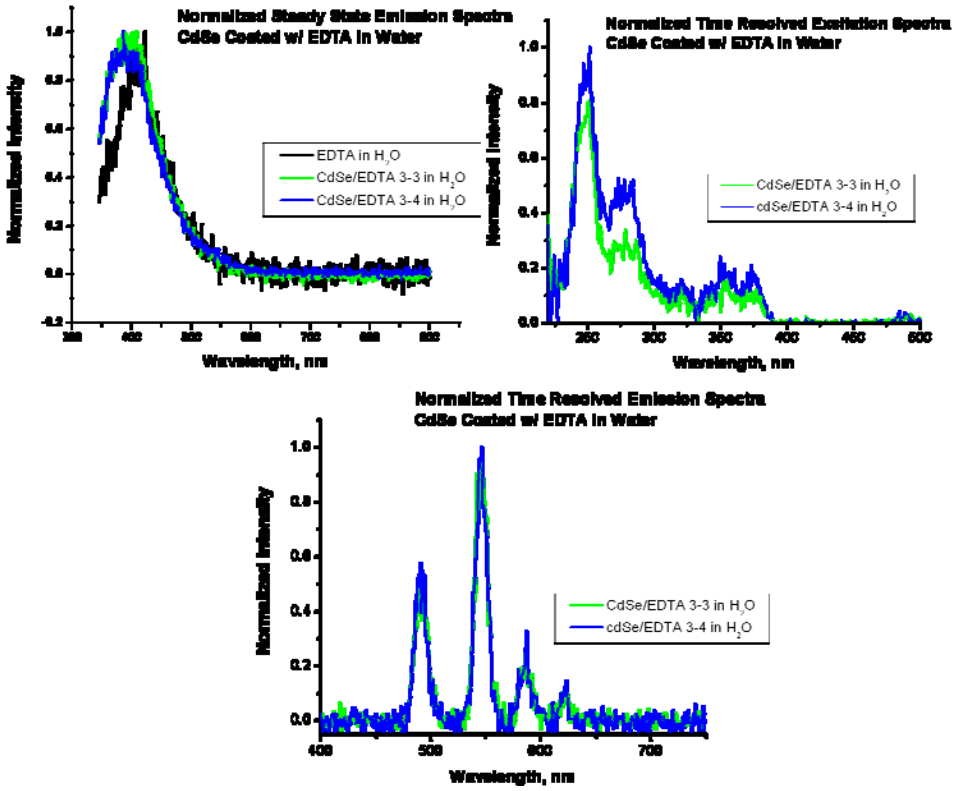

Figure B.2. Steady state and time resolved emission and excitation of EDTA coated CdSe:Tb nanocrystals in water.

Upon the addition of EDTA, no change in steady state emission spectra is observed relative to the water control. The nanocrystal emission is also quenched upon addition to the aqueous EDTA solution. The time resolved spectra is different from what has been described

previously. A broader band appears on the excitation profile and therefore gives indication of energy transfer in addition to direct excitation characteristics. The emission spectra upon excitation at 400 nm also show the characteristic Tb^{3+} transitions, which are at least partially contributed to by sensitization through the nanocrystal band gap. In order to better quantify the energy transfer within this system and better understand the extent of surface exchange/passivation and quenching, additional measurements such as luminescence lifetimes and quantum yields would need to be collected.

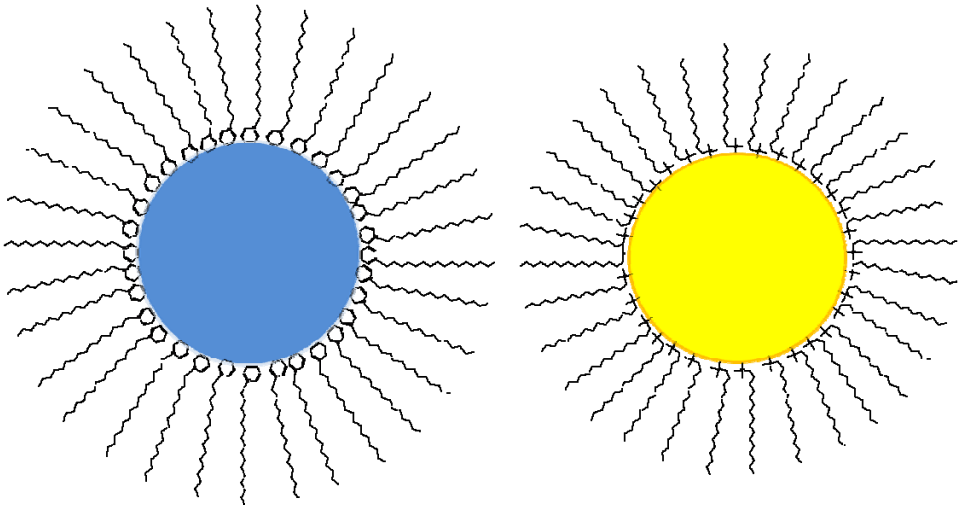

Figure B.3. Cartoon illustrating surface modification with 2 different micelles.

The second approach to nanocrystal surface modification was through the use of different types of micelles to encapsulate the nanocrystal. The detailed procedures are described in the experimental section above and the data presented here. The work with micelle 1, (hexadecylpyridinium bromide) results in very weak band gap emission centered at 550 nm (figure x) which is overshadowed by background emission from the micelle itself. It is expected that upon surface modification of core CdSe nanocrystals the emission is significantly quenched,

this is further illustrated in these experiments. The Time resolved excitation and emission spectra are also weak, and the signal is difficult to discriminate from noise. The terbium emission is still observed, but the signal to noise ratio is low even upon measuring with full instrument slit widths. As mentioned in the previous surface modification, additional spectroscopic studies would need to be conducted in order to obtain semi-quantitative information regarding the extent of micelle formation around the nanocrystal.

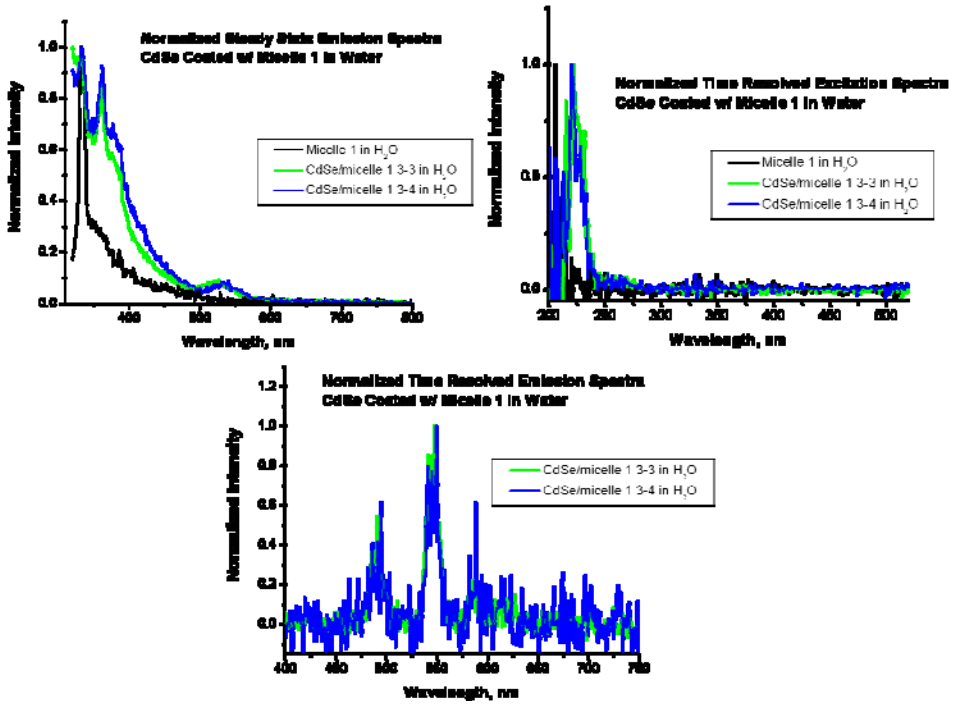

Figure B.4. Steady state and time resolved emission and excitation spectra of micelle 1 coated CdSe:Tb nanocrystals in water.

A second type of micelle was tested, hexadecyltrimethylammonium bromide, or micelle 2, in an attempt to increase the water solubility of the nanocrystals. Similar results were obtained for the second micelle as for the first. Steady state emission spectra of the combination of CdSe/micelle 2 particles in water were compared to a solution of micelle 2 in water in the

absence of nanocrystals. The emission spectra yielded inconclusive results in that the water/micelle solution an emission band was observed at approximately 475 nm, however only higher energy bands were observed in the micelle/CdSe solutions. Signals with very low intensity were observed on the time resolved excitation and emission spectra. Although the spectra illustrate low signal to noise ratios, an excitation band is observed spanning from 250 – 300 nm, the shape cannot be discriminated clearly however it is likely that this is the result of direct excitation of the Tb^{3+}. Due to initial studies on the 2 available micelles, the method was determined unsuccessful and alternative surface passivation methods were attempted.

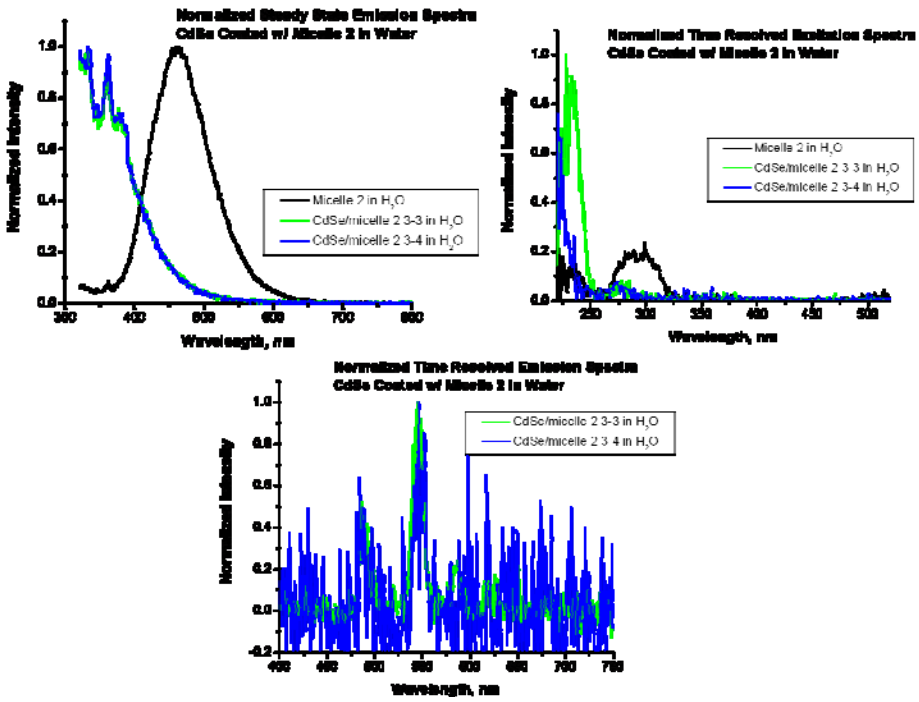

Figure B.5. Steady state and time resolved emission and excitation spectra of micelle 2 coated CdSe:Tb nanocrystals in water.

Procedures have been established in the literature for the surface exchange of CdSe nanocrystals with mercaptoacetic acid,[178] and it was therefore another attempt to try towards surface modification process. The TOPO coated nanocrystals were heated to 60° C while stirring for several hours in a solution of MAA. Upon completion of the reaction, potassium tert butoxide was added to precipitate out the materials and the nanocrystals were purified by centrifugation prior to dissolution in water for analysis.

The luminescence spectra obtained for the CdSe:Tb nanocrystals whose surface have been modified with MAA are shown in Figure B.6. Time resolved and steady state spectra are shown to quantify the effects of the MAA on both the Tb^{3+} and the CdSe emission properties. The spectrum on the right, CdSe after MAA surface exchange, exhibits significant quenching of both the lanthanide and of the CdSe emission. A slight red shift in the nanocrystal emission band upon surface modification indicates successful exchange of TOPO with the MAA.

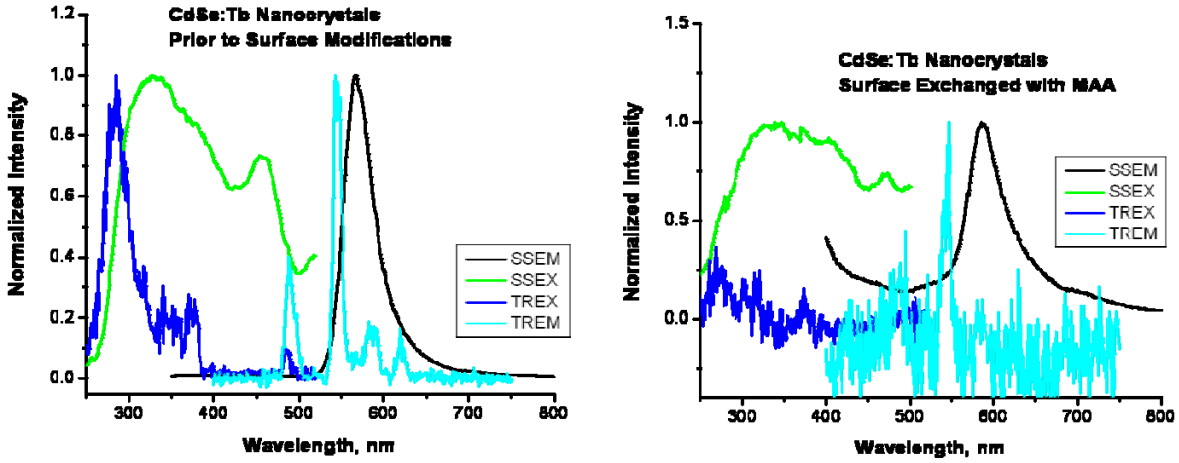

Figure B.6. Steady state and time resolved emission and excitation spectra of MAA surface exchanged CdSe:Tb in water.

While MAA modification was successful in that it did take place, the significant quenching effects of the surface thiol needed to be addressed. Since CdSe nanocrystals have shown enhanced luminescence properties through the addition of a shell of larger band gap material we have decided to test the effect of the coating of our CdSe nanocrystals with a ZnS shell prior to surface exchange with the goal of minimizing quenching of the lanthanide luminescence. The procedures are described in the experimental section above and the data resulting spectra are shown below.

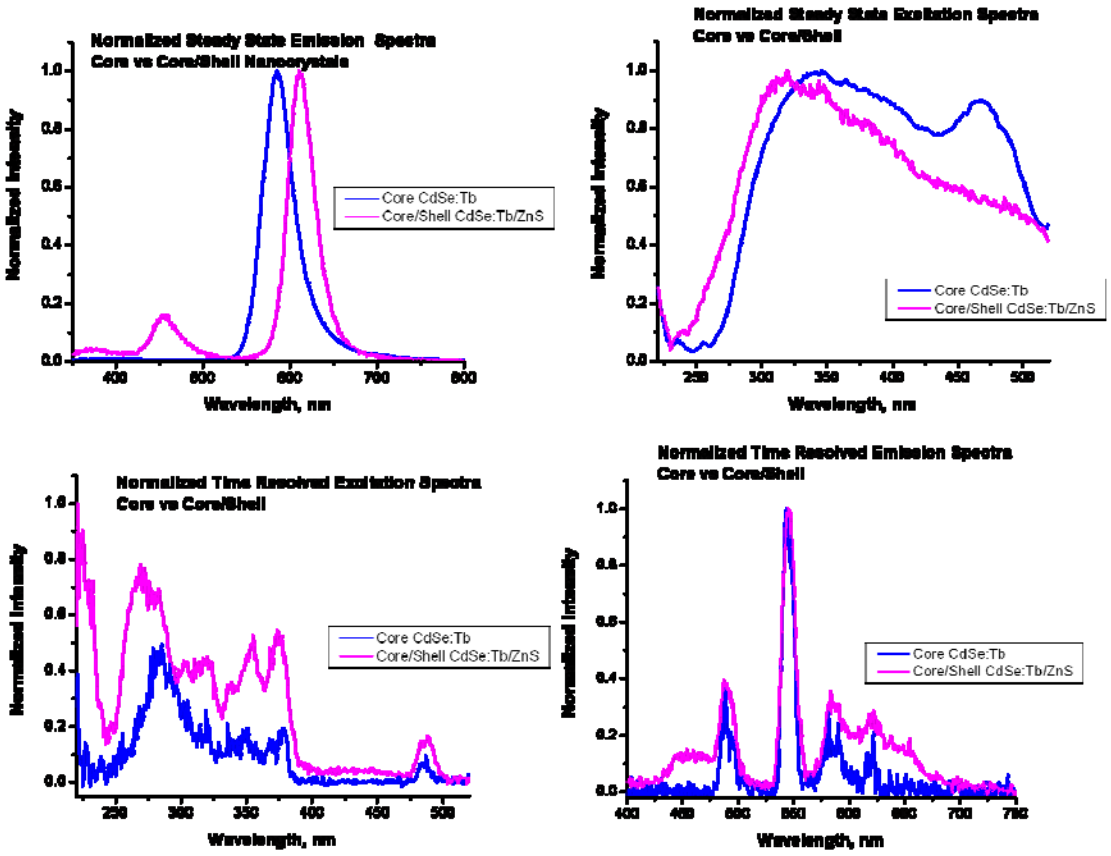

Figure B.7. Steady state ant time resolved emission and excitation spectra of core CdSe:Tb vs. core/shell CdSe:Tb/ZnS nanocrystals in chloroform.

The addition of a shell is evidenced by the observed shift of the band gap emission towards lower energy. The appearance of an additional band centered at 450 nm is hypothesized to result from ZnS band gap emission. The steady state and time resolved excitation spectra exhibit some overlap, however direct excitation appears to dominate the spectra.

Once addition of a ZnS shell was confirmed spectroscopically with the steady-state emission spectrum, we have compared the effects of MAA on core/shell systems relative to core nanocrystal systems. MAA surface exchanges were carried out using the same protocol as previously described for CdSe:Tb/ZnS as for CdSe:Tb. Steady state and time resolved emission and excitation spectra were recorded to determine the result of the surface exchange as well as to qualitatively determine quenching effects.

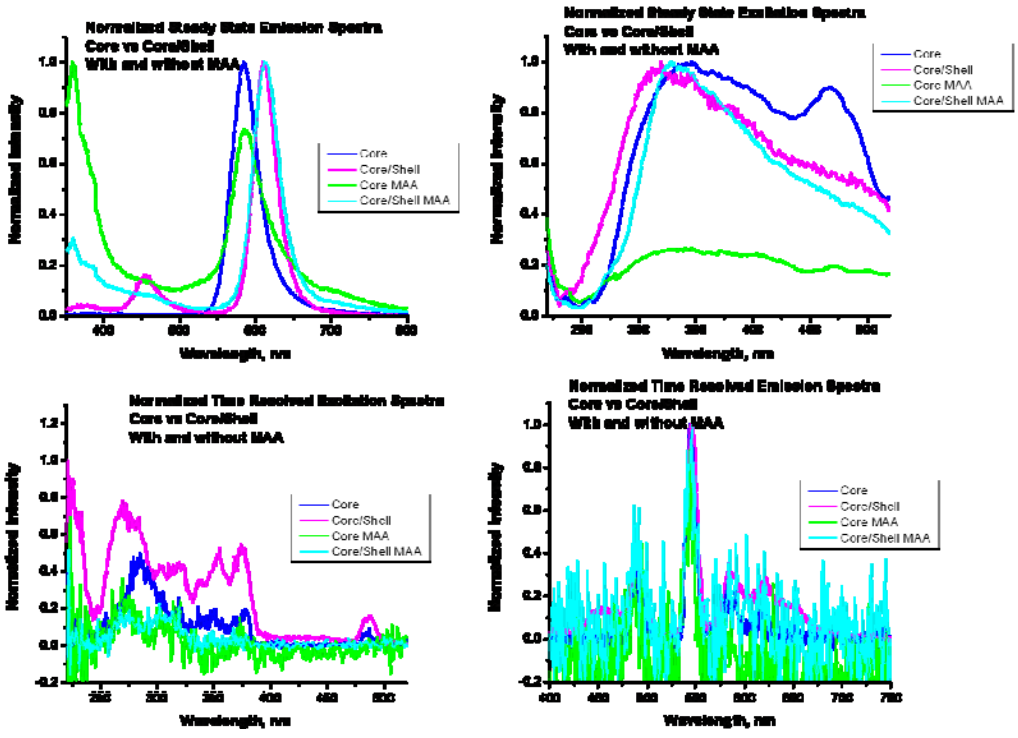

Figure B.8. Steady state and time resolved emission and excitation spectra of core/shell CdSe:Tb/ZnS and core CdSe:Tb nanocrystals with and without MAA surface exchange.

Upon comparison of the photophysical properties of the core and core/shell MAA coated nanocrystals; the data does not indicate a significant improvement for core/shell MAA over core MAA on the basis of Tb^{3+} emission. In both cases the lanthanide emission intensity is significantly reduced and the signal to noise ratio decreased, emission and excitation spectra collected for MAA coated samples were collected at maximum slit widths and may therefore be approaching the limit of detection of the instrument. Quantum yield data was not collected to determine the extent of quenching for all four systems, nor were luminescence lifetimes recorded to study the lanthanide environment within the nanocrystal structure.

APPENDIX C

TRANSMISSION ELECTRON MICROSCOPY IMAGES OF ZNS NANOCRYSTALS

Once we obtained access to the Hitachi H-7100 TEM operating at 75 kV at Carnegie Mellon University, we were able to obtain images of higher quality with less background interference than the previously used low resolution TEM instruments. The majority of the images herein were collected using this instrument operated by Joseph Suhan. The final high resolution TEM image was obtained using a JEOL-2100 CF operating between 120kv and 200kv operated by Dr. Andreas Kulovits. This high resolution instrument is housed in the Nanoscale Fabrication and Characterization Facility (NFCF) of the Petersen Institute of NanoScience and Engineering (PINSE) within the department of Materials Science and Engineering at the University of Pittsburgh.

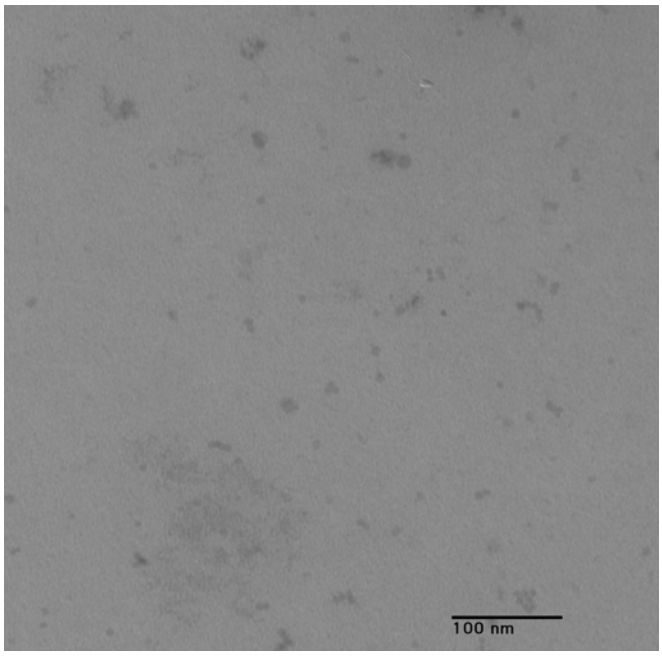

Figure C.1 Low resolution TEM obtained through collaboration with Joseph Suhan at Carnegie Mellon University using a Hitachi H-7100 TEM.

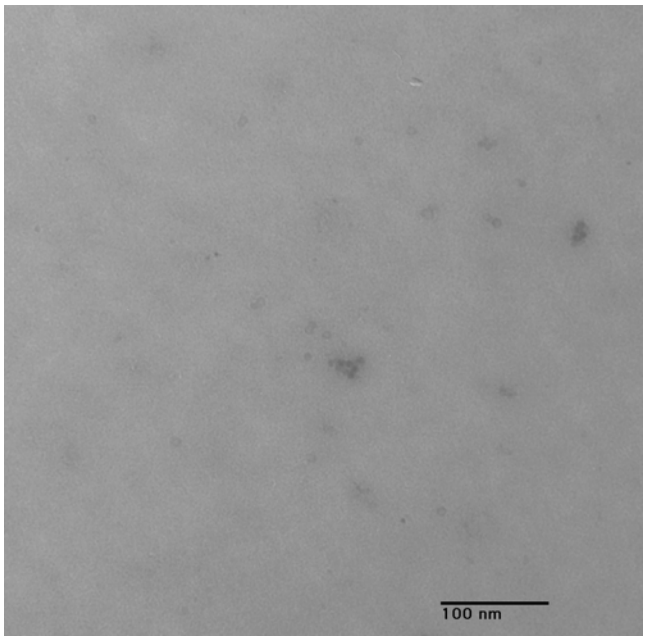

Figure C.2. Low resolution TEM obtained through collaboration with Joseph Suhan at Carnegie Mellon University using a Hitachi H-7100 TEM.

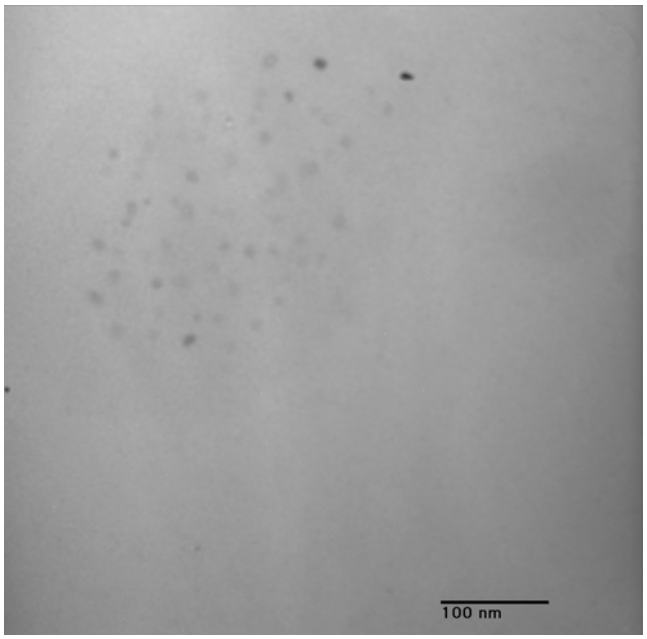

Figure C.3. Low resolution TEM obtained through collaboration with Joseph Suhan at Carnegie Mellon University using a Hitachi H-7100 TEM.

Figure C.4. Low resolution TEM obtained through collaboration with Joseph Suhan at Carnegie Mellon University using a Hitachi H-7100 TEM.

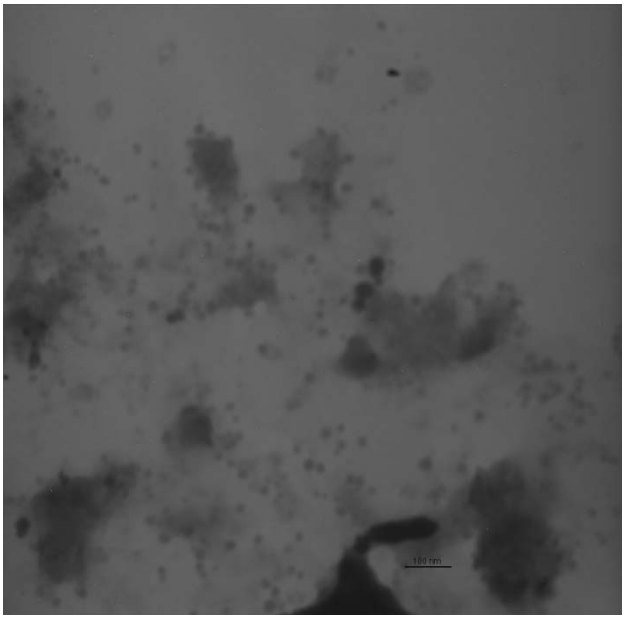

Figure C.5. Low resolution TEM obtained through collaboration with Joseph Suhan at Carnegie Mellon University using a Hitachi H-7100 TEM.

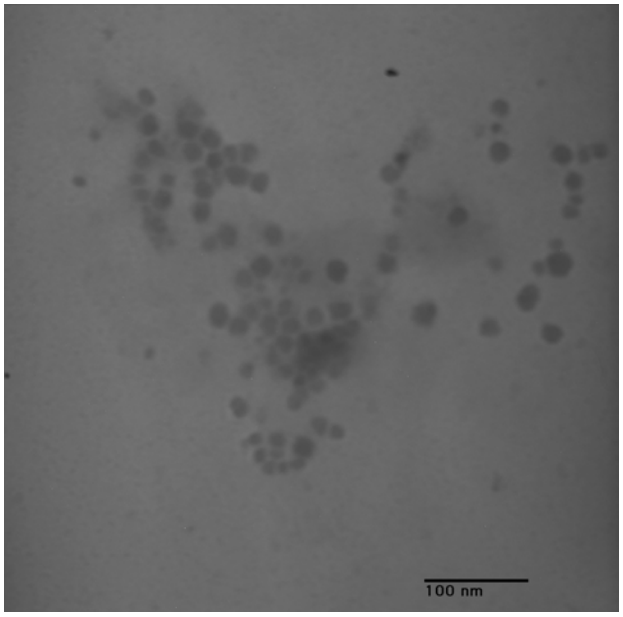

Figure C.6. Low resolution TEM obtained through collaboration with Joseph Suhan at Carnegie Mellon University using a Hitachi H-7100 TEM.

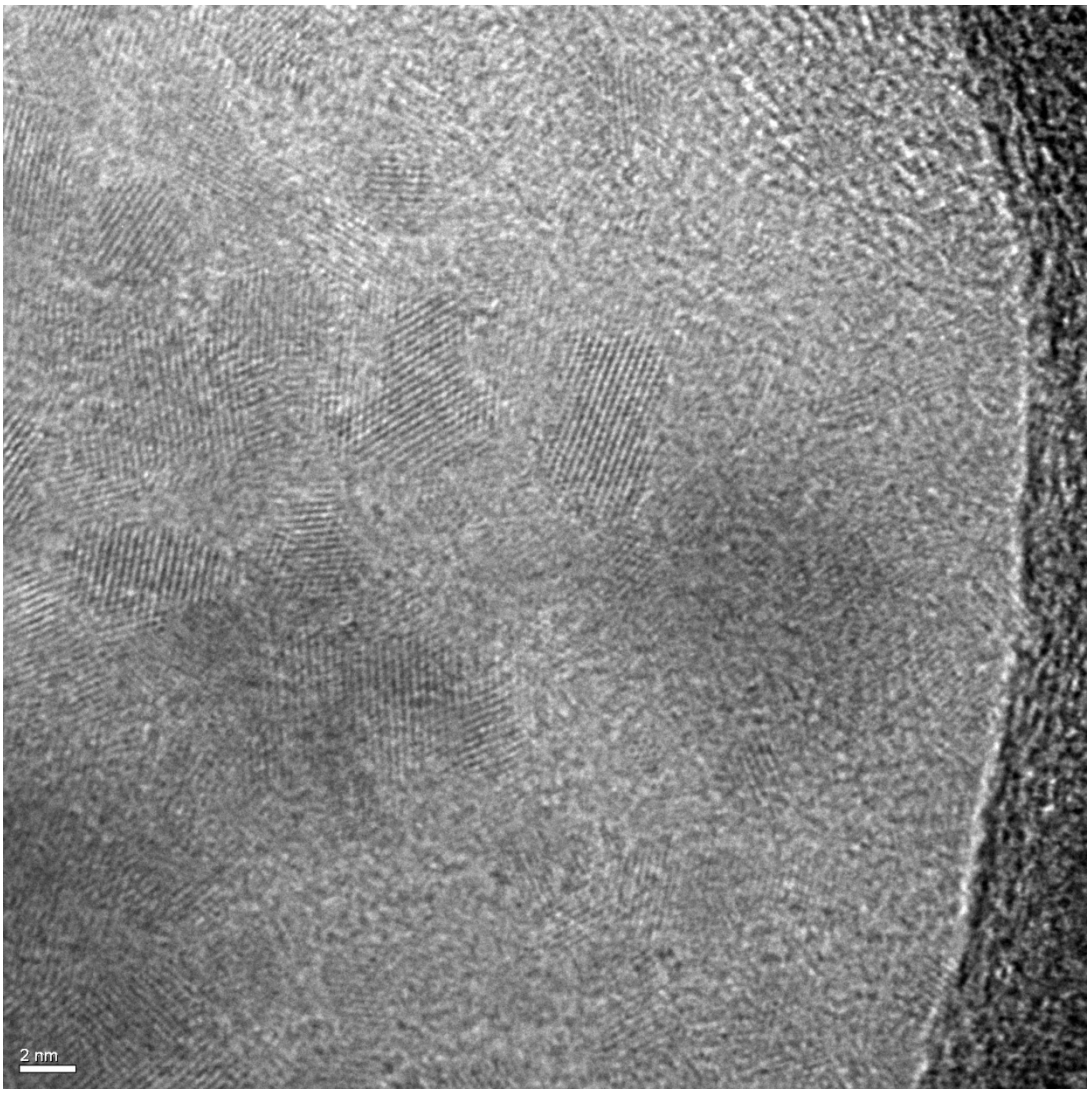

Figure C.7. This high resolution image was obtained through collaboration with Dr. Andreas Kulovits (Department of Engineering and Materials Science) and Chad Shade (Department of Chemistry) using a JEOL 2100 CF.

APPENDIX D

D.1 ZNS NANOCRYSTAL COATING INFORMATION

Preliminary work done on surface modification of the ZnS:Ln nanocrystal involved the use of micelles to promote nanocrystals solubility in aqueous solutions. A dilute Ivory Soap© solution (1:100 v/v, soap to water) was prepared and added to ZnS:Ln nanocrystals which had been previously purified through precipitation with methanol and dried under vacuum. The resulting emission spectra are shown below (Figure D.1). The nanocrystals were dissolved in the soap solution and emission spectra were collected over a period of several hours. Upon addition of the soap solution to the initial nanocrystals, a slight red shift in the emission profile of the band gap emission is observed. This red shift is also observed in more complicated surface exchanges such as MAA exchanges and is most likely the result of minimizing trap states resulting from dangling bonds on the particle surface. While the positions of the emission bands are relatively unchanged, the emission intensity of these nanocrystals is significantly quenched over time. This decrease in intensity may result from the micelle breaking down with time. If any organic solvent is trapped within the micelle it may interfere with the micelle formation around the nanocrystal, resulting in unstable materials which precipitate from aqueous solutions (it should be noted that nanocrystal precipitation was observed to an extent over time in the form of white precipitate lining the fluorescence cuvette).

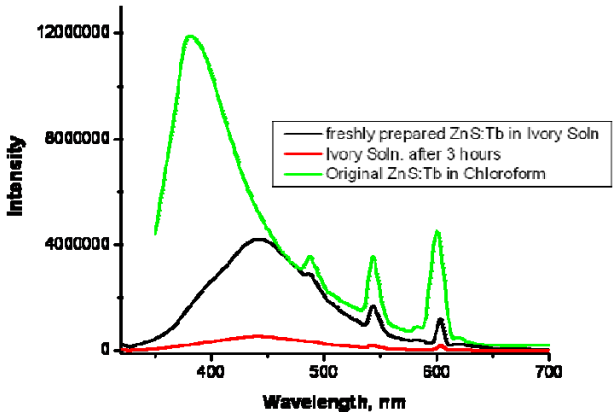

FigureD.1. ZnS:Tb nanocrystals passivated with micelle solution containing Ivory soap © in water. Emission spectra were collected upon excitation at 300 nm.

While soap solutions are a relatively simple approach to renduring ZnS nanocrystals water soluble, they are not the most stable of methods. Decreases in emission intensity are observed over time and nanocrystals do begin to precipitate from the aqueus media. More involved surface passivation procedures are necessary in order to eliminate precipitation and to minimize quenching.

D.2 SYNTHESIS OF ZNS NANOCRYSTALS USING 2 MATERIALS

In addition to synthesis of single lanthanide-containing ZnS nanocrystal systems, preliminary studies were conducted on the incorporation of two different lanthanide cations within the nanocrystal systems. The synthetic procedures were the same as for singly doped systems, with

the total dopant concentration remaining unchanged. By varying the doping ratio of the different lanthanide cations, we hypothesize that white emitting light is achievable.

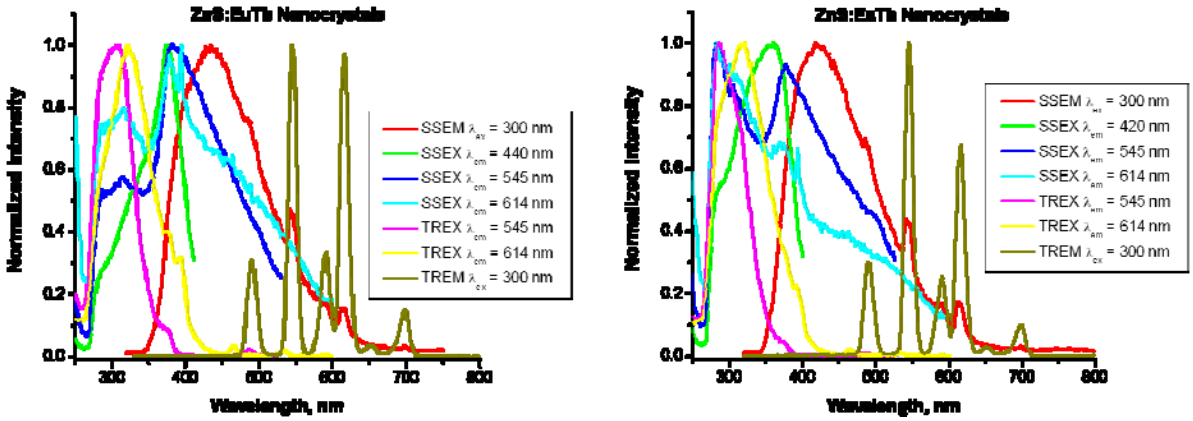

Figure D.2. Steady state and time resolved emission and excitation spectra of ZnS:EuTb batches. Both lanthanides were introduced into the reaction mixture without changing the total cation precursor or the total dopant percentage.

Figure D.2 above illustrates the presence of weak lanthanide signal arising from both Eu^{3+} and Tb^{3+} within this system. This emission is more clearly defined through time resolved measurments. Nanocrystal emission spectra were collected upon excitation at 300 nm and subsequent steady state excitation spectra were collected upon monitoring the nanocrystal band gap as well as the emission arising from the 545 nm emission band of Tb^{3+} and the 614 nm band of Eu^{3+}. Time resolved measurments were also recorded under the same conditions. The time resolved excitation spectra upon monitoring emission arising from both lanthanides does exhibit some overlap with the steady state excitation spectra upon monitoring nanocrystal band gap emission. This is indicative of some degree of sensitization within these doubly doped systems. These measurements are preliminary and further optimization of synthetic conditions is necessary to fully understand energy transfer as well as optimization of emission properties.

APPENDIX E

TRANSMISSION ELECTRON MICROSCOPY IMAGES OF LNS NANOCRYSTALS

The images shown in this appendix are the combined attempts at obtaining TEM images to determine particle size and crystallinity. While the experimental section outlines several different instruments, the specific instrument models and operating voltages, as well as the collaborator information is provided alongside the images herein. Initial imaging work was done through collaboration with Joseph Suhan at Carnegie Mellon University. The high resolution TEM instrument is housed in the Department of Engineering and Materials Science (PINSE).

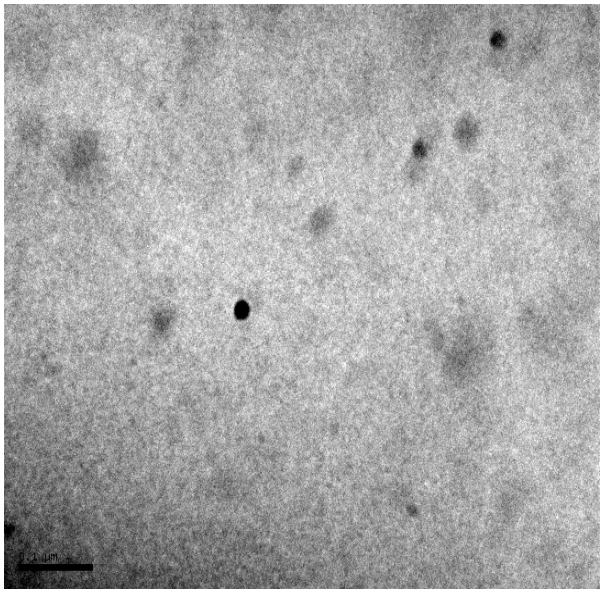

Figure E.1. Image obtained through collaboration with Joseph Suhan at Carnegie Mellon University using a Hitachi H-7100 TEM (TbS nanocrystals).

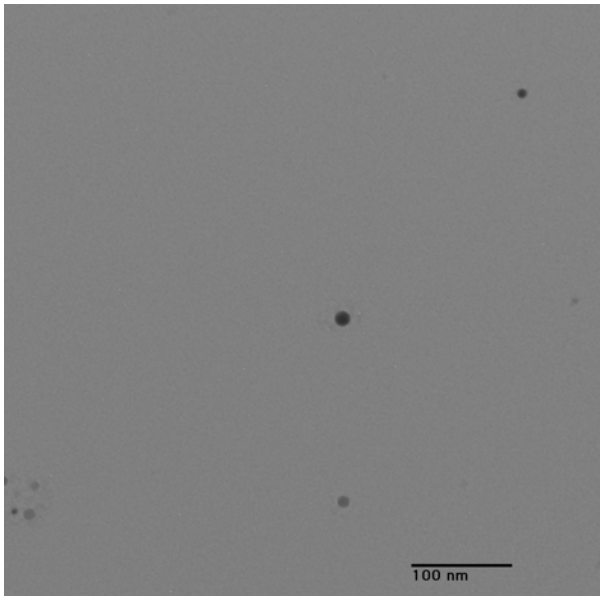

Figure E.2. Image obtained through collaboration with Joseph Suhan at Carnegie Mellon University using a Hitachi H-7100 TEM (TbS nanocrystals).

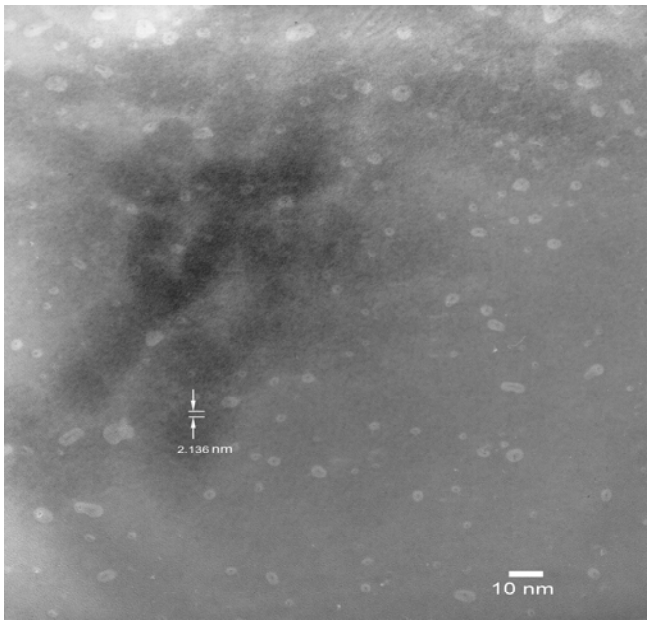

Figure E.3. Image obtained through collaboration with Joseph Suhan at Carnegie Mellon University using a Hitachi H-7100 TEM (TbS nanocrystals).

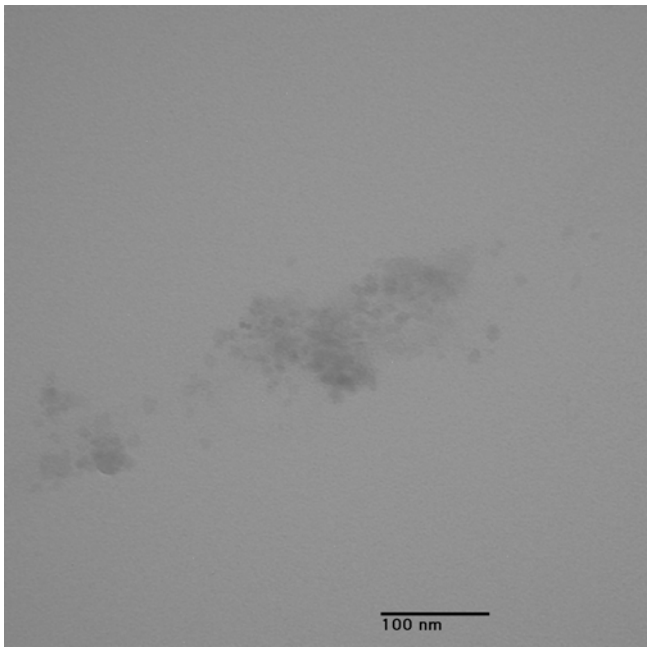

Figure E.4. Image obtained through collaboration with Joseph Suhan at Carnegie Mellon University using a Hitachi H-7100 TEM (TbS nanocrystals).

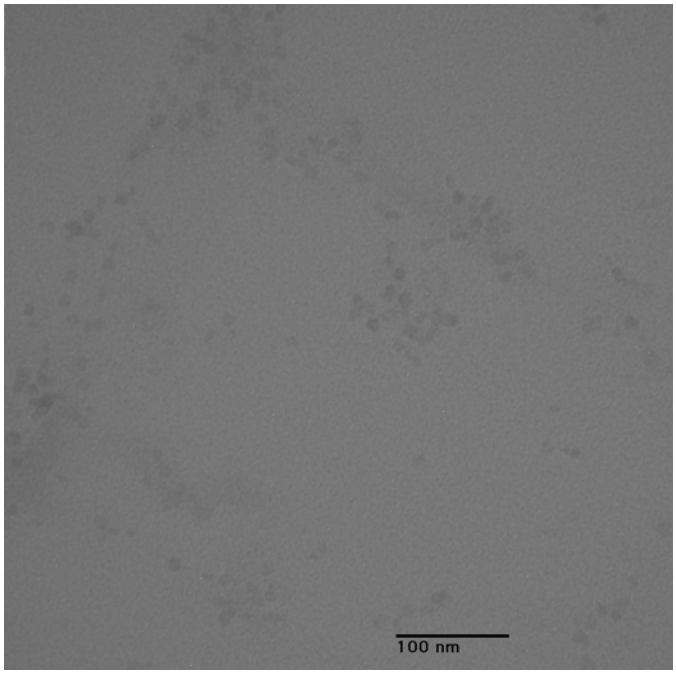

Figure E.5. Image obtained through collaboration with Joseph Suhan at Carnegie Mellon University using a Hitachi H-7100 TEM (TbS nanocrystals).

The following high resolution image was obtained through collaboration with Dr. Andreas Kulovits (Department of Engineering and Materials Science) and Chad Shade (Department of Chemistry) using a JEOL 2100 CF. Various LnS materials were imaged, images are identified appropriately.

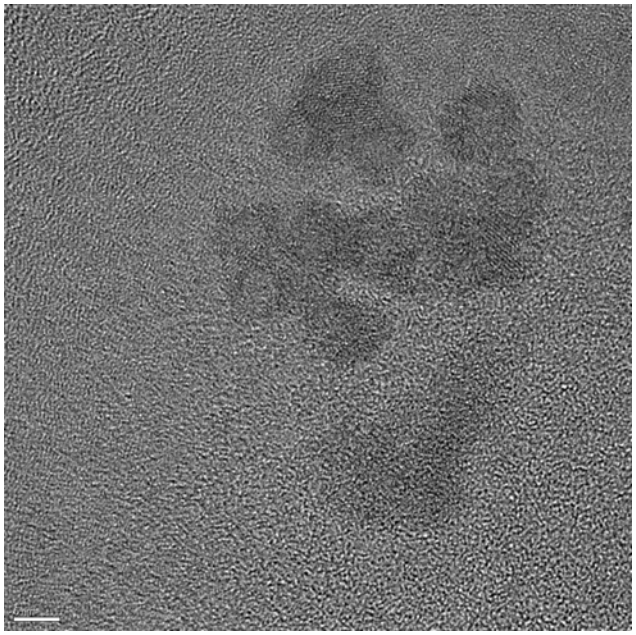

Figure E.6. TbS nanocrystals imaged using the JEOL 200CX.

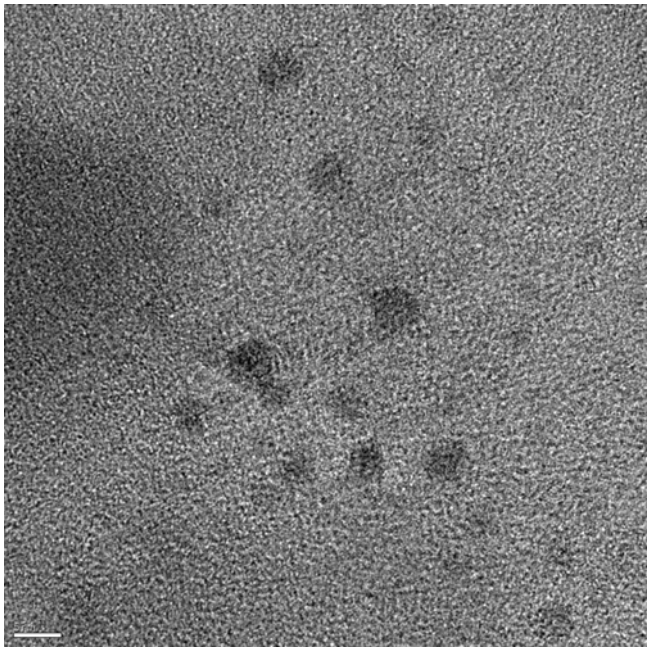

Figure E.7. TbS nanocrystals imaged using the JEOL 200CX.

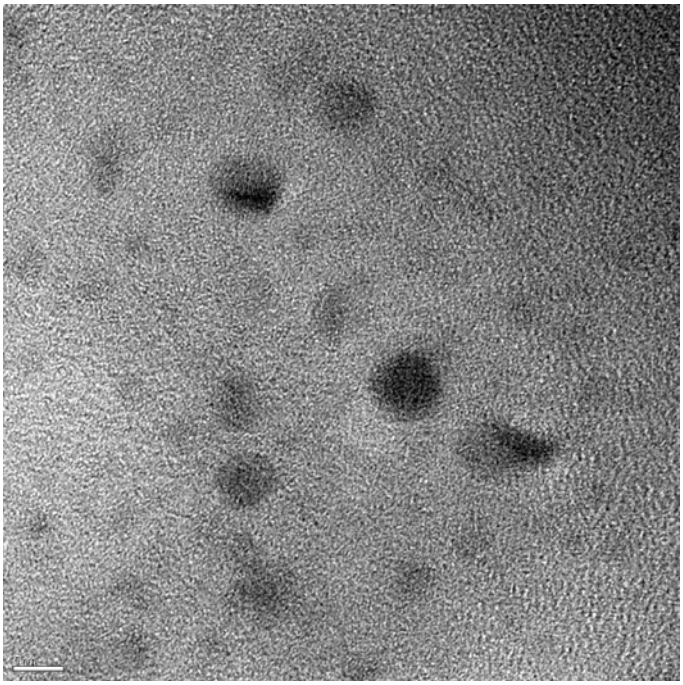

Figure E.8. TbS nanocrystals imaged using the JEOL 200CX.

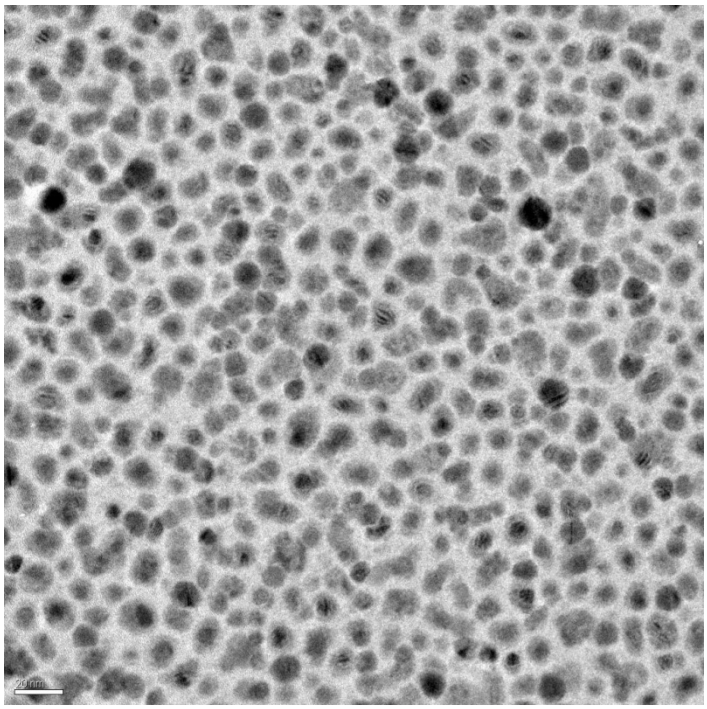

Figure E.9. High resolution TEM of TbS using JEOL 2100 CF.

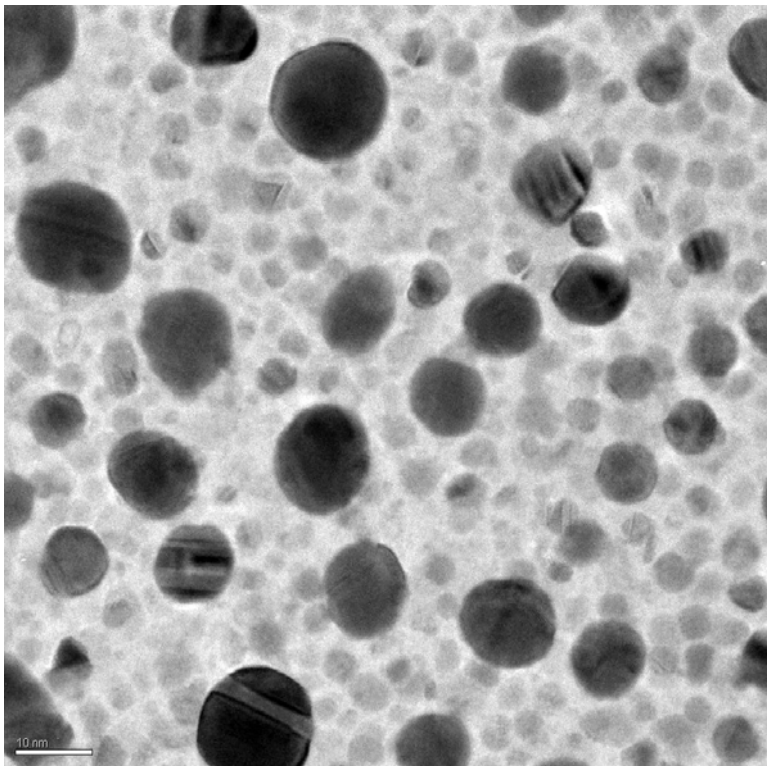

Figure E.10. High resolution TEM of TbS using JEOL 2100 CF.

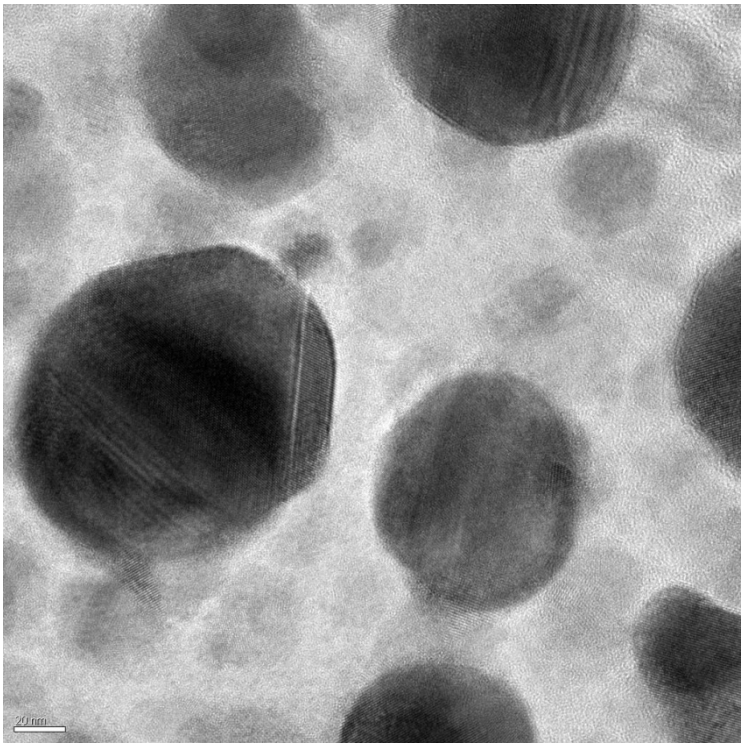

Figure E.11. High resolution TEM of TbS using JEOL 2100 CF.

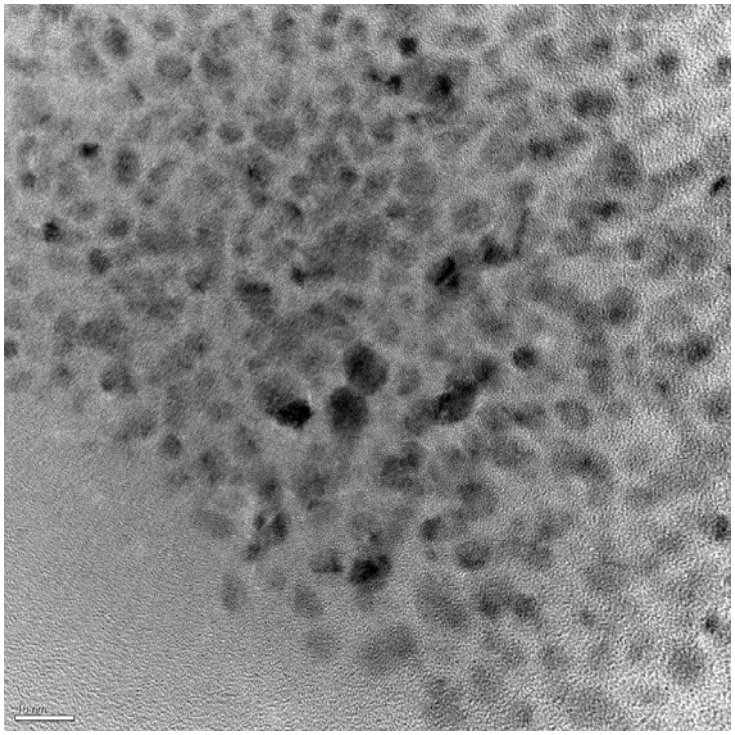

Figure E.12. High resolution TEM of EuS using JEOL 2100 CF

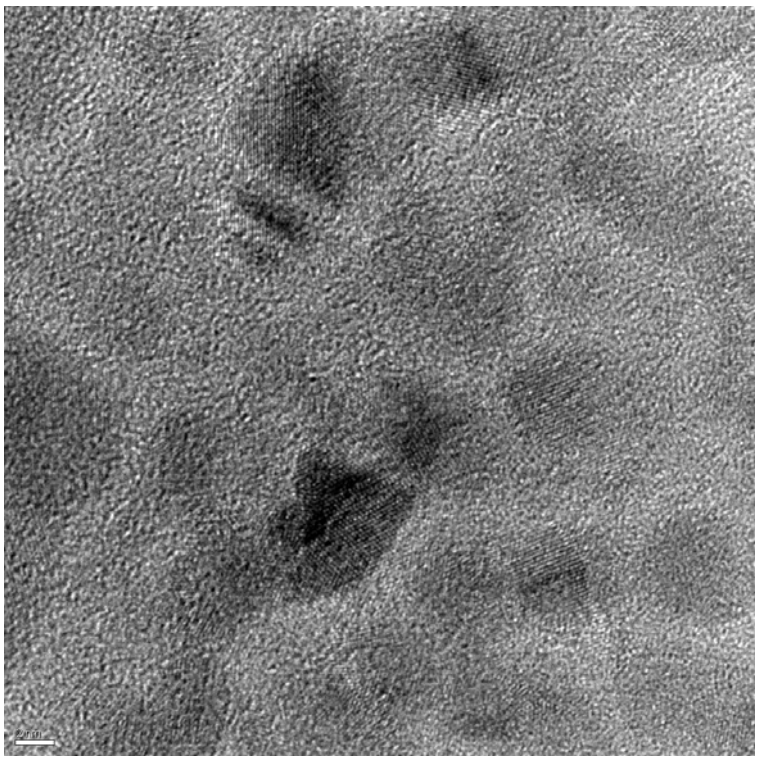

Figure E.13. High resolution TEM of EuS using JEOL 2100 CF

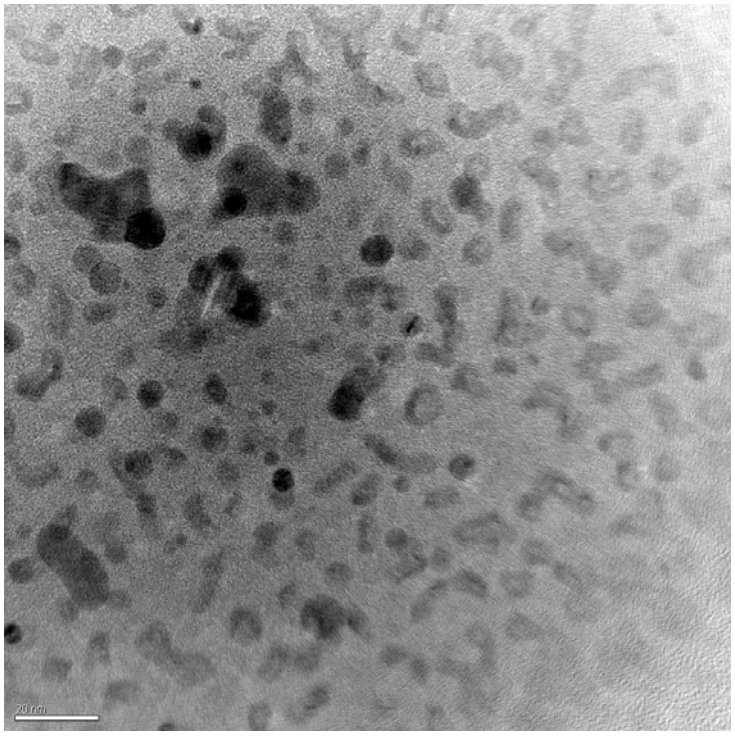

Figure E.14. High resolution TEM of NdS using JEOL 2100 CF.

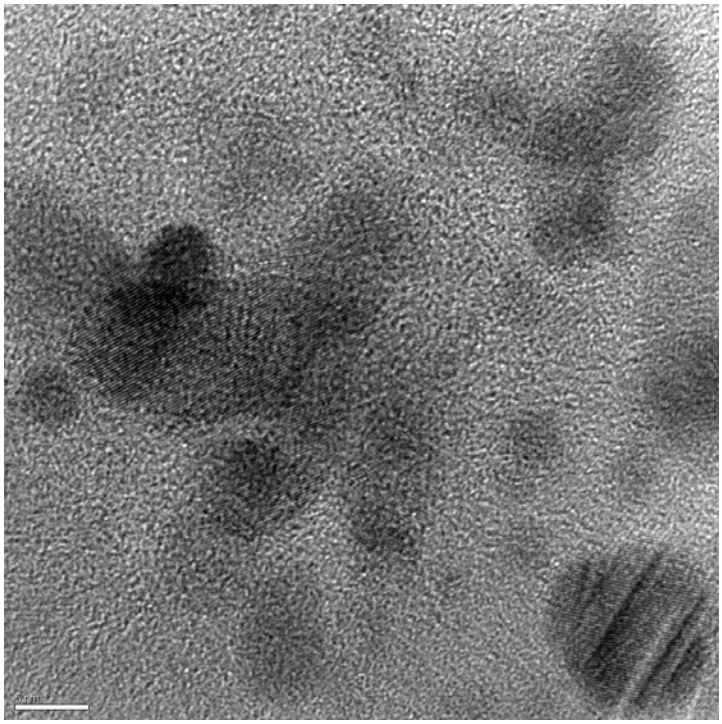

Figure E.15. High resolution TEM of NdS using JEOL 2100 CF.

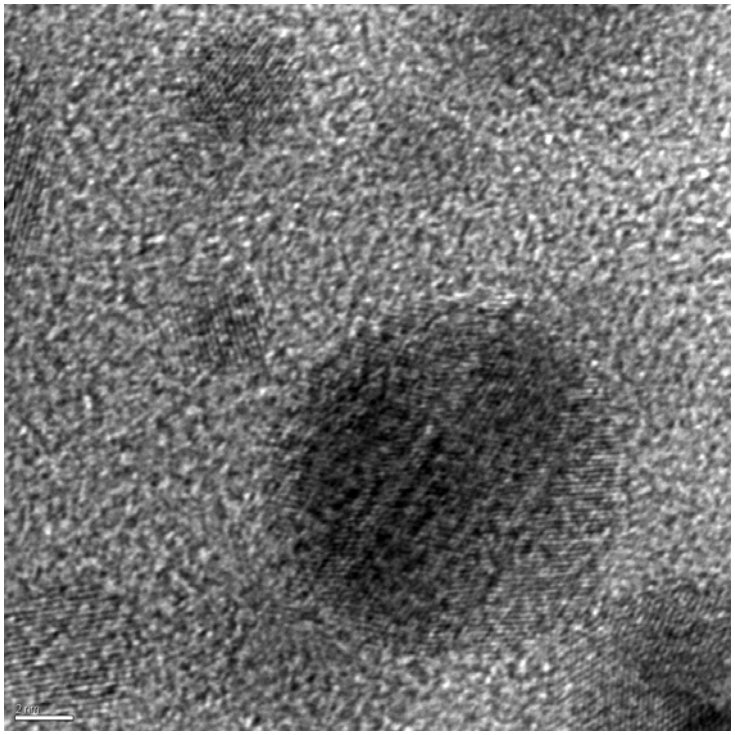

Figure E.16. High resolution TEM of NdS using JEOL 2100 CF.

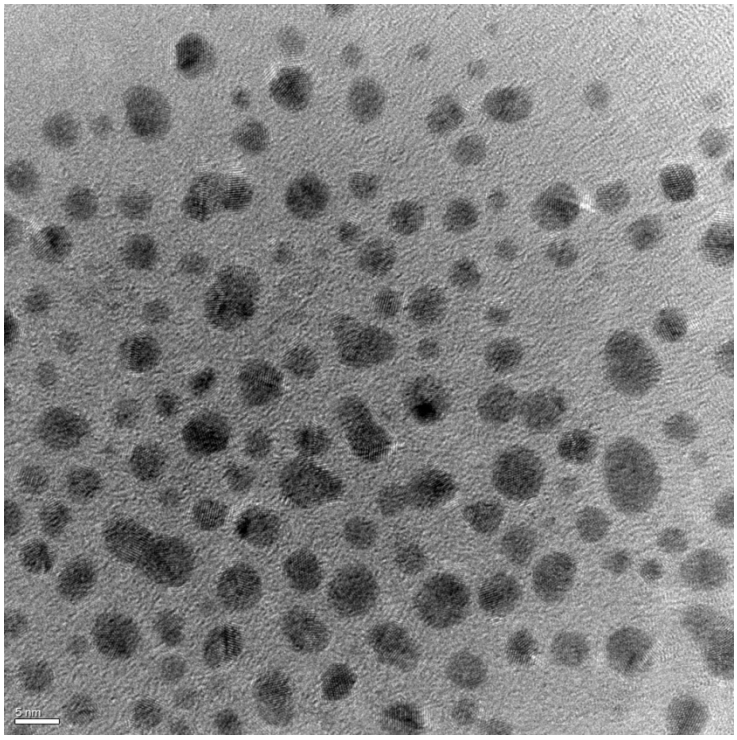

Figure E.17. High resolution TEM of YbS using JEOL 2100 CF

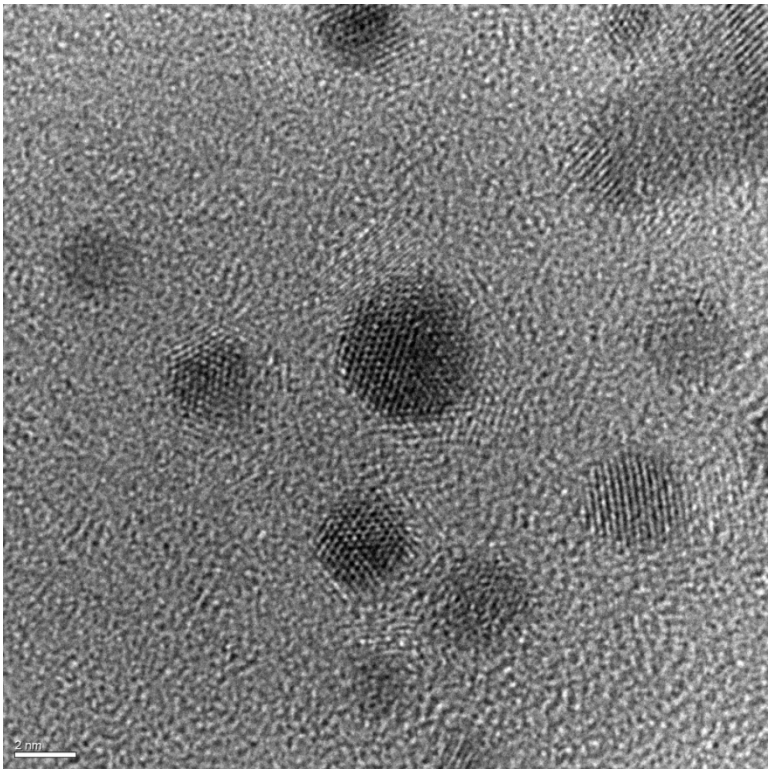

Figure E.18. High resolution TEM of YbS using JEOL 2100 CF

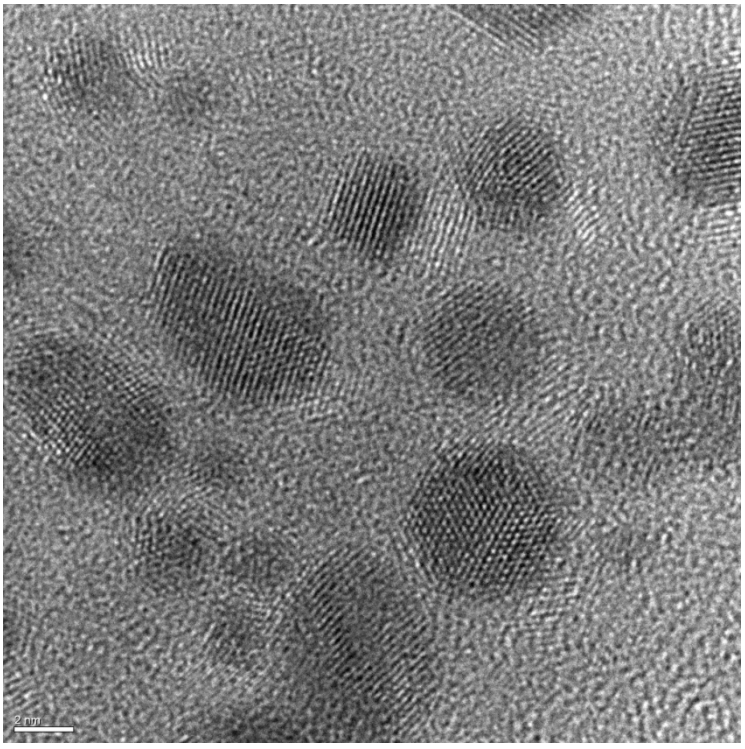

Figure E.19. High resolution TEM of NdS using JEOL 2100 CF

APPENDIX F

JUSTIFICATION FOR DTPA EXCHANGE PROCEDURES

We have thus far investigated many avenues for purifying our nanocrystals so that we might obtain information regarding the composition and/or structure (XPS/XRD/ICP/TEM). These purification methods have included column chromatography, precipitation procedures with various solvent systems, and modification of synthetic protocols. To date our success has been limited. We have therefore decided that we should attempt surface exchange procedures in order to purify our products and rid them of their excess organic solvents. DTPA is our first choice for modification of our nanocrystal surface. Ideally the DTPA will replace/displace any TOPO/TOP which might be on the surface of the particles. We will use extraction methods to achieve this.

A batch of TbS nanocrystals was synthesized and briefly analyzed for spectroscopic evidence of the presence of actual nanocrystals. A concentrated chloroform solution of nanocrystals was prepared. From this concentrated solution, 2 ml was placed into each of 5 vials.

A separate DTPA solution was prepared by deprotonating DTPA using KOH (a molar ratio of 1:5 in order to deprotonated all acidic protons). The solution was prepared in water and the pH was tested using pH paper to insure its basicity.

3 ml of DTPA was added to the 2 ml of nanocrystal solution in chloroform. The samples were then treated in a number of different ways in order to compare methods for surface exchange. The treatments are outlined per sample below.

Sample 10-1A: Sample was placed in a sonicator while heating overnight

Sample 10-1B: Sample was left to stir in ambient conditions overnight

Sample 10-1C: Sample was placed in a sonicator overnight (no heat)

Sample 10-1D: Sample was placed in a shaker while heating to 50°C for 3 hours

Sample 10-1E: Sample was placed in a shaker while heating to 50°C overnight

After samples were prepared, they were centrifuged to ensure separation of the aqueous and chloroform layers, and the aliquots were separated. All samples, aqueous and chloroform were then run on the spex for comparison. The 545 nm band of terbium was integrated and the ratios calculated for each sample (ratios are based on the particular aliquot with respect to the overall sample). The data is shown below.

Table F.1 Baselined integrated intensities

Sample	Integrated Intensity	Ratio	Percentage of Overall Sample
10-1ac	1224440	0.921554292	92.15542924
10-1aw	104228.3	0.078445708	7.844570756
10-1bc	489741.1	0.875963663	87.59636635
10-1bw	69347.27	0.124036337	12.40363365
10-1cc	506574.3	0.819859863	81.98598632
10-1cw	111304.8	0.180140137	18.01401368
10-1dc	12944861	0.970314627	97.03146274
10-1dw	396029.3	0.029685373	2.968537265
10-1ec	14291387	0.974183391	97.41833914
10-1ew	378732.7	0.025816609	2.581660864

Table F.2. Non-baselined integrated intensities

Sample	Integrated Intensity	Ratio	Percentage of Overall Sample
10-1ac	3234660.4		
10-1aw	21840.005	0.921554	92.15543
10-1bc	20362.314	0.078446	7.844571
10-1bw	270727.64	0.875964	87.59637
10-1cc	11169.031	0.124036	12.40363
10-1cw	129397.29	0.81986	81.98599
10-1dc	23204.435	0.18014	18.01401
10-1dw	7364896.7	0.970315	97.03146
10-1ec	108538.19	0.029685	2.968537
10-1ew	130464.84	0.025817	2.581661

Looking at the data and comparing the ratio or overall percentage of the nanocrystal (based on integrated intensity of 545 nm band of terbium), it seems as though the most effective method for this particular surface exchange procedure was the sonication overnight with NO heat. This achieved 82% of the sample staying in chloroform, but an impressive 18% going into the aqueous layer. The method was closely followed by the stirring method (samples were stirred on a stir plate overnight) which yielded 87.5% of the sample signal in chloroform and 12.5% in the aqueous DTPA sample. The later method is probably the most surprising in that the layers never really seemed in contact with each other and so one might not expect a great deal of mixing between the layers in order for the extraction process to occur.

This data does look promising; however there are a few issues which we may be neglecting here. First, we do not know if the samples are actually being coated with the DTPA or if we are simply getting micelle like conglomerates in the aqueous layer (initial experiments with the Weber group might suggest this, however they are inconclusive as they were preliminary data collected under different settings – buffer solution rather than DTPA). Another

possible problem we might face is that a great deal of sample will be needed to recover adequate amounts of DTPA coated materials for analysis.

Upon further spectroscopic study of our DTPA/Nanoparticle solution, it appears as though we may be simply binding free lanthanide cations with the DTPA (see spectra above). Upon monitoring the band gap emission we observe the typical excitation spectra for nanocrystals, however when monitoring the terbium emission centered at 545 nm we observe what appears to be a direct excitation profile of terbium. These findings introduce many new questions/problems. How are we monitoring band gap emission in the aqueous phase but the excitation spectra illustrates direct excitation of terbium. This would make more sense if these particles were ZnS doped, however being that the terbium is part of the material that forms the band gap, and therefore we must consider this closely. We need to analyze each solvent sample further to better understand their components.

The next step in this project should be to attempt to extract the nanoparticles back out of the aqueous layer. We can then attempt to re-dissolve them in water or just take them for analysis using XRD and XPS to test the sample structure and composition. Another thought is that we might want to look into solvents that maybe both DTPA and nanocrystals are slightly soluble in. If the substances are in the same phase it might be a better environment for surface exchange to occur.